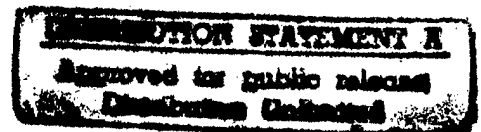# STUDIES OF THE EFFECT OF MICROSTRUCTURE ON THE DYNAMIC BEHAVIOR OF GRANULAR AND PARTICULATE MEDIA

(Final Report)

by

Arun Shukla and Martin H. Sadd

Department of Mechanical Engineering & Applied Mechanics
University of Rhode Island
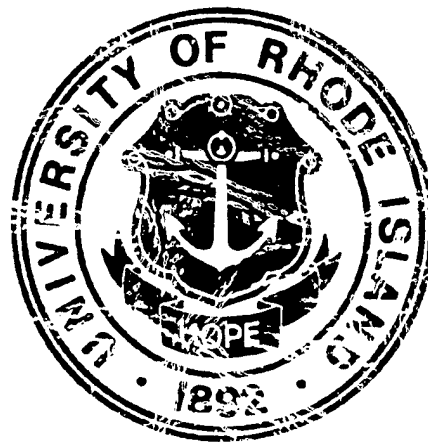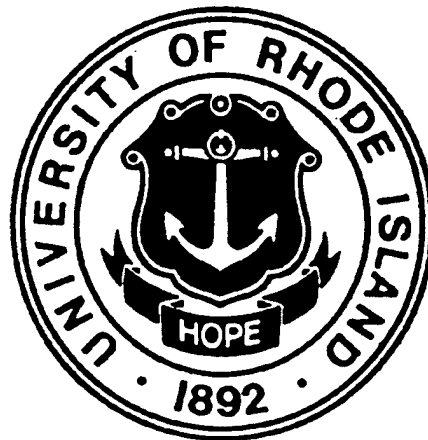Kingston, RI 02881

October 1996

STUDIES OF THE EFFECT OF MICROSTRUCTURE ON THE DYNAMIC BEHAVIOR OF GRANULAR AND PARTICULATE MEDIA

(Final Report)

by

Arun Shukla and Martin H. Sadd

Department of Mechanical Engineering & Applied Mechanics
University of Rhode Island
Kingston, RI 02881

October 1996

DTIC QUALITY INSPECTED 3

REPORT DOCUMENTATION PAGE

1. AGENCY USE ONLY *(Leave blank)*	2. REPORT DATE October 1996	3. REPORT TYPE AND DATES COVERED Final Report

4. TITLE AND SUBTITLE Studies of the Effect of Microstructure on the Dynamic Behavior of Granular and Particulate Materials	5. FUNDING NUMBERS F49620-93-1-0209
6. AUTHOR(S) Arun Shukla Martin H. Sadd	

7. PERFORMING ORGANIZATION NAME(S) AND ADDRESS(ES) Department of Mechanical Engineering & Applied Mechanics Wales Hall, 92 Upper College Road University of Rhode Island Kingston, RI 02881	8. PERFORMING ORGANIZATION REPORT NUMBER AFOSR 96

9. SPONSORING/MONITORING AGENCY NAME(S) AND ADDRESS(ES) Air Force Office of Scientific Research Particulate Mechanics Program Bolling Air Force Base Washington, DC 20332 N/A	10. SPONSORING/MONITORING AGENCY REPORT NUMBER 93-1-0209

11. SUPPLEMENTARY NOTES

12a. DISTRIBUTION/AVAILABILITY STATEMENT Approved for Public Release: Distribution is unlimited	12b. DISTRIBUTION CODE

13. ABSTRACT *(Maximum 200 words)*

Results are presented of a three year experimental and theoretical study dealing with wave propagation in particulate materials. The experimental program used dynamic photoelasticity, strain gages and fiber optic sensors to collect information on model granular materials. The theoretical program developed a numerical model using discrete element methods (DEM) to simulate the dynamic behavior of granular media. The general goal of the research program was to determine relationships between granular fabric and wave propagational characteristics.

DEM simulations on large two-dimensional systems with circular particles, investigated relationships of branch, wave and void vector fabric with wave speed and attenuation. Both experimental and numerical studies were conducted on model assemblies with elliptical particles. Results of the experimental study indicated that both branch and contact normal vectors play an important role in determining wave

(over)

14. SUBJECT TERMS Particulate media, wave propagation, dynamic contact load, dynamic photoelasticity, strain gages, discrete element method, wave velocity, explosive loading			15. NUMBER OF PAGES 258
			16. PRICE CODE

17. SECURITY CLASSIFICATION OF REPORT Unclassified	18. SECURITY CLASSIFICATION OF THIS PAGE Unclassified	19. SECURITY CLASSIFICATION OF ABSTRACT Unclassified	20. LIMITATION OF ABSTRACT SAR

ACKNOWLEDGEMENTS

Table of Contents

CHAPTER 1

DISCRETE ELEMENT STUDIES OF THE RELATIONSHIP
OF FABRIC TO WAVE PROPAGATIONAL BEHAVIORS

1.1 Summary

Wave propagation in granular materials is numerically studied through discrete element simulation. Two-dimensional model material systems composed of large numbers of circular particles were numerically generated. The particles in these model materials were randomly distributed with a biasing algorithm to produce fabric anisotropy so as to create preferred directions within the material. Wave motion is introduced through dynamic loadings to appropriate boundary particles to produce horizontal and vertical plane wave propagation within each model material. Discrete element simulation with a nonlinear hysteretic interparticle contact law is used to model the dynamic behavior of the model granular systems, and this yields information on the wave speed and amplitude attenuation. Through the investigation of several model systems, relationships are established between wave propagational characteristics and granular microstructure or fabric. Specific fabric measures which were used included branch vectors, path microstructures, and void characteristics. Distributions of these fabric descriptors were determined, and comparisons and correlations were made with the discrete element wave propagation results. Conclusions of this study indicated that while all three fabric measures provided some degree of correlation with the wave motion behaviors, the void fabric descriptor produced the best correlation for the assemblies under investigation.

1.2 Introduction

Granular materials are commonly described as a collection of distinct particles which can displace from one another with some degree of independence and which interact basically through contact mechanisms. The discrete nature of such materials establishes non-continuous and discrete load transfer behavior which can be related to the material microstructure or fabric. For example, it has been well establishe (Oda et.al 1982, Shukla et.al 1988 and Zhu et.al 1991) that load transfer in a dry cohesionless granular medium occurs

1

along a complex network of discrete paths. With regard to wave propagation, granular materials create a structured wave-guide network through which mechanical energy is transferred. Along a given wave path, the dynamic load transfer is determined by the contact interactions between neighboring particles. The propagational characteristics of wave speed, amplitude attenuation and wave form dispersion are thus related to the local fabric and the established wave paths.

Interest in dynamic geomechanics problems has produced considerable research over the past several decades, and numerous articles have appeared dealing with wave propagation in sand and rock materials. More recently over the past decade or two, research on granular material behavior has focussed on using micromechanical modeling incorporating local mechanics at the particulate level to predict the macro-constitutive response. A considerable amount of work (Duffy et.al 1957, Deresiewicz et.al 1958, Duffy et.al 1959, Hardin et.al 1989, Digby 1981, Thornton et.al 1986, Petrakis et.al 1988a, 1988b, Kishino 1988, Chang et.al 1990 and Walton 1987) has been done in modeling granular media as arrays of idealized (circular or spherical) elastic particles with the goal of determining equivalent macro elastic constitutive constants from the local interparticle contact behavior. Another large body of research dealing with microstructural effects in particulate media has used the approach of developing *fabric tensor theories*. Fabric of granular materials is normally described as the spatial arrangement of the solid particles and associated voids. Pioneering work by Oda, Nemat-Nasser, and Mehrabadi (1982 and 1983), and later followed by many other studies, e.g. Bathurst and Rothenburg (1988), Konshi and Naruse (1988) , Satake (1992) have developed several types of tensorial quantities which characterize local microstructure (fabric) and which can be used to construct constitutive laws to predict observed behaviors. Although some success in linking fabric to mechanical behavior has been obtained, no unique choice of fabric description has been universally accepted which can adequately describe the general mechanical response of particulate media.

Some research has categorized fabric into two types: *orientation fabric* (orientation of individual particles) and *packing fabric* (mutual relation of individual particles). Orientation fabric may be quantitatively defined by a vector mean direction and a vector magnitude to characterize orientation of non-spherical or non-circular particles. This fabric measure is commonly represented by an angular measure (with respect to a reference

2

direction) of the long axes of individual particles. Packing fabric measures have included *branch vectors, normal contact vectors, coordination or contact numbers, void characteristics, etc.* Examples of these fabric measures are illustrated schematically in Figure 1.1. Some of these fabric measures are solely *kinematical* in nature, determined primarily by the particle shape and packing geometry. Other measures such as those related to the contact conditions are *kinetic*, and are determined by the particle material and shape properties and also by the contact surface conditions.

Figure 1.2 shows a high-speed photograph of the dynamic photoelastic fringe patterns associated with an actual wave moving (from top to bottom) through a model particulate medium containing some of these fabric structures. Using such experimental techniques, it has been observed (Oda et.al 1982, Shukla et.al 1988 and Zhu et.al 1991) for both static and dynamic loading conditions that particulate materials transmit mechanical loadings along a series of complex discrete paths. These discrete paths are established, in relation to the loading direction, by many of the microstructural variables mentioned, and therefore local wave propagation is determined by granular fabric through the creation of local wave guides.

This article presents the results of a theoretical/numerical study which examines the relationship of granular fabric with wave propagational variables. The model granular materials under study were large random assemblies of circular particles created numerically using random media generator codes. Although these assemblies involved random assembly procedures, deliberate biasing was used in the generation process in order to construct materials with a variety of microstructures. Wave propagation through these model assemblies was simulated using the computational scheme of *discrete element modeling*. This study focusses primarily on the effects of packing fabric as measured by: *branch vector distributions* (which for circular particles coincide with normal contact vectors), *path fabric*, and *void polygon fabric*.

The modeling scheme presented here can be thought of as a *meso-domain* approach, attempting to bridge the micro-macro responses. Micromechanical modeling at the particulate level is applied to a sufficiently large assembly of particles such that averages of particular wave propagational characteristics will be meaningful. This issue is related to the *homogenization process* as discussed by Bourbié, Coussy and Zinszner (1987) in which they point out that

3

macroscopically meaningful results can only be found if the sample size is much larger than the minimum homogenization volume.

1.3 Discrete Element Method

Originally developed by Cundall et.al (1979), the *discrete element method* is a numerical scheme that has been successfully used to simulate the response of granular media by modeling the dynamic behavior of large assemblies of circular disks, spheres, and blocks (Thorton et.al 1988, Ting et.al 1989, Williams 1988, Walton et.al 1991, Ng et.al 1992, Rothenburg et.al 1993 and Sadd et.al 1993). The method makes simplifying constitutive assumptions for each particle (commonly assuming rigid body behavior) and then uses Newtonian mechanics to determine the translational and rotational motion of each particle in the assembly. In order to establish inter-particle contact behavior, the assumed rigid particles are allowed to have small overlapping contact, and thus contact forces are developed as a result of particular stiffness and/or damping characteristics. The technique establishes a discretized time stepping numerical routine, in which granule velocities and positions are obtained through numerical integration of the computed accelerations. Using the principle of *causality*, it follows that during an appropriately small time step, disturbances cannot propagate from any disk further than its immediate neighbors. Under these conditions, the method becomes explicit, and therefore at any time increment the resultant forces (and thus the accelerations) on any particle are determined solely by its interactions with its contacting neighbors. For applications to wave propagation, the movements of the individual disks are a result of the propagation through the medium of disturbances originating at particular input loading points. Consequently, the wave speed and amplitude attenuation (intergranular contact force) will be functions of the physical properties of the discrete medium, i.e. the microstructure or fabric.

The general concept of the method may be explained by considering a general two-dimensional particulate assembly as shown in Figure 1.3. Isolating attention to the i-th particle and applying Newton's laws yields

$$\sum_{j=1}^{N} F^{ij} + F^{i} = m_i \ddot{x}_i$$

$$\sum_{j=1}^{N} M^{ij} + M^{i} = I_i \ddot{\theta}_i$$

(1.1)

where F^{ij} are the j-contact forces on the i-th particle, F^{i} represents any non-contacting forces on particle i, M^{ij} are the moments (about the particle's mass center) resulting from contact forces F^{ij}, M^{i} is the resultant moment from any non-contacting forces, m_i is the particle mass, and I_i is the mass moment of inertia. With given contact and non-contact forces, the linear and angular accelerations of the i-th particle can thus be determined from this system of equations. With the accelerations known, the velocities and displacements may be obtained through numerical integration using simple finite differencing schemes.

It is obvious that the contact response between neighboring particles plays a very important role in the use of this numerical method to simulate wave propagation through granular materials. Past research, Sadd et al. (1993) has investigated the use of several contact laws within the discrete element modeling scheme. Establishing a local normal and tangential coordinate system at each contact between adjacent particles, a contact law can be constructed relating interparticle force to the overlapping deformation and deformation rate. In general such a contact law between adjacent particles could be written as

$$F_n^{ij} = F_n^{ij}(\delta_n, v_n, \delta_t, v_t)$$

$$F_t^{ij} = F_t^{ij}(\delta_n, v_n, \delta_t, v_t)$$

(1.2)

where δ_n and δ_t are the relative normal and tangential displacements between particles i and j, and v_n and v_t are the relative normal and tangential velocities. Contact relations (1.2) may also be *history dependent*, and a Coulomb-type friction law is commonly incorporated to place limits on the tangential response. Specific forms of such contact relations have included (Sadd et.al 1993) linear, non-linear, and non-linear hysteretic laws. Results have indicated that the non-linear hysteretic deformation law provided simulation results which compared favorably with experimental data (Sadd et.al 1993), and this particular law has been chosen for use in the current study.

1.4 Branch Vector Fabric

One popular fabric measure used for the static response granular materials has been the *branch vector*. This measure is defined as the vector drawn between the mass centers of contacting particles, see Figure 1.1. For the circular particles under study, dynamic loads are transmitted primarily through contact points which lie along branch vectors, and thus this fabric measure appears to be appropriate for wave propagation problems. Thus it seems reasonable to assume that branch vector distributions could be related to the wave propagational behaviors in such media.

To investigate such relationships, several large random particulate media assemblies were numerically generated. All assemblies contained 25 mm diameter particles of equal size. Generation schemes used various algorithims (Tai 1993) to construct model assemblies with different microstructures as reflected in the distributions of branch vectors These distributions can be classified as *strongly, moderately and weakly anisotropic* model systems. Six such assemblies are shown in Figure 1.4; where assembly S-1 was generated by a strongly anisotropic generator, assemblies M-1 and M-2 were constructed by a moderately anisotropic generator, and a weakly anisotropic scheme was used to construct assemblies W-1, W-2, and W-3. Table 1-1 lists additional parameters for each of these assemblies including the total numbers of particles, the void ratio (volume of void / volume of particle) and the average coordination number (average number of contacts per particle). Assembly S-1 has the highest void ratio of 0.43 and lowest coordination number of 2.87, while W-3 has the lowest void ratio of 0.22 and the highest coordinate number of 4.30.

Although it would be desirable to develop general relationships between fabric vectors/tensors and wave propagational variables, the current state of knowledge requires a simpler, pragmatic approach. Thus in order to investigate the relationship between branch vector fabric and wave propagational characteristics, all unit branch vectors were calculated for each assembly. Polar distributions of these branch vectors were then determined and are shown in Figure 1.5. In order to quantify such distributions, a *branch vector ratio*

$$R_b = \frac{\sum |b_y|}{\sum |b_x|} \tag{1.3}$$

was calculated, where b_x and b_y are the horizontal and vertical components of the unit branch vectors, and the summations go over all defined branch vectors in a given model assembly. Values of the ratio R_b for the six assemblies are listed in Table 1-1. For assembly S-1, all branch vectors are concentrated in the region approximately defined by $\pm 30°$ from the vertical direction. No branch vector is found along the horizontal direction, and R_b is 2.06 for this assembly. The branch vector distributions for assemblies M-1 and M-2 primarily occur in vertical and horizontal directions with preference in vertical direction, and both assemblies have the same R_b ratio of 1.19. For the weakly anisotropic assemblies W-1, W-2, and W-3, no highly preferred branch vector directions were found, and the branch ratios for these cases were all close to unity.

Each of the six constructed assemblies were subjected to dynamic loadings to create a wave propagation situation, and this behavior was modeled using our discrete element wave propagation code. The simulations involved the comparison of the propagation of plane type waves moving along horizontal (x-direction) and vertical (y-direction) paths in the generated assemblies. To generate the plane vertical wave, all particles along the bottom of the assembly were simultaneously loaded in the vertical direction with a transient input loading of triangular time history. The input pulse had a peak value of 1 kN and a period of 60 µs. From a continuum point of view, this type of loading will input primarily a planar P or dilatational wave. Of course, as the combined dynamic signal moves through the granular medium, some small tangential interparticle contact forces will develop, and thus at the micro-level, there will be some partitioning of the signal into a *shearing mode*. We would not however, classify this mode as a shear wave component. The generated input for the horizontal wave was created in a similar fashion.

To calculate the transmitted or output wave pulse, an imaginary horizontal or vertical line was drawn near the boundary opposite to where the input loadings were applied. If a branch vector of a pair of particles in contact or potential contact is intercepted by this imaginary line, the normal contact load component perpendicular to the imaginary line, i.e. either F_x or F_y, was recorded. In this fashion, the contribution of the individual particle contacts could be determined, and these recorded loads were then summed and normalized with respect to the sum of the peak values of the input loadings. These normalized contact loads or *load transimission ratios* for horizontal and vertical waves are thus given by

$$\bar{F}_x(t) = \frac{\sum F_x(t)}{\sum F_{peak\ input}}$$

$$\bar{F}_y(t) = \frac{\sum F_y(t)}{\sum F_{peak\ input}}$$

(1.4)

where the summation in the numerator is over the number of branch vectors intercepted by the imaginary line, while the summation in the denominator is over the number of input loadings. In order to compare these horizontal and vertical transmission ratios, the ratio of their peak values may be used, i.e.

$$R_F = \frac{\{\bar{F}_y(t)\}_{peak}}{\{\bar{F}_x(t)\}_{peak}}$$

(1.5)

This ratio is given in Table 1-1 for each of the six assemblies under study.

Figure 1.6 shows the transmission results of a discrete element wave propagation simulation for the media model S-1, and it is quite apparent that the vertical, y-component of load transimission is predominant for this assembly. Although it is not discernable from the figure, the wave speed as determined by the arrival time of these averaged transmission profiles is different for the two propagational directions, with a vertical wave speed approximately three times that of the horizontal motion. These results correlate with the branch vector distribution plot shown in Figure 1.5(a), thus indicating that the branch vector is related to the transmission of waves in particulate materials. Similar results occur for the moderately anisotropic assemblies M-1 and M-2; however, for these cases the fabric ratio R_b fails to correlate completely with the numerical model simulation results. For example, both the peak transmission ratios R_F and the wave speeds indicate that model assembly M-2 is more anisotropic than assembly M-1, but unfortunately this does not correlate with their branch fabric ratios as given in Table 1-1. The wave transmission results for the weakly anisotropic assembly W-2 are shown in Figure 1.7. Table 1 indicates that the R_F ratio for this case is much smaller than for the strongly and moderately anisotropic assemblies, and this correlates reasonably well with branch vector fabric.

8

1.5 Path Fabric

As mentioned previously, when waves propagate through granular media, the local or micro-dynamic loads are transferred through specific chains of particles linked through contact. Between these special chains, particles may carry little or no load. It would be expected that such load carrying paths which are relatively straight would act as a better propagator of waves than would a highly irregular path. Thus it appears that the local microstructure of load carrying paths within a particulate medium would also be an appropriate fabric measure to correlate with wave propagation.

In order to quantify the path fabric concept, a path is defined as a set of continuous branch vectors of particles in contact as shown in Figure 1.8. It has been observed experimentally by Shukla and Damania (1987) that for dry cohesionless materials, dynamic load can be transferred along a path only when every pair of neighboring branch vectors b_i and b_j in the path satisfy the relationship

$$b_i \cdot b_j > 0 \tag{1.6}$$

which means that the *branch angle* defined in Figure 1.8 is less than $90°$. Therefore, a *transferable* or *propagator load path* can be defined as a path in which the dot product of all pairs of neighboring branch vectors is positive.

One method of constructing a path fabric measure, based on the straightness of the path, would be to sum the dot products of all adjacent unit branch vectors in a given propagator path. For example, a path fabric measure between two arbitrary particles could be expressed as

$$F_p = \sum \frac{1}{\sum \dfrac{1}{b_i \cdot b_j}} \tag{1.7}$$

where the inner summation is over all connecting particles on a given path, while the outer summation is over all possible paths. For the special case of a single straight chain of particles, there exists only one path between any two particles, and equation (1.7) gives F_p = $1/(N-1)$, where N is the total number of particles in the path. This would constitute a

9

minimum value of F_P among all assemblies of single particulate chains.

Another method to construct a path fabric measure is to use x and y branch vector components by defining the following quantities between two arbitrary particles

$$\bar{P}_x = \frac{\sum \sum |b_x|}{\sum \sum 1}$$

$$\bar{P}_y = \frac{\sum \sum |b_y|}{\sum \sum 1}$$

(1.8)

where outer summations are over all possible paths between the two arbitrary particles, and inner summations are over individual paths. For granular media simulated by circular particles of the same size, the values of $\bar{P}_x$ and $\bar{P}_y$ will not be larger than the particle diameter, and will equal to the diameter only when the path is a straight chain along the x or y direction.

In order to do the necessary calculations specified by equations (1.7) or (1.8), considerable computational effort is required for the six assemblies under study. All propagator paths must be determined in these assemblies between input and output particles for both horizontal and vertical wave propagation simulations. Such calculations for assemblies with 10^3 particles typically yield 10^7 - 10^8 total possible paths. In order to reduce the size of this computational problem, the model assemblies are divided into sub-regions, and paths outside prescribed boundaries will be discarded.

Figure 1.9 illustrates such a scheme for the calculation of vertical propagation paths. A particular vertical propagator path is shown between a pair of arbitrary input and output particles. Equation (1.8) for this vertical path can be written as

$$\bar{P}_x = \frac{\sum \sum P_x}{\sum \sum 1} = \frac{N_{path}}{\sum_{path} N_{particle}} P_x$$

$$\bar{P}_y = \frac{\sum \sum P_y}{\sum \sum 1} = \frac{N_{path}}{\sum_{path} N_{particle}} P_y$$

(1.9)

where P_x and P_y are the x and y components of the vector from the input particle to the output particle, N_{path} is the total number of paths between the input and output particles , and $N_{particle}$

is the total number of particles along the given path. The determination of the number of paths and the number of particles on a given path may be carried out through calculations in subregions (Tai 1993), e.g. regions I, II and III shown in Figure 1.9. It should be pointed out that a particular vertical path under consideration will be discarded if it extends beyond a vertical zone of fixed width centered at the initiating input particle within a subregion. This is reasonable since a highly tortuous path will transmit negligible load, and by discarding these paths a reduction of computational effort will result. The vertical path fabric measure for the whole assembly can then be obtained by summing the values given by equation (1.9) for all the paths between all input and output boundary particles.

Using equation (1.9), the vertical and horizontal path fabrics of each of the six model assemblies have been computed. The ratios of the summations of vertical fabric to the summations of horizontal fabric

$$R_p = \frac{\sum \bar{P}_y}{\sum \bar{P}_x}$$

(1.10)

are given in Table 1-1. For the strongly anisotropic assembly S-1, there is no contiguous path along the horizontal direction and this gives a ratio of infinity, which correlates with the discrete element results which show that the horizontal wave is almost blocked. The R_p ratio has values of 5.88 and 2.08 for the two moderately anisotropic assemblies M-1 and M-2. Thus, there are more paths along the vertical direction rather than the horizontal direction, and waves prefer to propagate along the vertical direction in these assemblies as predicted by discrete element analysis. However, as with the branch vector case, the path fabric also fails to correlate with the stronger wave propagation anisotropy of assembly M-2 with respect to assembly M-1. The reason for this lack of correlation may be due to gap closing during the passage of the wave motion, and such phenomena can change the path fabric. Taking assembly M-2 as an example, during the process of vertical wave propagation, it appeared from our discrete element modeling that more than 40 new contacts had been created. The R_p ratios of the weakly anisotropic assemblies W-1, W-2, and W-3 are 0.95, 1.00, and 1.16, respectively, which indicates that these assemblies are indeed weakly anisotropic. These ratios provide a reasonable correlation between path fabric and wave behaviors for the W-

11

assemblies.

1.6 Void Polygon Vector Fabric

The previous two sections proposed fabric measures associated with the particles of granular systems. However, in addition to the solid particle phase, a granular material also consists of a void phase, and thus it would seem reasonable that a fabric measure based on voids could be useful to correlate with wave propagation. This concept of using voids to characterize fabric was first proposed by Konishi and Naruse (1988) for the static response of particulate materials.

To describe a void with N curved segments, a polygon is used as shown in Figure 1.10. The polygon consists of the branch vectors linking the particles around a void, and thus a *void polygon* is represented by this special group of branch vectors. Assuming that a void surrounded by N particles has N branch vectors $b^{(1)}$, $b^{(2)}$ ..., and $b^{(N)}$, a *local void tensor* can be defined as

$$p_{ij} = \sum_{k=1}^{N} b_i^{(k)} b_j^{(k)} \tag{1.11}$$

where $b_i^{(k)}$ are the components of $b^{(k)}$. The principal values of this void tensor are given by

$$p_1, p_2 = \frac{1}{2} \sum_{k=1}^{N} b_k^2 \pm \sqrt{\left(\sum_{k=1}^{N} b_k^2 \cos 2\theta_k \right)^2 + \left(\sum_{k=1}^{N} b_k^2 \sin 2\theta_k \right)^2} \tag{1.12}$$

and the major principal direction is calculated as

$$\theta_p = \frac{1}{2} \arctan \left[\frac{\left(\sum_{k=1}^{N} b_k^2 \sin 2\theta_k \right)}{\left(\sum_{k=1}^{N} b_k^2 \cos 2\theta_k \right)} \right] \tag{1.13}$$

Now a void can be described by the set $\{p_1, p_2, \theta_p\}$ in the following manner: $H = p_1 - p_2$ is related to the void anisotropy, $S = p_1 p_2$ represents the void area, and θ_p specifies the void orientation or direction. Konishi and Naruse (1988) proposed a fabric measure based on

12

a *local void vector p* with magnitude H and direction specified by θ_p. A modification of this definition is used in this study, whereby the void vector p is defined as a vector whose magnitude is HS with direction coinciding with the major principal axis. The reason for including S in the void vector definition is based on the premise that void size (area) will play a role in the dynamic response of granular materials, and thus it should appear explicitly in a proposed fabric measure. It should be pointed out that for the case of isotropic voids, $H = 0$, thus implying a zero void vector. However, this would be an unlikely situation for granular media generated through the random procedures used in this study.

Using this scheme of local void vectors, a polar rose diagram can be constructed similar to the branch vector distributions in Figure 1.4, and these plots are shown in Figure 1.11 for the six model assemblies under study. An examination of these plots along with a comparison of the corresponding branch vector diagrams reveals that void vector distributions appear to have some advantages in correlating wave propagation with the material microstructure. In the void vector distribution diagram for assembly S-1, all void vectors lie in the vertical direction to block horizontal wave paths, while the corresponding branch vector diagram fails to demonstrate this. For assemblies M-1 and M-2, the void vector diagrams show an overwhelming majority of void vectors lying in the vertical direction. This agrees with the numerical wave motion simulations, while the corresponding branch vector diagrams only show slightly more branch vectors in vertical direction than in the horizontal. The void vector diagrams for the W-assemblies also indicate preferred wave propagation directions, which was not apparent in the branch vector diagrams.

A *void vector ratio* defined as all void vector components in the vertical direction over all components in the horizontal, i.e.

$$R_v = \frac{\sum p_y}{\sum p_x} \tag{1.14}$$

can thus be used to measure the anisotropy of a medium with respect to voids. The values of this ratio R_v, for the six assemblies are given in Table 1-1. This ratio generally increases with the degree of assembly anisotropy except for assemblies W-2 and W-3, and it has a maximum value for assembly S-1, thus indicating the strongly anisotropic properties of this model medium. For moderately anisotropic assemblies M-1 and M-2, the ratio decreases and

successfully predicts a stronger anisotropy for assembly M-2 with respect to M-1. The values of R_v for the weakly anisotropic assemblies W-1, W-2 and W-3 are all close to unity. The void fabric ratio correctly indicates that the degrees of anisotropy in W-2 and W-3 are smaller than in W-1, but as with the other fabric measures it fails to identify W-2 as having the smallest degree of wave attenuation anisotropy among the W-assemblies. These differences among the W-assemblies are however, relatively small

1.7 Conclusions

Results of several discrete element simulations of wave propagation through model granular materials have been presented. The model materials included six numerically generated assemblies of circular particles with prescribed initial fabric anisotropy varying from strongly to weakly anisotropic. Plane type wave propagations were simulated in horizontal and vertical directions through each assembly by applying dynamic loadings to appropriate boundary particles. Wave propagation behavior such as wave speed and amplitude attenuation were determined from the discrete element model using specific nonlinear hysteretic interparticle contact laws developed in previous research.

In order to establish relationships between these simulated propagational characteristics and granular microstructure, specific fabric measures were employed. Based on observed experimental information and on previous studies, three particular fabric descriptors were chosen including branch vectors, path microstructures, and void characteristics. The spatial distributions of these fabric measures were determined for each of the six model assemblies under study. These distributions were then averaged over each assembly with respect to horizontal and vertical directions, and comparisons were made with the discrete element wave propagational results. It should be noted that the wave propagation-fabric relationships are thus limited to the simulations in the horizontal and vertical coordinate system. Planar wave propagation in other directions would be difficult to simulate is these assembly models.

Findings of the study indicated that each of the three fabric descriptors provided a reasonable degree of correlation with the wave motion results, and that the void vector fabric measure appeared to provide the best correlation for the six model materials. However, even though each model material system was randomly generated and contained hundreds of

14

particles, it is not possible to argue the point in general, that void fabric will be a better microstructural measure than branch vector or load/propagator path fabric schemes. Clearly additional research is needed to further narrow the wide choices of appropriate fabric measures to predict the dynamic response of granular materials.

It should be pointed out that in addition to microstructure or fabric, wave propagation in particulate media is also frequency or wavelength dependent. This type of medium acts as a nonlinear wave guide, and local microstructure and contact nonlinearity will produce dispersive, frequency dependent propagational behaviors. This aspect has been investigated by us (Shukla, et.al 1993) in some detail for one-dimensional material models. One particular aspect which was observed both experimentally and numerically was that signals of sufficiently long wavelength can excite resonant sub-units of the medium. For this behavior, a smooth input signal will undergo seperation into a series of short oscillatory waveforms, and this repartitioning of energy effects the local attenuation response. The 60 μs input pulse used in this study was sufficiently short enough so as not to produce this effect. Although it appears from the output signals shown in Figures 1.6 and 1.7 that wave form spreading has occurred, in reality this results from the fact that *averaged* output wave signals are being plotted. The averaging process sums individual contributions from several contacts along the output side of the assembly model, and because of small time shifts of each of the various signals, the time signature of the summed signal is broader (200-500 μs) than the individual signals (60 μs). The current study did not investigate frequency effects nor vary the input loading duration.

A longer term goal of this type of research would be to construct general relationships to connect wave propagation variables with averaged micro-fabric. For example, if we define volume-averaged, second order fabric tensors based on branch vectors $\bar{F}_{ij}^{(b)}$, path vectors $\bar{F}_{ij}^{(p)}$, and void vectors $\bar{F}_{ij}^{(v)}$, then it would be desirable to develop a general wave transmission law of the form

$$TR = f(\bar{F}_{ij}^{(b)}, \bar{F}_{ij}^{(p)}, \bar{F}_{ij}^{(v)}) \qquad (1.15)$$

where *TR* would represent the amplitude transmission ratio of output to input. This effort is currently underway. Clearly experimental determination of particulate media microstructural

fabric is needed to be able to use such theoretical relationships. Such efforts to determine microstructure or fabric of actual granular materials have been conducted, see for example Gill (1993) or Hryciw and Raschke (1995).

Assembly	No. of Particles	Void Ratio	Coor. No	R_F	R_b	R_p	R_v
S - 1	822	0.43	2.87	200.7	2.06	no path$_x$	85.18
M -1	778	0.28	3.43	33.3	1.19	5.88	2.44
M - 2	854	0.28	3.41	100.0	1.19	2.08	2.58
W - 1	1042	0.25	4.17	1.7	1.01	0.95	1.12
W - 2	1296	0.25	4.04	0.9	0.99	1.00	1.05
W - 3	1338	0.22	4.30	1.2	1.01	1.16	1.00

Table 1. Summary of Various Fabric Measures and Wave Transmissions

for Six Model Assemblies
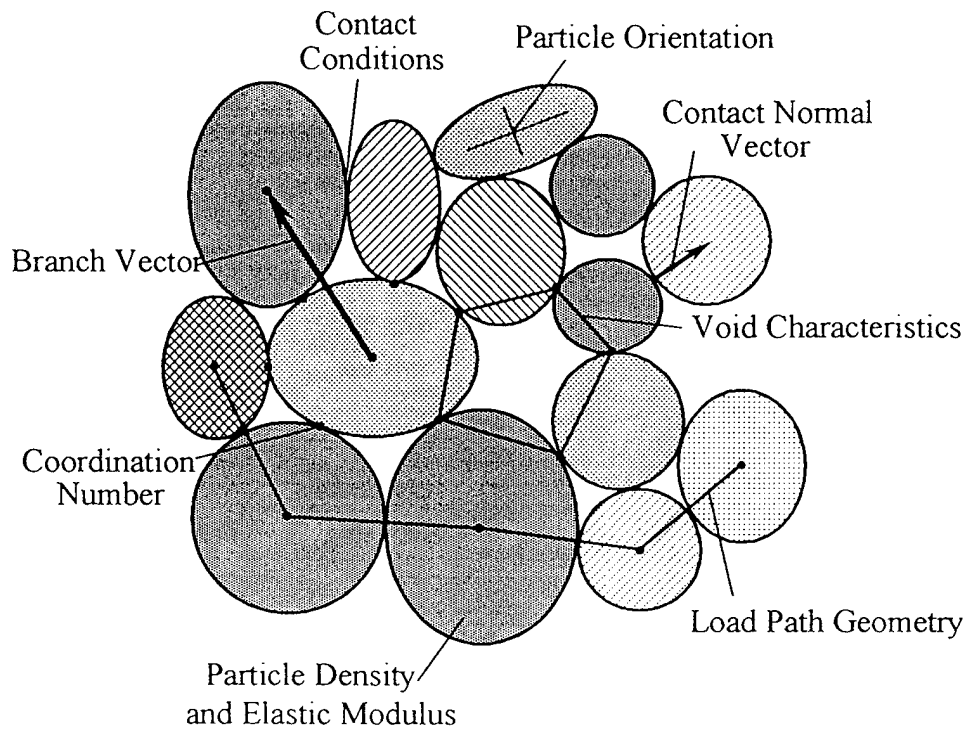
Figure 1.1. Typical Microstructure or Fabric in Granular Materials

input loading
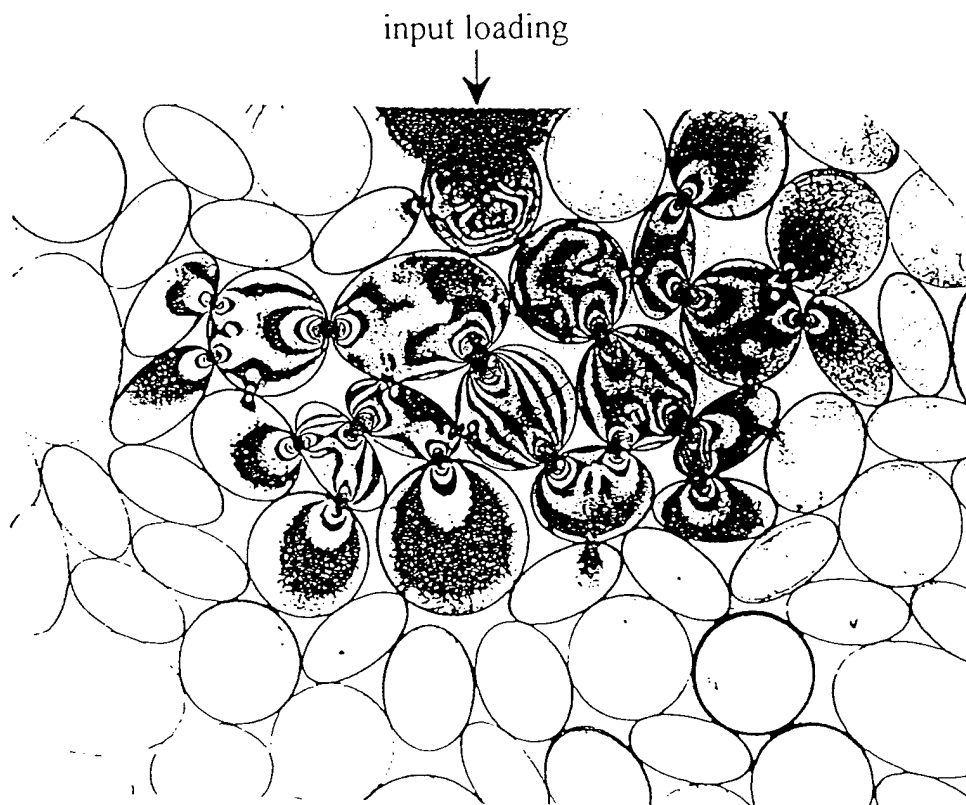
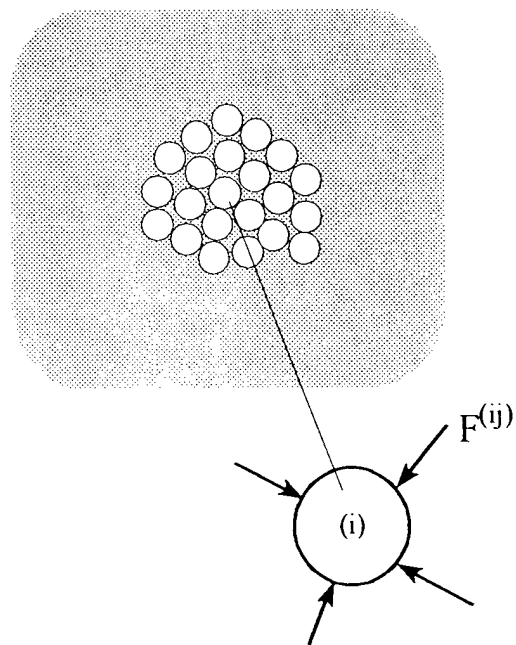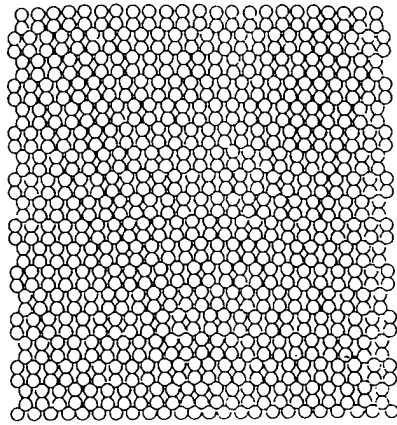Figure 1.2. Dynamic Photoelastic Photograph of Wave Propagation in
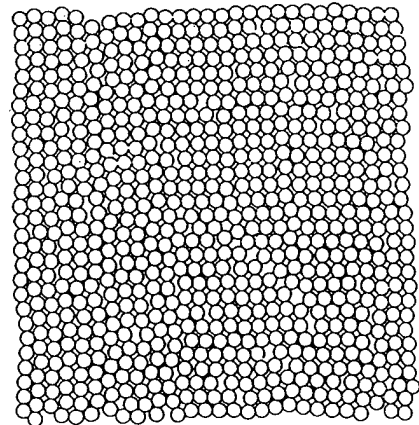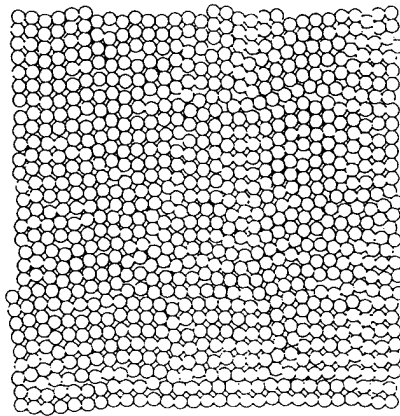a Model Granular Medium

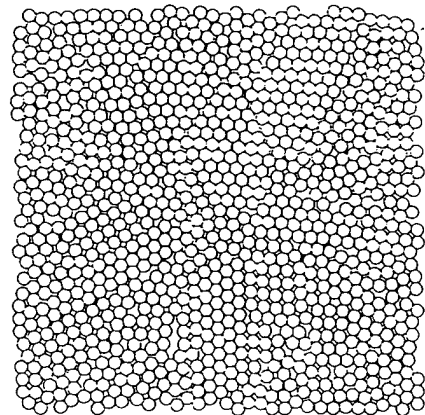Figure 1.3. Discrete Element Modeling
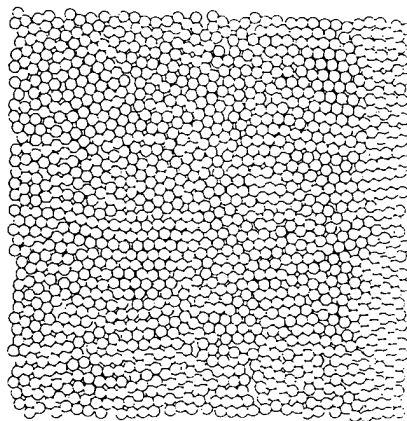
Strongly Anisotropic Assembly S-1

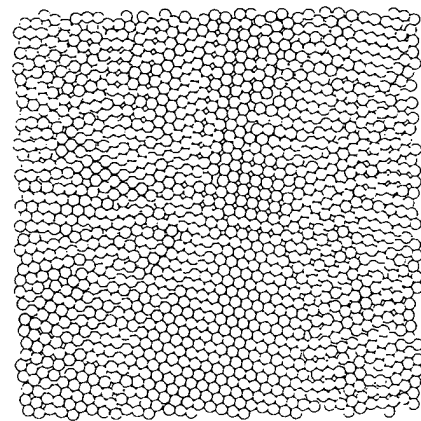Moderately Anisotropic Assembly M-1

Moderately Anisotropic Assembly M-2

Weakly Anisotropic Assembly W-1

Weakly Anisotropic Assembly W-2
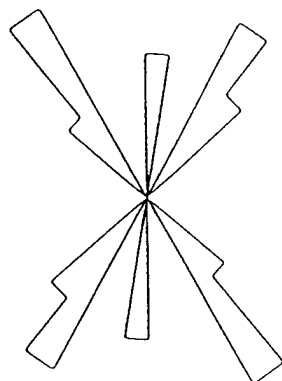
Weakly Anisotropic Assembly W-3

Figure 1.4. Six Model Granular Material Systems

Assembly S-1
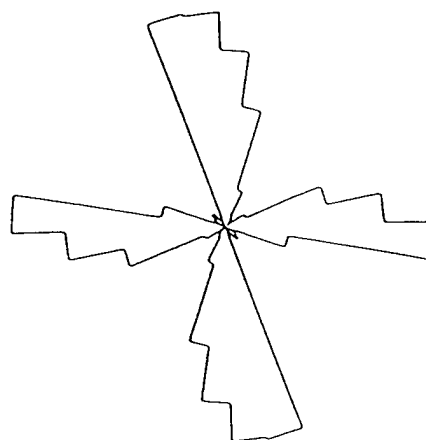
Assembly M-1
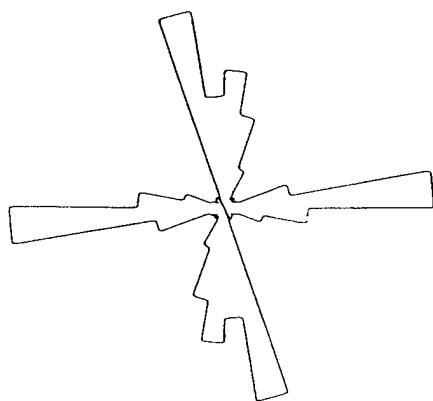
Assembly M-2

Assembly W-1
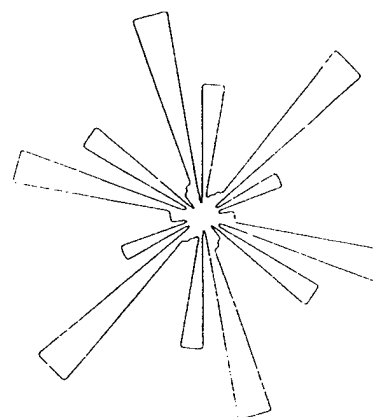
Assembly W-2

Assembly W-3

Figure 1.5 Branch Vector Distribution Plots of Model Assemblies

Figure 1.6. Wave Transmission Results for Assembly S-1

Figure 1.7. Wave Transmission Results for Assembly W-2

Figure 1.8. Schematic of Path Fabric Concept

Figure 1.9. Vertical Propagator Path

Figure 1.10. Void Fabric Schematic

$b^{(k)}$

Assembly S-1

Assembly M-1
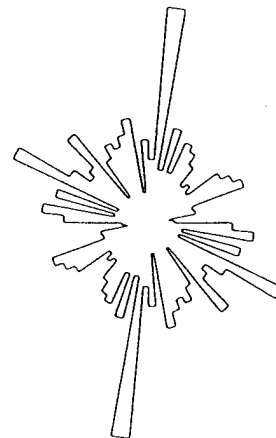
Assembly M-2
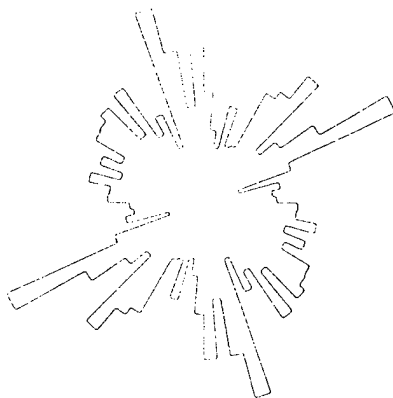
Assembly W-1
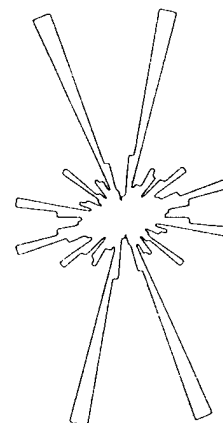
Assembly W-2

Assembly W-3

Figure 1.11. Void Vector Distribution Plots of Model Assemblies
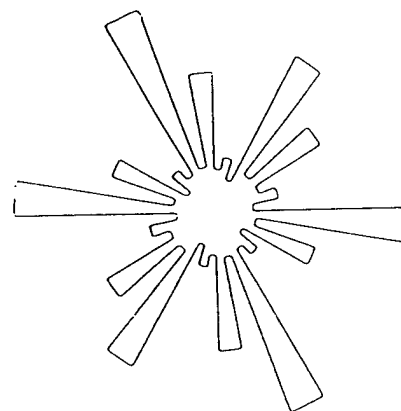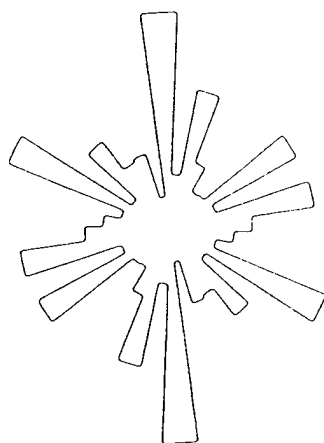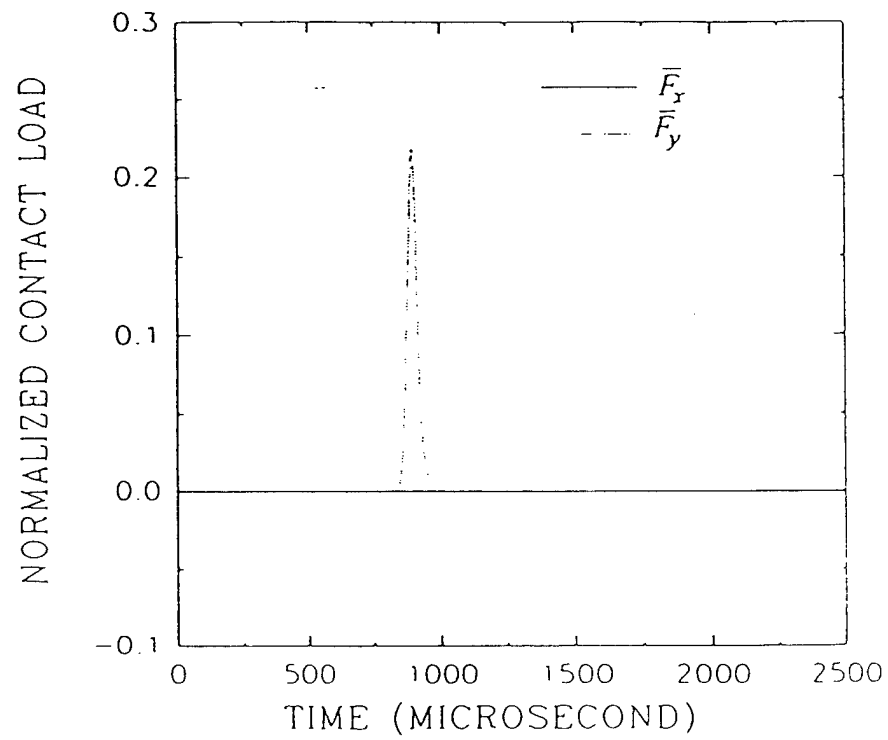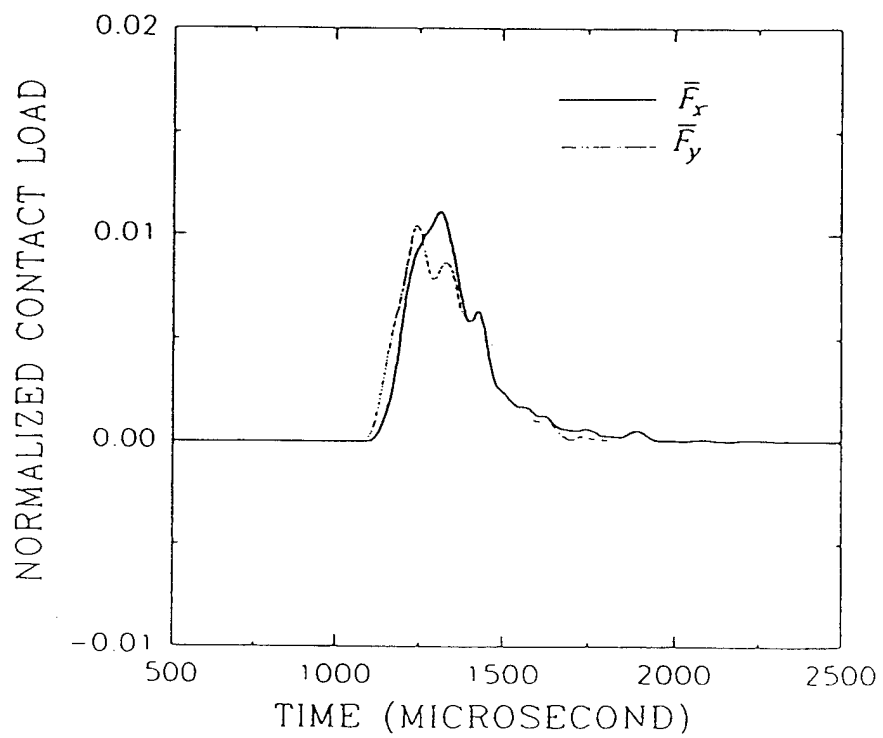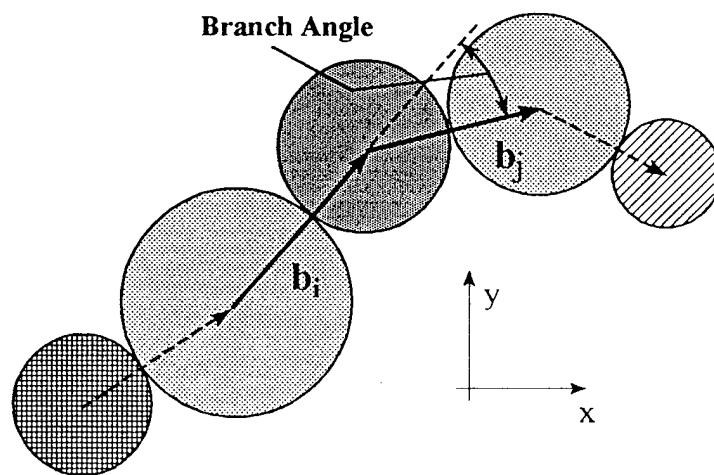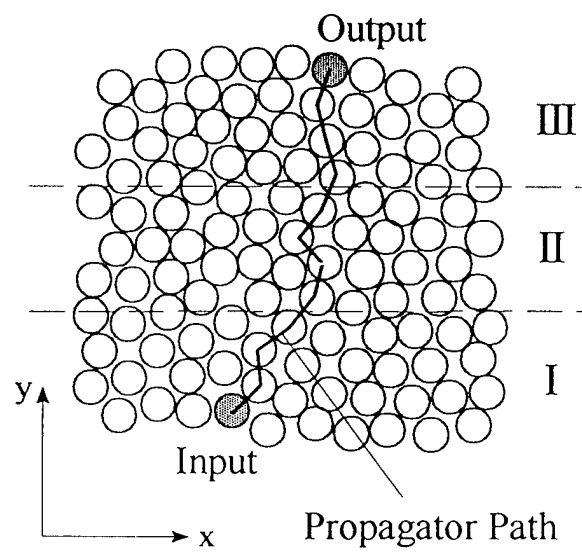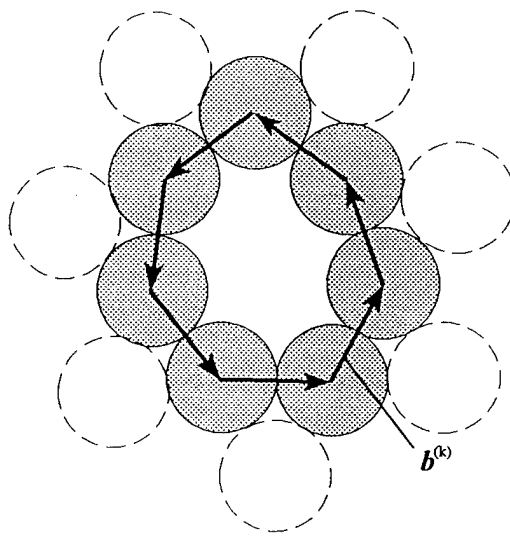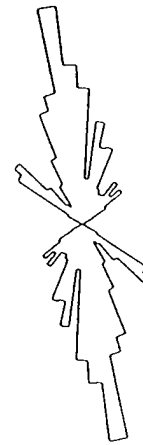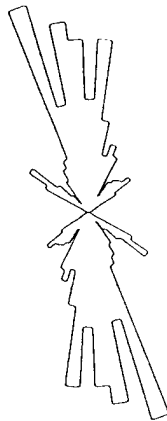
CHAPTER 2

THE EFFECT OF MICROSTRUCTURAL FABRIC ON DYNAMIC LOAD TRANSFER IN TWO DIMENSIONAL ASSEMBLIES OF ELLIPTICAL PARTICLES

2.1 Summary

Experimental and numerical studies have been conducted to investigate the effect of microstructural fabric, such as major axis orientation, contact normal and branch vector distributions, on dynamic load transfer behavior in two dimensional granular material. The granular medium was simulated by assemblies of elliptical particles. The experimental method utilizes the combination of high speed photography and photoelasticity to study the local load transfer behavior in granular assemblies subjected to explosive loading. Numerical studies employed a computational scheme based on the discrete element method. Results indicate that the microstructural fabric has significant effect on the load transfer phenomenon, such as stress wave velocity, load pulse wavelength and contact load attenuation.

2.2 Introduction

A granular medium may be defined as a complex collection of discrete particles of varying shape, size, and orientation. Understanding the dynamic behavior of granular materials has important scientific a.nd practical applications. A large number of geomechanics problems dealing with seismic and blast loading of sands and rock require such knowledge. Additional applications can be found in the processing of powders related to metallurgy and pharmaceutical operations.

The mechanical behavior of granular materials depends strongly on their microstructure or fabric which is generally defined as the spatial arrangement of solid particles and associated voids. Such microstructure can be further classified as: orientation fabric (orientation of individual particles) and packing fabric (mutual relation of individual particles to each other). Orientation fabric may be quantitatively defined by a vector mean direction and a vector magnitude to characterize orientation of non-spherical or non-circular particles. This fabric is usually represented by the angle between the long axes of particles and a

reference direction. Many packing fabric measures have been proposed for granular media. Some examples of fabric measures include branch vectors between the mass centers of adjacent grains, normal vectors in the direction normal to particle contact, coordinate or contact number, void characteristics etc. Examples of some fabric measures are illustrated schematically in Figure 2.1. No unique set of fabric measures has been universally accepted which can adequately describe the mechanical response of such media.

The important role of the fabric in the mechanical properties of granular materials has been recognized in recent years. Oda (1978) observed thin sections of material under a microscope to investigate the significance of fabric in granular mechanics. Nemat-Nasser (1982) also observed the influence of fabric on the overall shear-induced rate of volume expansion and volume contraction. Konishi (1978) studied the effects of fabric on the mechanical behavior of granular materials using two-dimensional photoelastic models. Most of these studies have assumed that the individual particles were circular. Assemblies of such simple shapes can only produce restricted types of material fabric. For example, such cases lead to contact normal vectors which are always directionally coincident with the branch vectors. Also since circular disks are symmetrical about their centers, it is not possible to use orientation fabric to describe a granular assembly of circular disks.

However, particles in actual granular materials are rarely circular. Oda et al (1982) and Subhash et al (1991) investigated the relation between the fabric and mechanical behavior of granular materials experimentally using assemblies of elliptical particles to simulate the granular media. Ting (1991, 1992) and Rothenburg and Bathurst (1992) also used assemblies of elliptical particles to numerically study the response of granular materials. Unlike assemblies of circular particles, for any two contacting elliptical particles in a two dimensional assembly, the branch vector will not necessarily coincide with the contact normal vector (see Figure 2.2) and also orientation fabric will be needed to describe such a granular assembly.

The research works mentioned above were restricted to static loading. Investigation of the dynamic response of granular materials started several years ago. Rossmanith et al (1982), Shukla et al (1987, 1988), and Zhu et al (1991) simulated granular materials using circular disks to study dynamic wave propagation phenomenon. Shukla et al. (1987) found that the particle to particle load-transfer process is controlled by the angle made by contact normals. Load transfer only occurs when this angle is obtuse. Recently our group (Shukla

et al. 1993) has initiated the study of dynamic response of elliptical-shaped particulate media. This research has focused on the particle aspect ratio and has studied the effect of particle shape on the inter-granular load transfer, contact load attenuation, stress wave velocity and the load pulse wavelength. However, this research work dealt primarily with load transfer behavior in single chain assemblies where only orientation fabric measures and aspect ratio apply.

Based on this initial dynamic work, the present study focuses on the relationship between the microstructural fabric and load transfer behavior in two dimensional assemblies of elliptical particles. The major axis orientation was chosen as the measure of orientation fabric. Since normal contact and branch vectors are no longer coincident, both are needed as measures of packing fabric. So to describe the fabric of a two dimensional assembly of elliptical particles at least three parameters (branch, normal and orientation vectors) will be needed. A series of experiments has been conducted to investigate the effect of these three fabric parameters on the wave propagation behavior in regular assemblies of elliptical shaped particles. In addition, numerical modeling of the dynamic response of these assemblies was also conducted using the *discrete element method*. This computational scheme has been very useful in simulating the response of discontinuous and particulate materials (see for example Sadd et al., 1991 and 1993, and Shukla et al., 1993).

2.3 Experimental Procedure

The experimental method used for this study employed dynamic photoelasticity which in conjunction with high-speed photography provided whole field data as a stress wave propagated through the various assemblies. The elliptical particles (all of 38mm x 25mm) were made from Homalite-100, a photoelastic material, and these particles were arranged into various regular model geometries.

The experimental models were placed in the optical bench of a high speed Cranz-Schardin type camera. The particles were loaded by exploding a small amount of Lead Azide in a specially designed charge holder located at the top of the assembly. The camera was triggered at some prescribed delay time after igniting the explosive. The high speed photography system operated as a series of high intensity, extremely short duration pulses of light and provided twenty photoelastic images at discrete times during the dynamic event. A

31

sampling of 3 photoelastic images obtained from the high speed camera is shown in Figure 2.3(a). These images of the propagation phenomenon were enlarged and digitized to facilitate analysis. The Hertz stress field equations along with the stress optic law were used to calculate the contact load at a particular contact point and time by applying the multi-point, non-linear least square method developed by Shukla and Nigam(1986). The wavelength of the stress wave pulse can be measured directly from the photographs of the wave propagation process. In all experiments, the wavelengths were observed to be approximately three to four times the particle size. Past studies (Shukla, et al., 1993) have found that resulting wave motion depends on the particle size relative to the wavelength of the loading pulse. The propagation distance is plotted as a function of time to obtain the wave velocity.

Experiments started with the body centered cubic (BCC) assemblies (see Figure 2.3, 2.4, 2.5). The names BCCH (Figure 2.3) and BCCV (Figure 2.4) represent arrangements with the major axis of the ellipses parallel to the *H*orizontal and *V*ertical directions, respectively. BCCR, as shown in Figure 2.5, is an assembly obtained by *R*otating the BCC assembly. In these BCC assemblies, contact normal and branch vectors are directionally coincident. These particular assemblies have the symmetry feature that one can change the major axis orientation 90 degrees without changing the contact normal and branch vector directions. This feature allows us to investigate the effect of major axis orientation on wave propagation behavior. This effect was also studied using hexagonal close-packed (HCP) assemblies. One example assembly shown in Figure 2.6(a) was named HCPH, for the case with major axes oriented in the horizontal, with a similar notation HCPV for the vertical orientation case. To investigate the effect of contact normal and branch vector orientation, modified HCP assemblies were used. One example shown in Figure 2.6 (b) was named HCPS1. In these assemblies, by changing the space between the particles, the major axis orientation was kept horizontal while the contact normal and branch vector directions were varied.

2.4 Numerical Simulation

The discrete element method was used to model the dynamic load transfer in the simulated granular materials. This method, originally proposed by Cundall and Strack (1979) for the static case, has been applied to dynamic load transfer processes in granular materials by various authors (Sadd et al 1989, Walton et al 1991, and Trent et al 1989) The numerical

strategy uses Newtonian rigid-body dynamics to calculate the translational and rotational motion of each particle in these model assemblies. For wave propagation applications, these movements of the individual particles are a result of the propagation through the medium of disturbances originating at particular input loading points. In this fashion, the dynamic response of the model system can be determined, and parameters such as wave speed and amplitude attenuation can be calculated for specific models. Furthermore, these wave propagational characteristics can be related to the model material's microstructure which for this case could be correlated with size and orientation of the elliptical particles.

For particles of non-circular shape, the determination of the various particle contact geometries becomes a significant computational task. Following the procedures originally proposed by Ting, (1993), algorithms have been established to determine particle contact detection, and to calculate normal and tangential contact deformation (overlap). With respect to determining the inter-particle contact behavior, considerable research has been done starting with the fundamental work of Duffy and Mindlin, (1957) and continuing with Walton, (1978) and Johnson, (1985). Because of the added complexity of the boundary shape, the contact law between elliptical particles is dependent upon the location of the contact along the ellipse's boundary. This effect occurs due to differences of the radii of curvature at the contact point. A general non-linear hysteretic contact law that was originally developed for circular particles (Sadd, et al. 1993) has been incorporated into this elliptical particulate code. This particular non-linear contact law prescribes different loading and unloading behavior with a hysteresis (energy loss) proportional to the amount of contact deformation between the particles. Different values of the contact law parameters have been used to account for the contact response differences due to contact location.

2.5 Experimental Results and Discussion

To investigate the effects of microstructural fabric on the dynamic load transfer process, a series of experiments was conducted on assemblies with the geometries of BCC and HCP with different major axes orientations and various spacings. The results are discussed separately, as the effect of major axis, contact normal, and branch vector orientations. The distributions of these fabric parameters for the entire assembly as a function of the angular direction were plotted as rose diagrams, see for example Figure 2.3(b). The

direction of the input load becomes the reference direction for the measurements of these fabric parameters.

2.5.1 *The Effect of Major Axis Orientation*

BCC assemblies were used to investigate the effect of the major axis orientation, as shown in Figures 2.3 and 2.4. A difference in the load transfer process in these two assemblies only results from the major axis orientation variation. The stress wave propagation phenomenon in two different BCC assemblies are shown in Figures 2.3 (a) and 2.4 (a). It can be seen that the energy was channeled along a single chain of disks in each assembly. No energy was transferred to other chains. Previous research work using assemblies of circular disks by Shukla et al (1987) has shown that the load-transfer path was related to the angle made by contact normals and load transfer only occurs when this angle was obtuse. The load transfer phenomenon observed in assemblies of elliptical particles also shows that load transfer only occurs when

$$\{ \theta_{ij}, \beta_{ij} \} > \frac{\pi}{2} \tag{2.1}$$

where θ_{ij} and β_{ij} are the angles made by contact normals and branch vectors respectively.

A simple experiment was conducted to verify this load-transfer rule for elliptical particles. The loading direction remained vertical but the BCC assembly was rotated through an angle of approximately 40^0, as shown in Figure 2.5. If the proposed rule of load-transfer path is true for assemblies of elliptical particles, the energy should only transfer along the two mutually perpendicular chains which emanate from the particle on which the explosive loading takes place. The experimental results are shown in Figure 2.5. The wave propagated as expected with no energy transfer into particles where the angle between the contact normals (or branch vectors) is acute. A small amount of energy which goes into the side chain is because of the inaccuracy of the spatial arrangement of particles.

Data for the average wave velocities in these assemblies are shown in Figure 2.7, and the computed values were 960 m/s for BCCH and 1160 m/s for BCCV. This difference in wave speed may be qualitatively explained using an approximate equation (Takahashi, 1949)

34

for wave velocity in one dimensional granular media given by

$$V \cong d \sqrt{\frac{K}{m}} \qquad (2.2)$$

where d is a distance measure usually taken to be between the centers of two particles in contact, K is the effective contact stiffness, and m is the mass of the particle. For our case, the particle mass is the same for both BCC assemblies. However, by changing major axis orientation the radius of curvature at the contact has been changed. For assembly BCCH, the radius of curvature at the contact is large, so the contact stiffness is large and one would expect a higher velocity. On the other hand, the distance between the centers of two particles, d, is larger in BCCV than that in BCCH. Evidently it is this particle distance effect that produces the reduced wave velocity in assembly BCCH when compared with that in BCCV.

The wave velocity in the two mutually perpendicular chains of the BCCR assembly were computed from the distance versus time plots. It was found that the velocity in major axis direction is 1080 m/s while the velocity in minor axis direction is 890 m/s. Again the velocity is influenced by the direction of the major axis. However, these numbers are about 10% lower than that in the BCCH and BCCV assemblies, possibly because of the different intensity of initial loadings in the two chains.

Figures 2.3 and 2.4 show the wavelengths in these two BCC assembles. In BCCH, the loading direction is perpendicular to the major axis of ellipses and the wavelength in this assembly is about four particles (94.4mm) along the propagation direction. In BCCV, the loading direction is parallel to the major axis of the ellipses and the wavelength in this assembly is about three particles (119.5mm) along the propagation direction. Variation of major axis orientation brings about two major fabric changes in these two assemblies, radius of curvature at contact, i.e. contact stiffness, and the distance between the center of particles. Research work by Shukla et al (1993) has shown that radius of curvature at contact has no appreciable effect on wavelength. This fact would lead one to believe that the difference in wavelength for assemblies HCPH and HCPV is caused by the distance between the centers of particles. Granular assemblies behave like frequency filters. The behavior of these filters may be determined by the distance between the centers of particles which results in the

35

different dispersion behavior.

Using the method mentioned in section 2 data collected from isochromatic fringes were used to calculate contact loads. A typical plot of the contact load variation with respect to time for BCCH assembly is shown in Figure 2.8. As the loading pulse reaches the contact points, the load builds up. The contact load monotonically increases to a peak value and then decays to zero as the pulse passes by. The contact load profiles show very little change in shape except that the peak load attenuates with the propagated distance. This attenuation is plotted for both BCCH and BCCV assemblies in Figure 2.9. From this figure one can see that load attenuation in BCCH is more severe than that in BCCV. The reason for this, similar to the velocity drop, is that the distance between the centers of particles is different in these two assemblies. At the contact point some energy will be reflected and lost from the main stress wave pulse which passes through the contact. Energy reflection occurs at free surfaces and the larger radius of curvature at the contacts in the BCCH assembly provide more free surfaces nearly normal to the direction of wave propagation.

The effects of major axis orientation can also be observed from experiments using HCP assemblies (see Figure 2.10 (a) and (b)). Typical photoelastic fringes for these experiments at a common time are shown in Figure 2.10. As can be seen in these photographs, stress wave propagation occurred in all particles below the input loading. In these assemblies the contact normals and branch vectors are no longer coincident (see Figure 2.11). However, both fabric parameters satisfy the load transfer condition, $\{\theta_{ij}, \beta_{ij}\} > \pi/2$.

From Figure 2.10 one can see that the global wave fronts in the two HCP assemblies have different shapes. The wave front shape depends not only upon where the wave is allowed to go, which is determined by the load transfer condition, but also upon the wave velocity. From the previous discussion, we know that the load transfer condition depends upon the contact normal and branch vectors while the stress wave velocity is dependent on the major axis orientation. Figure 2.11 shows that the contact normal and branch vector distributions are slightly different in the two assemblies; however, the major axis orientation is considerably different. Careful observation of the stress wave propagation phenomenon in these two assemblies shows that the stress wave always propagates further along the direction of major axis of particles. This observation is consistent with the results of the BCC assemblies, which indicated that the stress wave velocity is greater along the major axis

direction. Thus changes in the global wave front in HCP assemblies would be mostly attributable to the major axis orientation variation.

2.5.2 *The Effect of Contact Normal and Branch Vector Orientation*

Having investigated the effects of the major axis orientation on the dynamic load transfer process, additional assemblies were studied in which the major axes were fixed in the horizontal orientation. By fixing the major axis orientation, the effects of contact normal and branch vectors could be explored independently. The contact normal and branch vectors are intimately related through the particles size, shape and relative location. Changing one of the parameters invariably changes the other. The load transfer rule can be investigated by cleverly choosing appropriate fabric for particular assemblies under study.

Starting with an HCP assembly, with the major axes orientated horizontally, the horizontal spacing between mass centers can be set in such a way that the angle made by the branch vectors is less than 90 degrees and the angle made by the contact normals is greater than 90 degrees for certain particle pairs. Alternatively, the spacing can be chosen in such a way that both the branch vector and the contact normal angle is less than 90 degrees for certain particle pairs. These two assemblies are shown in Figure 2.12(a) and 2.13(a), respectively. These two assemblies do not allow particle arrangement such that the angles between the contact normals are acute while the angles between the branch vectors are obtuse. To create such an assembly where the contact normals will be acute and the branch vectors obtuse, the major axis orientation had to be changed. By rotating the assembly illustrated in Figure 2.12(a) 90 degrees with respect to the input loading direction, an assembly is created in which the angle made by the contact normals, θ_{ij}, was approximately 70 degrees and the angle made by the branch vectors, β_{ij}, was approximately 120 degrees (see Figure 2.14). By utilizing these three assemblies and the knowledge gained from the BCC assemblies (recall that $\theta_{ij} = \beta_{ij} = 90$ degrees was a critical angle for load transfer), the effects of branch vector and contact normal on load transfer path can be obtained.

Figure 2.12 shows typical isochromatic fringes obtained from a modified HCP assembly, namely HCPS1, where the contact normal angle was greater than 90 degrees and the branch vector was less than 90 degrees. Based on the load transfer rule presented earlier, if the angles made by both parameters are not in excess of 90 degrees, load transfer should

not occur between say the (i) and (j) particle pairs. However, it is observed that load transfer does occur between these particle pairs.

Figure 2.13 shows typical isochromatic fringes obtained from another modified HCP assembly, namely HCPS2. In this case both the contact normals and the branch vectors make an angle that is less than 90 degrees. In this case no load transfer occurs between the (i) and (j) particles.

Figure 2.14 shows typical isochromatic fringes obtained from the assembly created by rotating HCPS1 assembly 90 degrees with respect to the input loading direction. In this assembly, the angle between the contact normals is acute and the angle between the branch vectors is obtuse for certain particle pairs. In this case load transfer also occurs between the typical (i) and (j) particle pairs.

In light of these observation coupled with the BCC experiments, the load transfer rule in a two dimensional elliptical-shaped assembly can be obtained. The photographic data of Figures 2.12, 2.13 and 14 have shown that if the angle made by either the contact normals or the branch vectors is obtuse, load transfer will occur and if the angles made by both the contact normals and the branch vectors are acute, no load transfer will occur. The load transfer rule can now be modified from equation (2.1) to reflect this information

$$\theta_{ij} \ or \ \beta_{ij} > \frac{\pi}{2} \tag{2.3}$$

where again θ_{ij} is the angle made by contact normals and β is the angle made by branch vectors.

The contact normal and the branch vector not only control the load transfer path but also affect the stress wave velocity. To evaluate these effects one can examine the global wave front in assemblies HCPH(Figure 2.10), HCPS1(Figure 2.12) and HCPS2(Figure 2.13). The global wave front in these assemblies are obviously different from each other, and the front is determined by the load-transfer path and the stress wave velocity. The stress wave velocity depends on radius of curvature at the contact and the distance between the particles. In the regular assemblies used in this study the major axis orientations are fixed. So the contact normal uniquely defines the radius of curvature at the contact while branch vector

uniquely determines the distance between the particles. Recall the discussion for BCC assemblies that both parameters will affect loading velocity. However, the distance between the particles plays a predominant role in stress wave velocity. So it is reasonable to assume that the distribution of branch vectors has a more intimate relationship with the shape of the global wave front. The decomposition of the magnitude of branch vectors in the rose diagram for these three assemblies into x and y components, is shown in Figure 2.15. The contours made by x and y components qualitatively coincide with the global wave front obtained from experiments.

It should be pointed out that the global wave front shapes shown in these photographs are in the near field. Since the loading velocity is different along the various direction, the global wave front shape could change at later times.

2.6 Numerical Results

Several discrete element simulations were conducted using the two HCP assemblies shown in Figure 2.10. In this computational code, there are three primary model parameters which need to be selected depending upon the assembly type and/or loading condition. The parameters are the peak value of the input load, P, the duration of input loading, ΔT, and the stiffness coefficient, α, used in the nonlinear hysteretic contact model (see Sadd et al, 1993). The dynamic input load was simulated by a triangular time-dependent impulse determined by this peak value P and the duration ΔT. The parameter α is related to material properties and the geometry of the contact region. These three parameters effect the wave velocity, wavelength and the load attenuation. They should be rationally selected according to the real experimental conditions and contact features of the granular assemblies. Since the assemblies used in these simulations are regular, it can be seen that there are only two varieties of contacts based on contact radii of curvature (see Figure 2.10). According to these contact locations two different stiffness coefficients were selected to model these contacts. The parameters used in the simulations of the experiments are given in Table 2.1. The α_{L1}'s were used to model the contacts along the 'main chain' and 'secondary chain' while α_{L2}'s were used to model the contacts in the horizontal direction (see Figure 2.6 for description of different chains).

Using this numerical scheme, the total time period of interest is discretized into a

series of small intervals. These time steps are chosen to be small enough (2µs for this case) so that in a single step the wave cannot propagate more than one particle length. In other words, the wave can at most only propagate from one particle to any or all of its immediate neighbors in a single step. This eliminates inertial coupling with other particles in the assembly, and produces an explicit numerical procedure.

For HCP assemblies under study the disks are in their closest packing arrangement with six contacts per disk. The wave motion occurs in several different paths determined by the assembly micro-structure and the input load location and direction. Figures 2.16-2.19 show the DEM contact load histories for the 'main' and 'secondary' chains in the two HCP assemblies. The plots show that the arrival time predicted by the numerical model match experimental data very well, i.e. wave speeds are closely matched. Most peak contact loads predicted by DEM simulations match experimental data within 10%, although some comparisons did produced differences as high as 20%. It is felt that since the experimental data itself contains scatter of approximately 10%, the computational scheme does provide reasonable predictions to the stress wave propagation process.

2.7 Conclusion

The experimental and numerical studies were conducted to investigate the effect of specific fabric, such as the major axis orientation, contact normal and branch vectors, on stress wave propagation behavior in two dimensional regular assemblies of elliptical particles. The results indicate the following:

1) Characteristic wave propagation parameters, such as wave velocity, wavelength and load attenuation, are dependent on the major axis orientation. Higher stress wave velocity and lower contact load attenuation were observed along the direction of major axis. Also the wavelength changes as the major axis orientation changes 90 degrees in BCC assemblies. This difference in wavelength is mainly due to the change in the distance between adjacent particles' centers.

2) Both contact normals and branch vectors control the load transfer path. If the angles made by the contact normals and the branch vector are less than 90 degrees, load-transfer will not occur. However, if the angle made by either the contact normal or the branch vector is greater than 90 degrees, wave motion will propagate through the

contact.

3)   A branch vector uniquely determines the distance between a particle pair along the direction of this branch vector. This distance significantly affects the wave velocity, and since wave velocity is one of the major factors in the determination of global wave front shape, the branch vector plays an important role in the determination of the wave front.

4)   Comparisons of the experimental and numerical results indicated that the discrete element numerical technique provides good correlation with observed experimental data. Based on these successful correlations the numerical code will be used to predict load transfer behavior in large, random assemblies which would not be practical to handle experimentally.

Based on the observations from the study it appears that the load transfer process in assemblies of elliptical particles can be represented as

$$\frac{P_o}{P_i} = f(\underline{n}, \underline{b}, \underline{m}) \qquad (2.4)$$

where P_i is the peak input load to the particle, P_o is the peak output load at any contact point on the particle, $\underline{n}$ is the contact normal vector, $\underline{b}$ is the branch vector and $\underline{m}$ is the major axis orientation vector. The determination of this load transfer relation is currently being investigated using the numerical scheme presented here.

41

Table 2.1 Numerical modeling parameters for HCP assemblies of elliptical disks

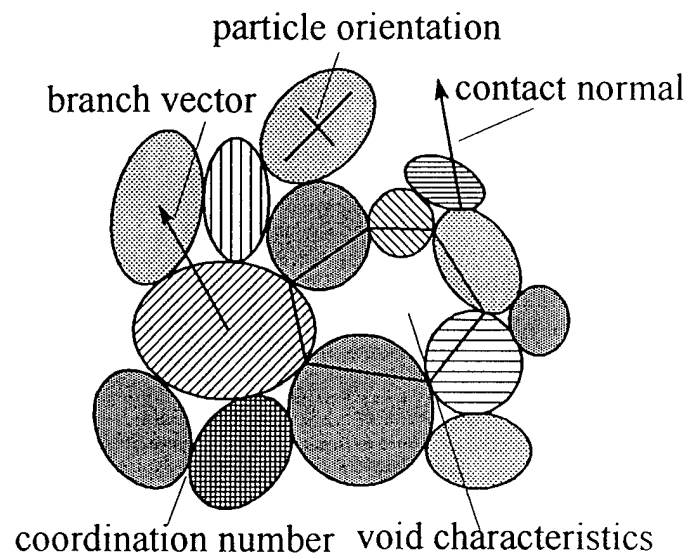| Assembly	Peak input load P (N)	Duration of input loading ΔT (μs)	Stiffness coeff α_{L1} (10^8x N/m$^{1.4}$)	Stiffness coeff α_{L2} (10^8x N/m$^{1.4}$)
HCPH	3300	120	2.4	2.0
HCPV	3100	100	2.0	2.3

Figure 2.1. Some fabric measures

(a)

(b)
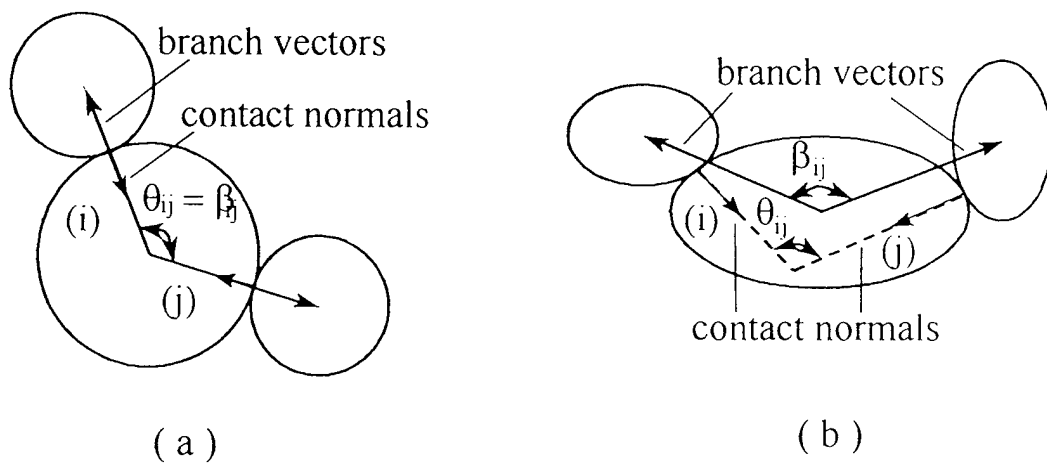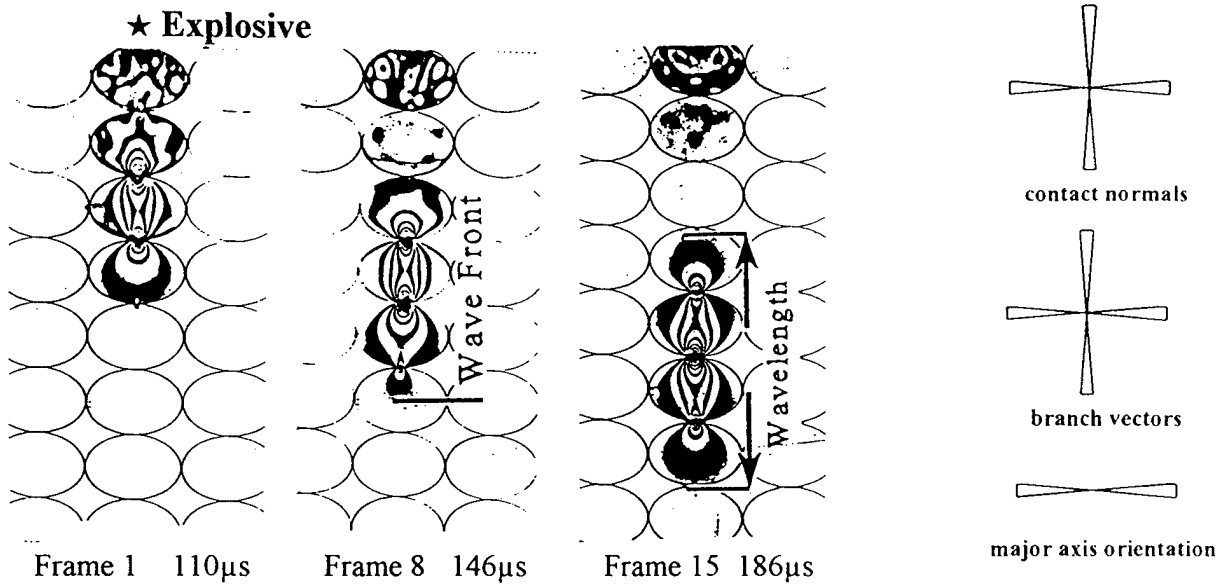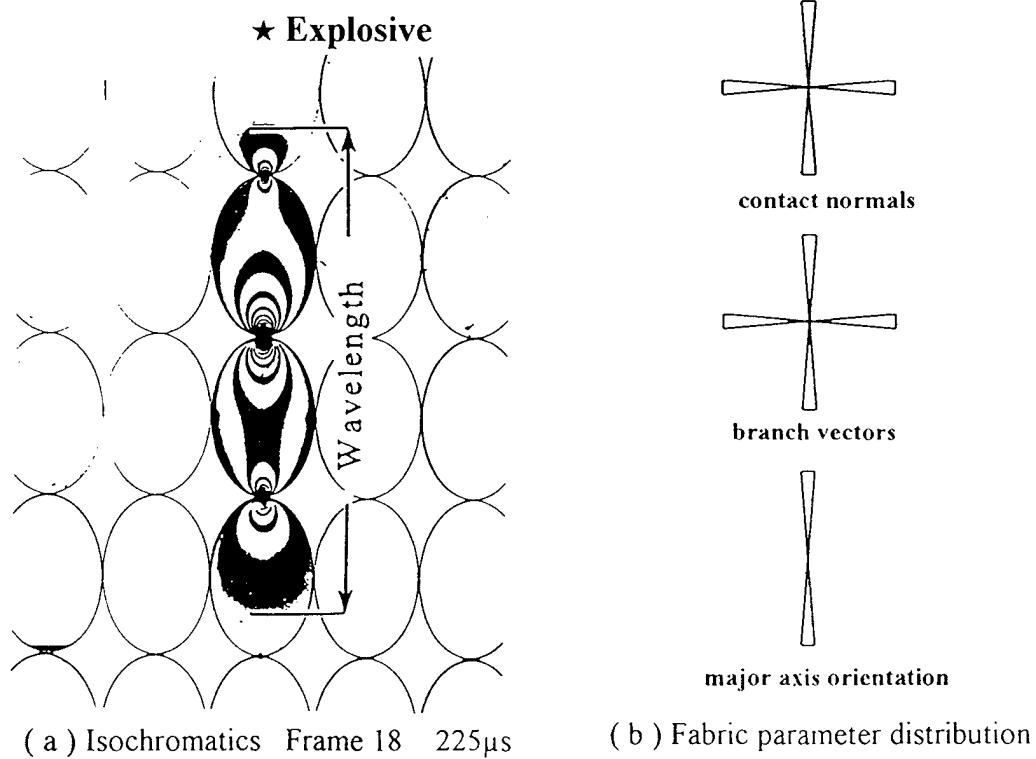
Figure 2.2 The angle made by contact normals, θ_{ij}, and the angle made by branch vector, β_{ij}.

★ Explosive

Frame 1   110μs   Frame 8   146μs   Frame 15   186μs

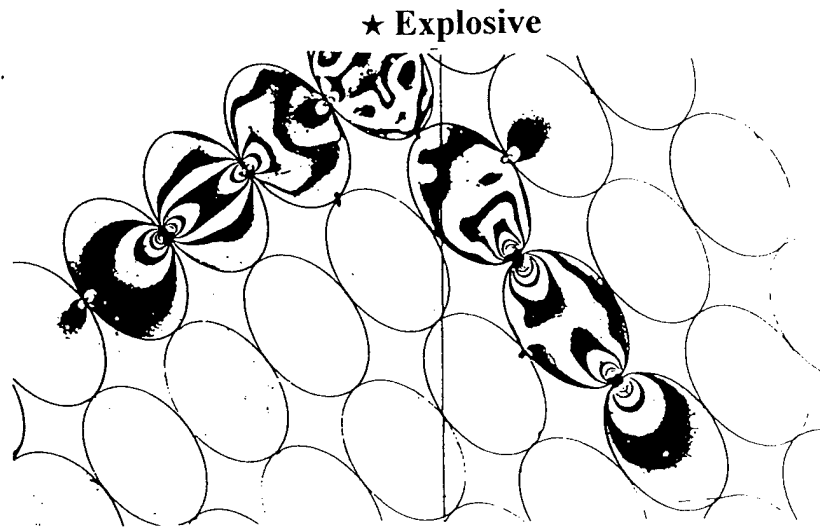(a) Isochromatics   (b) Fabric parameter distribution

Figure 2.3. Typical isochromatic fringes obtained from a two dimensional body centered
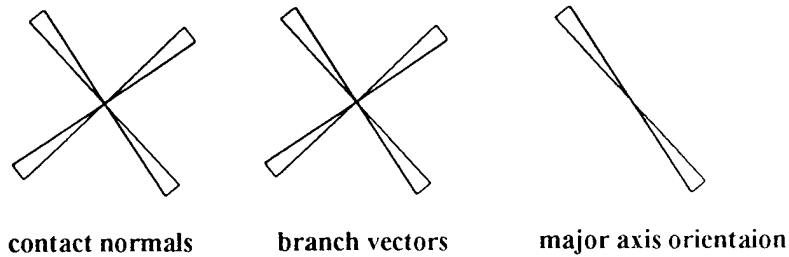
cubic assembly of elliptical particles (BCCH)

★ Explosive

(a) Isochromatics   Frame 18   225μs   (b) Fabric parameter distribution

Figure 2.4. Isochromatics and fabric parameter distribution in BCCV assembly

★ **Explosive**

(a) Isochromatics   Frame 10 117μs

contact normals   **branch vectors**   **major axis orientaion**

(b) Fabric parameter distribution

Figure 2.5. Isochromatics and fabric parameter distribution in BCCR assembly

main chain   secondary chain

(a) HCPH $\theta_{ij}=140°$ $\beta_{ij}=100°$

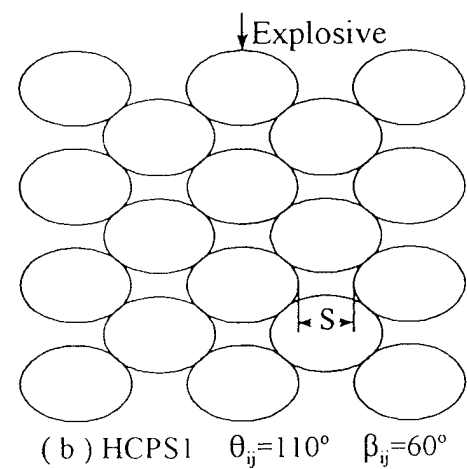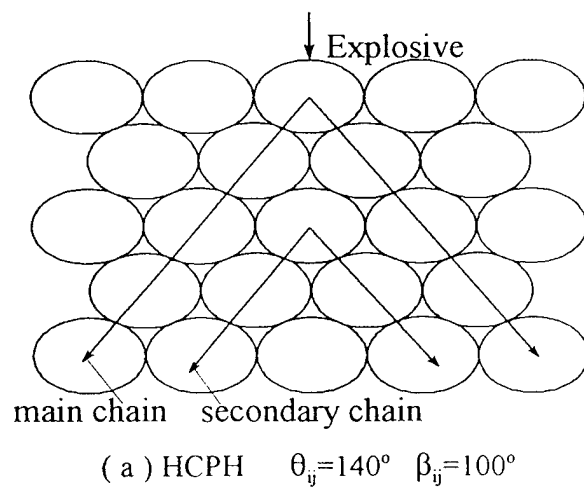(b) HCPS1 $\theta_{ij}=110°$ $\beta_{ij}=60°$

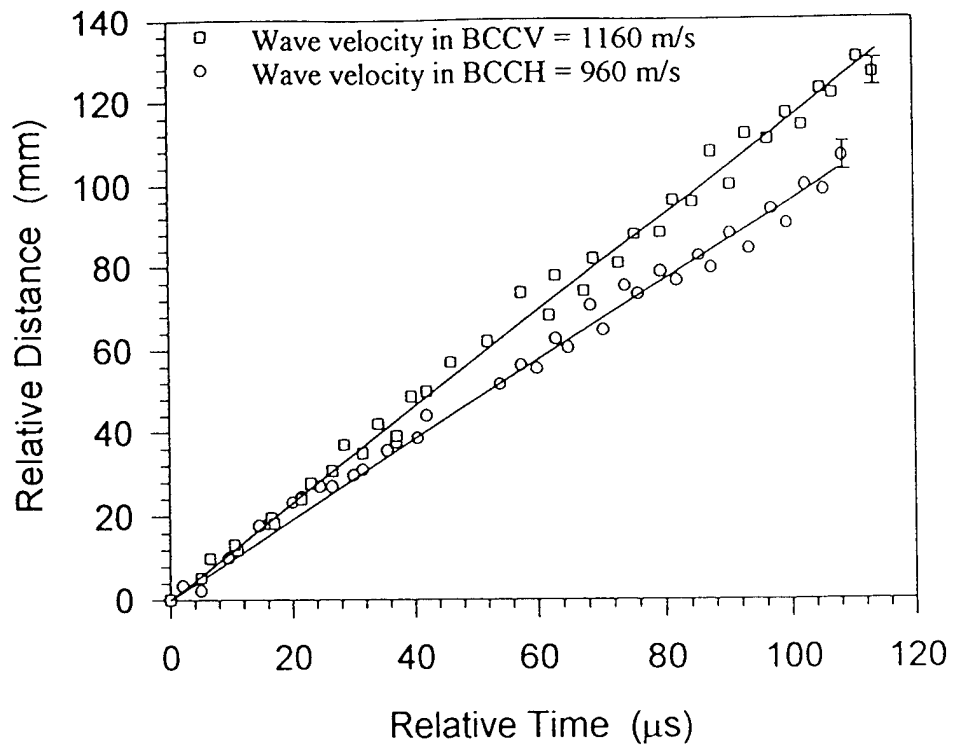Figure 2.6. Some assemblies used in this study

45

Figure 2.7. The wave-front position as a function of propagated time for BCC assemblies.
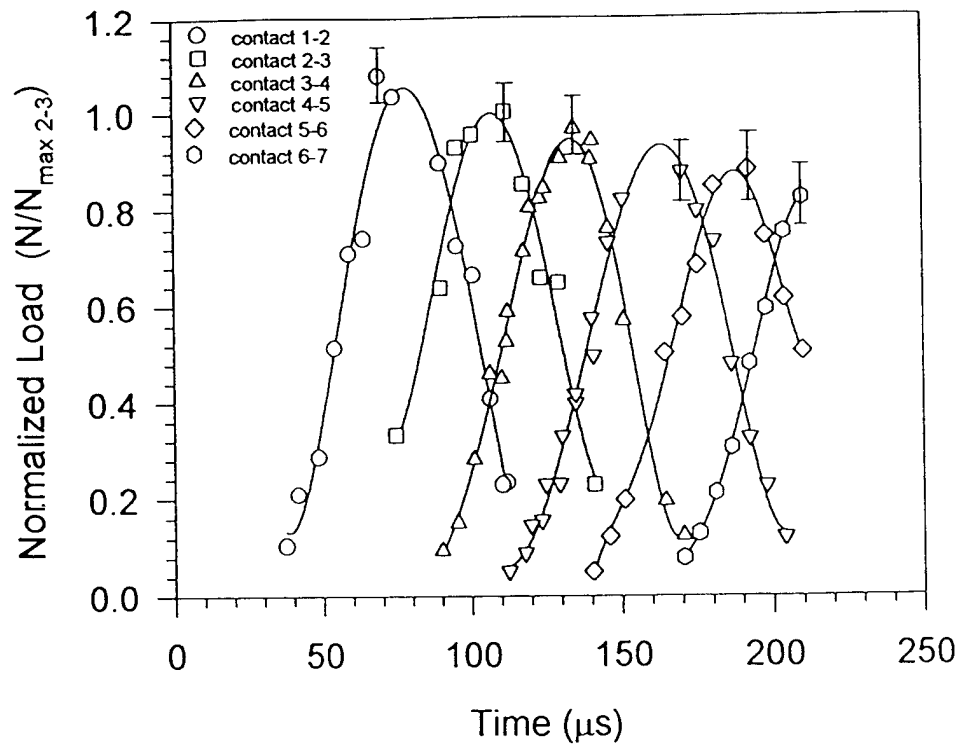
Figure 2.8. Normalized contact load histories for the assembly BCCH.
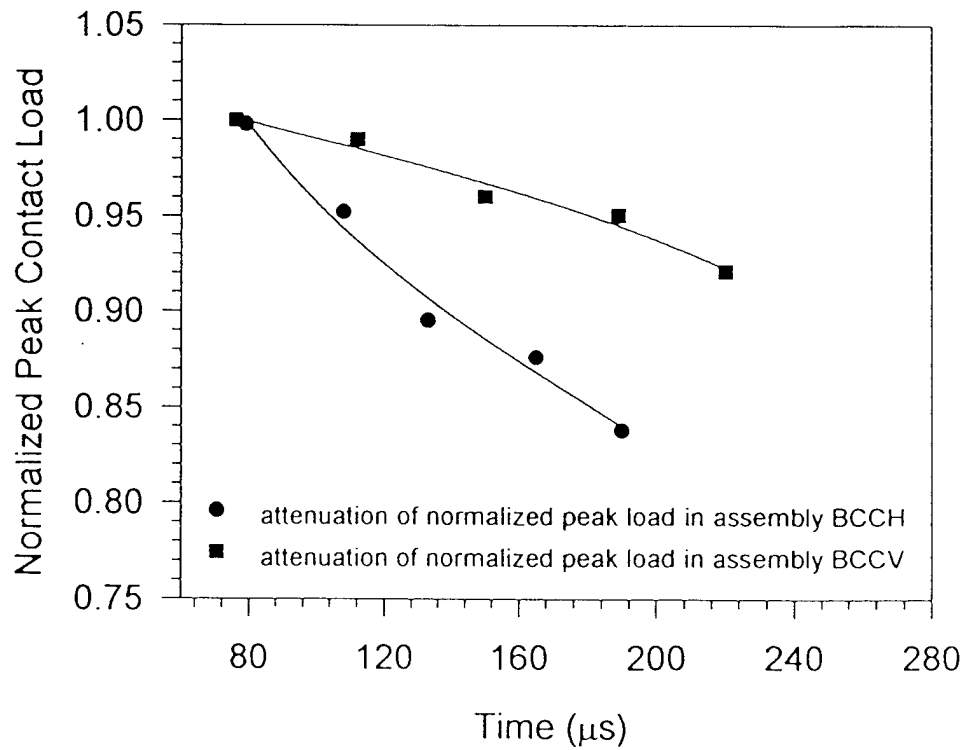
Figure 2.9. The attenuation of the normalized peak contact load with propagated time for the BCC assemblies.

47

★ Explosive

Frame 15
129 μs
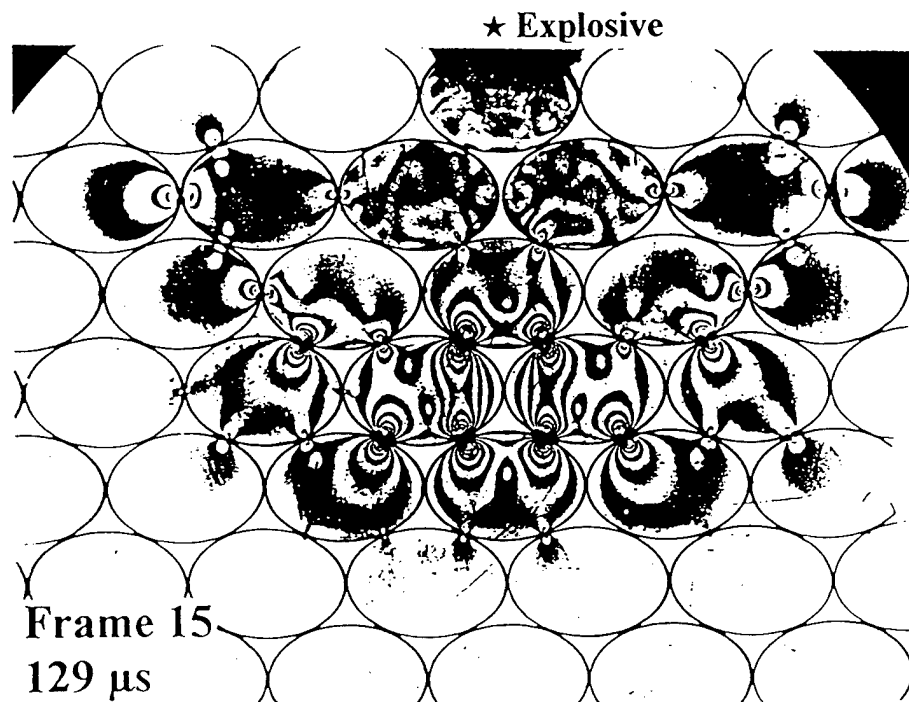
(a) Isochromatics of HCPH assembly

★ Explosive

Frame 9
129 μs
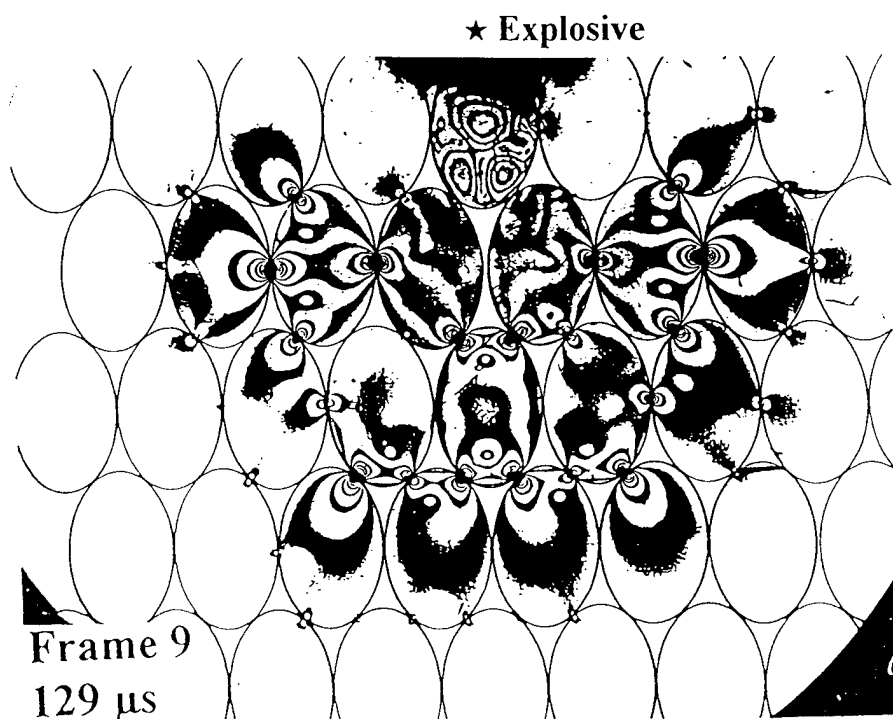
(b) Isochromatics of HCPV assembly

Figure 2.10. Isochromatics of HCP assemblies

contact normal distribution　branch vector distribution　major axis orientation distributio

HCPH assembly

HCPV assembly
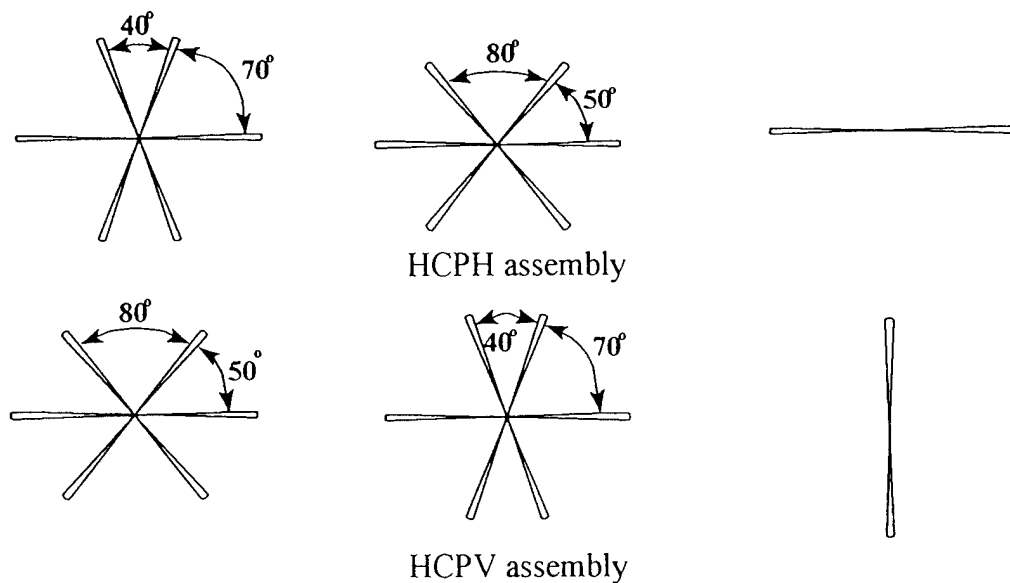
Figure 2.11. The dsitribution of fabric parameters in HCP assemblies

★ Explosive

(a) Isochromatics　　　　　　　Frame 9　　129μs

contact normals　　　　branch vectors　　　　major axis orientaion

(b) Fabric parameter distribution
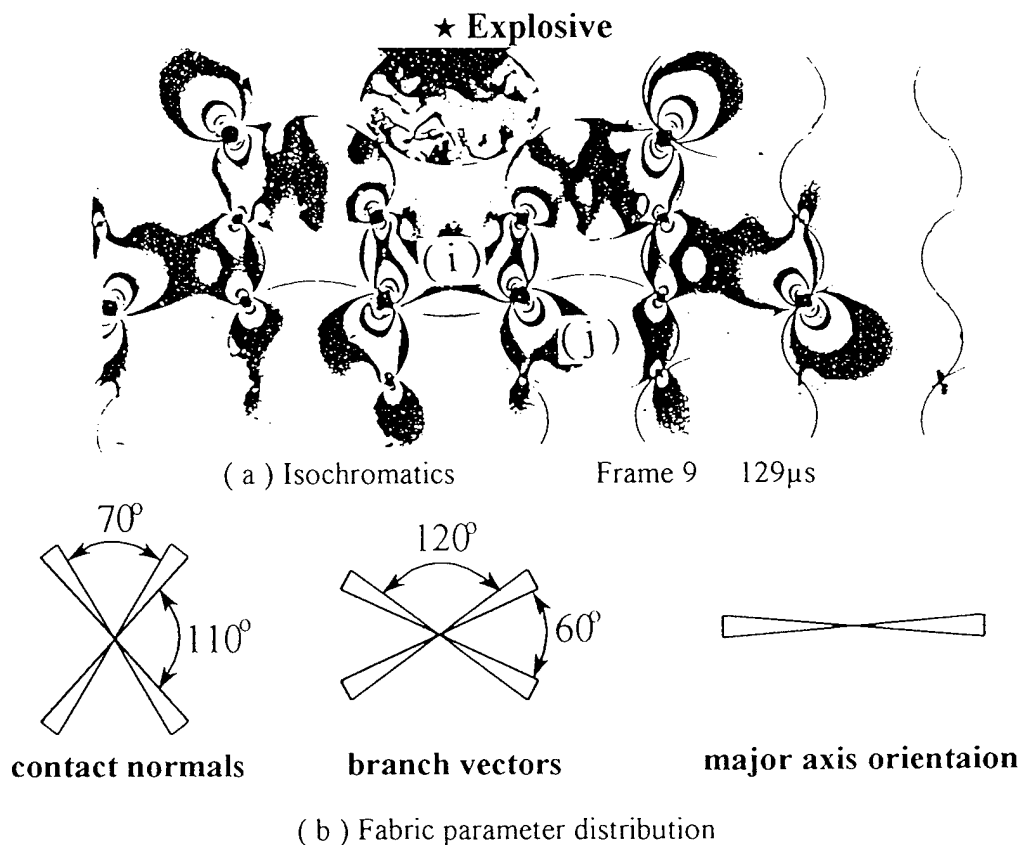
Figure 2.12. Isochromatics and fabric parameter distribution in HCPS1 assembly

49

★ **Explosive**

(a) Isochromatics   Frame 9   130μs

contact normals   branch vectors   major axis orientation
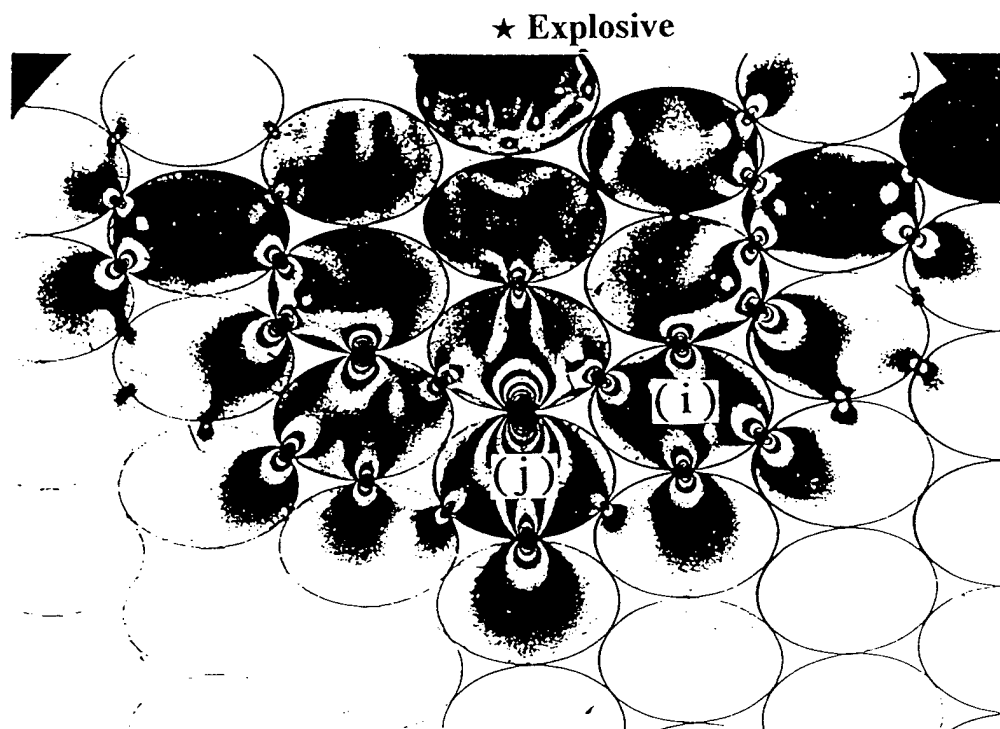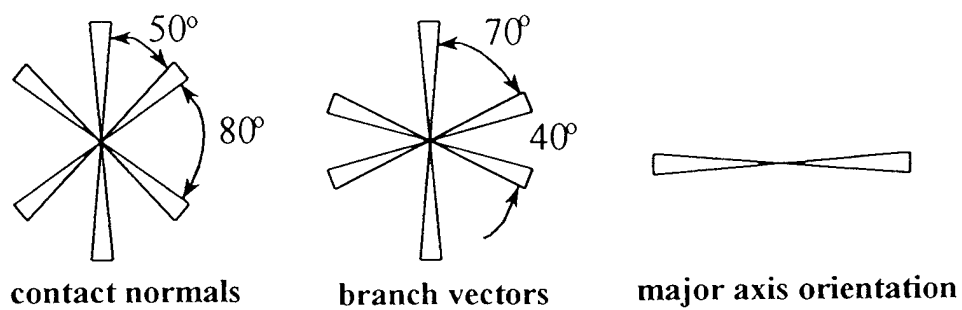
(b) Fabric parameter distribution

Figure 2.13. Isochromatics and fabric parameter distribution in HCPS2 assembly

★ **Explosive**

(a) Isochromatics   Frame 9   129μs

contact normals   **branch vectors**   **major axis orientation**

(b) Fabric parameter distribution
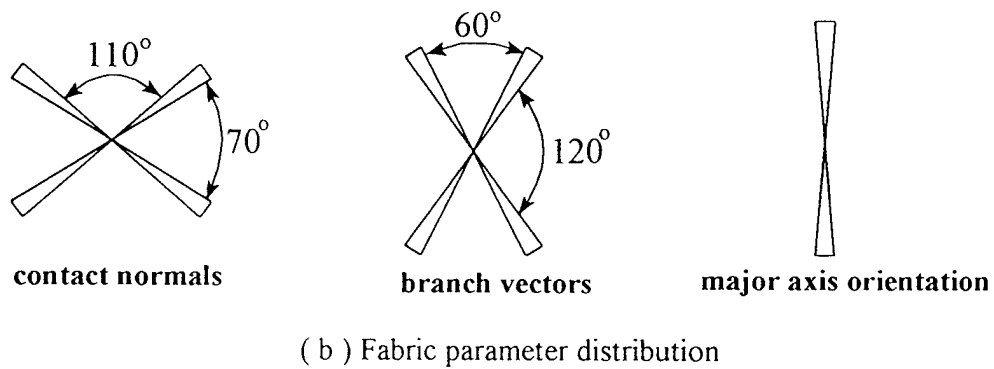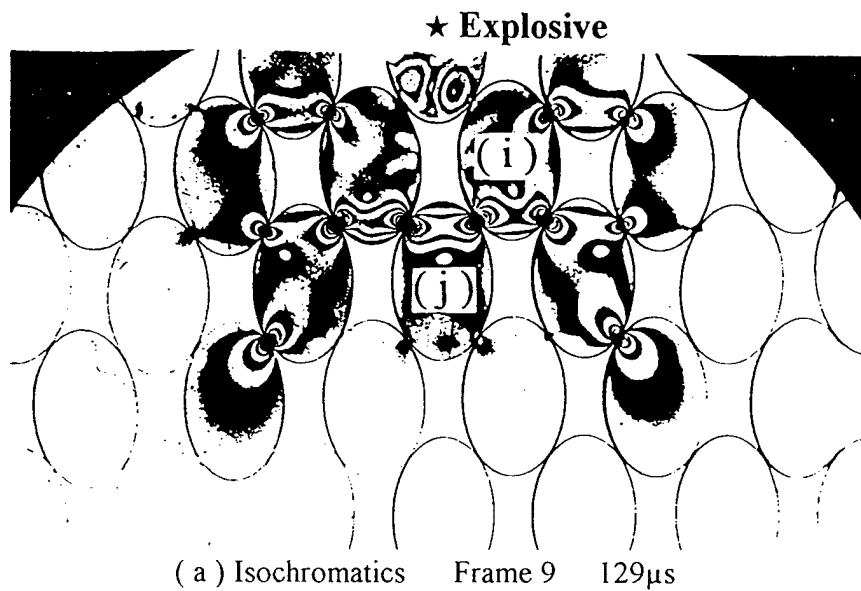
Figure 2.14. Isochromatics and fabric parameter distribution in HCPS3 (rotated HCPS1) assembly

• HCP assembly
■ HCPS1 assembly
▲ HCPS2 assembly
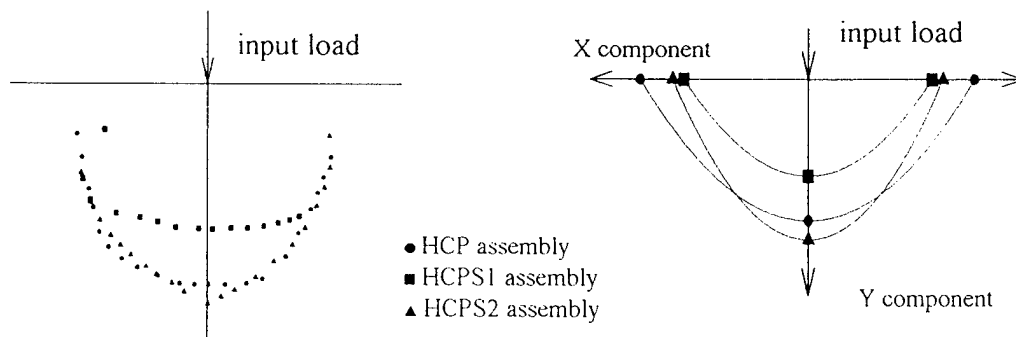
(a) The global wave front in experiments

(b) The contour made by X and Y compoments of branch vector

Figure 2.15. The qualitative correlation of global wave front with branch vector distribution

51
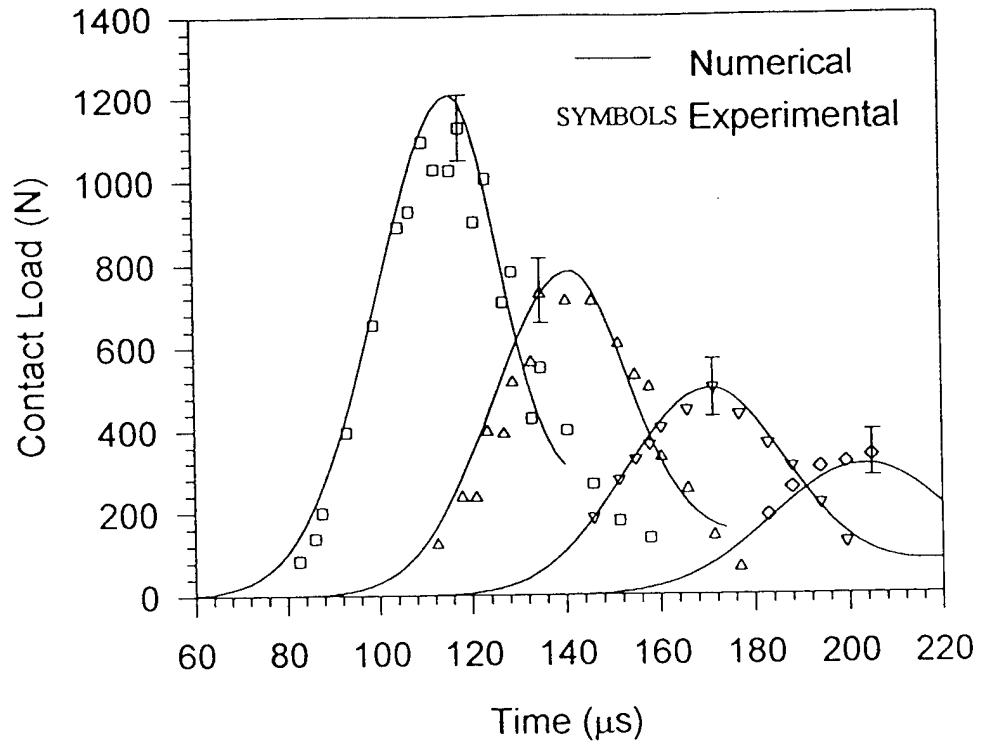
Figure 2.16. The contact load profile for main chain in assembly HCPH.
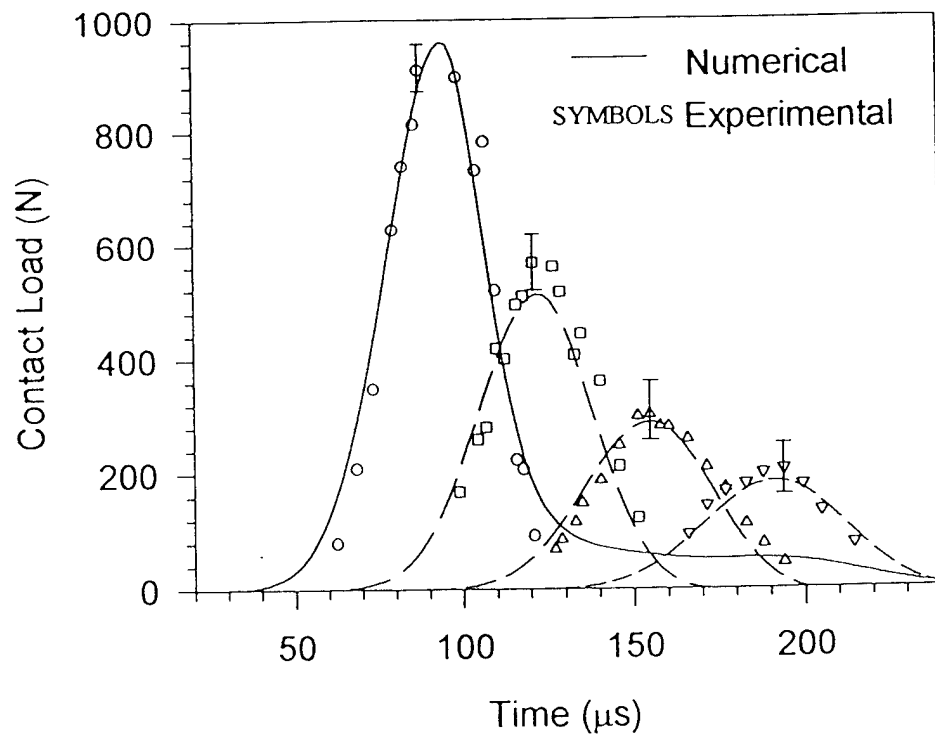
Figure 2.17. The contact load profile for secondary chain in assembly HCPH.
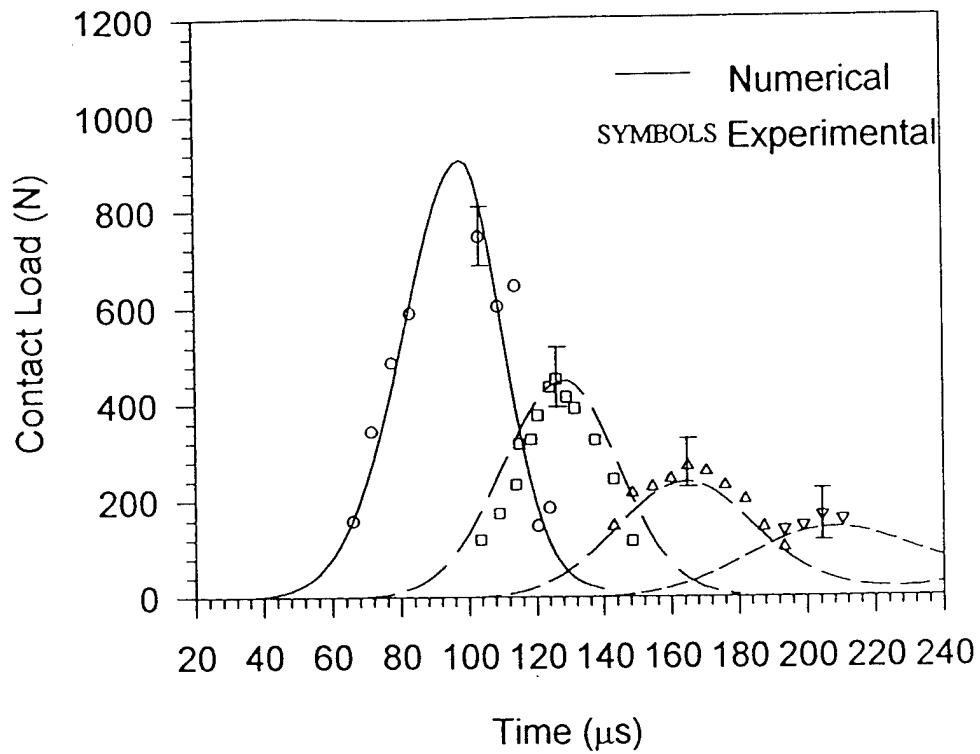
Figure 2.18. The contact load profile for main chain in assembly HCPV.
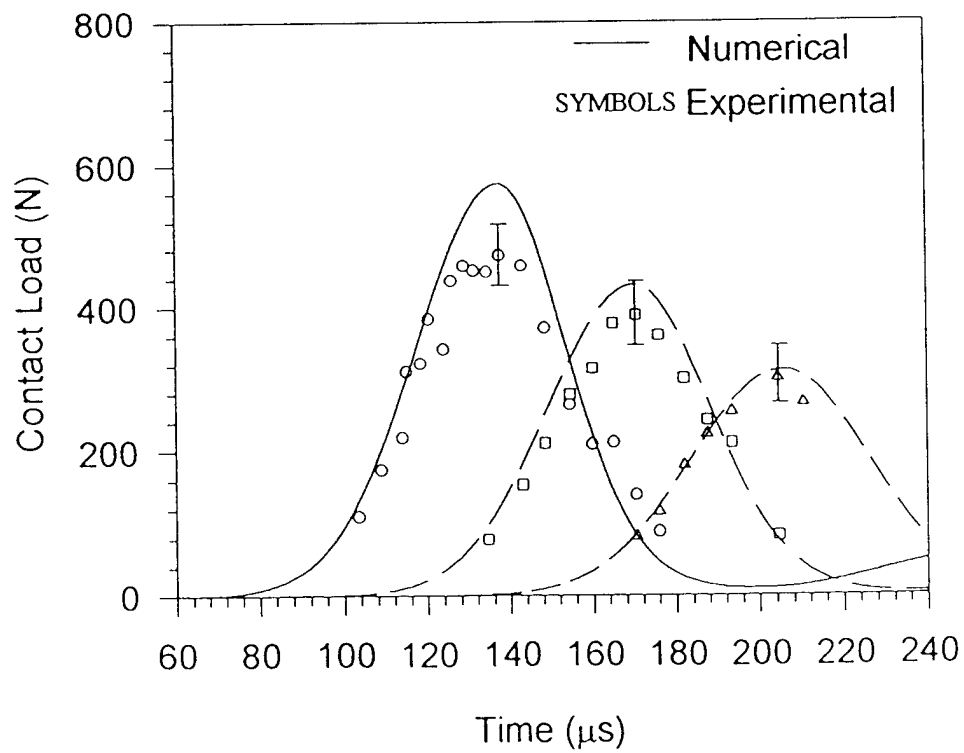
Figure 2.19. The contact load profile for secondary chain in assembly HCPV.

53

CHAPTER 3
WAVE PROPAGATIONAL BEHAVIORS THROUGH ASSEMBLIES
OF ELLIPTICAL PARTICLES

3.1 Summary

Wave propagation in granular materials is numerically studied using discrete element simulation. Primary interest is concerned with linking material microstructure with wave propagational behaviors for materials composed of elliptical particles. The discrete element scheme uses a non-linear hysteretic contact law which accounts for differences related to the radius of curvature at the interparticle point of contact. Modeling results yield information on wave speed and amplitude attenuation on two-dimensional, meso-domain model systems of both regular and random assemblies. Particulate models were numerically generated using a biasing scheme whereby partial control of particular fabric measures could be achieved. Three specific fabric measures which were used to characterize the granular material models include *branch, contact normal* and *orientation vectors*. DEM wave simulation results indicated that attenuation and wave speed generally correlated with the orientation and contact normal vector distributions. A power law relation between averaged fabric variables and wave speed and attenuation was proposed.

3.2 Introduction

The mechanical response of granular and particulate materials is governed by the interparticle contact behavior between individual grains. The discrete nature of such materials establishes non-continuous and discrete load transfer behavior which can be related to the material microstructure or fabric. It has been well established [Oda et.al 1982, Shukla et.al 1988 and Zhu et.al 1991] that load transfer in a cohesionless granular medium occurs along a complex network of discrete paths. With regard to wave propagation, granular materials create a structured wave-guide network through which mechanical energy is transferred. Along a given wave path, the dynamic load transfer is determined by the contact interactions between neighboring particles, and thus propagational characteristics of wave speed, amplitude attenuation and wave form dispersion are related to the local fabric along

established wave paths.

Considerable interest in dynamic geomechanics problems has produced numerous studies dealing with wave propagation in sand and rock materials. Much of the current research has focussed on using micromechanical modeling incorporating local mechanics at the particulate level to predict the macro-constitutive response. Some work (Duffy, 1959, Hardin, 1989, Digby, 1981, Thornton, 1986, Petrakis, et.al, 1988, Kishino, 1988, Chang, et.al, 1990, and Walton, 1987) has been done in modeling granular media as arrays of idealized (circular or spherical) elastic particles with the goal of determining equivalent macro elastic constitutive constants from the local interparticle contact behavior. Another area of research has developed *fabric tensor theories* whereby particular microstructures are described by volume averages of vector/tensor measures and constitutive relations are proposed using these fabric tensors. Pioneering work by Oda (1982), Nemat-Nasser, and Mehrabadi (1983), and later followed by many other studies, e.g. Bathurst and Rothenburg (1988), Konshi and Naruse (1988), Satake (1992) have developed several types of fabric tensor theories to predict static or quasi-static particulate material behaviors.

Although some success in linking fabric to mechanical behavior has been obtained, no unique choice of fabric description has been universally accepted which can adequately describe the general mechanical response of particulate media. Fabric can be categorized into two types: *orientation fabric* (orientation of individual particles) and *packing fabric* (mutual relation of individual particles). Orientation fabric may be quantitatively defined by a vector mean direction and a vector magnitude (e.g. *orientation vector*) to characterize orientation of non-spherical or non-circular particles. This fabric measure is commonly represented by an angular measure (with respect to a reference direction) of the long axes of individual particles. Packing fabric measures have included *branch vectors* (drawn between adjacent particle mass centers), *normal contact vectors, coordination or contact numbers, void characteristics, etc.* Examples of these fabric measures are illustrated schematically in Figure 3.1.

By considering material models with *elliptical shaped* particles, various orientation and packing fabric interactions will occur which would not be present for circular or spherical particles. Obviously particles found in natural granular materials have complex non-circular shapes, and thus a better understanding of the behavior of such materials may be found by

considering particles of more general shape. Several previous studies have investigated the static behavior of granular systems with elliptical particles. Konishi, et.al. (1982) conducted one of the first experimental studies on the relationship between fabric and mechanical behavior of granular systems with elliptical/oval particles. Discrete element simulations have been conducted by Rothenburg and Bathurst (1992,1993), Ting, et.al. (1993,1995), Sawada and Pradham (1994) and Lin and Ng (1994) on elliptical and ellipsoidal particles. Additional theoretical work related to grain shape has been conducted by Pande (1987). Results of these previous studies have been primarily concerned with the static behavior including shear strength, friction angle and anisotropy.

The present article is concerned with the role *particle shape* plays in the *dynamic response* of granular media. An initial paper focusing on an experimental investigation of this topic has been previously published by our research group (Zhu et.al 1996). Results are herein presented of a theoretical/numerical study which examines the relationship of granular fabric with wave propagational variables. The model granular materials under study were large assemblies of elliptical particles created numerically using random media generator codes. Although these assembly generating procedures were random, deliberate biasing was used in the generation process in order to construct materials with a variety of microstructures. Because many natural granular materials are deposited with preferred directions of the particle long axis, our goal was to focus on this type of *inherent anisotropy* by creating model assemblies with this type of fabric. Wave propagation through these model assemblies was simulated using the computational scheme of *discrete element modeling*. This study concentrated primarily on the relationship between material fabric (as measured by the distributions of branch, normal and orientation vectors) and the propagational characteristics of wave speed and attenuation.

The modeling scheme presented here can be thought of as a *meso-domain* approach, attempting to bridge the micro-macro responses. Micromechanical modeling at the particulate level is applied to a sufficiently large assembly of particles such that averages of particular wave propagational characteristics will be meaningful. This issue is related to the *homogenization process*, see for example, (Bourbié, Coussy and Zinszner 1987) in which they point out that macroscopically meaningful results can only be found if the sample size is much larger than the minimum homogenization volume.

3.3 Discrete Element Modeling

3.3.1 General Theory

Originally developed by Cundall et al.(1979), the *discrete element method* is a numerical scheme that has been successfully used to simulate the response of granular media by modeling the dynamic behavior of assemblies of model particles (e.g., circular disks, spheres, blocks, etc.). A large body of previous research (for example, Thorton 1988, Ting 1989, Willams 1988, Walton 1991, Ng 1992, Rothenbrug 1993, Sadd et.al 1993) have established the usefulness of this numerical modeling scheme for particulate materials. The method makes simplifying constitutive assumptions for each particle (commonly assuming rigid body behavior) and then uses Newtonian mechanics to determine the translational and rotational motion of each particle in the assembly. In order to establish inter-particle contact behavior, the assumed rigid particles are allowed to have small overlapping contact, and thus contact forces are developed as a result of particular stiffness and/or damping characteristics. The technique establishes a discretized time stepping numerical routine, in which granule velocities and positions are obtained through numerical integration of the computed accelerations. Using the principle of *causality*, it follows that during an appropriately small time step, disturbances cannot propagate from any disk further than its immediate neighbors. Under these conditions, the method becomes explicit, and therefore at any time increment the resultant forces (and thus the accelerations) on any particle are determined solely by its interactions with its contacting neighbors. For applications to wave propagation, the movements of the individual particles are a result of the propagation of mechanical disturbances through the medium. Consequently, the wave speed and amplitude attenuation (intergranular contact force) will be functions of the physical properties of the discrete medium, i.e., the microstructure or fabric.

The general concept of the method may be explained by considering a general two-dimensional particulate assembly as shown in Figure 3.2. Isolating attention to the i-th particle and applying Newton's laws yields

$$\sum_{j=1}^{N} F^{ij} + F^{i} = m_i \ddot{x}_i$$

$$\sum_{j=1}^{N} M^{ij} + M^{i} = I_i \ddot{\theta}_i$$

<div align="right">(3.1)</div>

where F^{ij} are the j-contact forces on the I-th particle, F^{i} represents any non-contacting forces on particle I, M^{ij} are the moments (about the particle's mass center) resulting from contact forces F^{ij}, M^{i} is the resultant moment from any non-contacting forces, m_i is the particle mass, and I_i is the mass moment of inertia. With given contact and non-contact forces, the linear and angular accelerations of the I-th particle can thus be determined from this system of equations. With the accelerations known, the velocities and displacements may be obtained through numerical integration using finite differencing schemes.

It is obvious that the contact response between neighboring particles plays a very important role in the use of this numerical method to simulate wave propagation through granular materials. Past research, Sadd et al. (1993) has investigated the use of several contact laws within the discrete element modeling scheme. Establishing a local normal and tangential coordinate system at each contact between adjacent particles, a contact law can be constructed relating interparticle force to the overlapping deformation and deformation rate. In general such a contact law between adjacent particles could be written as

$$F_n^{ij} = F_n^{ij}(\delta_n, v_n, \delta_t, v_t)$$

$$F_t^{ij} = F_t^{ij}(\delta_n, v_n, \delta_t, v_t)$$

<div align="right">(3.2)</div>

where δ_n and δ_t are the relative normal and tangential displacements between particles I and j, and v_n and v_t are the relative normal and tangential velocities. Contact relations (3.2) may also be *history dependent*, and a Coulomb-type friction law is commonly incorporated to place limits on the tangential response. Specific forms of such contact relations have included Hertz-Mindlin theory and linear, non-linear, and non-linear hysteretic laws (Sadd et.al 1993). Previous results have indicated that the non-linear hysteretic deformation law for the normal

forces provided simulation results which compared favorably with experimental data, and this particular law has been chosen for use in the current study.

3.3.2 Particle Contact Detection Algorithims

The discrete element scheme requires the determination of particle contact detection and establishment of contact normal and tangential directions. Elliptical shaped particles have unique outward surface normals with no singularities, and thus such contact detection and geometry can be rather easily calculated. Our approach uses the robust schemes originally developed by Ting (1993). Figure 3.3 illustrates two elliptical particles in contact with some overlap which is taken as contact deformation. Based on analysis of particle (I), the normal and tangential directions at contact point B (established with virtual ellipse) can be determined, and the intersection of the determined normal direction with ellipse (j) occurs at point A. The distance AB is thus taken as an approximation of the normal contact deformation. The same procedure is repeated for particle (j), thus yielding another set of normal and tangential directions and contact overlap. Each of these sets are then averaged between the two particles to determine the final values of the normal and tangential directions and contact deformation. The tangential contact displacement increment is determined by the relative tangential displacement of the contacting elliptical particle mass centers and the relative rotational displacements of each particle.

3.3.3 Inter-Particle Contact Laws

The overall wave propagational characteristics including wave speed and amplitude attenuation depend on the micro-processes of dynamic load transfer between particles. Since the load transfer is governed by the particle to particle contact mechanics , the wave propagation characteristics will depend on the inter-particle contact laws. A nonlinear-hysteretic normal contact law illustrated in Figure 3.4 was developed by Sadd et al. (1993) and has been effectively used in DEM simulation of dynamic load transfer. This law may be specified as:

59

$$F_n = \begin{cases} F_{nL} = \alpha_L \, \delta^p & \ldots \text{ loading} \\ F_{nU} = \alpha_U \, \delta^{p+q} & \ldots \text{ unloading, reunloading} \\ F_{nRL} = \beta \, F_{nL} + (1-\beta)F_{nU} & \ldots \text{ reloading} \end{cases} \tag{3.3}$$

The value of q and β are determined by

$$q = (A\,\delta_{n,max})^r$$

$$\beta = \frac{\delta_n - \delta_{n,min}}{\delta_{n,max} - \delta_{n,min}} \tag{3.4}$$

while the value of α_U is determined from the continuity requirement at the inception of unloading. The values of α_L, p, r, and A are related to material and geometric properties of the particles. Our previous research for a photoelastic granular material (Homalite 100) found that DEM simulations matched experimental data with p = 1.4 and r = 2 .

It was also found however, that α_L and A should be related to the particle's radius of curvature at the contact point, and for non-circular, elliptical particles, the surface curvature varies with surface location. To investigate this contact surface curvature relationship, several wave propagation tests were conducted on regular assemblies with simple fabric. These assemblies include straight single chains, body-centered cubic, and hexagonal close-packed geometries. The results of these characterization studies are shown in Figure 3.5 which illustrates the contact parameter values used in the DEM modeling of each regular assembly. These simulations gave reasonable agreement with the corresponding data collected from dynamic photomechanics experiments for Homalite 100 material (Zhu et.al. 1996). These results then provide an estimate of the behavior of the contact law parameters as a function of contact radius of curvature. A curve fitting algorithm gave the relations

$$\alpha_L = (1.34 + 41.44r) \times 10^8 \quad (N/m^{1.4})$$
$$A = -405.9 + (5.13 \times 10^5)r - (1.12 \times 10^7)r^2 \quad (m^{-1}) \tag{3.5}$$

and these are included in our numerical simulation code. If two contacting elliptical particles have different radii of curvature, averaged values for A and α_L are used. With regard to the

tangential contact law, the form (with some modifications) proposed by Walton et.al.(1991) was adopted . This law includes a decreasing tangential contact stiffness with an increase of the tangential force, and provides for a zero stiffness during full sliding.

3.4 Material Model Generation

To investigate the fabric effect of wave propagation through granular materials with elliptical particles, large model assemblies need to be constructed with various degrees of granular anisotropy and microstructure . In order to characterize microstructure in assemblies of elliptical particles, three vector fabric measures were chosen including: *branch vectors, contact normal vectors and orientation vectors* (see Figure 3.1). It was felt that these three measures could adequately describe most of the important microstructural properties of such materials. A random elliptical particle assembly generator was developed whereby assemblies were created by a starting line of randomly spaced particles of a specified orientation. Subsequent vertical layers were added to fill out the assembly. By controlling the random spacing limits, particle eccentricity and orientation vectors, assemblies can be created with controllable microstructure. As shown in Figures 3.6-3.11, a total of six model assemblies have been generated in this fashion, for different values of orientation vectors. All models have elliptical particles of identical size with major axis of 50mm, minor axis of 20mm and a thickness of 6mm. Large size particles were used to allow for future comparisons with anticipated experimental efforts. The two cases with orientation of 0° and 90° had uniform spacing between particles. Also included in Figures 3.6-3.11 are the respective distribution plots of the branch and contact normal vectors for each assembly model. Other characteristics of the six models are listed in Table 3.1.

Each of the constructed assemblies were subjected to dynamic loadings to create a wave propagation situation, and this behavior was modeled using our discrete element wave propagation code. The simulations involved the propagation of plane-type compressional waves moving in the vertical direction generated by simultaneously loading all particles along the bottom of each assembly with a transient input of triangular time history. The input pulse had a peak value of 2.5 kN and a period of 110 µs. From a continuum point of view, this type of loading will input primarily a planar P or dilatational wave. Of course, as the combined dynamic signal moves through the granular medium, some small tangential interparticle

contact forces will develop, and thus at the micro-level, there will be some partitioning of the signal into a *shearing mode*. We would not however, classify this mode as a shear wave component.

The primary interest of the DEM simulations are to determine the wave speed and amplitude attenuation behaviors. The original time-coherent input plane wave will gradually become spatially and temporally discontinuous with propagation distance, and thus determination of the wave front and wave amplitude need to be established. The wave speeds are calculated by determining the propagation time of the averaged wave profile, while attenuation is calculated through a *transmission ratio* of averaged output to input signal per length of propagation. To calculate the transmitted or output wave signal, an imaginary horizontal line was drawn near the boundary opposite to where the input loadings were applied. If a branch vector of a pair of particles in contact or potential contact is intercepted by this imaginary line, the normal contact load component perpendicular to the imaginary line is recorded. In this fashion, the contribution of the individual particle contacts can be determined, and these recorded loads are then summed and averaged over all contacts associated with the output line. This procedure then establishes the average output wave signal. Because load transfer through the initial first layer of particles occurs with special attenuation and dispersion characteristics, it was felt that simply using the boundary loadings to represent the input signal would not provide a correct value for determination of material transmission. Therefore the input loadings were collected from the interparticle contacts after one layer of propagation using the same scheme used for determining the average output loadings.

To investigate the amplitude attenuation in each material model, the following transmission ratio was used,

$$TR = \frac{\bar{F}_{output}/\bar{F}_{input}}{D} = \frac{\dfrac{1}{N_o}\sum_{n=1}^{N_o} F_{output}^{(n)}}{\dfrac{1}{N_i}\sum_{n=1}^{N_i} F_{input}^{(n)}}\frac{1}{D} \qquad (3.6)$$

where $\bar{F}_{output}$ and $\bar{F}_{input}$ are the averages of the peak output and input contact loads, N_o and N_i are numbers of contacts along the output and input lines, and D is the propagation distance

between input and output lines.

3.5 Results

Discrete element simulations of the dynamic, wave propagation response of each model assembly in Figures 3.6-3.11 were conducted, and the results of the wave speed and transmission ratio are summarized in Table 3.1. Figure 3.12 shows a specific transmission result for model A-4 in which the time dependent behavior of the transmission ratio is plotted. This averaged output signal contains contributions from numerous individual propagation paths through the medium, and significant attenuation and dispersion are observed. The arrival time of the peak amplitude of this averaged signal is used to calculate the wave speed of the simulation.

Results in Table 3.1 indicate that the wave speed and transmission ratio correlate to some degree with the orientation vector of the media. For example, with the exception of media model A-5, the smaller the angle made by the input loading and orientation vector, the larger the transmission ratio will be. The apparent contradiction observed in model A-5 may be explained by viewing the contact normal vector distributions. For model A-5, many of the contact normals lie very close to the wave propagation direction, thus indicating preferred propagational directions in the vertical. This indicates that contact normal vectors are also an important factor in relationships with wave propagation and it can be observed for all assembly models that there is an increase in wave speed as the contact normal distribution becomes more vertical. With regard to the void ratio, it is observed (again with exception of model A-5) that wave transmission varies inversely with the void content; however, other fabric factors in these models probably play a more significant role in the attenuation behavior.

Another interesting micromechanical behavior to consider for elliptical particulate media is the particle rotation. When waves propagate through such granular media, higher attenuation may be accountable from kinetic energy losses through individual particle rotations. In order to investigate this behavior, the average rotation per particle for each of the model assemblies was determined. This value was calculated over a fixed duration of time (400µs), corresponding to the approximate transit time for the wave to propagate across a typical sample. Values of this rotation measure for each model assembly are shown in Table 3.1, and it is observed that a correlation does seem to exist between the attenuation and

particle rotation. Simulations having higher wave attenuation correspond to assemblies with high average particle rotation.

In order to evaluate effects of boundaries and numbers of particles, one particular case with orientation angle of 30°, was simulated with two models (A2 and A6) with different numbers of particles. As shown in Figures 3. 7 and 3.11, the fabric of these two assemblies are almost identical, and thus DEM simulations will isolate the effects related to assembly size. Results in Table 3.1 for these two assemblies indicate that very little differences exist in the predicted wave speed and attenuation. Therefore it appears that the chosen meso domain size is reasonable for the wave propagation simulations.

3.6 Wave Propagation - Fabric Relationships

In order to construct a relationship between wave propagation and material fabric, averaged fabric vector measures are needed. Since our wave motion also contains a propagation direction, averaged fabric should be measured with respect to this direction. With this in mind and denoting the unit normal vector to the input wave front as p, we can define three *averaged projected fabric measures* based on orientation, contact normal and branch vectors as

$$
\begin{aligned}
\bar{m} &= \frac{1}{N} \sum_{i=1}^{N} p \cdot m^{(i)} \\
\bar{n} &= \frac{1}{N_c} \sum_{i=1}^{N_c} p \cdot n^{(i)} \\
\bar{b} &= \frac{1}{N_b} \sum_{i=1}^{N_b} p \cdot b^{(i)}
\end{aligned}
\tag{3.7}
$$

where N, N_c and N_b are the number of particles, contacts and branch vectors, respectively.

It is expected that the wave propagational characteristics are related to these fabric measures, and a simple power law relation for the wave speed and amplitude attenuation is proposed in the following form

$$\left\{ \begin{matrix} TR \\ V \end{matrix} \right\} = F_i(m,n,b) = A_i \bar{m}^{P_i} + B_i \bar{b}^{q_i} + C_i \bar{n}^{r_i} \tag{3.8}$$

A reasonably good fit with the DEM simulations may be attained with parameter values

$$A_i = \left\{ \begin{matrix} 0.0768 \\ 495.3 \end{matrix} \right\} , B_i = \left\{ \begin{matrix} 0.0326 \\ 18.1 \end{matrix} \right\} , C_i = \left\{ \begin{matrix} 0.192 \\ 380.2 \end{matrix} \right\}$$

$$P_i = \left\{ \begin{matrix} 2.8 \\ 0.01 \end{matrix} \right\} , q_i = \left\{ \begin{matrix} 4.2 \\ -3.15 \end{matrix} \right\} , r_i = \left\{ \begin{matrix} 3.3 \\ 3.2 \end{matrix} \right\}$$

$$\tag{3.9}$$

Comparisons of DEM simulations with values from this power law relation are given in Table 3. 2. The average difference between the two is approximately 7%, thus indicating that the relationship (3.8) may be appropriate for assemblies of this type.

3.7 Conclusions and Discussion

Using discrete element methods, the wave propagational response of several granular material models composed of equal-sized, elliptical particles has been determined. Wave speed and amplitude attenuation has been calculated for a planar input wave of transient triangular time history. Because of the coupled nature of the three primary fabric measures (branch, contact normal and orientation vectors), it was not possible to develop random assemblies of elliptical particles with independent control of each fabric measure. Natural granular materials formed under gravitational action commonly yield anisotropy because particles tend to deposit with a preferred direction of their long axis. Thus the models under study were generated primarily to provide comparisons with the orientation fabric; however, some relationships with the contact normal distributions were also made. Based on the fact that the branch vector distributions of the media models A-2, A-3 and A-4 are not markedly different (see Figures 3.7-3.9), it was concluded that contact normal and orientation vectors play the predominant role in determining wave propagational characteristics for assemblies with elliptical particles. Results generally indicated that higher wave speeds and amplitude transmissions occur in assemblies with larger distributions of contact normal and orientation

vectors along the direction of propagation.

Some anomalous behavior occurred in the regular symmetric assemblies in models A-1 and A-5. However, it can be observed that because of the special nature of the packing fabric in these assemblies, very little particle rotations occurred during wave propagation. Studies of average particle rotation demonstrated that a correlation generally existed between wave attenuation and particle rotation. Simulations having higher wave attenuation corresponded to assemblies with high average particle rotation, thus indicating that micro-rotations provide an energy loss mechanism.

Propagational characteristics of attenuation and wave speed were related to material fabric through an empirical power law relation involving averaged projected fabric vectors. These projected fabric measures were based on the distributions of orientation, contact normal and branch vectors with respect to the direction of wave propagation. Reasonably good comparisons with DEM simulations resulted from this relationship. Although it would be difficult to argue general validity of the power law relation, results do indicate that the idea of relating such propagational variables to averaged projected fabric measures is reasonable.

Assembly Model	Orientation Angle	No. of Particles	Coord. No.	Void Ratio	Rotation (θ^0)	Trans. Ratio (TR)	Wave Speed (m/s)
A-1	0	328	3.65	0.188	0	0.110	438
A-2	30	333	3.68	0.205	0.407	0.091	570
A-3	45	367	3.67	0.226	0.763	0.062	587
A-4	60	465	3.73	0.243	0.979	0.043	603
A-5	90	336	3.69	0.184	0	0.120	400
A-6	30	1341	3.68	0.205	0.407	0.093	574

Table 3.1. Summary of Various Fabric Measures and Wave Transmissions for Six Model Assemblies (Orientation Angle = the acute angle between major axis and vertical)

Orientation Angle	Average Projected Contact Normal Vector	Average Projected Branch Vector	Transmission Ratio (TR)		Wave Speed (V)	
			DEM	Formula	DEM	Formula
0	0.5	0.866	0.110	0.114	438	565
30	0.3718	0.845	0.091	0.075	570	541
45	0.5061	0.79	0.062	0.061	587	574
60	0.5665	0.732	0.043	0.049	603	603
90	0.866	0.5	0.120	0.121	400	400
Average Relative Error			7.12%		0.072	

Table 3.2. Summary of DEM Simulation and Empirical Formula, Equation (8) Results for Five Model Assemblies

67
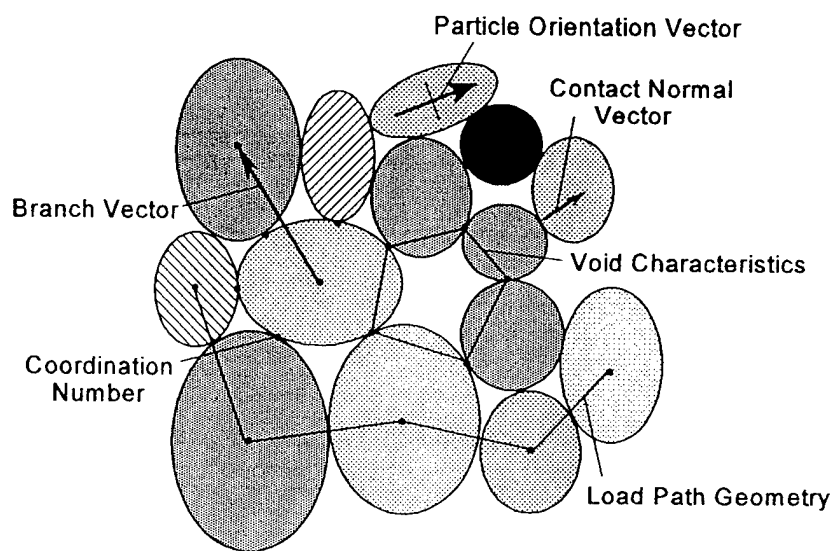
Figure 3.1. Common Fabric Measures for Granular Materials

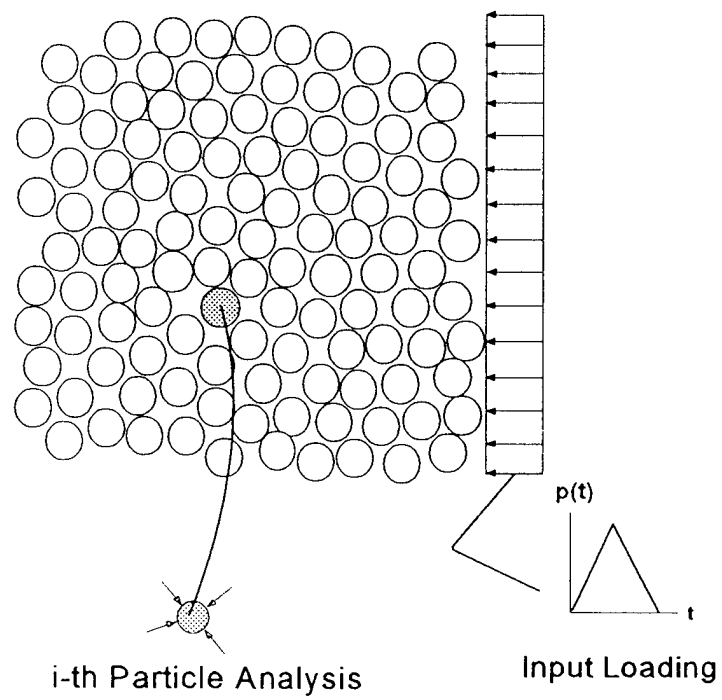i-th Particle Analysis   Input Loading

Figure 3.2 Discrete Element Modeling Procedure
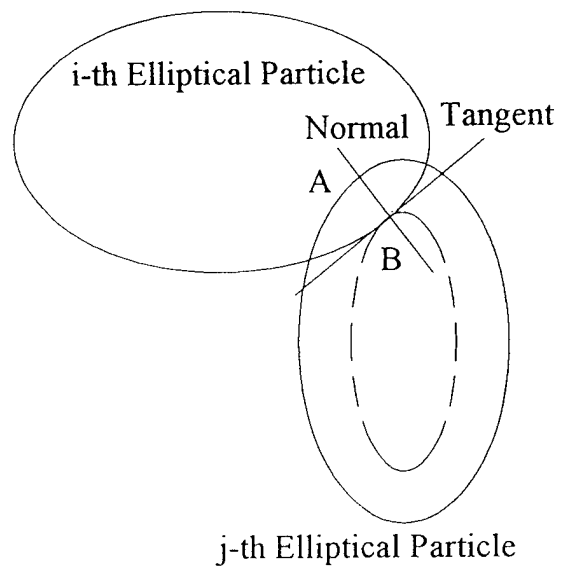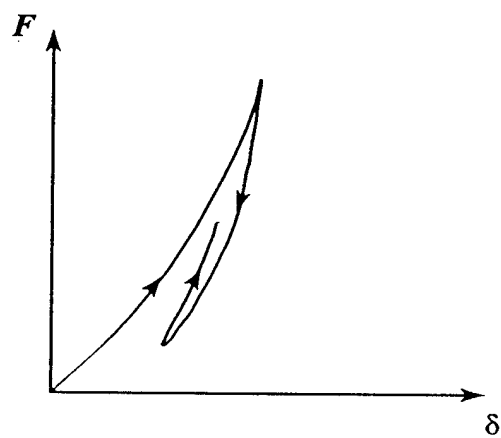
Figure 3.3. Deformation for Two Overlapped
Elliptical Particles
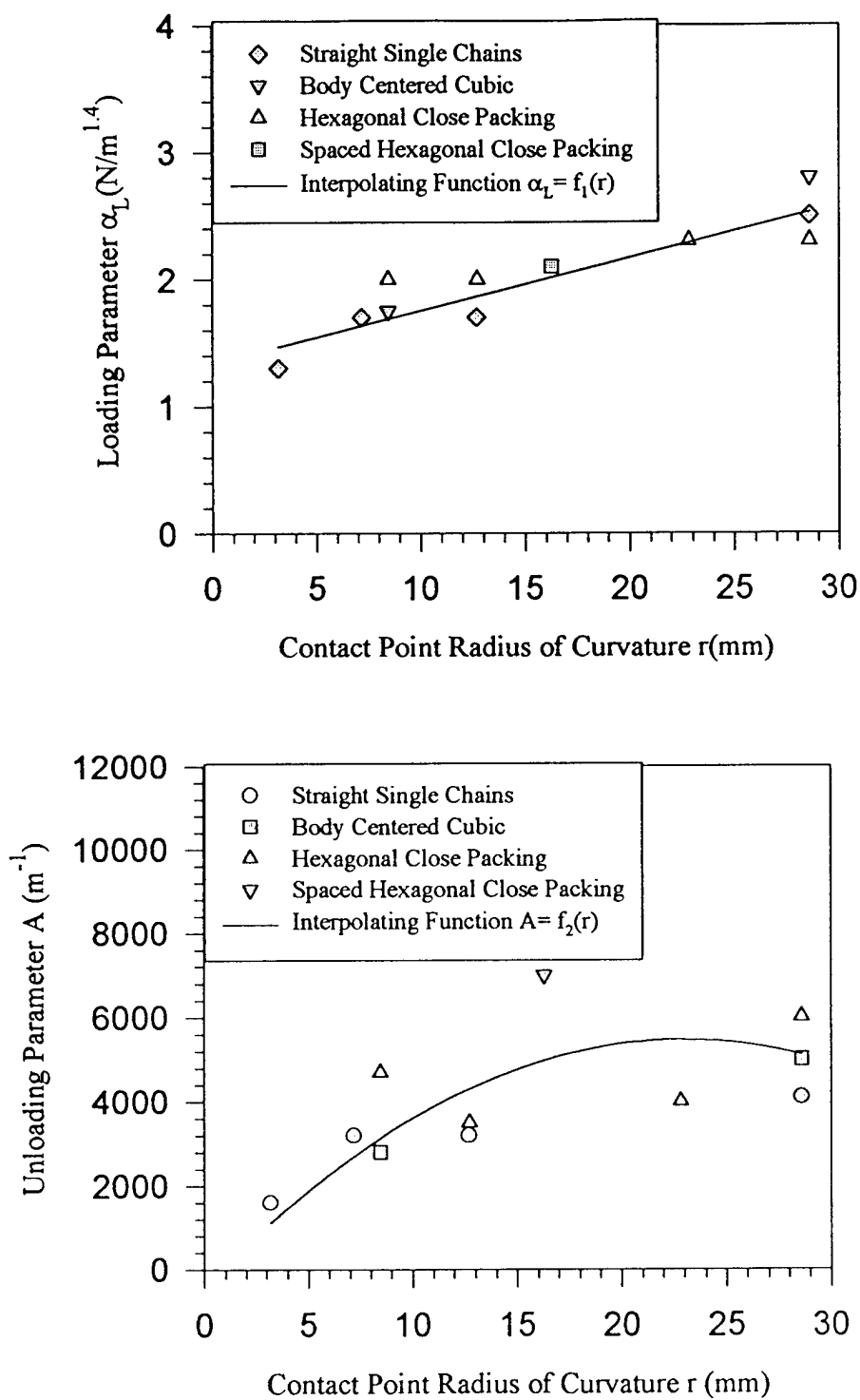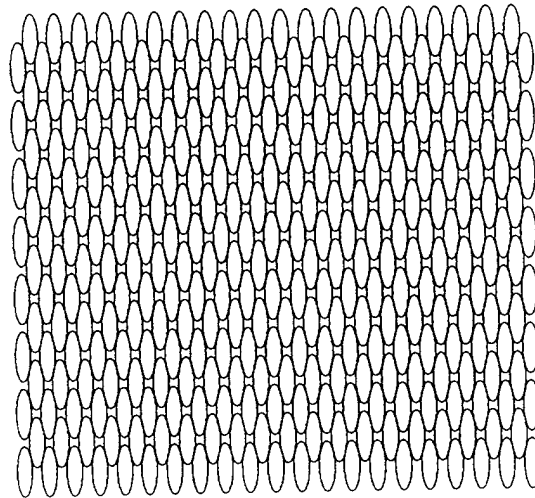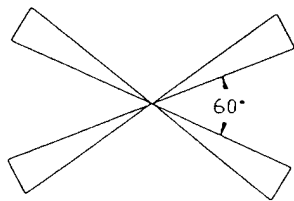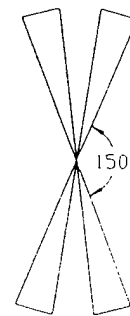
Figure 3.4. Nonlinear Hysteretic Contact Law

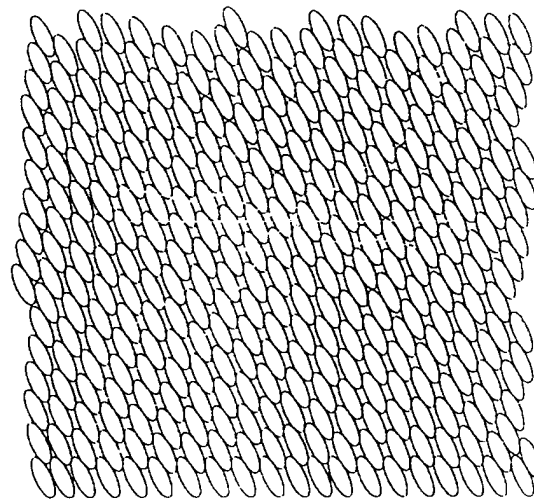Figure 3.5. The Relationship of Contact Law Parameters with Radius of Curvature

Assembly

Contact Normal Vectors
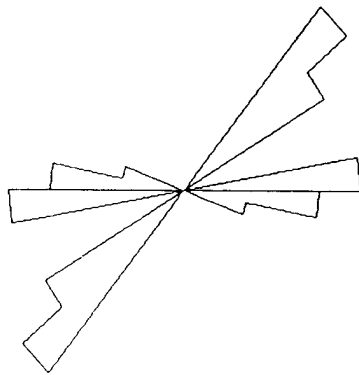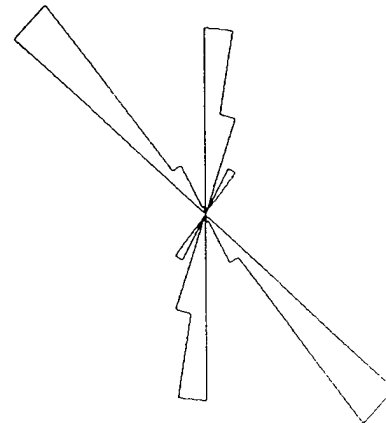

Branch Vectors

Figure 3.6. A-1 Media Model and Its Fabric Parameter Distributions
(Orientation Angle $=0^0$)

Assembly

Contact Normal Vectors

Branch Vectors

Figure 3.7. A-2 Media Model and Its Fabric Parameter Distributions
(Orientation Angle = 30^0)

Assembly

Contact Normal Vectors

Branch Vectors

Figure 3.8. A-3 Media Model and Its Fabric Parameter Distributions
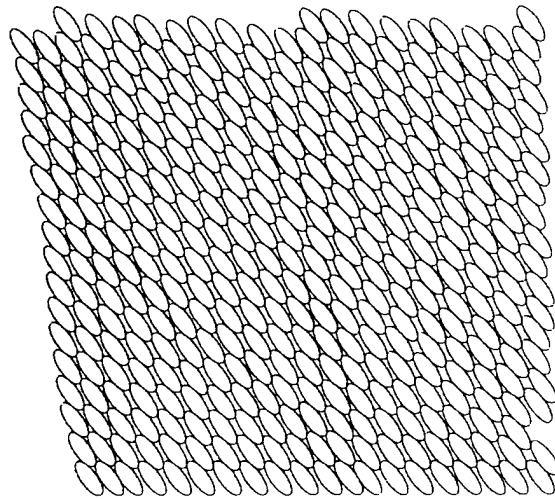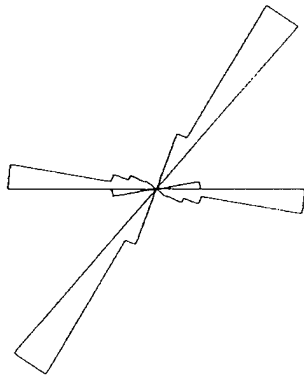(Orientation Angle = 45^0)

Assembly

Contact Normal Vectors

Branch Vectors

Figure 3.9. A-4 Media Model and Its Fabric Parameter Distributions
(Orientation Angle = 60^0)

Assembly

Contact Normal Vectors

Branch Vectors

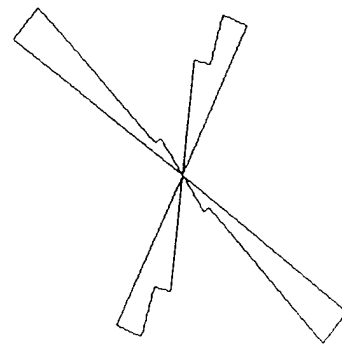Figure 3.10. A-5 Media Model and Its Fabric Parameter Distributions
(Orientation Angle = 90^0)

Assembly

Contact Normal Vectors

Branch Vectors

Figure 3.11. A-6 Media Model and Its Fabric Parameter Distributions
(Orientation Angle = 30^0 , Large Assembly)
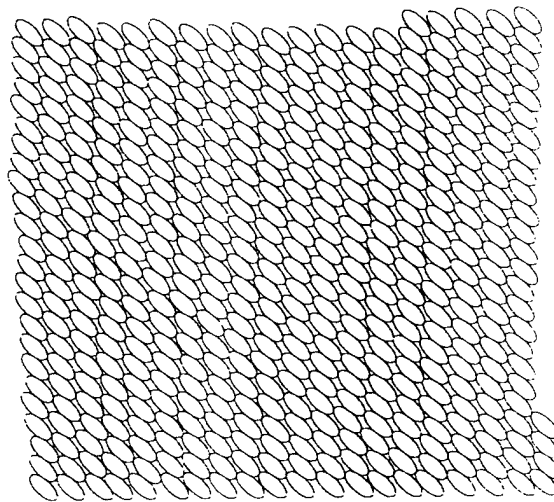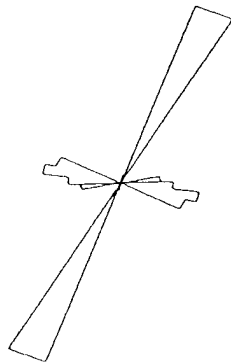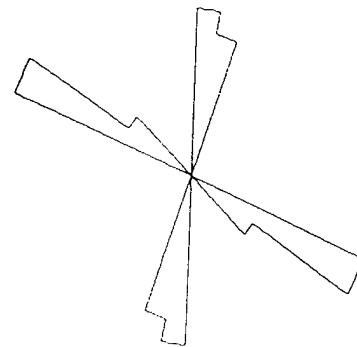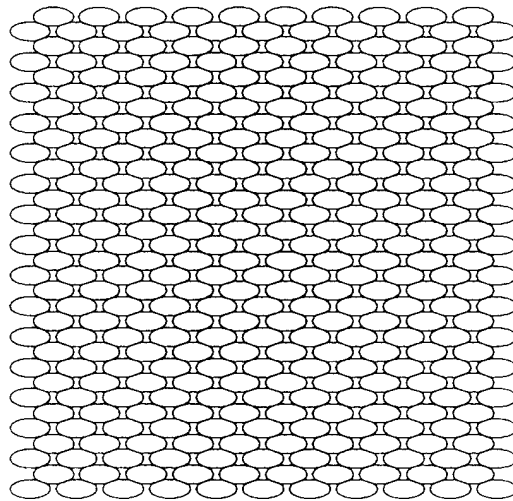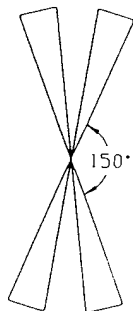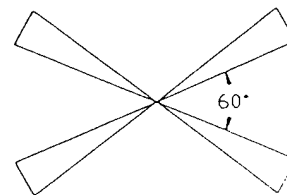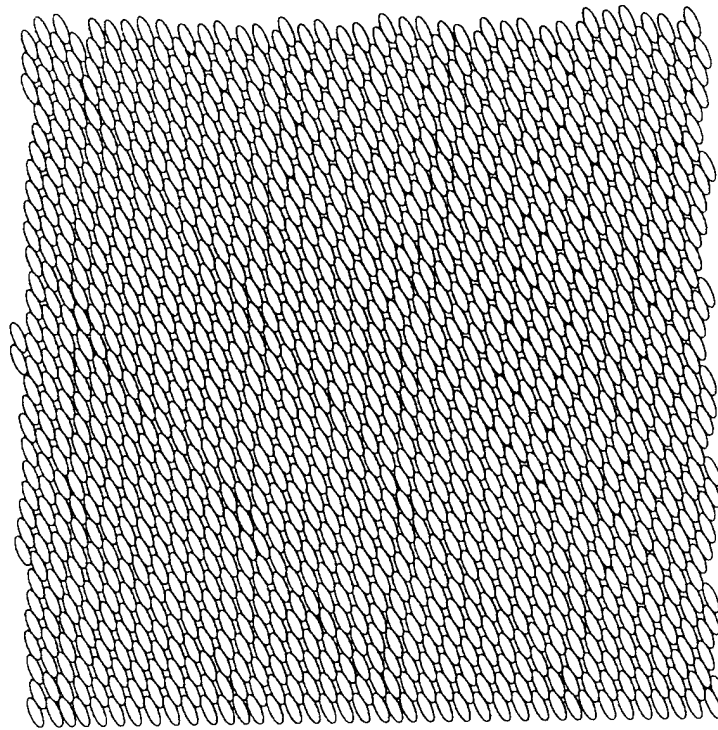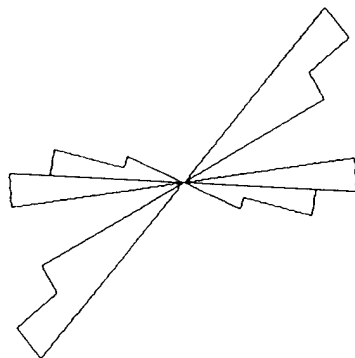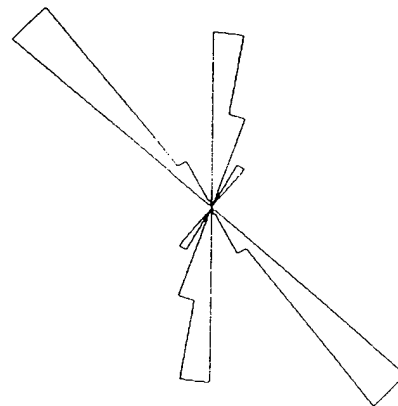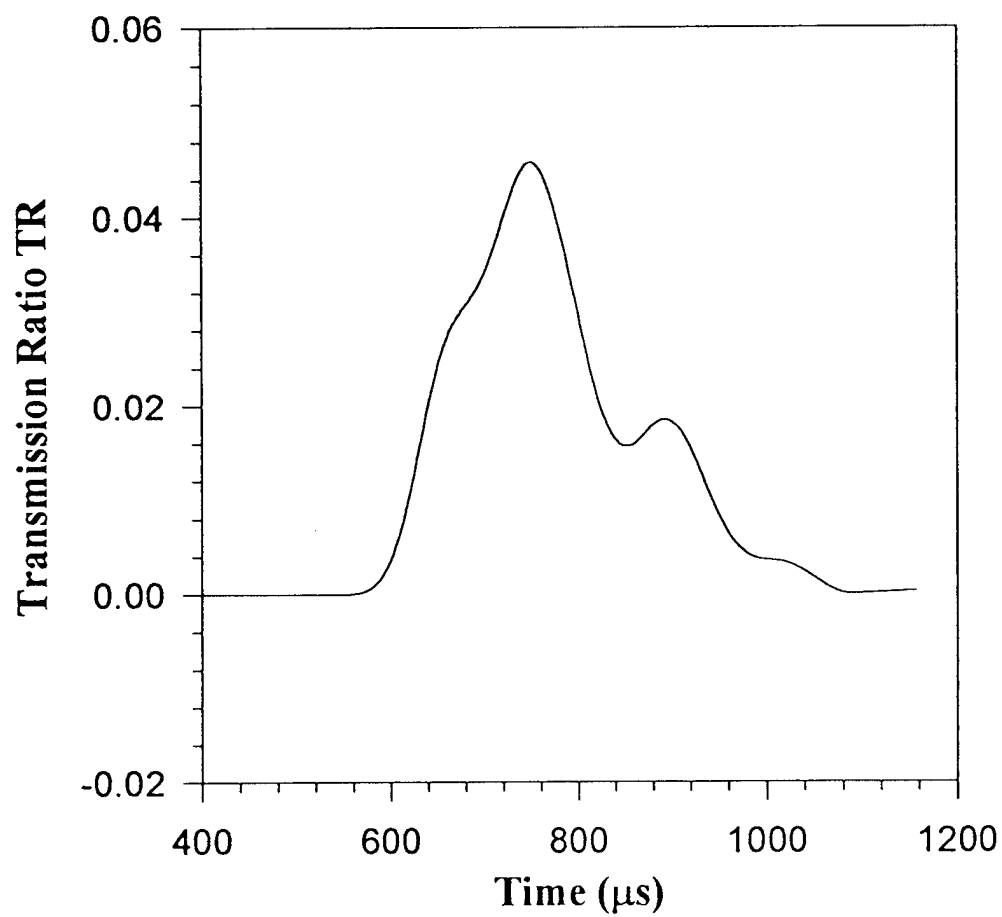
Figure 3.12. Wave Transmission Result for Assembly A-4

CHAPTER 4

AN EXPERIMENTAL INVESTIGATION OF STRESS WAVE PROPAGATION BEHAVIOR IN GRANULAR ASSEMBLIES OF CONCAVE-CONVEX PARTICLES

4.1 Summary

An investigation was conducted to study stress wave propagation phenomenon in granular assemblies of concave particles. In particular, attention was focused on the effect of contact profile and granular media porosity on inter-granular load transfer, wave velocity, and wavelength of a stress wave. The stress wave was generated by an explosive loading. Dynamic photoelasticity, the combination of high speed photography and photoelasticity, was employed as the experimental method. The photographs thus obtained were analyzed to determine contact load as a function of time, wave velocity and wavelength. Specimens were made of Homalite-100, an optically birefringent material. Since some of the specimens were not circularly symmetric, experiments were conducted with the specimens oriented with the major physical feature both toward the incoming pulse and away from the incoming pulse. The experimental results indicate that stress wave travels faster in the single chain assemblies with higher contact stiffness, which changes with the variation of contact profile. Also, stress wave propagates faster in single chain assemblies with lower porosity. Contact profile does not appear to change wavelength. However, porosity does affect wavelength. The experimental results also show that contact profile changes reflection mechanism within a particle therefore varying the contact load attenuation behavior.

4.2 Introduction

The study of stress wave propagation in granular materials is important to many branches of science and engineering including geomechanics and powder metallurgy. Dynamic loads may occur due to earthquake motion, underground explosions, and construction operations. The ability to predict the behavior of structures and foundations necessitates the understanding of wave motion in granular media such as sand, rock, and clay. Granular materials, having spatial discontinuities in their mass density, are modeled here as an array of

80

elastic particles interacting only through contact mechanics, and wave propagation in them is strongly dependent on their microstructure. A sizeable amount of work has been done to study the wave propagation phenomenon in granular materials from a microstructural standpoint. Some of the earliest work is due to Ida, (1939), who used a simple lumped mass-spring model. Contemporary work has proposed new modeling approaches such as the fabric tensor theory (Nemat-Nasser, 1983), the distributed body theory (Goodman and Cowin, 1972), and the distinct element method (Cundall, et al., 1979, and Sadd 1993) in order to predict the behavior of granular media.

Experimental techniques, such as the dynamic photoelasticity, have been employed to study the dynamic response of granular materials under explosive loading (Shukla, 1985 and 1992). Later studies by Shukla, et al., (1991) using photoelasticity in conjunction with high speed photography further investigated the effects of particle shape on wave propagation behavior in granular assemblies of elliptic particles. They showed that the wave velocity was dependent on the particle shape. The wavelength of the stress wave pulse showed no change with the particle shape as long as the contact interval (the number of contact points per unit wavelength which was four disk diameters) is kept constant. The load transfer characteristics change with variations in particle shape. However, in most of the past work the granular media was simulated by assemblies of circular or elliptical particles. All contacts were therefore between two convex surfaces. In real life, some contacts are between concave and convex surface. The change of particle shape and thus of contact profile causes the contact stiffness to change. If the radius of curvature at the contact is increased, while keeping the contact interval constant, the contact stiffness will increase, and this would imply a higher wave velocity. This may also change the wave propagation characteristics.

An experimental study has been conducted on the dynamic response of granular materials with specific interest in investigating the effect of contact profiles such as concave-convex contact, dual-contact, and porosity on stress wave propagation characteristics. The experimental results indicate that stress wave travels faster in the single chain assemblies with higher contact stiffness, which changes with the variation of contact profile. Also, stress wave propagates faster in single chain assemblies with lower porosity. Contact profile does not appear to change wavelength. However, porosity does affect wavelength. The experimental results also show that contact profile changes reflection mechanism within a particle and

therefore varies the contact load attenuation behavior.

4.3 Experimental and analytical procedure

Dynamic photoelasticity, the combination of photoelasticity and high speed photography, was used as the experimental technique throughout this investigation. This method has been shown by many researchers to be very efficient in the study of dynamic wave characteristics in granular media (for example Shukla 1991). As stated earlier, Homalite-100 was chosen to make specimens. To fabricate the various particles, one inch diameter circular disks were machined into the geometries shown in Table 4.1. A cooling system was used during machining of the specimens to avoid producing any heat related residual stresses in the specimens.

The granular media was simulated by single chain assemblies of similar shaped particles in contact. One such setup is shown in Figure 4.1 (a). The same shaped particles were also used in an alternative setup, as shown in Figure 4.1 (b), to investigate the effect of incident direction of the wave pulse on the propagation characteristics. The ten different single chain assemblies used in this study are shown in Figure 4.2.

The experimental models were placed on the optical bench of a high speed Cranz-Schardin type camera. The particles were loaded by exploding a small amount(10 mg) of Lead Azide in a specially designed charge holder. The camera was triggered at some prescribed delay time after igniting the explosive that was placed on top of the model (see Figure 4.1). The high speed photography system generates a series of high intensity, extremely short duration, pulses of light and provides twenty photoelastic images at discrete times during the dynamic event.

A typical sequence of six images for the single chain setup is shown in Figure 4.3. These images of the propagation phenomenon were enlarged and digitized to facilitate the analysis. The Hertz stress field equations along with the stress optic law (reference previous chapter) were used to calculate the contact load at a particular contact point and time, by applying the multi-point, non-linear least square method suggested by Shukla and Nigam(1986). The wavelength of the stress pulse can by measured directly from the photographs of the wave propagation process (Figure 4.3). The propagation distance is plotted as a function of time to obtain the wave velocity.

82

4.4 Experimental results and discussions

To investigate the phenomenon of stress wave propagation in granular assemblies of concave particles, a series of experiments were conducted on several single chains of various particles. The geometries of these particles are shown in Table 4.1 and single chain assemblies used in the study are shown in Figure 4.2. The results from the experiments are discussed in two subsections with the first dealing primarily with the effect of contact profiles and second the effect of porosity on wave propagation behavior.

4.4.1 The effect of contact profile

Typical isochromatic fringe patterns for chains 1 and 2 of Figure 4.2 are shown in Figures 4.3 and 4.4, respectively. These two chains have identical particles, however in chain 2, the particles were rotated 180° to investigate the effect of the incident direction of the wave pulse on wave propagation behavior. Likewise, Figures 4.5 and 4.6 show the isochromatic fringe patterns for chains 3 and 4, (see Figure 4.2), respectively.

The discrete images of the wave propagation phenomenon as shown in these figures give the position of the wave front at that instant of time. These pictures are enlarged using a Beseler enlarger and the wave front is digitized using a Hitachi digitizer interfaced with an IBM personal computer. Thus the wave propagation distance as a function of time is obtained, the slope of which gives the wave velocity.

Data for the average wave velocities in chains 1 and 2 are shown in Figure 4.7, and the computed values were 960 m/s and 950 m/s, respectively. Figure 4.8 shows that the average wave velocities in chains 3 and 4 are 1080 m/s and 1110 m/s, respectively. The velocities in chain 1 and 2 are approximately the same, as well as the velocities in chain 3 and 4. This shows that the incident direction of the wave pulse has not affected the average pulse velocity for these particle shapes. However, the velocities in chain 1 and chain 2 are more than 10% lower than those in chain 3 and chain 4. Notice that in chain 1 and chain 2, the contact of two adjacent particles is between a flat and a convex surface. On the other hand, the contact of two adjacent particles in chain 3 and chain 4 is between a concave and a convex surface. The fact means that contact stiffness in chain 1 and 2 is lower than that in chain 3 and 4. Recall an approximate equation (Takahashi, 1949) for wave velocity in one dimensional granular media

$$V \cong d \sqrt{\frac{K}{m}} \qquad\qquad (4.1)$$

where d is a distance measure usually taken to between the centers of two particles in contact, K is the effective contact stiffness, and m is the mass of the particle. For the case studied, both group of chains have same d value. The particle mass of first group (chain 1 and 2) is slightly lower than that of second group (chain 3 and 4). However, higher contact stiffness in the second group makes velocities in this group higher than those in the first group.

Compared with the pulse velocity in one inch diameter circular disk chain, which was 1070 m/s (Shukla, 1990), the wave velocities in chains 3 and 4 are slightly higher because of larger contact stiffness. However, the wave velocities in chains 1 and 2 are slightly lower than that in one inch diameter circular disk chain despite the larger contact stiffness. The reason for this is the decreased distance between the centers of two particles in contact, d, in chains 1 and 2 as compared with a one inch diameter circular disk chain.

The wavelengths for chains 1, 2, 3 and 4 were directly measured from Figures 4.3-4.6. The pulse lengths for chains 1 and 2 were found to be equal (81mm). Chains 3 and 4 also produced equal pulse lengths (87mm). This would lead one to believe that the incident direction of propagation has no effect on the pulse length. It was also noticed that wavelengths of chains 1 and 2 are approximately the same as those of chains 3 and 4. The stress pulse lengths in these chains were nearly four particle lengths.

Experimental data, obtained from photoelastic experiments on various single chain assemblies, were used to determine the normal contact loads at different contact points. The analysis method consists of the Hertz stress field equation provided by Smith and Liu (1953) coupled with a multi-point non-linear technique proposed by Shukla and Nigam (1986). This technique makes use of the method of least squares in conjunction with the Newton-Raphson method to compute the contact stresses and loads. Figure 4.9 shows the typical normal contact load variation for a single chain assembly. The contact loads P were normalized with respect to the peak contact load occurring between particles 4 and 5 ($P_{4-5\,max}$). This contact was chosen for normalization, because at this point the wave had traveled through four particles (one wavelength) and thus had stabilized. This normalization allows for easy

comparison between different experiments. Figures 4.10 and 4.11 give the contact load attenuation plots for these two group assemblies (chain 1 and 2, chain 3 and 4) as the stress wave traveled down the single chain assemblies. As shown, the contact load attenuation in chain 1 is larger than that in chain 2, and the contact load attenuation in chain 3 is larger than that in chain 4. Carefully comparing the two figures, one can also find that contact load attenuations are approximately the same between chains 1 and 3, as well as between chains2 and 4. It was known that wave propagation through a granular media occurs by contact mechanisms which result in load transfer from particle to particle. Within a particle, however, the wave propagation process is through a reflection mechanism. In other words, reflection mechanism within a particle is a very important factor on load attenuation behavior. Figure 4.12 shows the sketches of reflection mechanisms in chains 1 to 4. One can see that the reflection mechanisms in chains 1 and 3 are the same and have a "convergent feature". On the other hand, the reflection mechanisms in chains 2 and 4 possess a "divergent feature". This may be an explanation for the difference in contact load attenuation for various chains.

One of the most important feature in granular assemblies of concave particles is that concave particles will allow two or more neighboring contacts. This feature provides a unique fabric mechanism to alter the mechanical response of such materials, and therefore could have significant effects on the wave propagational characteristics. Figures 4.13 and 4.14 show isochromatic fringe patterns for chains 5 and 6 (see Figure 4.2). In these two chains, there are two contacts between adjacent particles. Chain 6 was used to investigate the effect of the incident direction of the stress pulse on wave propagation behavior. One obvious fabric change is that the contact normals are no longer along the direction of the wave propagation in these chains. From Figure 4.15 one can see that the wave velocities in these two chains (v=740 m/s for chain 5 and v=760 m/s for chain 6) drop dramatically compared with the velocities in single contact assemblies (v=960 m/s, 950 m/s for chains 1,2, and v=1080 m/s, 1110 m/s for chains 3, 4, respectively). Variation of contact normal direction may be one of the important reasons for velocity drop. Also, velocity data shows that the incident direction has not affected the wave velocities.

Figures 4.13 and 4.14 show that the wavelengths for both chain 5 and chain6 are approximately 7 particles (109 mm). They are much longer than that in chains 1-4. The elongation of wavelengths in chains 5 and 6 may be caused by contact mechanism.

A major difficulty in running the experiments with dual-contact particles is that too much input load will result in the breaking of particles. Data thus collected cannot demonstrate the real load attenuation characteristics. On the contrary, less input load will not allow to collect sufficient data to describe the whole contact load history. An alternative photoelastic material is suggested to investigate the load attenuation behavior in multiple contacts granular assemblies.

4.4.2 The effect of porosity

From geometry point of view, the particles with ring shape belong to concave group. Ring particles, as shown in Figure 4.2 (chains 7-10), have same contact profile as convex particles, that is contact between two convex surfaces. However, the porosity of granular assembly will change with the variation of the hole size in ring particles. Figures 4.16 and 4.17-4.20 show isochromatic fringe patterns for solid disk chain and chains 7-10 in Figure 4.2, respectively. Experimental results for solid disk chain is demonstrated here for the purpose of comparison. Using velocity calculation technique described before, one can determine the velocities in these chains. We define the porosity, η, as in equation 2,

$$\eta = \frac{area\ of\ hole}{area\ of\ disk} \tag{4.2}$$

The relation between velocity and porosity is shown in Figure 4.21. The plot shows that when η increases, i.e. the hole is made larger, the average velocity decreases. Compared with the wave velocity in circular disks, the average velocity changes very little for small values of η, i.e. a very small hole. Pulse velocity decrease (from 1100 m/s to 810 m/s) as porosity, η, increase (from 00.0 to 0.25) because particle stiffness decrease as porosity increase.

Wavelengths in ring particle assemblies were measured directly from the isochromatics pictures. Compared to the solid disk, these ring particles have lower stiffness. Therefore, one should expect a longer wavelength in these ring particle chains than that in solid disk chain which was four particle diameters (Shukla and Damania, 1987). However, as shown in Figure 4.22, when porosity, η, is very small (chain 7), wavelength does not change too much. As porosity increases, i.e. the stiffness decreases, the wavelength first decreases to

86

approximately three particle diameters (chains 8 and 9), then increases to about five particle diameters (chain 10). It appears that there may be a threshold at which the size of the hole, i.e. structural stiffness of the chain, becomes a significant factor in the wavelength.

Figure 4.23 shows typical isochromatic fringes for a solid disk and a ring particle under static diametrical compression. The fringes in solid disk appear Hertzian in shape while the fringe patterns become distorted in ring particle because of the boundary effects produced by the hole. Due to the fringe distortion, Hertz contact equations can not be used to analyze the contact load data any more for ring particles. Other experimental techniques, such as caustics, are suggested to be used to investigate dynamic contact load characteristics in assemblies of ring particles.
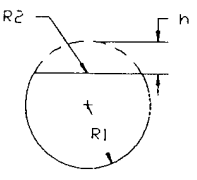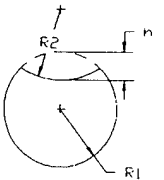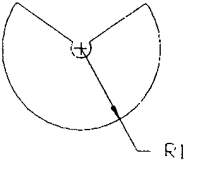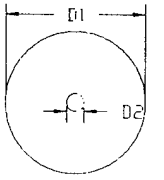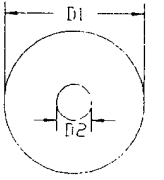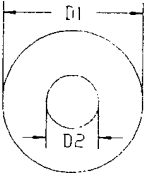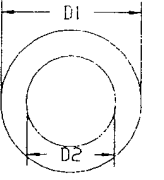
4.5 Conclusions

The experiments conducted in this study demonstrate the effects of contact profiles and porosity in granular assemblies of concave particles on stress wave propagation behavior. The results indicate the following:

- The variation of contact profile changes the contact stiffness between the particles, therefore changes the wave velocity in the granular materials. The higher contact stiffness allows stress wave to travel faster in granular materials. For the same contact profile, incident direction of pulse has no effect on the wave velocity.

- For the same contact profile, the incident direction has effect on contact load attenuation behavior. The variation of the incident direction changes the reflection mechanism within concave particles. It was seen that the reflected wave from a concave or flat surface provides a "divergent feature", which makes contact load attenuate more severe. Conversely, reflected wave from a convex surface provides a "convergent feature", which makes contact load attenuate gently.

- Contact profile and incident direction of pulse do not appear to change the wavelength.

- The porosity of granular media changes the wave velocity. The wave velocity decreases as porosity increases. The porosity also has effect on the wavelength and contact load characteristics. However, the detailed reasoning for the change in wavelength and quantitative evaluation of contact load need further study.

87

Table 4.1. Geometric parameters for different particles used in the experiments

Group No.	Specimen Geometry	R1 or D1 (inch)	R2 or D2 (inch)	h (inch)
1		0.5	infinite	0.25
2		0.5	0.625	0.25
3		0.5	NA	NA
4		1	0.12	NA
5		1	0.25	NA
6		1	0.365	NA
7		1	0.5	NA

88

charge holder

explosive charge

non-convex disks

support frame

(a)

(b)
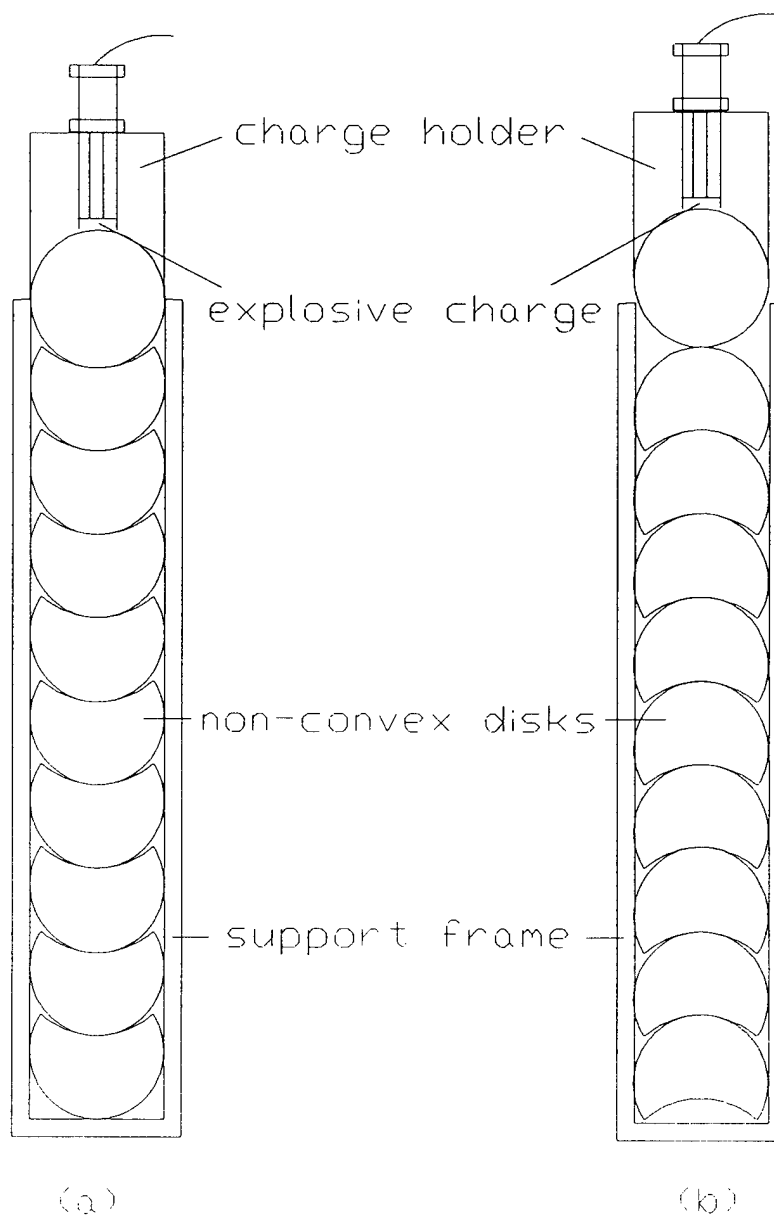
Figure 4.1. Experimental set up
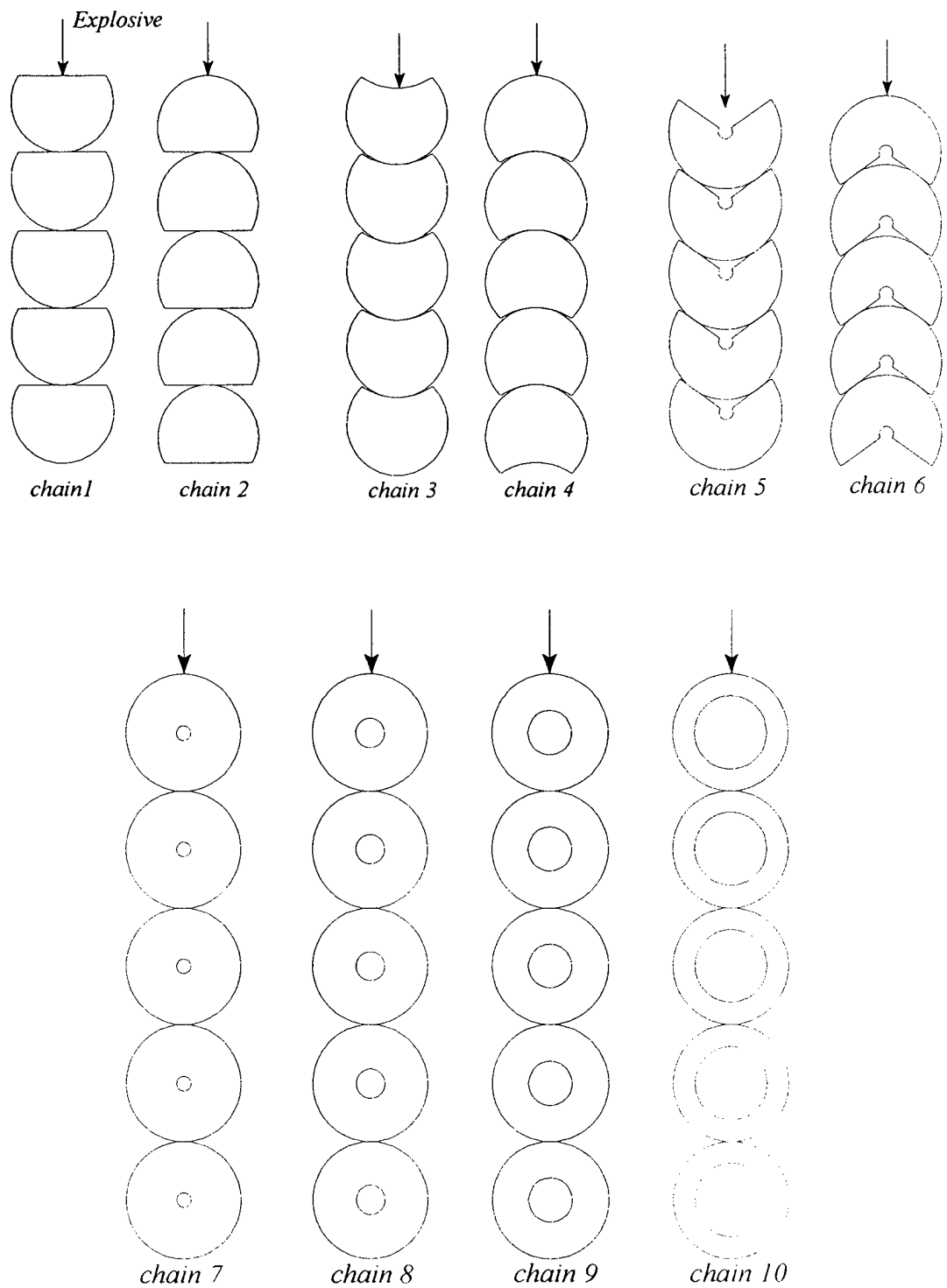
Figure 4.2. The ten different single chain assemblies used in the study

★ Explosive

| Frame 2 | Frame 7 | Frame 10 | Frame 12 | Frame 15 | Frame 19 |
| 91μs | 119 μs | 136 μs | 181 μs | 198 μs | 220 μs |
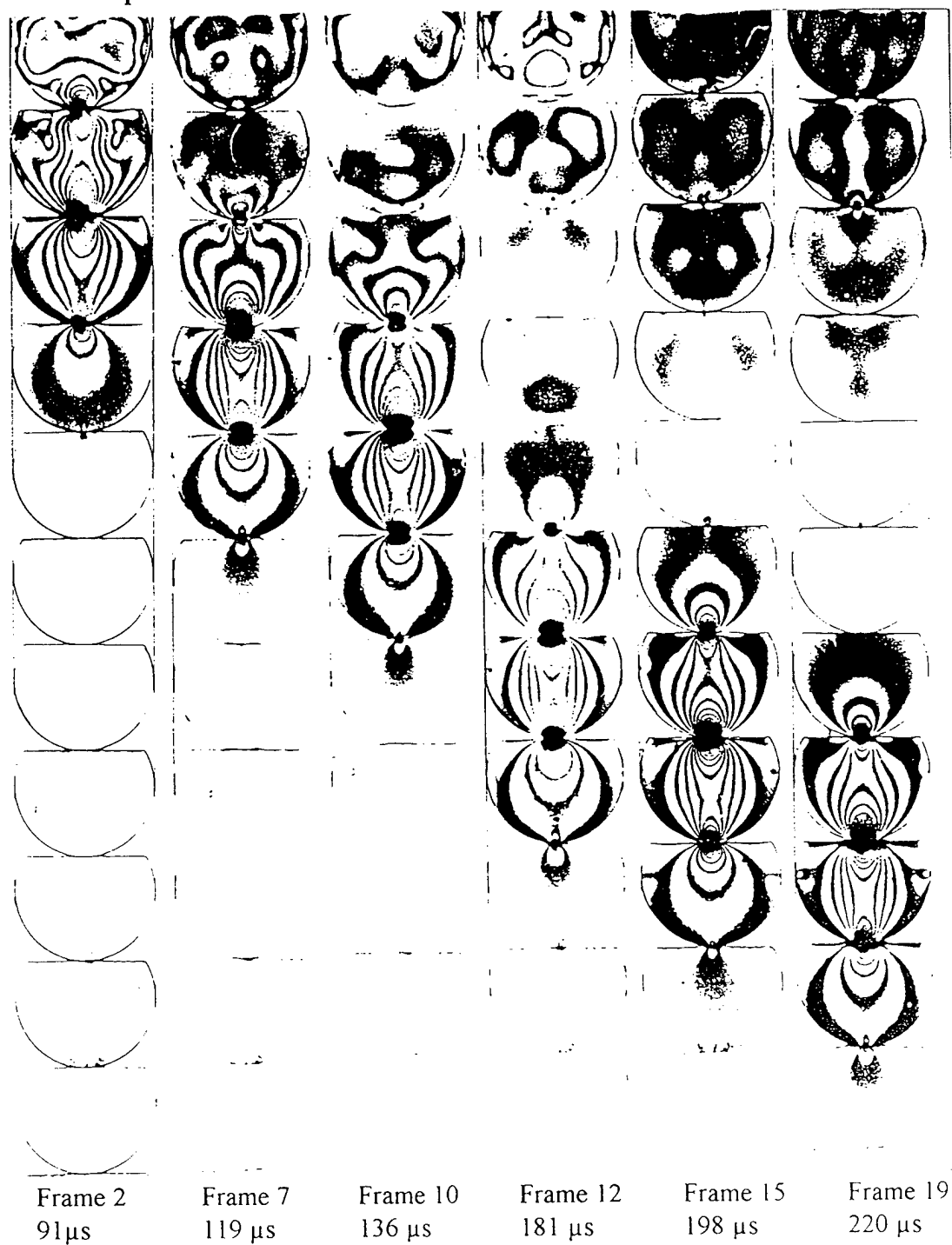
Figure 4.3. Typical isochromatic fringe patterns for chain 1.

★ Explosive

| Frame 2 | Frame 7 | Frame 10 | Frame 12 | Frame 15 | Frame 19 |
| 96 μs | 125 μs | 141 μs | 186 μs | 203 μs | 226 μs |
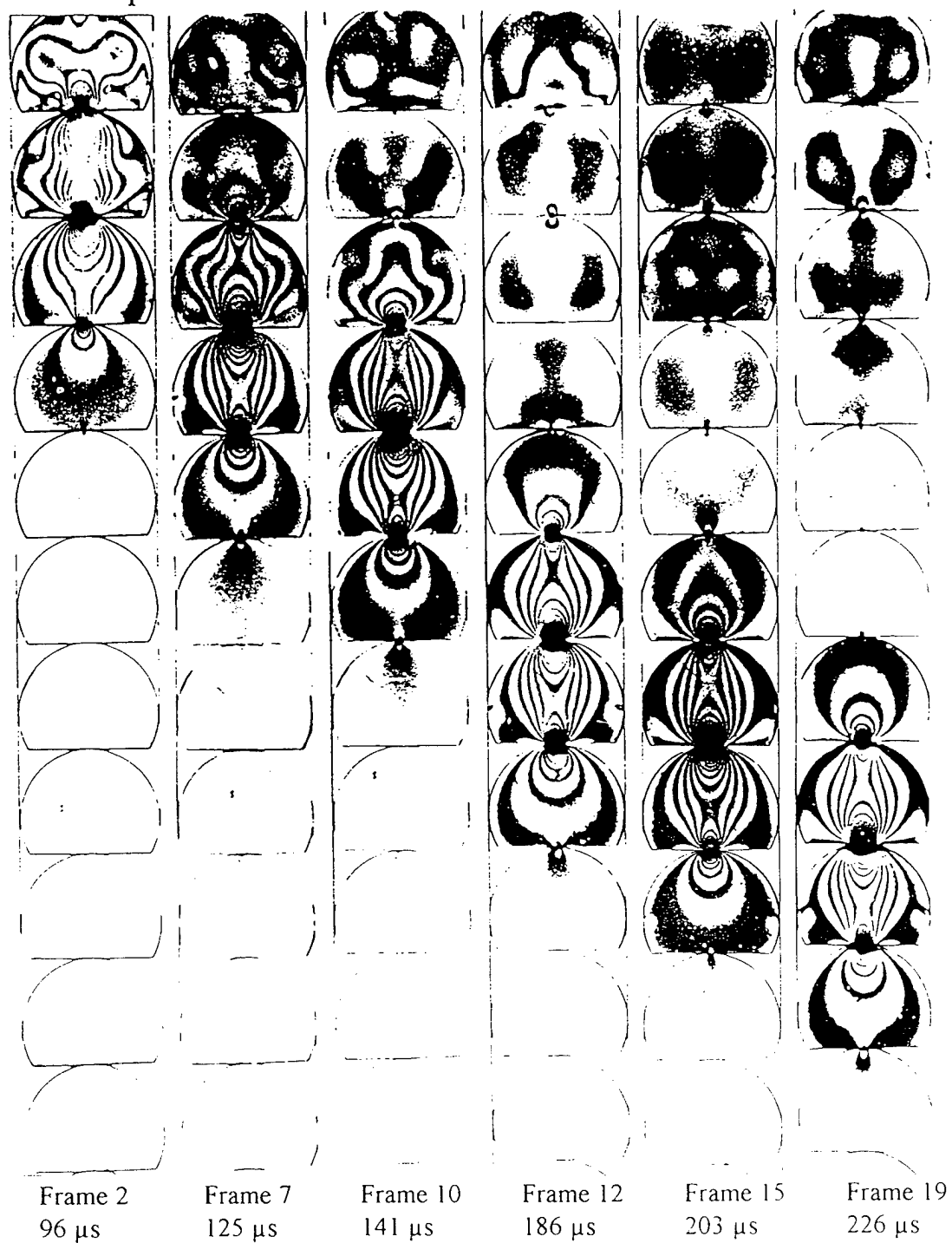
Figure 4.4. Isochromatic fringe patterns for chain 2.

92

★ Explosive

| Frame 3 | Frame 6 | Frame 10 | Frame 12 | Frame 15 | Frame 19 |
| 100 μs | 119 μs | 139 μs | 186 μs | 203 μs | 225 μs |
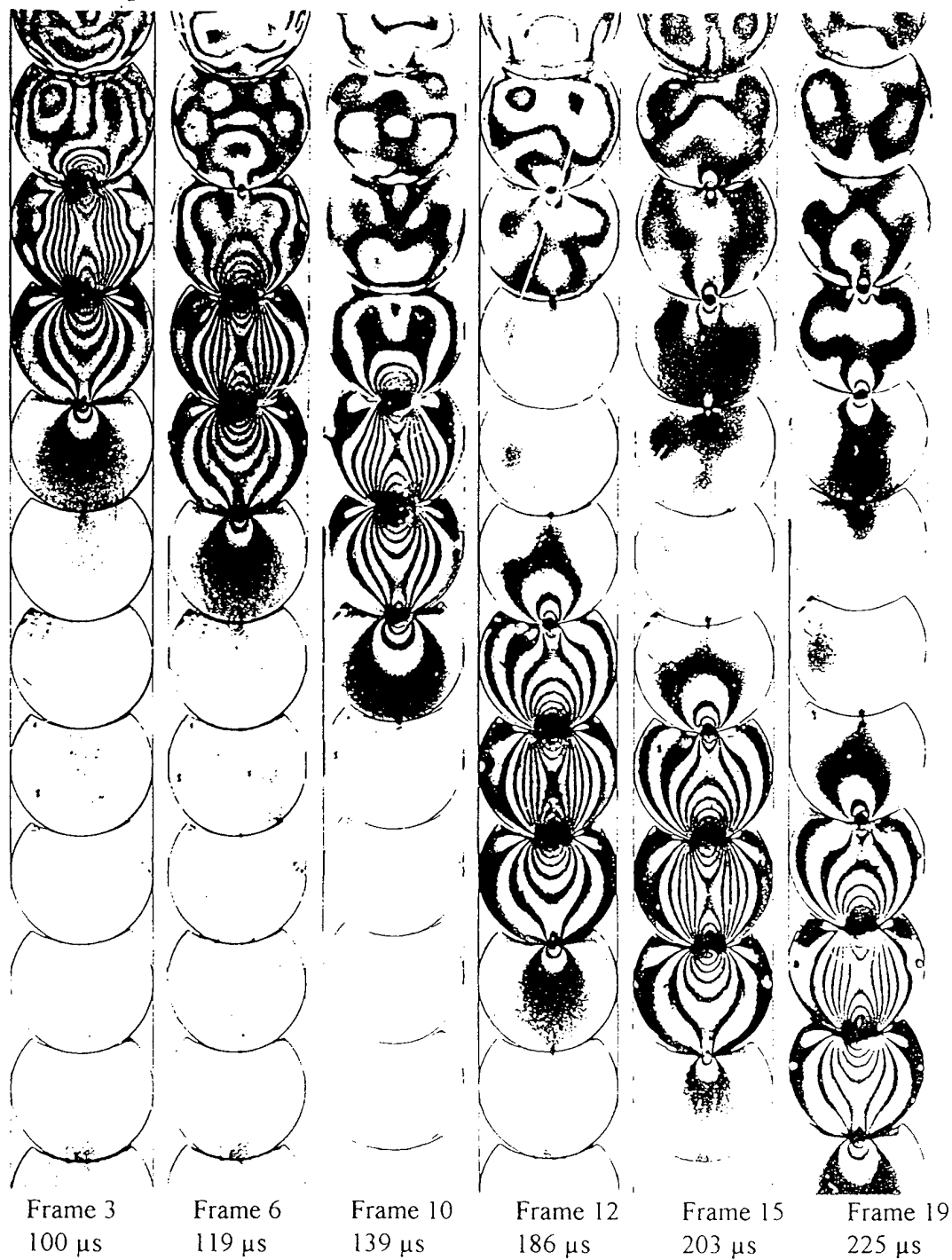
Figure 4.5. Isochromatic fringe patterns for chain 3.

★ Explosive

| Frame 3 | Frame 6 | Frame 9 | Frame 11 | Frame 15 | Frame 19 |
| 100 μs | 117 μs | 133 μs | 181 μs | 203 μs | 225 μs |
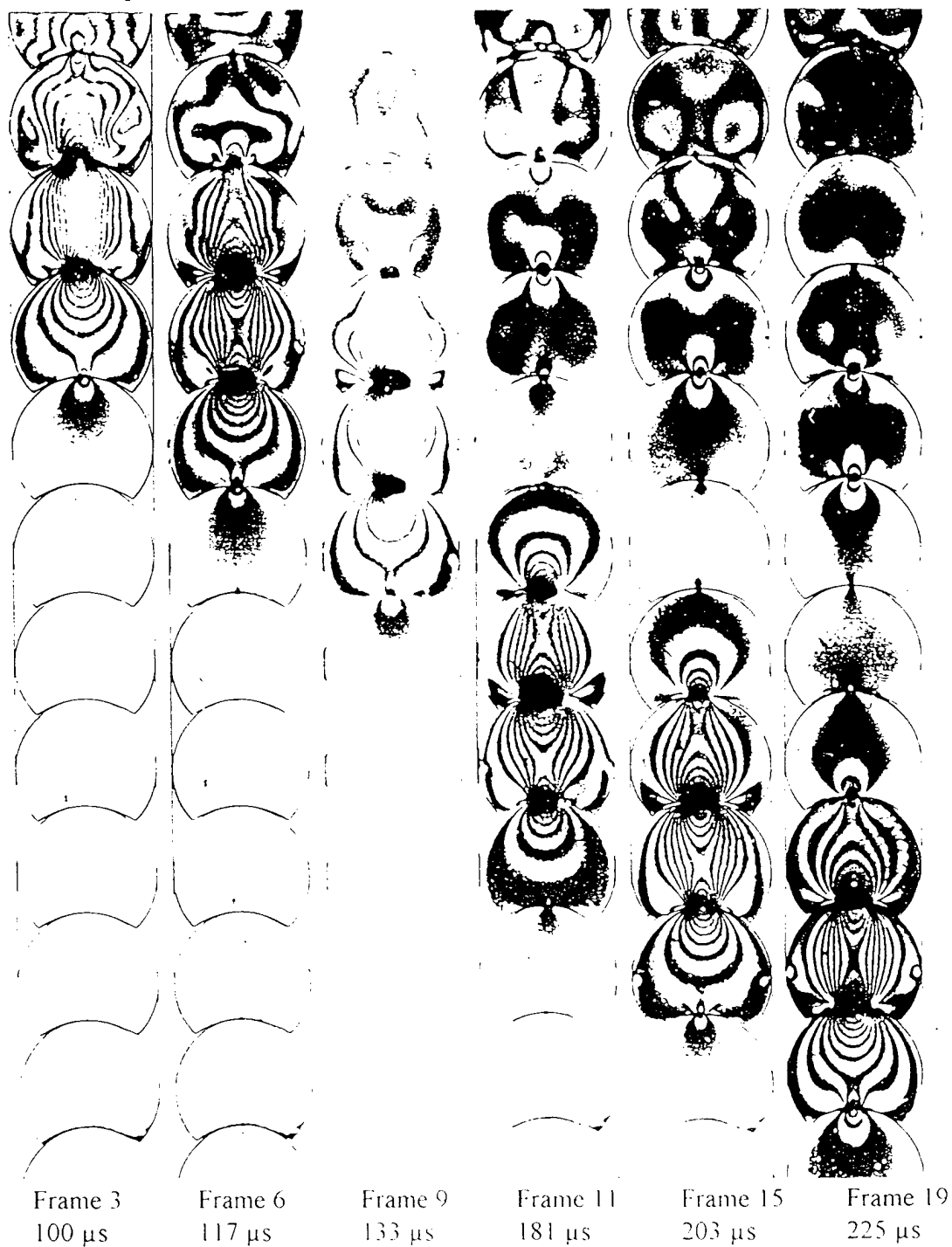
Figure 4.6 Isochromatic fringe patterns for chain 4
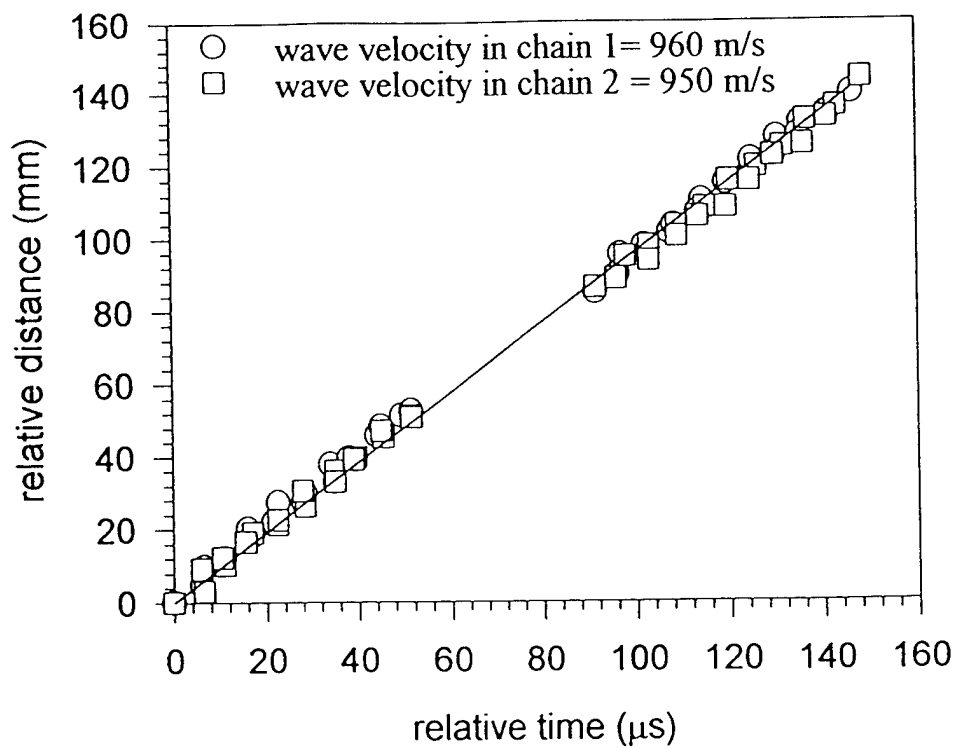
Figure 4.7. Wave velocities in chains 1 and 2.
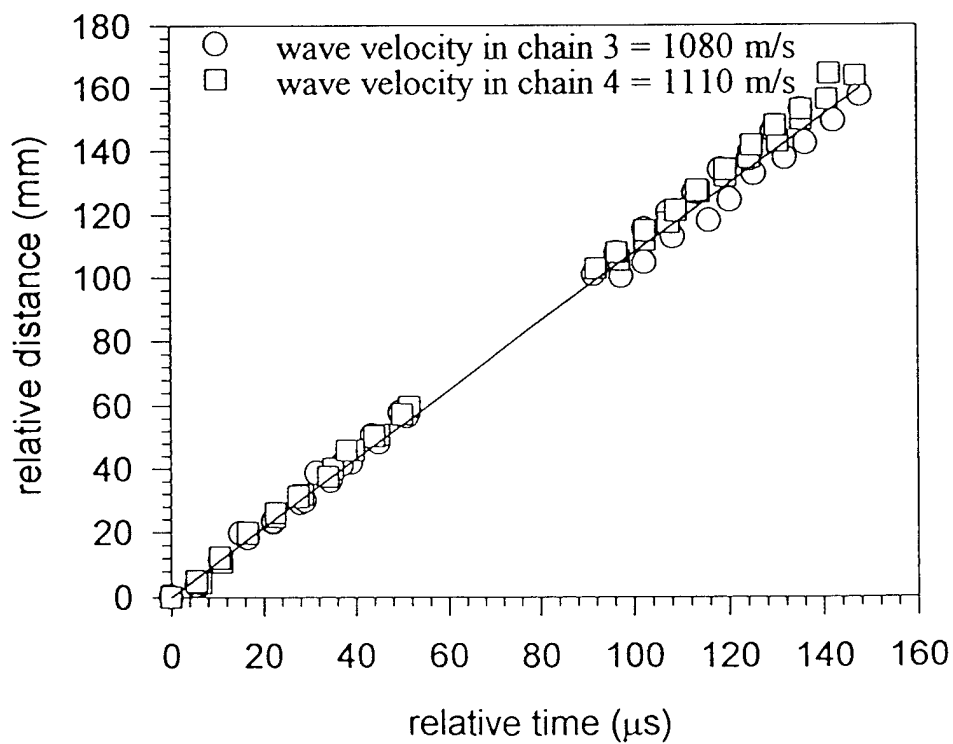
Figure 4.8. Wave velocities in chains 3 and 4.
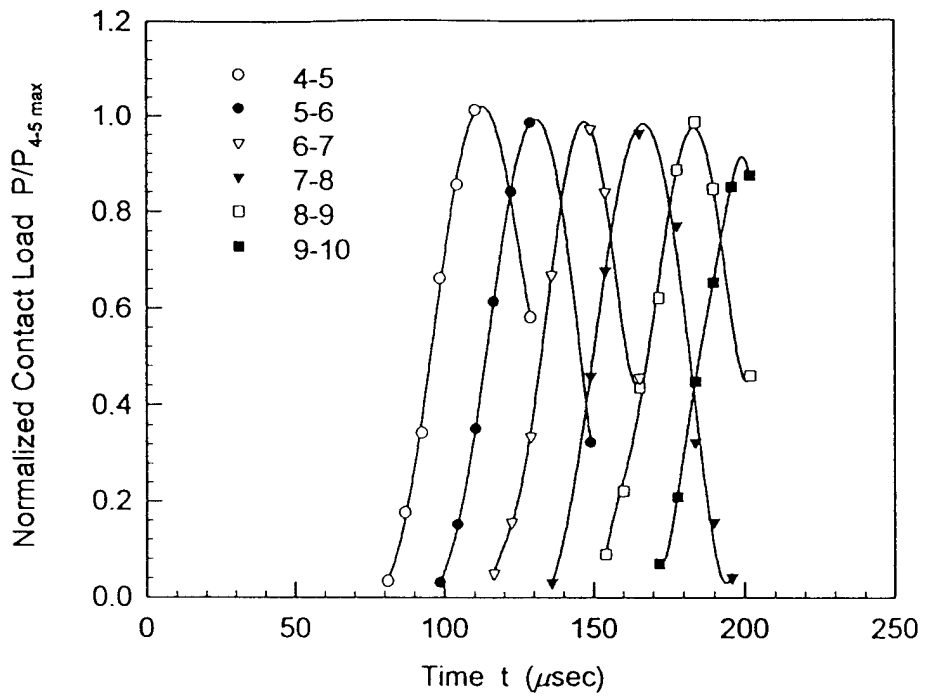
Figure 4.9. Normalized contact load contours for the chain 1.
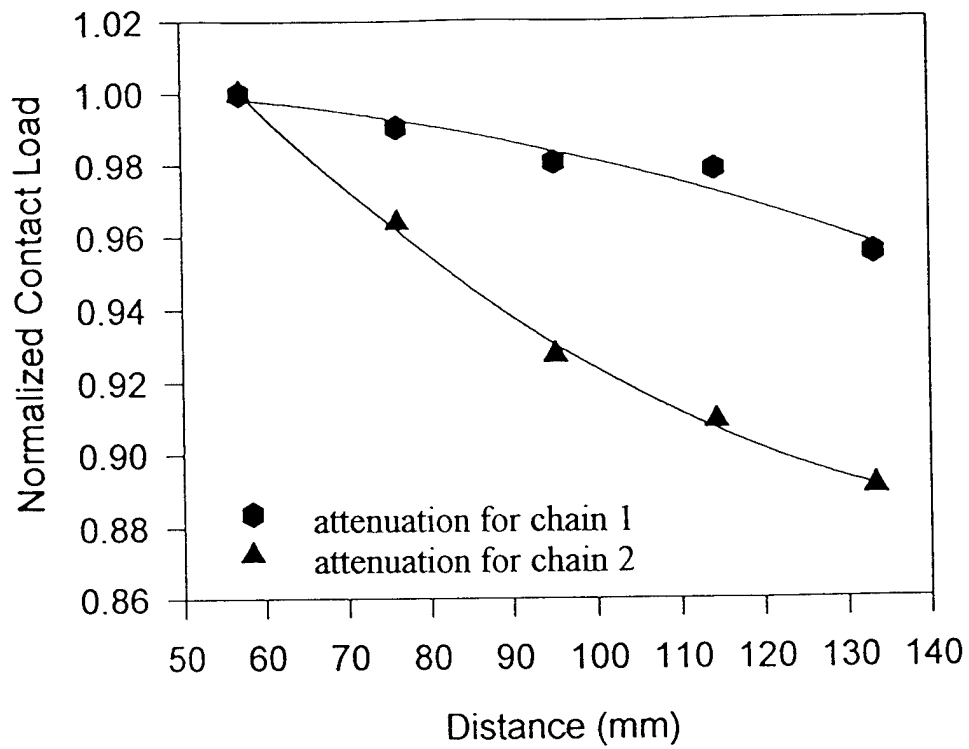
Figure 4.10. Attenuation of the normalized contact load with distance propagated down the chains 1 and 2.
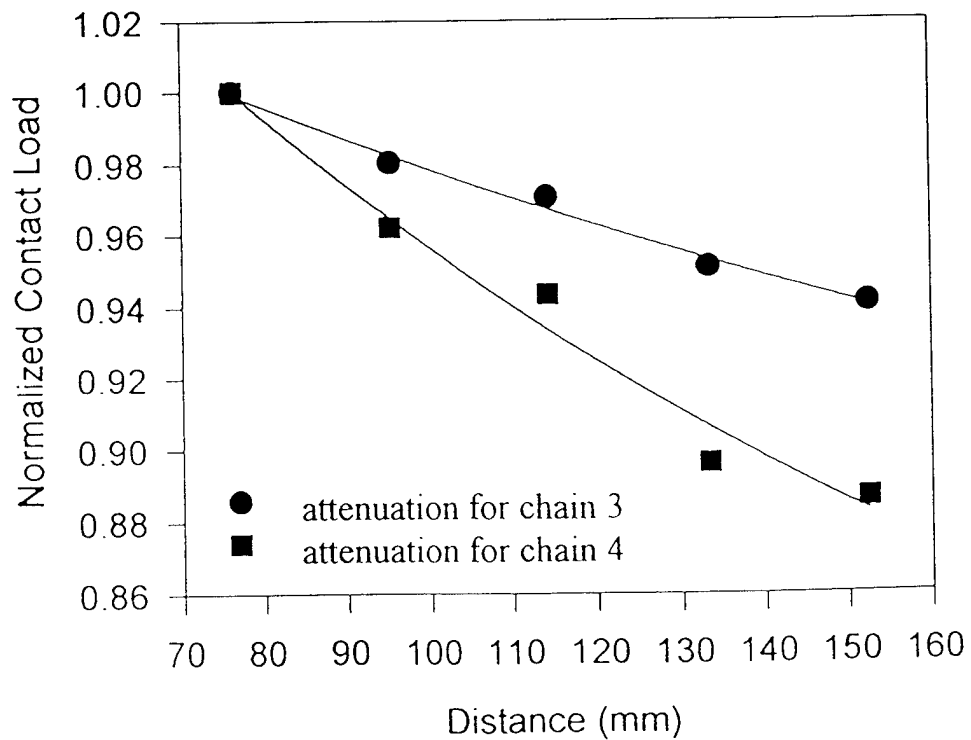
Figure 4.11. Attenuation of the normalized contact load with distance propagated down the chains 3 and 4.

incident wave

reflection▼ wave

chain 1

incident wave

reflection wave

chain 2

incident wave

reflection▼ wave

chain 3

incident wave

reflection▼ wave
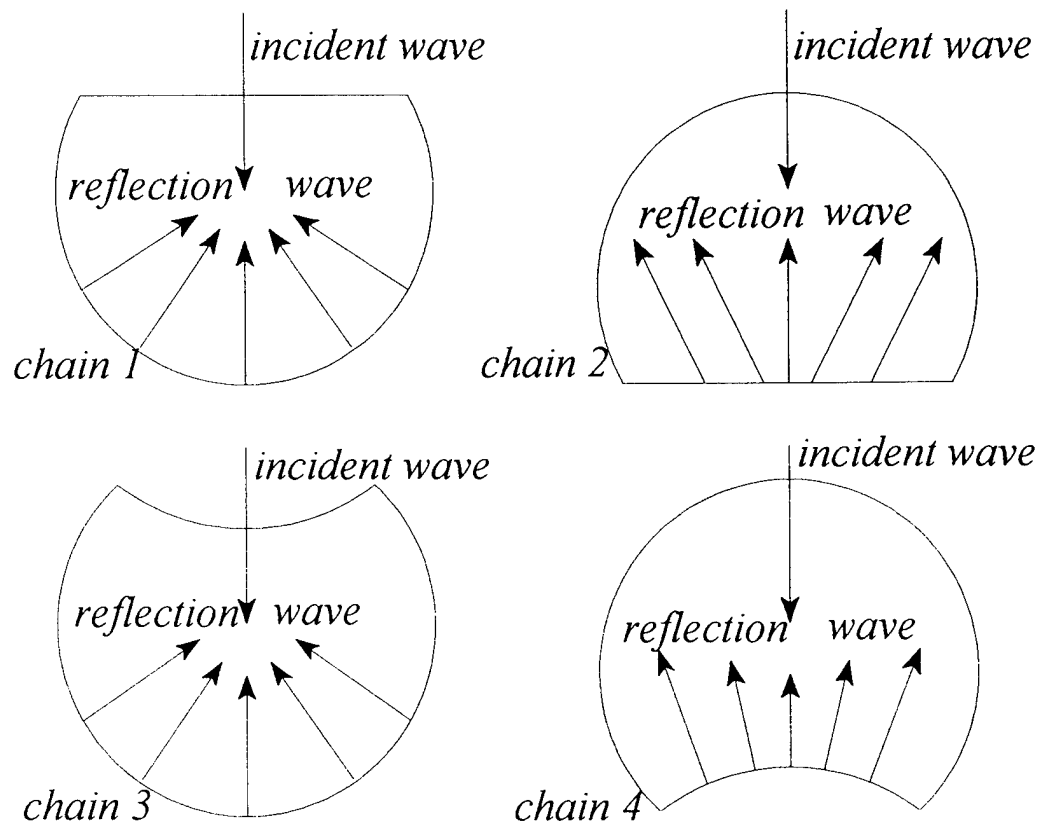
chain 4

Figure 4.12. Reflection mechanism in single chain assemblies 1-4

★ Explosive

| Frame 2 | Frame 7 | Frame 9 | Frame 12 | Frame 15 | Frame 19 |
| 106 µs | 134 µs | 144 µs | 202 µs | 219 µs | 241 µs |
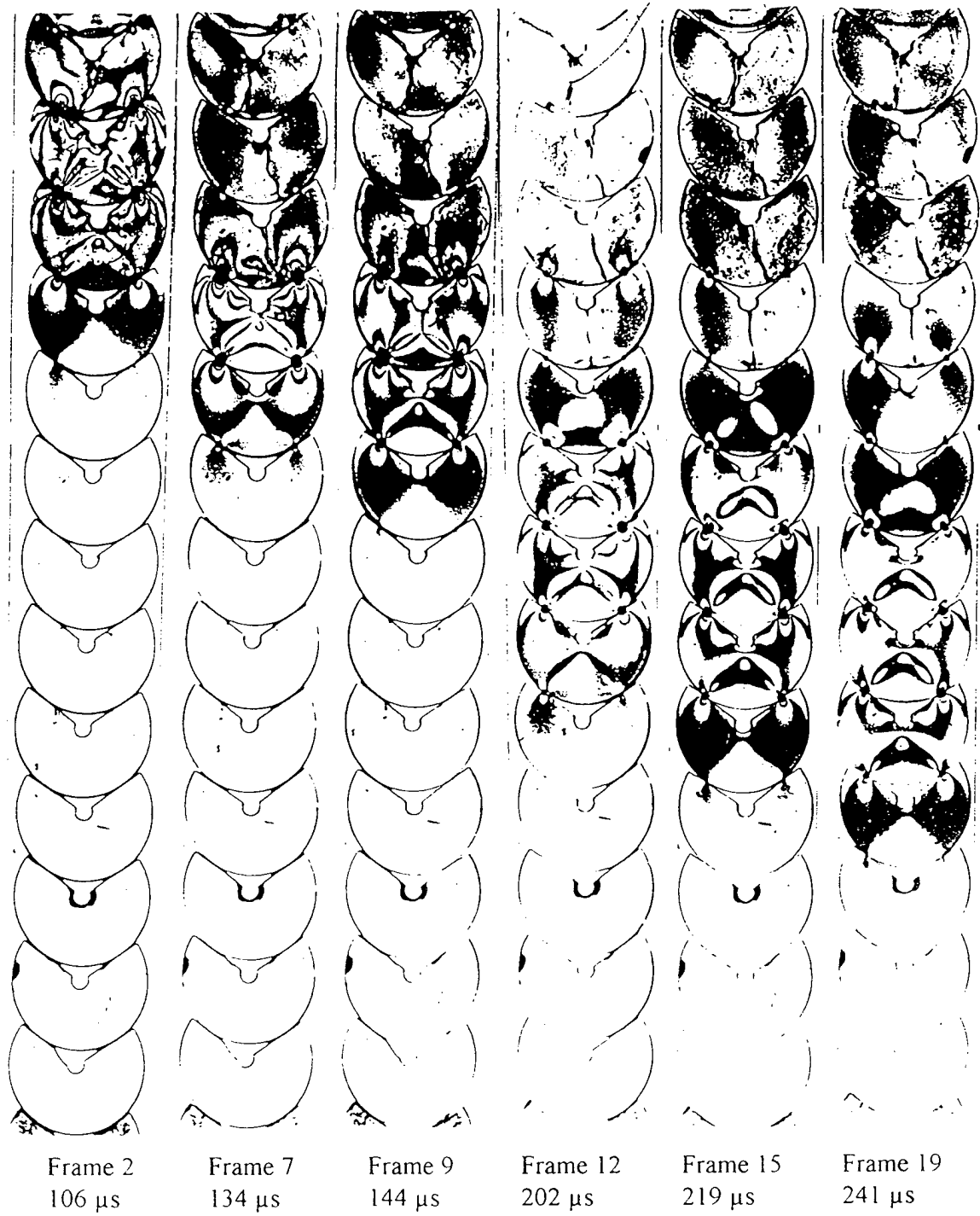
Figure 4.13. Isochromatic fringe patterns for chain 5.

★ Explosive

| Frame 3 | Frame 6 | Frame 10 | Frame 12 | Frame 15 | Frame 19 |
| 112μs | 128μs | 151μs | 202μs | 219μs | 241μs |
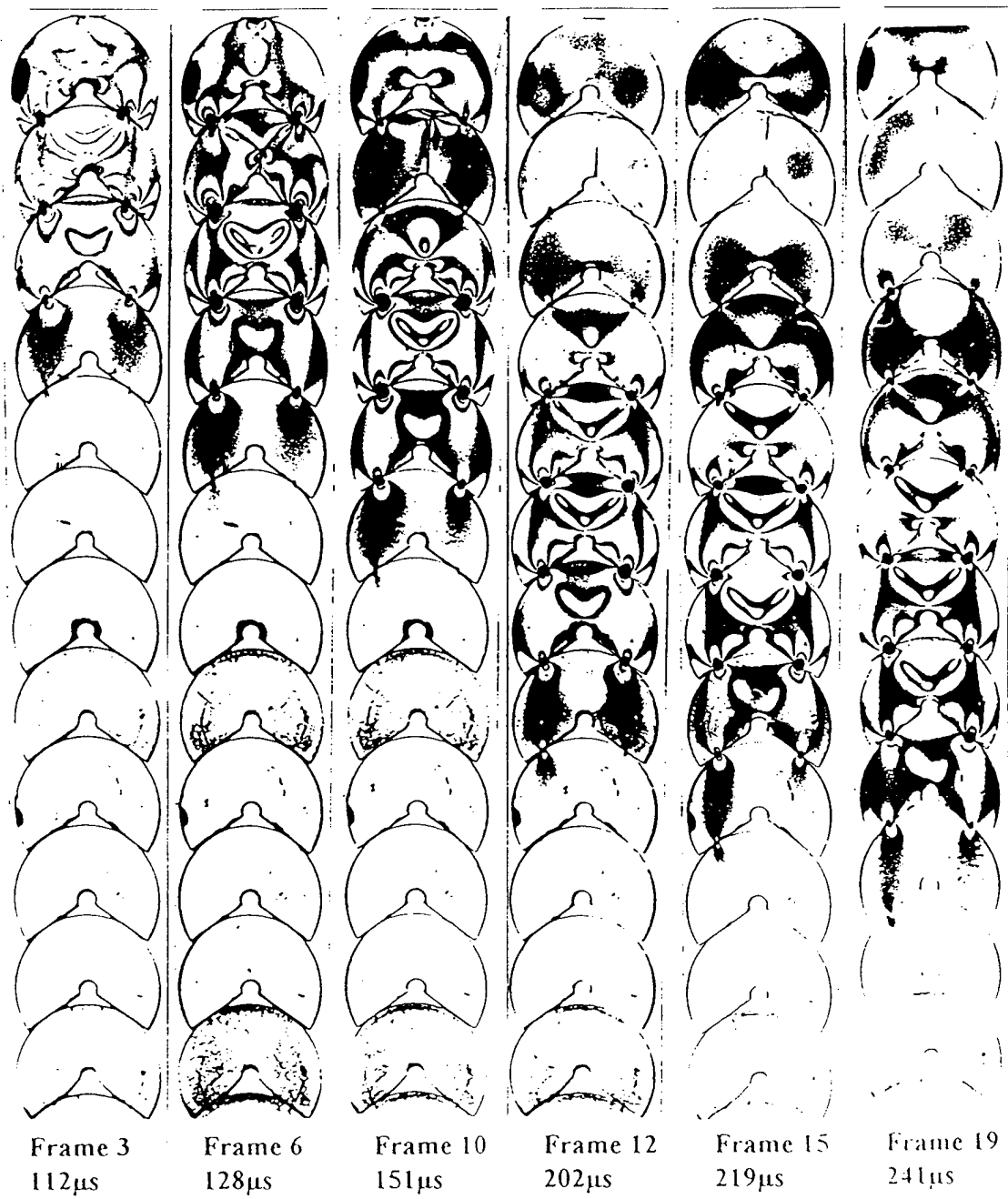
Figure 4.14. Isochromatic fringe patterns for chain 6.
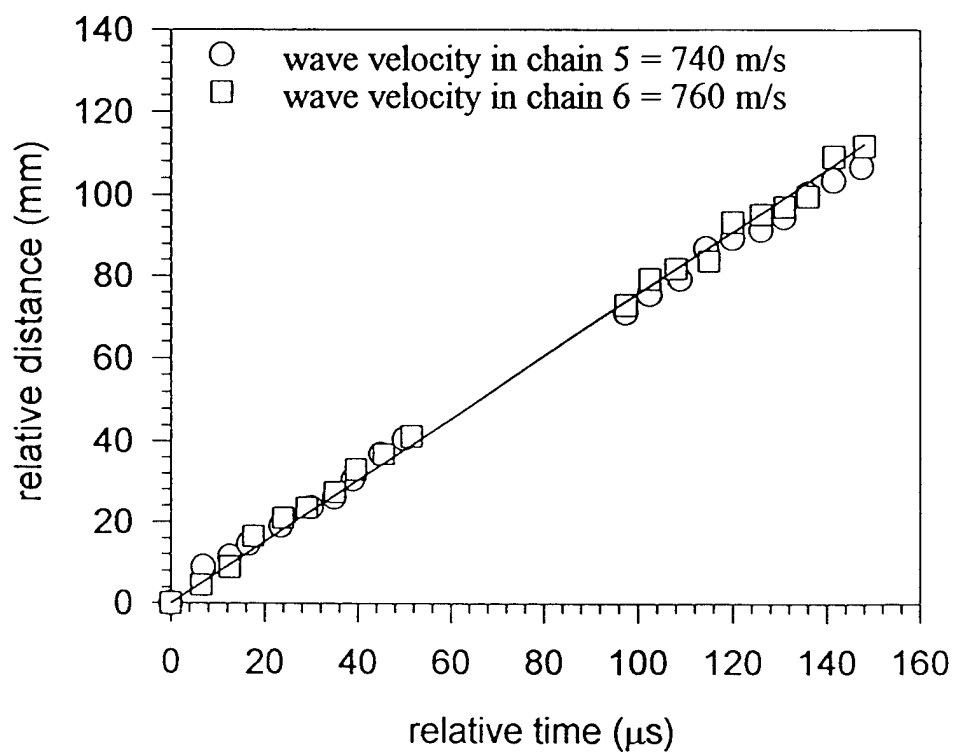
Figure 4.15. Wave velocities in chains 5 and 6.

★ Explosive

| Frame 3 | Frame 6 | Frame 10 | Frame 11 | Frame 15 | Frame 19 |
| 115µs | 132µs | 153µs | 201µs | 223µs | 245µs |
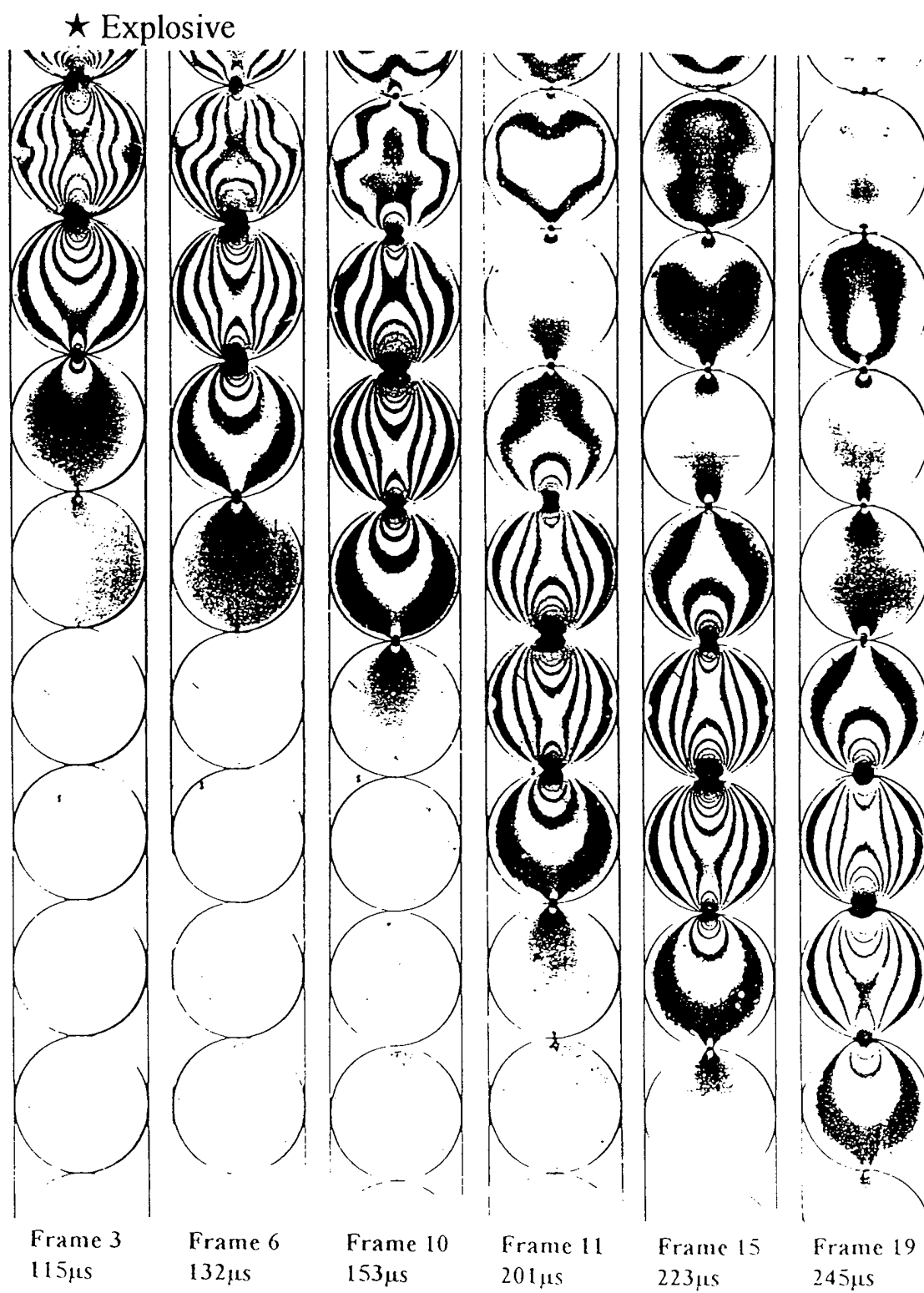
Figure 4.16. Isochromatic fringe patterns for solid disk chain

★ Explosive

| Frame 3 | Frame 7 | Frame 10 | Frame 12 | Frame 15 | Frame 19 |
| 112 μs | 135 μs | 151 μs | 202 μs | 218 μs | 240 μs |
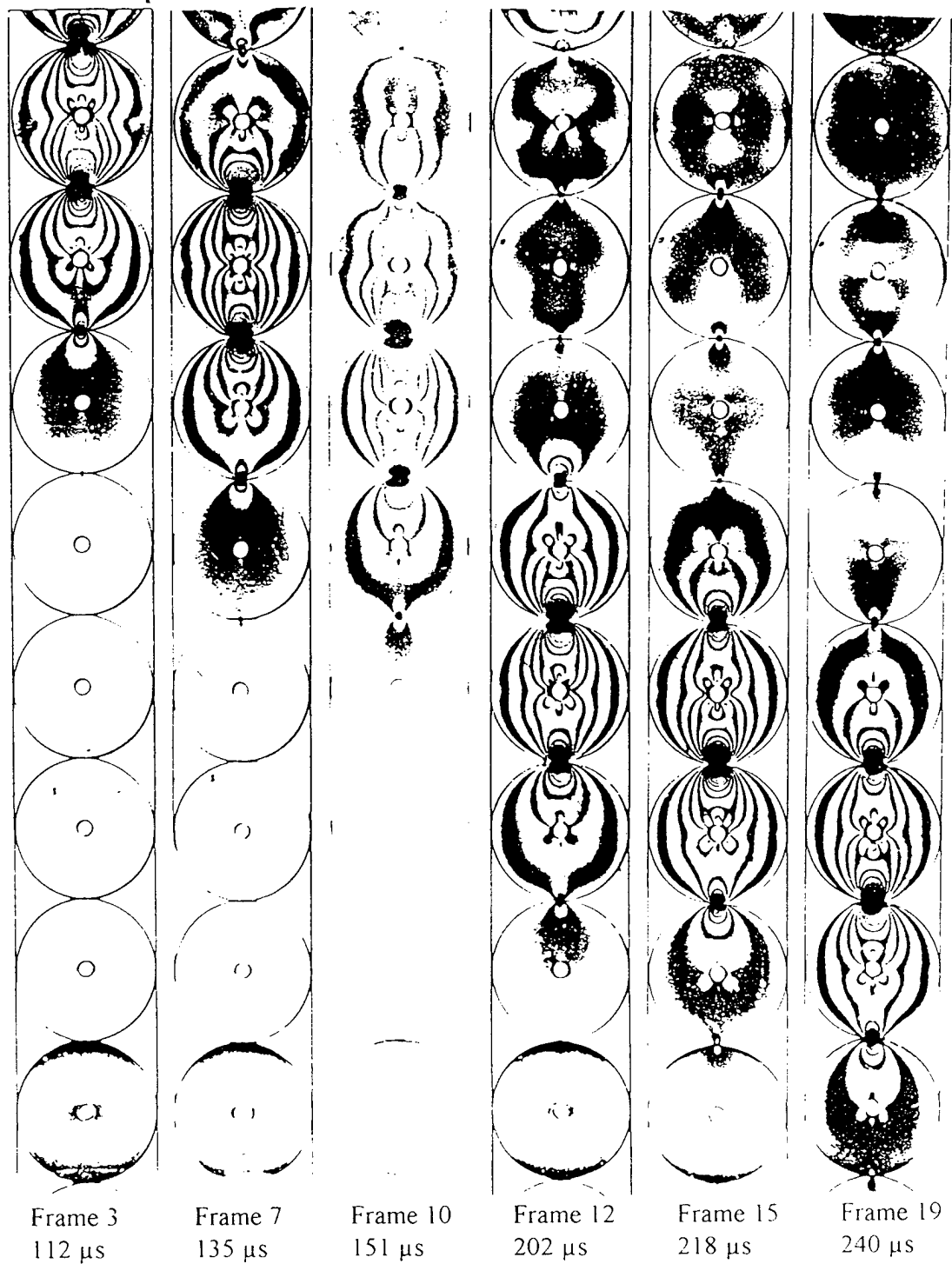
Figure 4.17. Isochromatic fringe patterns for chain 7.

★ Explosive

| Frame 3 | Frame 7 | Frame 9 | Frame 12 | Frame 15 | Frame 19 |
| 116 µs | 139 µs | 150 µs | 206 µs | 223 µs | 244 µs |
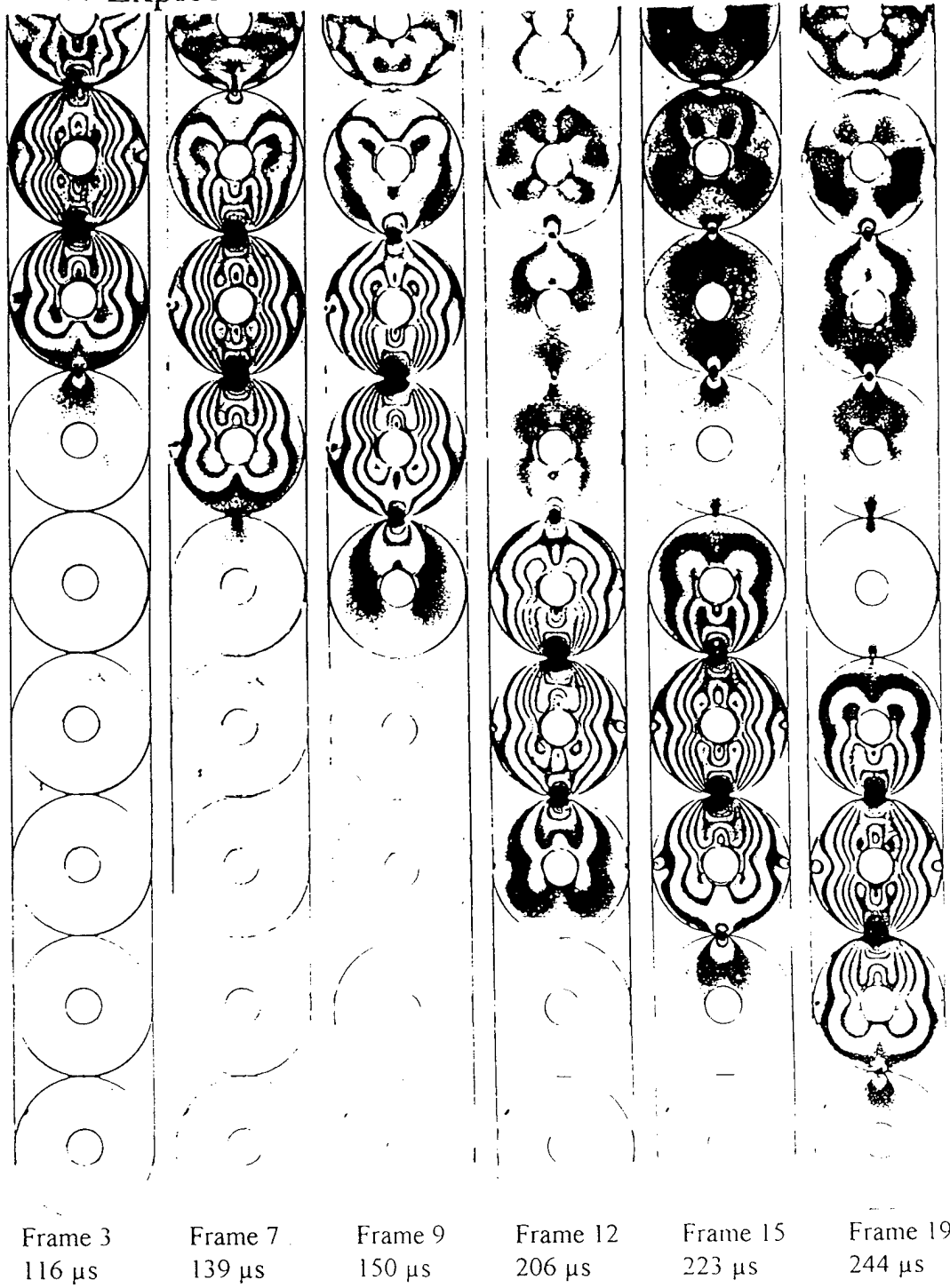
Figure 4.18. Isochromatic fringe patterns for chain 8.

★ Explosive

Frame 3	Frame 6	Frame 9	Frame 12	Frame 15	Frame 19
110 μs	128 μs	142 μs	201 μs	218 μs	240 μs
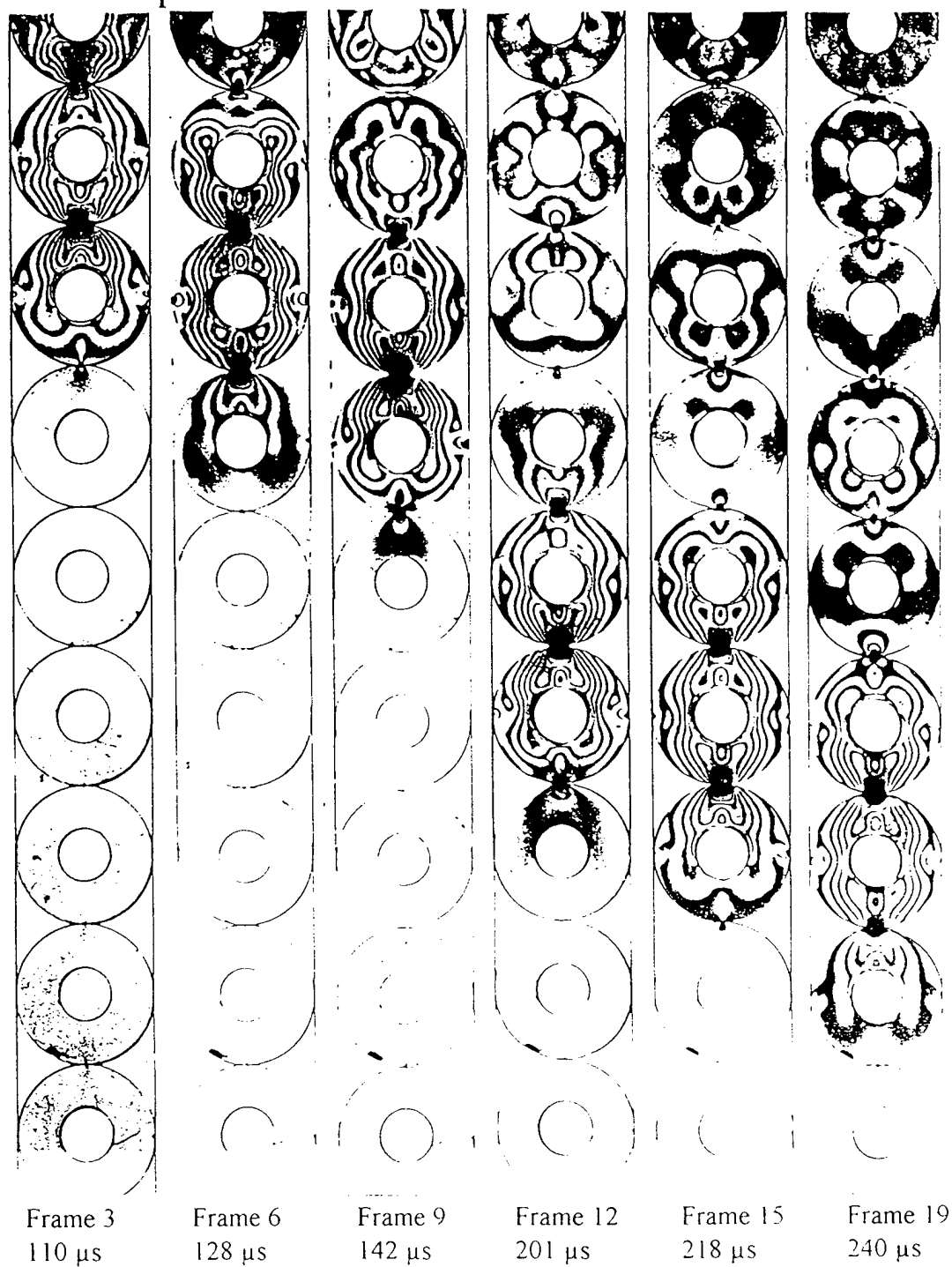
Figure 4.19. Isochromatic fringe patterns for chain 9

★ Explosive

Frame 2
185 μs

Frame 3
191 μs

Frame 7
214 μs

Frame 12
297 μs

Frame 15
313 μs

Frame 19
336 μs

Figure 4.20. Isochromatic fringe patterns for chain 10.

Figure 4.21. Relation of porosity and velocity in ring chains.
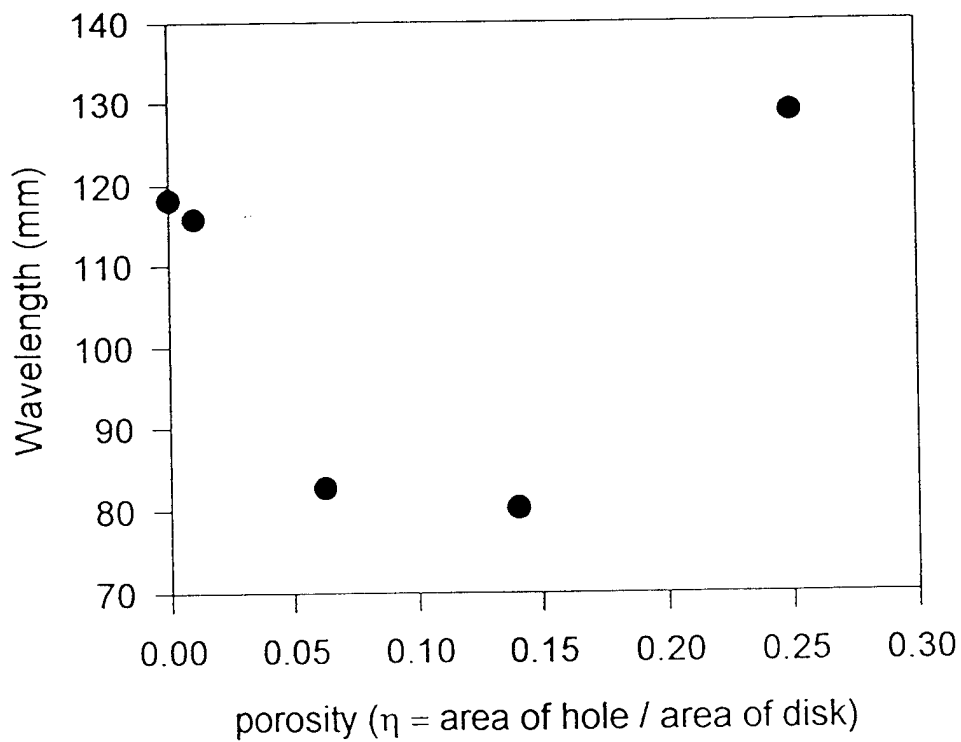
Figure 4.22. Relation of porosity and wavelength in ring chains.

d/D = 0.375   Load = 718 N   **d/D = 0.5   Load = 713 N**

Figure 4 23 Isochromatics under diametral compression for ring and solid disk

CHAPTER 5

A COMPARISON OF EXPLOSIVELY GENERATED PULSE PROPAGATION IN ASSEMBLIES OF DISKS AND SPHERES

5.1 Summary

An experimental investigation has been conducted to compare and contrast the dynamic load transfer process in single chain assemblies of two and three dimensional particles. In particular, single chain assemblies of disks and spheres were subjected to explosive loadings and strain gages were employed to collect the resulting strain pulse information. The data was analyzed to compare the pulse velocity, contact load attenuation, dispersion, and pulse break up in disks and spheres. The comparison shows that the average pulse velocity in disks is higher than in spheres and the pulse attenuation is lower in the disks. The results also show that there is a characteristic pulse which will propagate through a single chain of disks without significant dispersion. The characteristic pulse propagating in assemblies of spheres, however, shows dispersion. For both disks and spheres, when the input pul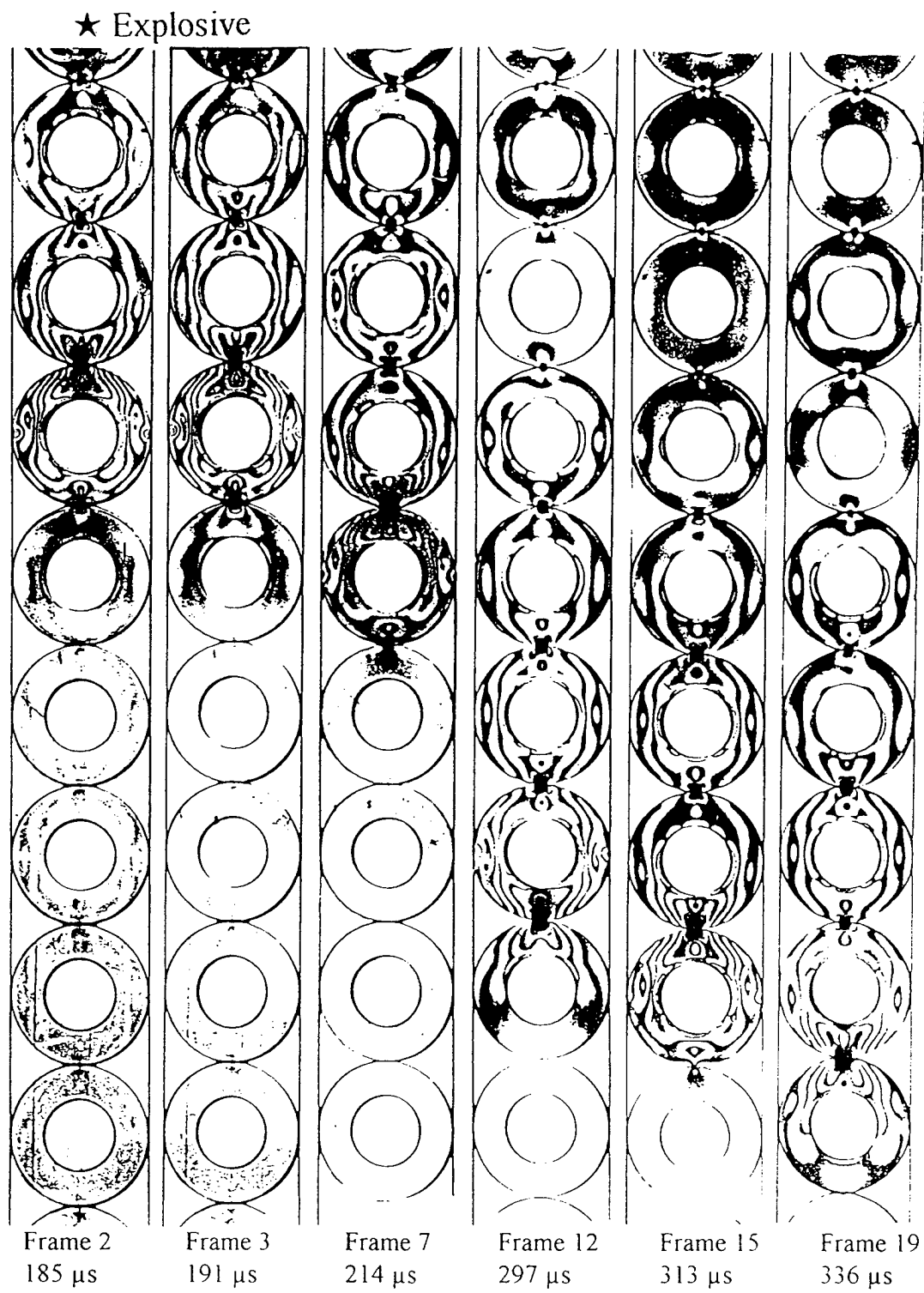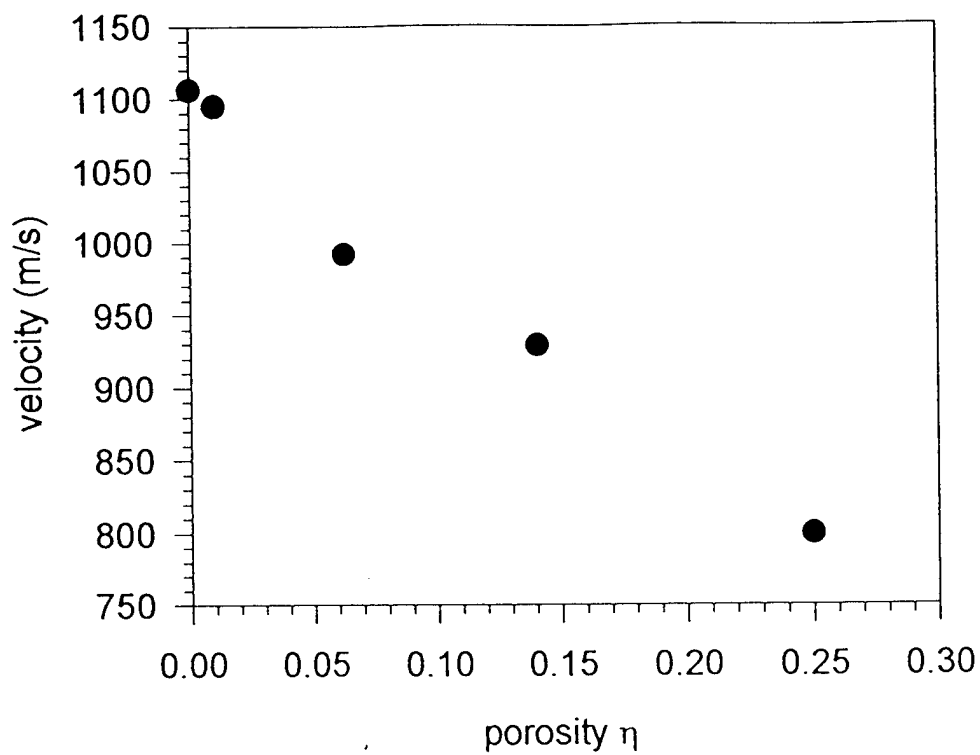se is sufficiently long, it undergoes a ringing process which breaks the long pulse up into smaller signals of size approximately equal to the characteristic length. The larger the input pulse is with respect to the characteristic pulse length, the longer the break up takes. This break up is also accompanied by a redistribution of energy which is easily seen in the frequency domain.

5.2 Introduction

The study of wave propagation and dynamic load transfer in granular and particulate media has been of interest to many different fields of science and engineering including geomechanics, powder metallurgy, pharmaceutical and agricultural processes. With regard to geomechanics, various seismic interests are related to wave propagation in sands and rocks produced from earthquake or explosive loadings. Due to the discrete nature of granular materials, mechanical loadings are transmitted in a discontinuous fashion through contact mechanisms between adjacent particles resulting in the establishment of finite numbers of load carrying paths within the material (Oda et al., 1982, Shukla et al., 1988). Such load transfer

mechanisms are primarily controlled by the particles' material and geometric properties. These local geometric properties include such variables as particle size, shape and relative location, and are generally referred to as the *material fabric*. It has been clearly demonstrated that this local microstructure plays a dominant role in the transmission of both static and dynamic loadings through such materials. For several years our research group has studied the effects of various micro-fabric variables on wave propagation, and have correlated wave speed, amplitude attenuation, and dispersion with several fabric measures (see for example, Shukla, et.al., 1985, 1992, 1993a, 1993b and Sadd, et.al. 1993). To date our investigations have primarily focussed on two-dimensional granular systems. Because real granular materials are composed of three-dimensional particles, our studies have been broadened to include this case. The current article describes some of our preliminary work dealing with the extension of our studies to three-dimensional situations, and comparisons with our previous two-dimensional results are made.

Several static studies of the behavior of particulate media using three-dimensional modeling have been conducted. Cundall (1988) has developed a three dimensional discrete element model where by spherical grains can be analyzed. Ghaboussi and Barbosa (1990) went further by using the discrete element method to analyze three dimensional particulate assemblies where the particles were modeled as six sided solids with six degrees of freedom. The model was applied with success to granular flow problems. Using superquadrics, Williams (1992) developed a three-dimensional discrete element code capable of handling particles of general shape.

Our study uses model assemblies of single chains of spherical particles to simulate the basic features of real granular materials. Experimental studies have been conducted using electrical resistance strain gages to collect dynamic information associated with the propagation of explosive loadings with pulse durations on the order of 100-1000μs. Previous studies using such experimental techniques (Shukla, et.al., 1993a) have demonstrated the usefulness of this scheme. In order to investigate basic features of the non-linear wave propagation process, Fast Fourier Transform analyses of the transmitted wave profiles were conducted. It was found that the dispersion processes are related to material microstructure. The non-linear behavior was also analyzed through the use of soliton dynamics.

5.3 Experimental Procedure

The experimental set-up used in this study is shown in Figure 5.1. In this work, 25.4 mm diameter acrylic disks and spheres were used to simulate the granular media. The model assemblies consisted of long, straight, single chains of particles. An assembly of particles was then subjected to explosive loadings utilizing 10-30 mg of lead azide, where the variation in the amount used will be explained later in this section. The explosive loading initiated a compressive stress pulse which propagated down the assembly of disks or spheres via particle to particle contact.

Electrical resistance strain gages (Micro-Measurements EA-13-031DE-120) were used to record the dynamic strain profiles as the stress wave passed through the granular medium. For the disks, the strain gage was positioned 5 mm from the contact location and for the spheres the gage was located along the equator where the particle to particle contact points are considered the poles of the sphere. The choice of strain gage locations will be explained in a later section. The gages were connected to a bank of bridge amplifiers (Ektron model 563F) and these in turn were digitally sampled by a high speed data acquisition system (Lecroy Data Acquisition System) operating at a 1 MHZ sampling rate. From six to eight strain gages were used for each experiment, placed on discrete disks or spheres in the assemblies. This technique provided the strain pulse profile for a number of disks or spheres as the pulse propagated down the assembly.

Using a small amount of explosive (10 mg) and passing the energy of the explosion directly into the chain results in a short duration (100-150 μsec) pulse. If instead the energy is first passed through a material with a lower acoustic impedance and then into the assembly, the result will be an input pulse with a longer wavelength. By placing a soft or a semi-soft urethane between the charge holder and the first particle, input pulse lengths of 490 μsec and 1330 μsec were obtained in the disk chain and 480 μsec and 1190 μsec for the sphere chain. However, in order to input sufficient energy, the amount of explosive had to be increased to a maximum of 30 mg.

5.4 Theoretical Considerations

5.4.1 Contact Load Analysis

The technique of extracting contact load from strain gage data in the case of disks has

111

been well documented (Xu and Shukla, 1993) so it will be covered only briefly here. The normal and tangential stresses in the vicinity of the contact (Smith and Liu, 1953) are governed by the Hertz contact law and are given as

$$\sigma_{zz} = -\frac{bz}{\pi\Delta}\left(b\,\phi_1 - x\,\phi_2\right)$$

$$\sigma_{xx} = -\frac{bz}{\pi\Delta}\left(\frac{b^2 + 2z^2 + 2x^2}{b}\,\phi_1 - \frac{2\pi}{b} - 3\,x\,\phi_2\right) \qquad (5.1)$$

$$\sigma_{zx} = -\frac{b\,z^2\,\phi_2}{\pi\Delta}$$

where

$$\phi_1 = \frac{\pi\,(M + N)}{MN\sqrt{2MN + 2x^2 + 2z^2 - 2b^2}}$$

$$\phi_2 = \frac{\pi\,(M - N)}{MN\sqrt{2MN + 2x^2 + 2z^2 - 2b^2}}$$

$$M = \sqrt{(b + x)^2 + z^2} \qquad\qquad N = \sqrt{(b - x)^2 + z^2} \qquad (5.2)$$

$$\Delta = \frac{1}{A}\left(\frac{1 - \nu_1}{E_1} + \frac{1 - \nu_2}{E_2}\right) \qquad A = \frac{1}{2}\left(\frac{1}{R_1} + \frac{1}{R_2}\right).$$

The co-ordinate system is defined in figure 5.2. The subscripts 1 and 2 refer to the two bodies making contact. R_i are the radii of the particles and E and ν are the Young's moduli and Poisson's ratios. The space variables are x and z which identify the point at which the stresses are to be determined. The unknowns, b and β, are the half contact width and the friction factor, respectively.

For the single chain assembly of disks used in our experiments, the bodies are of the same material and have the same geometry which allows for the reduction of the constants Δ and A. Also, the strain gages were located along the z axis (x=0) and the particles were subjected to only normal stresses ($\beta = 0$). This reduces the field equations to

$$\sigma_{zz} = -\frac{b^2}{\Delta\sqrt{b^2 + z^2}}$$

$$\sigma_{xx} = -\frac{b^2 + 2z^2}{\Delta\sqrt{b^2 + z^2}} + \frac{2z}{\Delta} \qquad (5.3)$$

$$\sigma_{zx} = 0$$

The normal strain ϵ_{zz} can be calculated using Hooke's law as

$$\epsilon_{zz} = \frac{1}{E}(\sigma_{zz} - \nu\sigma_{xx}) \qquad (5.4)$$

and substituting for the stresses in equation (5.4) from equation (5.3) we get

$$\epsilon_{zz} = -\frac{1}{E}\left[\frac{(1 - \nu)b^2 - 2\nu z^2}{\Delta\sqrt{b^2 + z^2}} + \frac{2\nu z}{\Delta}\right] \qquad (5.5)$$

Once the strain gage location has been fixed at x=0 and at some value of z near the contact, ϵ_{zz} is obtained from the strain gage and equation (5.5) can be solved for the half contact width b. From the half contact width, the contact load can be determined from the following relation

$$w = \frac{\pi b^2}{2\Delta} \qquad (5.6)$$

where w is the load per unit depth and Δ is as defined earlier. The above procedure was used to calculate the contact loads in disks. For spheres the technique used was more simple and straightforward.

Researchers have developed field equations for a sphere under static diametrical compression (e.g. Sternberg and Rosenthal, 1952). However, the equations are best suited

113

for a point along the z axis at r=0 (i.e. inside the sphere where locating strain gages is difficult). Consequently, a simple calibration experiment was conducted to determine the load-strain relation.

For this experiment, one of the instrumented spheres used in the dynamic studies was placed in an Instron testing machine and compressed. Recall that the strain gages on the spheres were located on the equator of the sphere with the loading taking place at the two poles. The gage was orientated to measure strain along the longitudinal line. During compression the applied load and the resulting strain were recorded on a digital storage oscilloscope. The experiment was repeated three times.

Figure 5.3 shows the applied load and the recorded strain for the three separate experiments. The figure shows that the strain is linearly proportional to the applied load and that there was very little scatter introduced due to potential misalignment. The data set was fit with a least squares line yielding a calibration constant, k = -0.671 μm/m per newton. Thus a static calibration constant was determined for the acrylic sphere used in the dynamic experiments.

One may argue that the static calibration is not applicable to the dynamic experiment but it is proposed that when the strain recorded by a strain gage located at the equator of a sphere subjected to a dynamic strain pulse reaches the peak strain value, the sphere will be loaded in a state of quasi-static diametrical compression. This assumption will hold as long as the strain pulse length is larger than several sphere diameters. For the cases studied, the strain pulse was at least four times the sphere diameter.

5.4.2 Fourier Transforms

The explosive loading of granular assemblies produces a group wave that propagates through the assembly. This group wave is comprised of many discrete frequencies which travel together as a single pulse. It has been proposed (Shukla, et al., 1993a) that the particles making up a granular assembly act as a filter and that there is a characteristic pulse length that will travel in the assembly without significant dispersion. If the input pulse is not of this characteristic length or period, the pulse will break up into wavelets, each of which is of the characteristic period. In this paper the Fast Fourier Transform is used to study the effects of input pulse period in single chain assemblies of disks and spheres by looking at the frequency

domain of the propagating wave.

Fast Fourier Transforms (FFT) allow one to calculate the frequency spectrum associated with discretely sampled time domain data. The continuous Fourier transform pair for a function, F(t), defined for the time interval $-\infty$ to ∞ is given

$$F(t) = \frac{1}{2\pi} \int_{-\infty}^{\infty} C(\omega)\, e^{i\omega t}\, d\omega,$$

$$C(\omega) = \int_{-\infty}^{\infty} F(t)\, e^{-i\omega t}\, dt. \qquad (5.7)$$

$C(\omega)$ represents the continuous Fourier transform, ω is the angular frequency and I is the imaginary unit. The continuous Fourier transform is then the constituent sinusoidal (spectrum) of the original waveform F(t). Plotting $C(\omega)$ versus frequency yields a diagram of the amplitude of each constituent sinusoid.

One obvious difficulty in applying equation (5.7) directly to an engineering problem is that the integral needs to be evaluated over an infinite interval. The technique becomes suitable to computer algorithms if the integral can be approximated over a finite interval without losing any of the relevant signal information.

The discrete Fourier transform provides the means for the integral approximation whereby the integral has been replaced by a summation. The discrete Fourier transform of the function F(t) is given

$$G\left(\frac{2n\pi}{NT}\right) = T \sum_{k=0}^{N-1} F(kT)\, e^{\frac{-2nk\pi i}{N}} \qquad n = 0, 1, 2, \ldots, N-1, \qquad (5.8)$$

where T>0 (T is the sampling period) and N is a positive integer. Now if C and G are in sufficiently "good" agreement for the points ($2n\pi/NT$), the approximation is suitable. The accuracy of this approximation is a function of the sampling period T and the number N of samples used.

The fast Fourier transform itself is not really a transform but rather an algorithm by

115

which the computation time needed to evaluate the discrete Fourier transform can be reduced. There are many algorithms for reducing the problem and all are generally based on the same idea. The fundamental idea is to recognize and utilize patterns of repeated numbers. Most simply, the Fast Fourier Transform is not a new transform but rather a more efficient method of computing the coefficients of the discrete Fourier transform where the end results in the frequency domain are the amplitudes of the individual sinusoids which make up the signal in the time domain.

5.5 Results and Discussion

The dynamic strain profiles obtained during the experiments were analyzed to study the wave velocity, dispersion, and attenuation of the propagating wave as well as its frequency components. The results from the experiments are discussed in two subsections with the first dealing primarily with the short input pulse experiments and the second the longer input pulses which result in a ringing behavior

5.5.1 Short input wave loading

The arrival times of the strain pulses were obtained directly from the data acquisition system and plotted against the distance of propagation to compute the average pulse velocity. Figure 5.4 shows typical results from the short input pulse (120 and 150 μsec for disks and spheres, respectively). The data shows that the average velocity for the spherical particles was 600m/s while for the disks it was 930m/s. The experiment was repeated for input pulse durations of approximately 500 and 1200 μsec and a plot of average wave velocity versus input pulse duration is shown in figure 5.5. The figure shows that the pulse velocities decrease by about 12% for disks and 16% for spheres as the input pulse duration is increased from about 120μsec to 1200μsec. Moreover, the spherical particles showed consistently about 35% slower pulse propagational velocity when compared to the disk chain for the various input pulse durations tested

To explain this phenomena the following approximate theoretical development is used. The equation for the approximate wave velocity, V, in one dimensional granular media is given as (Takahashi, 1949)

116

$$V \simeq d\sqrt{\frac{K}{m}} \tag{5.9}$$

where d is the distance between the centers of two particles in contact, K is the effective contact stiffness, and m is the mass of a particle. For the cases studied, the distance between centers was kept constant (25.4mm), so this term does not contribute to the observed difference in velocities. The two remaining terms in the expression must then be the causal factors. The mass of the particles is easily measured or computed but the effective contact stiffness is not known quantitatively.

Forming the ratio V_d/V_s and canceling the distance term yields

$$\frac{V_d}{V_s} = \sqrt{\frac{K_d m_s}{K_s m_d}} \tag{5.10}$$

where the subscripts d and s refer to the disk chain and the sphere chain, respectively. We can now consider the ratios of the effective contact stiffness and mass separately. The ratio m_s/m_d reduces to $(4\,r)/(3\,t)$ where r and t are the particle radius and the disk thickness, respectively. Using the measured quantities for these constants yields a value of approximately 8/3 for the mass ratio.

Utilizing equations from Johnson, 1985, to compute the mutual approach of two distant points in contacting solids, one can calculate the load versus relative displacement for static compression of disks and spheres. Figure 5.6 shows such a plot for a sphere and a disk (the disk is considered under plane stress) for various compressional loads. The calculated values are shown as symbols and the curves were fit with a power law expression

$$P = K_{eff}\delta^n \tag{5.11}$$

Proceeding to define stiffness as the slope of the curves, one can plot the stiffness ratio versus load which is shown as figure 5.7. The average value of the ratio is approximately 1.1. Substituting this into equation (5.10) yields $V_d/V_s = 1.7$. This value compares well with the

experimentally obtained $V_d / V_s = 1.6$. The difference in the values could be partly attributed to the static equations (Johnson 1985)being used to explain the dynamic phenomenon.

Figures 5.8 and 5.9 show the strain gage output as a function of time from the instrumented disks and spheres, respectively. The strain pulses are the result of an initial input pulse duration of 120 μsec for the disks and 150 μsec for the spheres. For the disks, the pulse propagates down the assembly without significant dispersion. In the assembly of spheres, however, the pulse undergoes approximately a 30% increase in pulse length. This is further illustrated by figure 5.10 where the pulse length is plotted as a function of distance propagated for both the spheres and disks. This figure shows that while the pulse length does elongate in the assembly of disks, the increase is only 8% over approximately 80 particles while the assembly of spheres shows a 30% increase in pulse length over approximately 60 particles.

One possible explanation for the dispersion of the pulse in spherical particles is the fact that the spheres do not represent as good a wave guide as do the disks. In the thickness dimension, the disks are quite narrow with smooth parallel surfaces which provide a good surface for wave reflection. The parallel surfaces act as an excellent wave guide with a constant angle of incidence. The sphere on the other hand offers the impinging wave an expanding medium first, and second, a converging medium with rapidly changing angle of incidence. Near the sphere to sphere contact patch, opposite the incoming wave, the angle of incidence is approaching $90°$. For all directions in spherical particles this condition exists while in disks this condition is only present in one dimension.

The peak contact loads were determined for the instrumented particles as per the methods described earlier and these values were normalized by the maximum value. Figure 5.11 shows the normalized contact load as a function of distance propagated for the short input pulses. The plot shows that by the fifth particle the load has dropped by 20% in the disk assembly and by more than 60% in the spheres. Previous work using assemblies of elliptical disks (Shukla et al., 1993b) has shown that the larger the contact stiffness, the higher the contact load attenuation rate. Also, the more massive the particle, the higher the attenuation rate. The initial drop occurring in the first five particles is more severe for the sphere chain when compared to the drop occurring in the disk chain. This effect could be attributed to the three dimensional nature of the spherical particles where higher order modes of vibration can

occur. Previous work has shown that the wave begins to take its characteristic shape after propagating through approximately 4-5 particles. The attenuation as a function of distance propagated becomes more gradual after the first five particles with the sphere chain showing greater over all attenuation.

5.5.2 Long input wave loading

A series of experiments were conducted where the input pulse lengths were elongated. Figures 5.12 and 5.13 show the strain gage data obtained from a chain of disks subject to an initial pulse length of 490 μsec and a chain of spheres subject to an initial pulse length of 480 μsec, respectively. Both figures illustrate a ringing behavior that tends to separate the single long input pulse into pulses of shorter duration. This shorter wave length corresponds to the characteristic wave length observed in the short input pulse experiments which propagated relatively undisturbed.

Figure 5.12 shows that the magnitude of the peak strain in the disk assembly first increases as the pulse propagates down the chain and then decreases. For the sphere assembly, figure 5.13, the 480 μsec input pulse shows that the peak strain does not first increase before decreasing. Rather, the peak strain follows the same trend seen for the shorter input pulse durations. This may be explained by the fact that the attenuation rate in an assembly of spheres has been shown to be more severe than it is in an assembly of disks. The leading pulse does not initially gather sufficient energy to overcome the effect of amplitude attenuation.

When the input pulse duration is increased to about 1330 μsec for disks and 1190 μsec for spheres, an increase in the peak strain value occurs in both assemblies (see figures 5.14 and 5.15). Also, as seen in the disk assembly subject to an input pulse length of 490 μsec, the peak magnitude of the leading pulse is not the largest magnitude of all of the pulses and therefore does not reflect the maximum contact load. The peak contact load corresponds to the pulse with the largest strain magnitude and the pulse with the maximum strain value changes with distance propagated. This is most evident in figure 5.14 (the disk assembly) where the maximum strain in disk 15 occurs in the third pulse and shifts to the first pulse between disks 15 and 40. There is also an increase in peak amplitude.

This shifting is evident in the strain plots for the assembly of spheres also but it is not as obvious. The reader is directed to the strain profile for sphere 20 in figure 5.15 where the

leading pulse is just forming and the second pulse has the largest magnitude. By the time the pulse reaches sphere 30, the leading pulse has the largest amplitude. Careful observation of the wave propagation phenomenon in these experiments shows that the longer the input load duration the longer the time required to separate into wavelets.

Figure 5.16 shows the normalized peak contact load as a function of distance propagated. The contact load was generated from the maximum value of strain occurring in each disk/sphere regardless of whether or not the maximum occurred in the leading pulse or a following pulse. The most significant increase in contact load appears in the disk chain when the input pulse duration was 1330 μsec. An increase of approximately 75% in the maximum contact load is shown. The assembly of spheres also shows an increase in contact load for the longest input pulse duration (1190 μsec) but the increase is only about 25%. This is the result of a redistribution of energy in the chain. The redistribution is in the breaking up of the main pulse into the smaller pulses. As the main pulse breaks up into wavelets that are of shorter duration there is a subsequent rise in magnitude of the wavelets corresponding to the shortening of the pulse length.

5.5.3 Theoretical Description of the Ringing Behavior

The granular medium acts as a nonlinear wave guide, and local microstructure and contact nonlinearity will allow input signals of sufficiently long wavelength to excite resonant sub-units of the medium to produce this observed ringing separation. Nesterenko (1983) suggested that compression pulses in granular media are dominated by soliton dynamics. He found that an initial compressional pulse soon broke up into a series of soliton modes, each propagating with unique amplitude and velocity, and such a system model could be approximated by a nonlinear wave equation similar to the well-known Korteweg-de Vries equation. The velocity of a soliton is dependant upon, among other things, the amplitude of the wave. The soliton with higher amplitude travels slightly faster than that with lower amplitude. This would explain why after some time, the largest amplitude peaks forming in the middle of the original pulse shift so that the leading pulse shows the largest amplitude.

To expound on the ringing behavior in detail, an analysis is performed following the procedure developed by Nesterenko (1983). The analysis evaluates the characteristic wavelength which could be supported in single chain assemblies of disks and spheres. The

120

analysis also uses a simplified version of contact law proposed by Sadd *et al.*, (1993). This contact law can be expressed as

$$F_n = \alpha \delta_n^p \tag{5.12}$$

The coefficients in the contact law, α and p, can be determined by matching the results from a discrete element numerical code with a dynamic calibration experiment performed in our laboratory. These values are $\alpha=0.58\times10^8$ $Nm^{-1.24}$, p=1.24 for the disks and $\alpha=3\times10^8$ $Nm^{-1.4}$, p=1.5 for the spheres. The equation of motion for the *i*th disk can be written as

$$m\ddot{u}_i = \alpha(u_{i-1} - u_i)^p - \alpha(u_i - u_{i+1})^p \tag{5.13}$$

where u_i is the displacement of the *i*th disk, m is the disk mass, and α is the loading coefficient in the contact law.

Using $\delta_{i,i+1} = u_i - u_{i+1}$ to denote the deformation between the *i*th and (*I*+*I*)th disks, the equation of motion becomes

$$m\ddot{\delta}_{i,i+1} = \alpha(\delta_{i-1,i}^P - 2\delta_{i,i+1}^P + \delta_{i+1,i+2}^P) \tag{5.14}$$

In order to apply this equation to investigate the ringing behavior, consider small deformations of the granular system measured from a uniform initial compressive deformation $\delta_0 > 0$. Thus for each pair of disks, $\delta_{i,i+1} = \delta_0 + \delta'_{i,i+1}$, with $\delta'_{i,i+1} \ll \delta_0$. Substituting this into equation (5.14)

$$\ddot{\delta}'_{i,i+1} = \frac{K_0}{m}(\delta'_{i-1,i} - 2\delta'_{i,i+1} + \delta'_{i+1,i+2}) \tag{5.15}$$

where

$$K_0 = p\,\alpha^{(1/p)}F_{average}^{(p-1)/p} \tag{5.16}$$

where the higher order terms of $\delta'_{i,i+1}/\delta_0$ have been dropped, and $F_{average} = \alpha \delta_0^p$ being the average value of normal contact force during the wave propagation. The above equation can be rewritten as

$$\delta'(x,t) = \frac{K_0}{m}(\delta'(x-d,t) - 2\delta'(x,t) + \delta'(x+d,t)) \qquad (5.17)$$

Looking for a harmonic traveling wave solution, let $\delta'(x,t) = \Delta_0 \sin(kx - \omega t)$, and substituting this into equation (5.16) yields the frequency equation

$$\omega = 2\sqrt{\frac{K_0}{m}} \sin\left(\frac{kd}{2}\right) \qquad (5.18)$$

where k is the wave number. For disk chains, the characteristic wavelength obtained in the experiments for the ringing behavior was approximately 4.4 disk diameters. Thus the wave number becomes $k = 2\pi/4.4d$ and according to equation (5.18), this wavelength gives a frequency

$$\omega = 2\sqrt{\frac{K_0}{m}} \sin\left(\frac{\pi}{4.4}\right) \qquad (5.19)$$

The average contact load was found to be $F_{average} = 480$ N from the experiments. Substituting $F_{average}$, p and α into equation (5.19) gives a time period of 106 μsec. This compares favorably with the experimentally obtained value of 120 μsec.

For the sphere chain, experimental results show that the average characteristic wavelength is approximately 4 sphere diameters, and this wavelength gives a frequency

$$\omega = \sqrt{\frac{2K_0}{m}} \qquad (5.20)$$

Following the same procedure as for the disk case, and load using the experimentally found $F_{average} = 440$ N, the characteristic time period was obtained to be approximately 198 μsec.

122

The experimental results show that the sphere chain can support the characteristic pulse duration in the range of 150μsec to 200μsec.

5.5.4 Fast Fourier Transform Analysis

The strain pulses which exhibited ringing (the medium and long input pulse lengths) were also analyzed using the Fast Fourier Transform technique. Figure 5.17 shows the power spectral density as a function of frequency for the 480 μsec input pulse as it propagates in a chain of spheres. The plot shows that above approximately 15-20 kHz, there is no significant energy when compared to the energy contained within the lower frequencies. The magnitude of the frequency components in the 0-2.5 kHz range is quite large and the same basic shape appears in each of the transformed strain pulses. This basic phenomena occurred in all transformed strain pulses regardless of the length of the input pulse or the particle type (disks or spheres). The more interesting information is found in the frequency range between 2.5-15 kHz. Further plots will omit the frequency components that are less than 2.5 kHz for clarity.

Figure 5.18 shows the evolution of high frequency energy build up in the 7.5-12.5 kHz range for an input pulse length of 490 μsec in a chain of disks. Before the pulse breaks up (before the strain pulse reaches disk 30), the energy is all contained in the low frequency components. Once the pulse breaks up, the energy associated with the frequency components in the 7.5-12.5 kHz range begins to build. Disk 30 shows a build up in the 10-12.5 kHz range and then the frequency components of the FFT shift from the 10-12.5 kHz range down to approximately 9.5 kHz and the magnitude increases by around 60% by the 70th disk. This increase corresponds to the increase in peak strain for the pulse as seen in the strain versus time plots.

Similar behavior is exhibited by the chain of spheres when subject to an input pulse of 480 μsec. The FFT of the strain pulses (figure 5.19) shows that initially the energy is contained in the frequency range between 0-2.5 kHz but by the time the pulse has reached the 30th sphere the energy around the 5 kHz range has increased. However, unlike the disks where the energy build up was seen in the 7.5-10 kHz range, the spheres exhibit the build up of energy in the 2.5-7.5 kHz range.

When we consider the FFT plots for the long input pulses, the build up of energy occurs around 12.5 kHz for the disk chain and 5-7.5 kHz for the sphere chain. The plots are

shown as figures 5.20 and 5.21 for the disk chain subject to an input pulse of 1330 μsec and a sphere chain subject to an input pulse of 1190 μsec, respectively. These FFT plots clearly show that the energy associated with particular frequency components changes during the experiments with a clear shift into the higher frequencies and thus lower characteristic wavelength.

At this time a point should be made about the resolution capability of the Fast Fourier Transform with respect to the data presented. The frequency resolution, f_{min}, of the algorithm is dependant upon both the sampling period, T, and the number, N, of samples taken. Given in equation form

$$f_{min} = \frac{1}{NT}.$$
(5.21)

The sampling period for the data presented was 1 μsec per point and the number of data points varied between 1000 and 2000 yielding frequency resolution of approximately 500 and 1000 Hz for the medium length and long length input pulses, respectively.

FFT results show that the pulse breakup was associated with the energy shifting from low frequency to high frequency. For sphere chain, the energy built up in 2.5-7.5 kHz range when pulse broke up. On the other hand, the energy build up in the range of 7.5-10 kHz for disk chain.

5.6 Conclusions

Experiments have shown that single chain assemblies of disks yield higher average wave velocities (approximately 35%) than similar chains of spherical particles. This result was shown to be independent of input pulse length. A simple approximation for average wave velocity showed that while the velocity was dependant upon the ratio of the effective particle stiffness and the ratio of the particle masses, the mass ratio is the dominant and controlling factor. As a result, the velocity was always higher in assemblies of disks because of the lower particle mass.

While the assembly of disks consistently showed an average wave velocity greater than the assembly of spheres, both assemblies showed similar behavior with increasing input pulse length. Increasing the input pulse length resulted in a decrease in average wave velocity

124

of approximately 12% for the disks and 16% for the spheres.

Even though the velocity characteristics were similar for both types of particles, the dispersion characteristics of a short duration (120-150 μsec) input pulse were dramatically different. The chain of disks showed virtually no dispersion (8%) after having traveled through eighty particles while the chain of spheres showed 30% dispersion after only sixty particles. This difference in dispersive behavior has been attributed to the three dimensional nature of the spheres which results in more multiple internal reflections of the stress wave. In contrast, the disks are two dimensional in shape with flat parallel sides which results in less reflective losses.

The results have also shown contact load attenuation differences between disks and spheres. The initial drop in peak contact load between the first and fifth particle for the disk chain was approximately 20% while the sphere chain suffered approximately 60% attenuation for the same distance. After about 30 particles, both assemblies show approximately the same attenuation *rate* with the disk chain suffering approximately 80% overall attenuation and the sphere chain about 90% after traversing 70 particles. The dramatic difference in the initial attenuation was attributed mainly to higher order vibrations and the three dimensional nature of the spheres.

It has been shown that there is a characteristic pulse which will propagate relatively undisturbed through a single chain of acrylic disks (approximately 120 μsec in duration). Acrylic spherical particles showed the same basic phenomena qualitatively, however the pulse suffered dispersion. The result is that a single characteristic pulse could not be defined for the sphere chain, but rather this case will support a pulse duration between approximately 150 μsec and 200 μsec. If the input pulse is sufficiently longer than this characteristic length, the pulse undergoes a ringing process which breaks it up into smaller pulses of the characteristic length. The larger the input pulse is with respect to the characteristic pulse length, the longer the break up takes.

Lastly, the Fast Fourier Transform analysis of the longer input pulses demonstrated a shifting of the energy associated with the propagating pulse. The initial low frequency dominated pulses shifted energy into the higher frequencies and this shifting corresponded to the break up of the initial input into wavelets of the characteristic length.
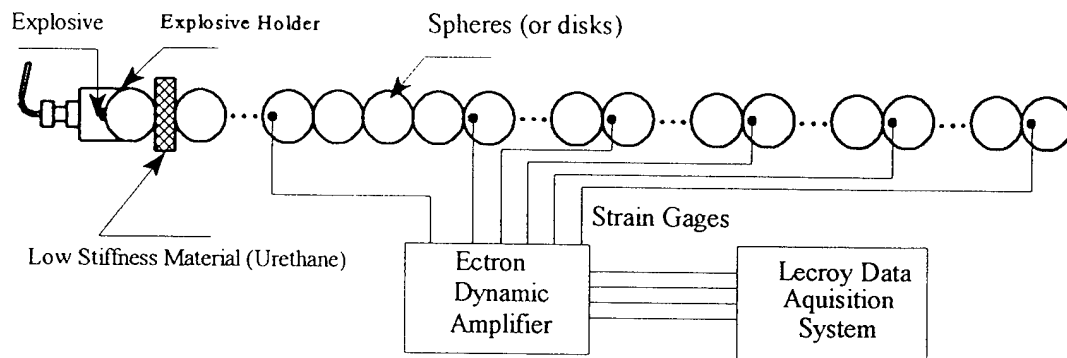
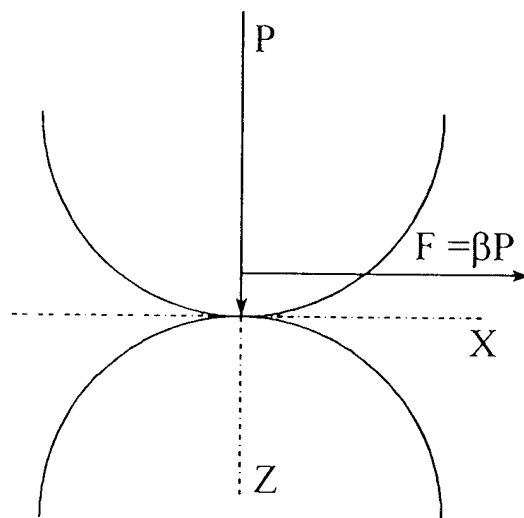Figure 5.1. Experimental set up

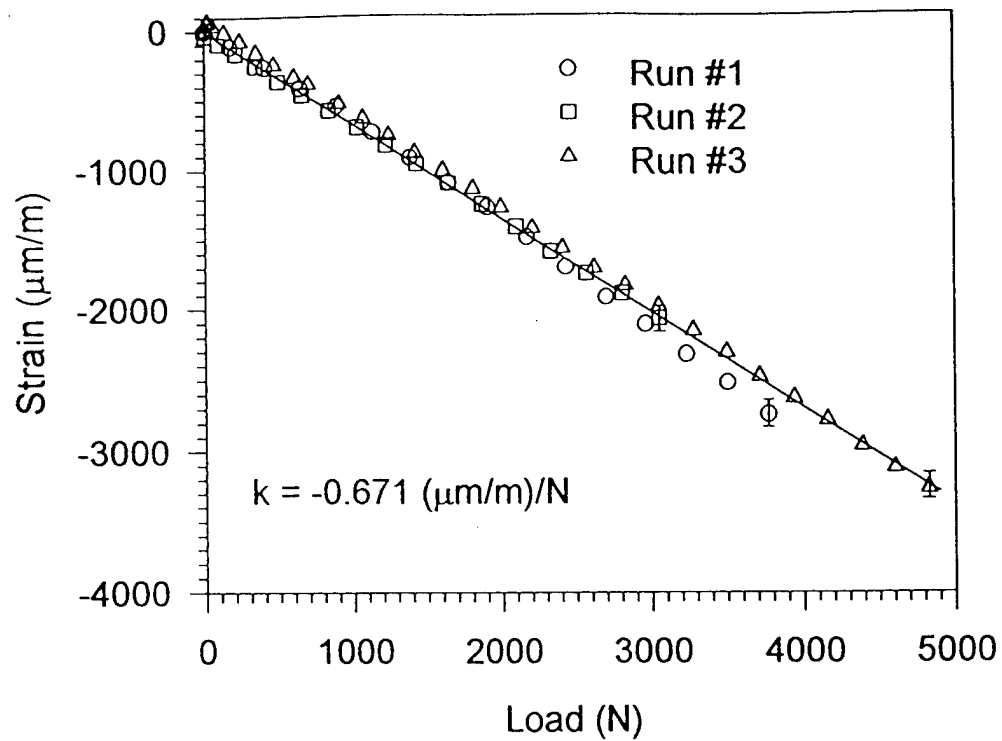Figure 5.2. The coordinate system for two bodies in contact

Figure 5.3. The static calibration for the sphere used in the dynamic experiments.
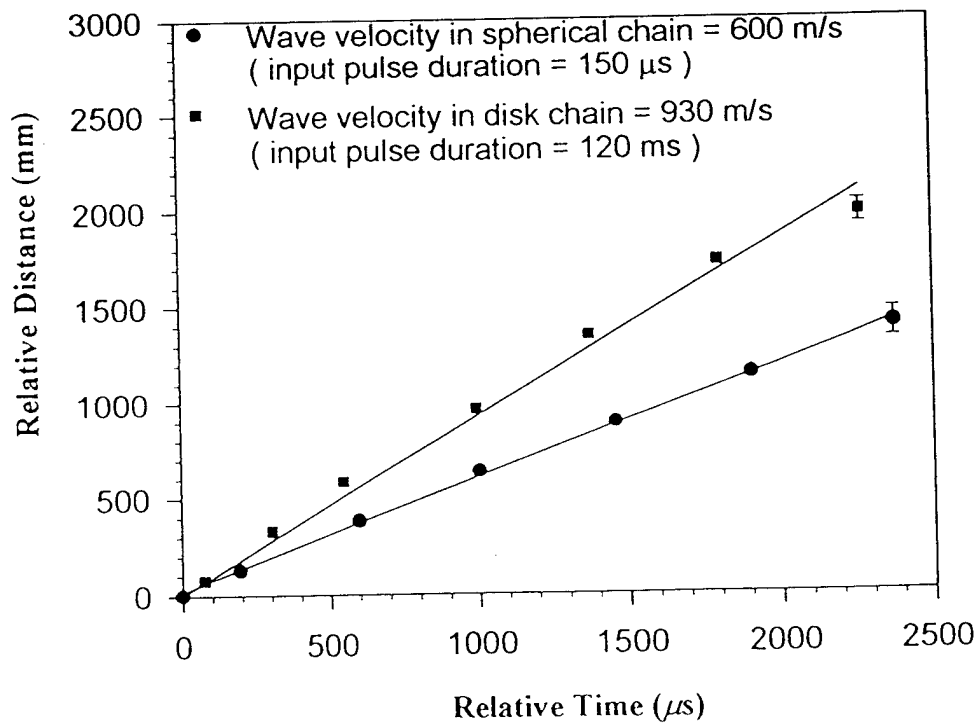

Figure 5.4. Average wave velocity in spherical and disk chains for short input pulse duration.
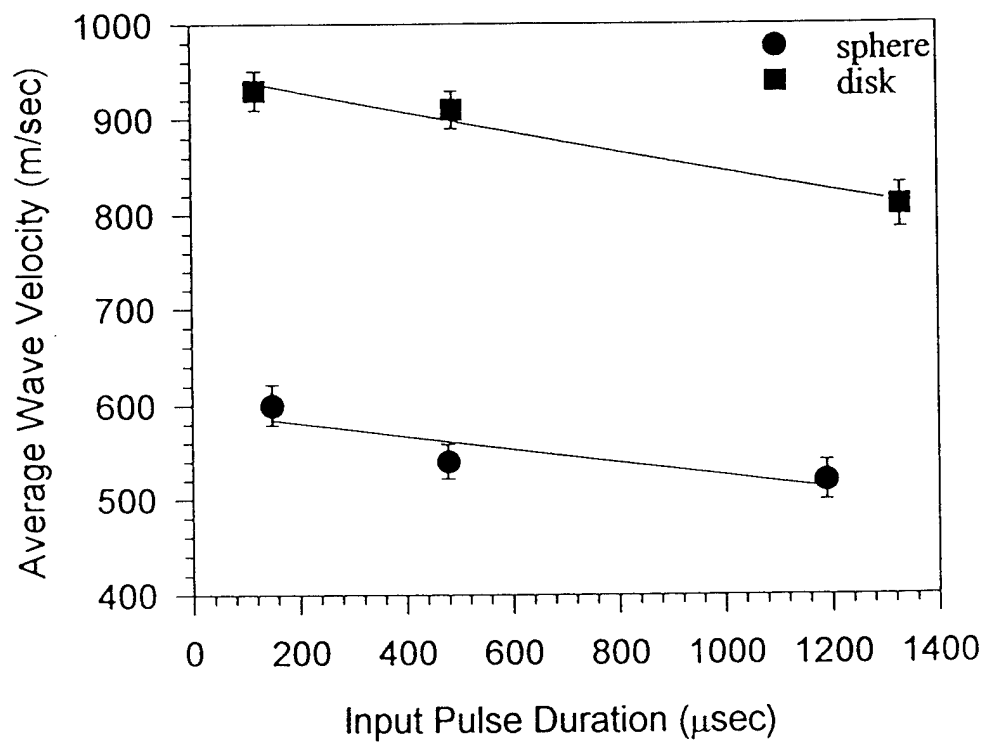
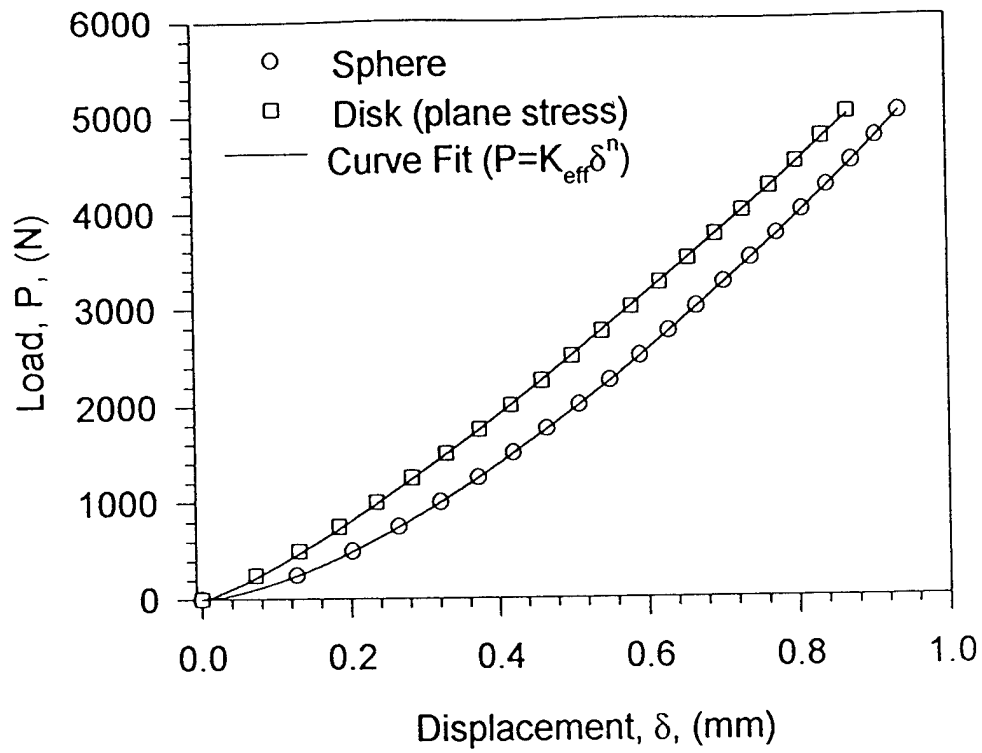Figure 5.5. The velocity variation with the input pulse period.

Figure 5.6. Relative displacement for static compression of disks and spheres.
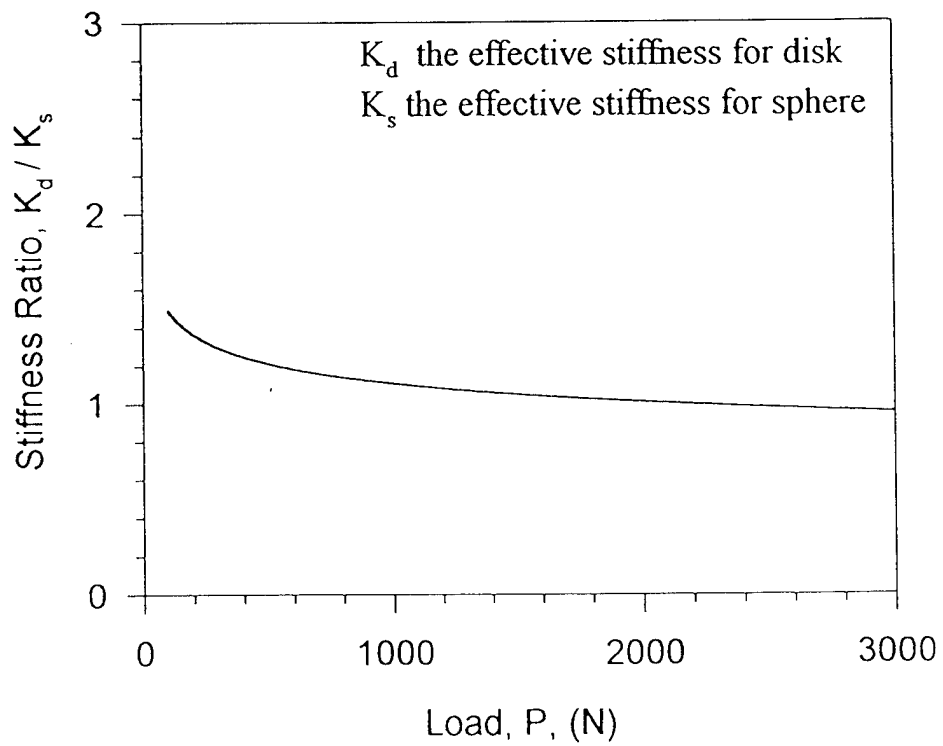

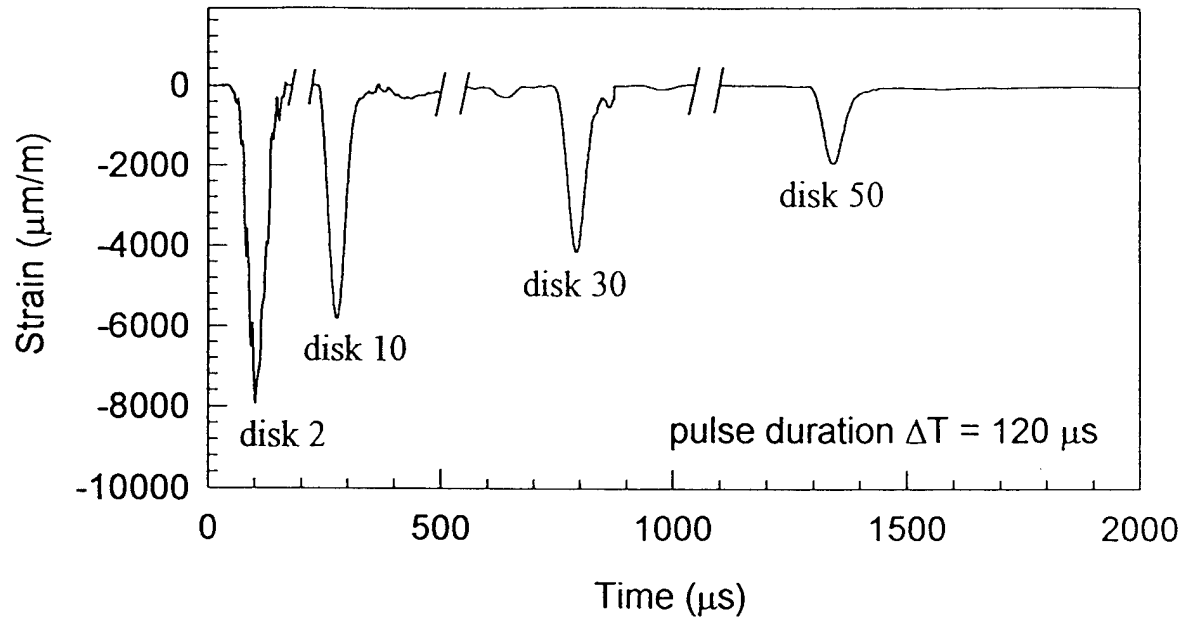Figure 5.7. The effective stiffness ratio of disk and sphere.

Figure 5.8. Strain pulses as recorded by the gages on different disks.
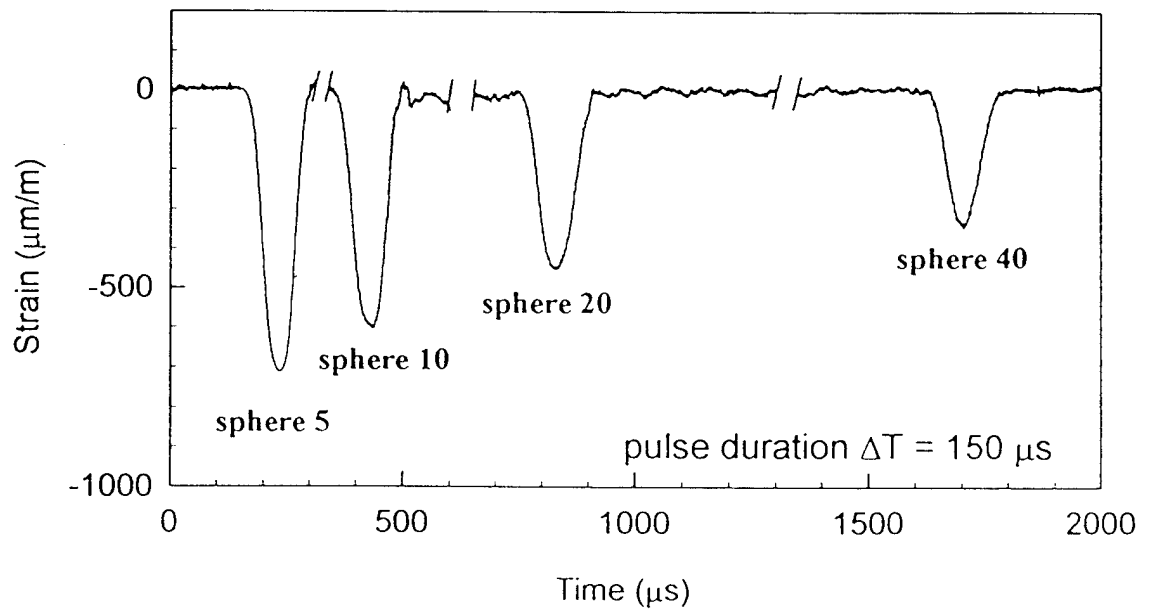

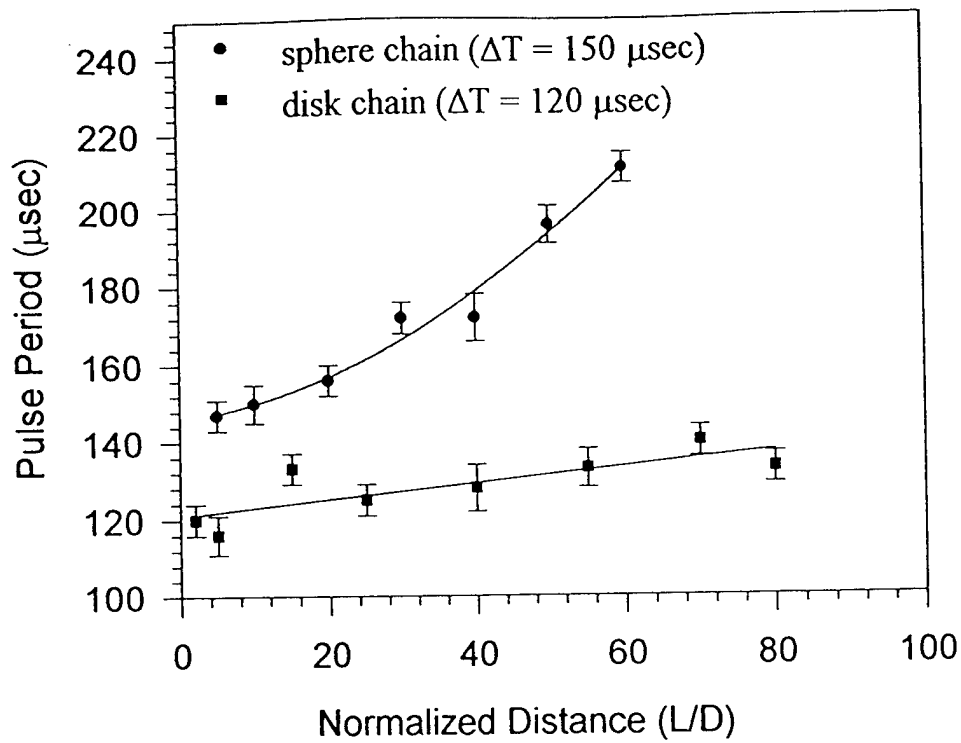Figure 5.9. Strain pulses as recorded by the gages on different disks.

Figure 5.10. Input pulse dispersion with propagated distance in disk and sphere chains.
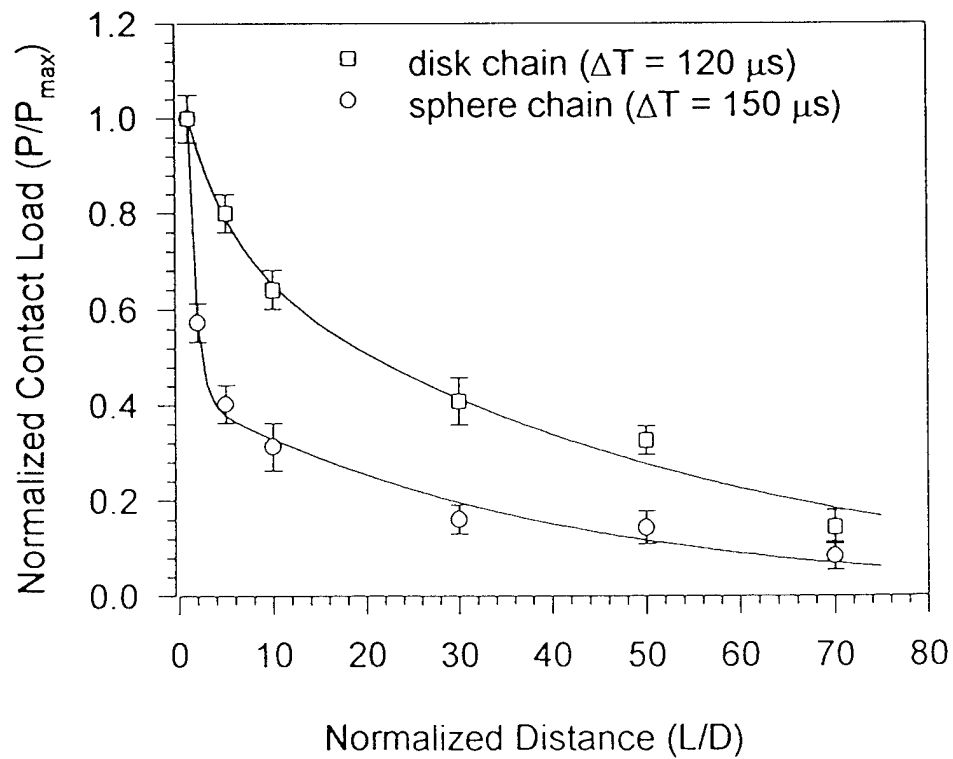

Figure 5.11. The normalized peak contact load attenuation in disk and sphere chains.
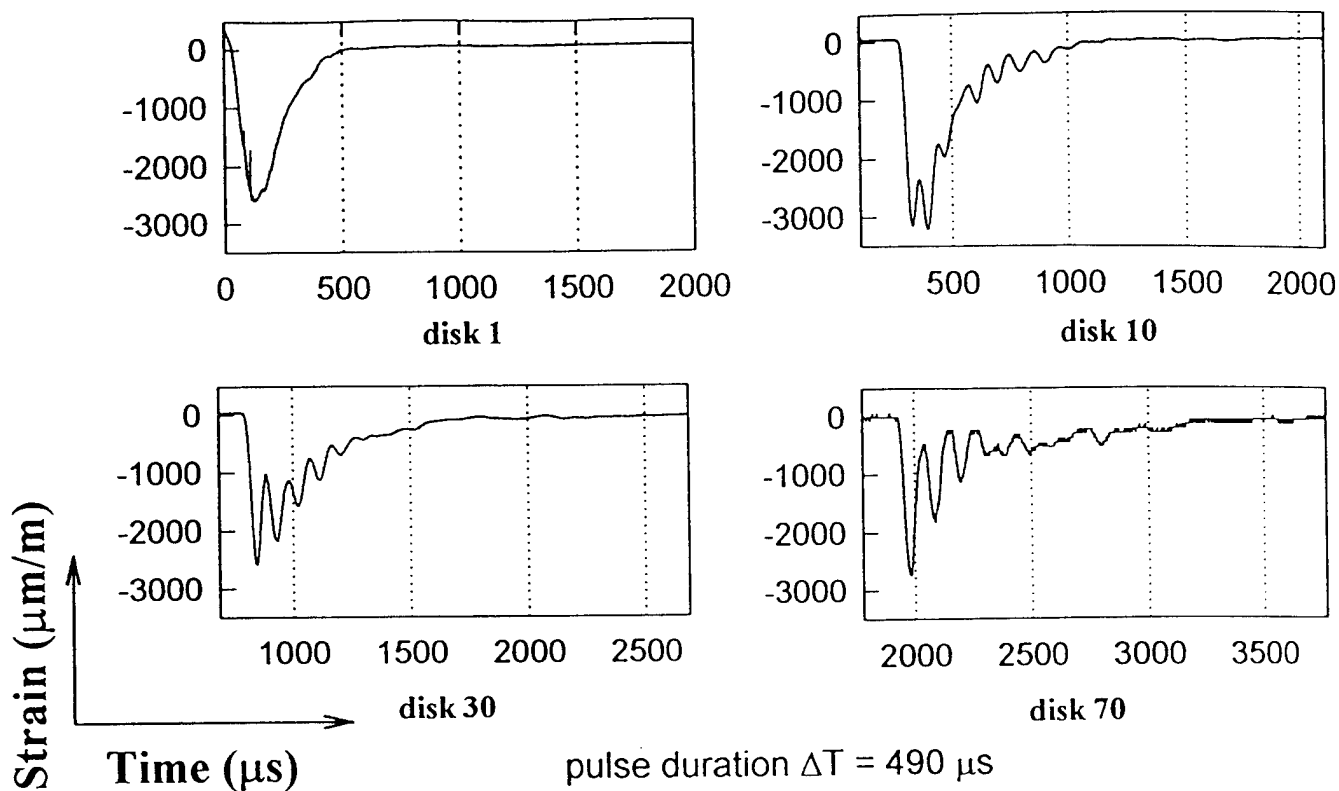
Figure 5.12. Strain pulses as recorded by the gages on different disks.
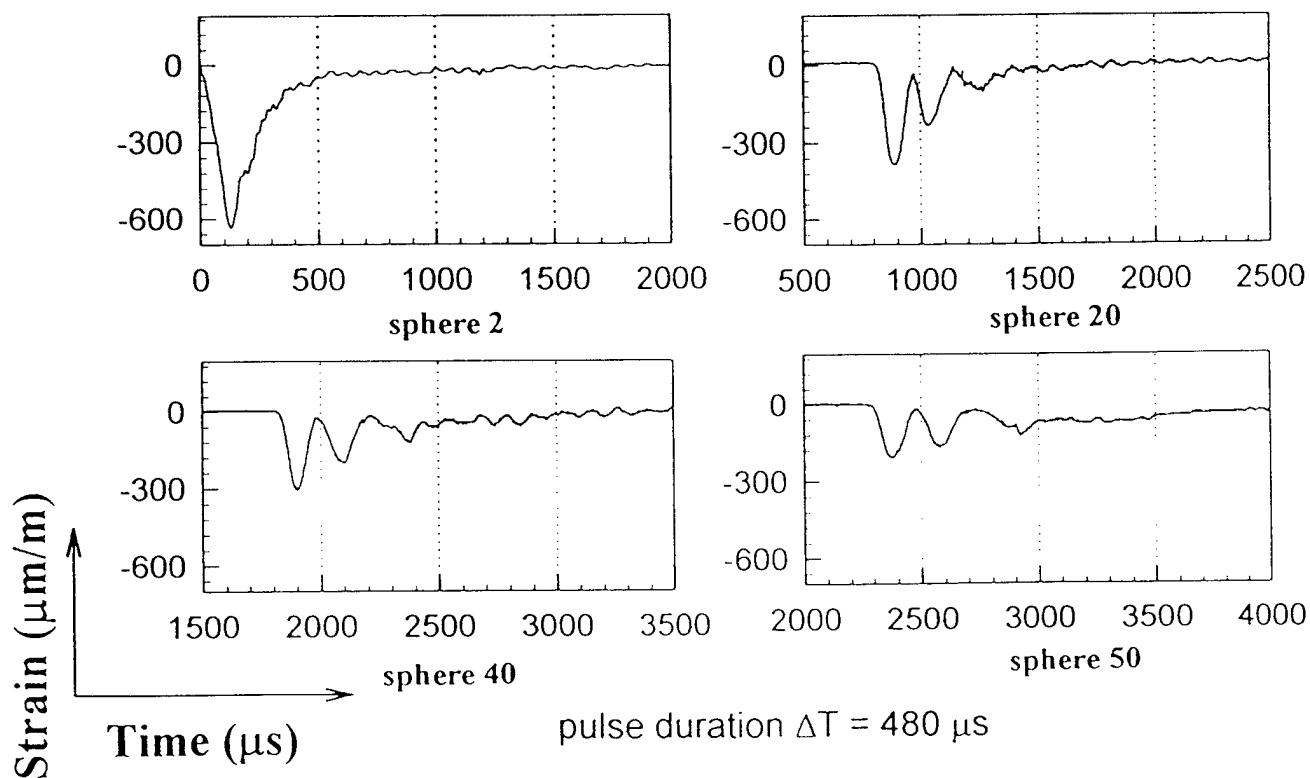
Figure 5.13. Strain pulses as recorded by the gages on different spheres.

132
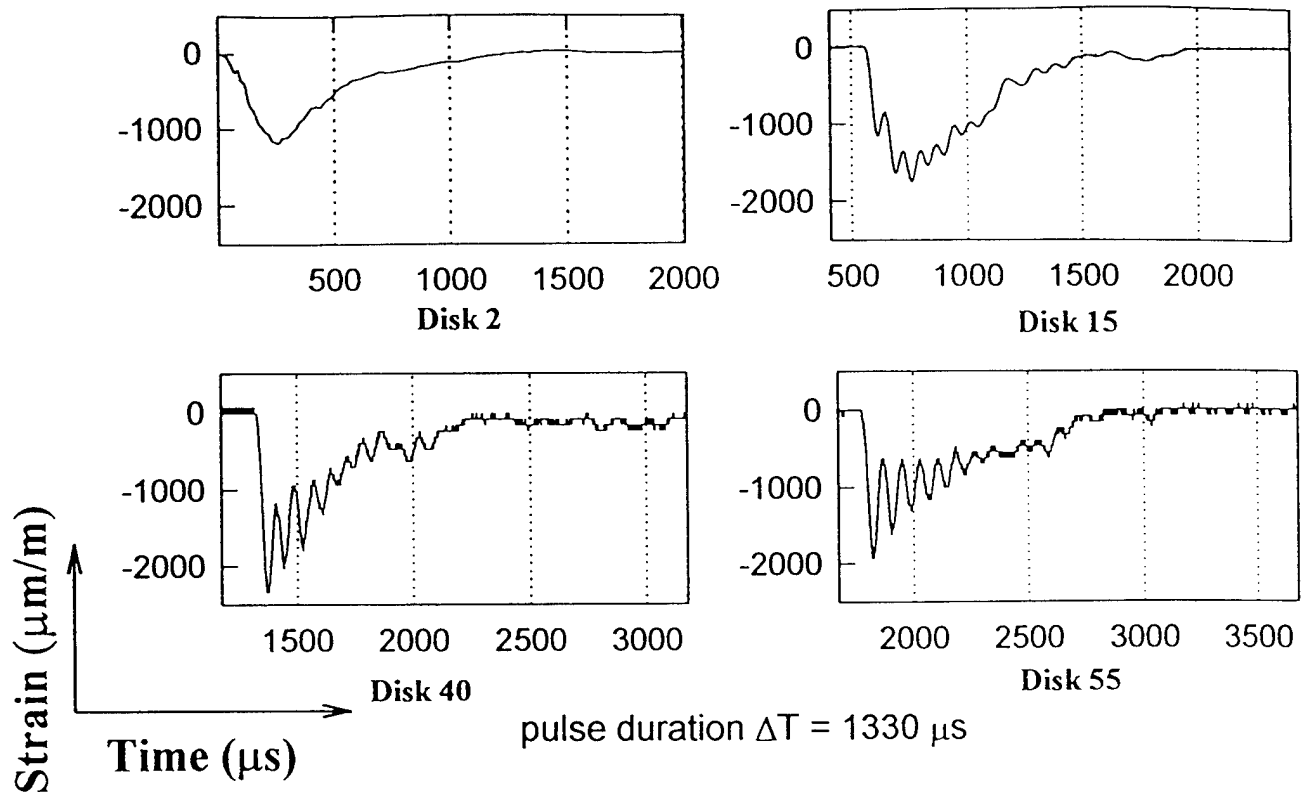
Figure 5.14. Strain pulses as recorded by the gages on different disks.
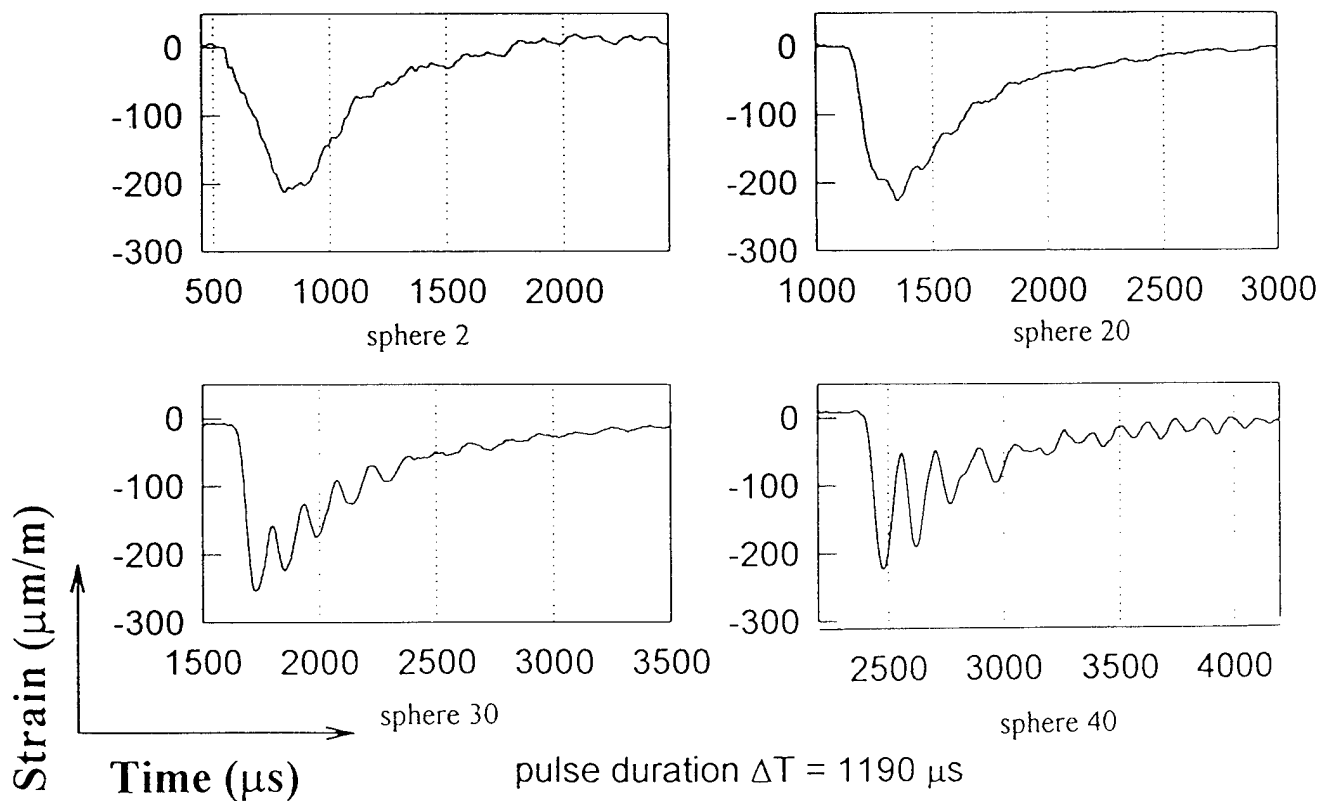
Figure 5.15. Strain pulses as recorded by the gages on different spheres.
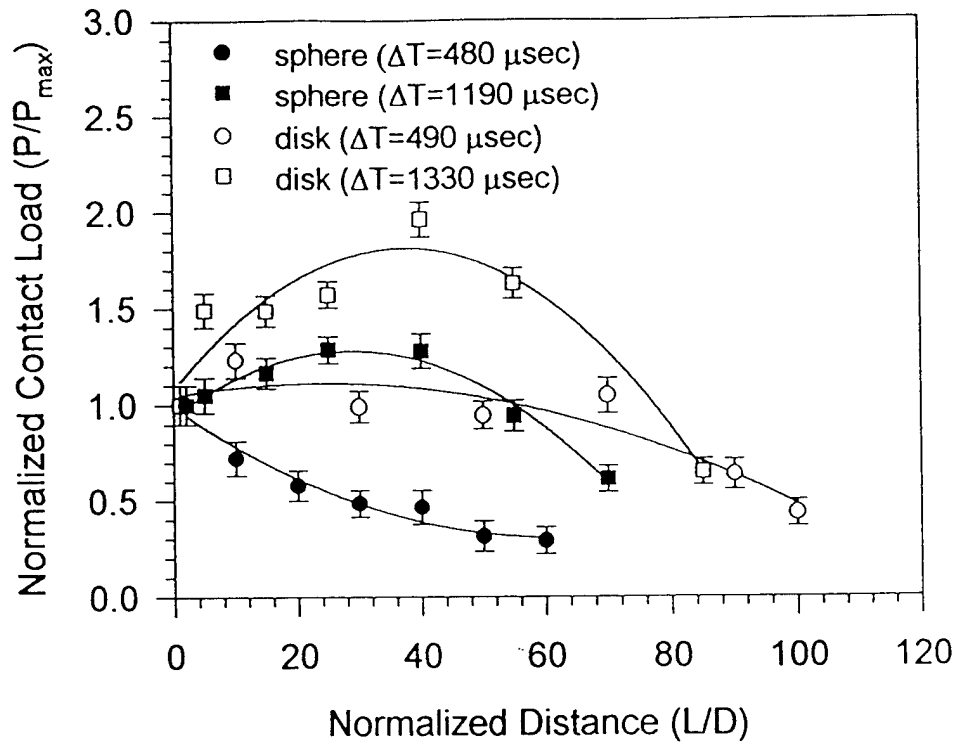
Figure 5.16. Peak contact load attenuation in disk and sphere chains.
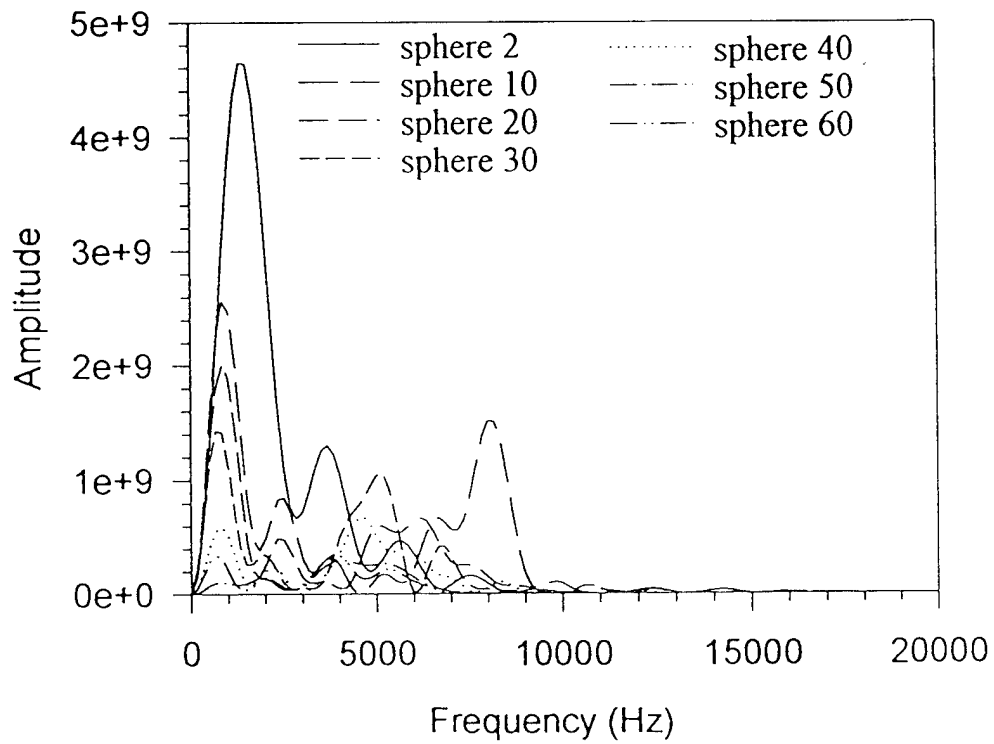
Figure 5.17. Power spectra for strain in sphere chain (input pulse duration ΔT = 480 μs).
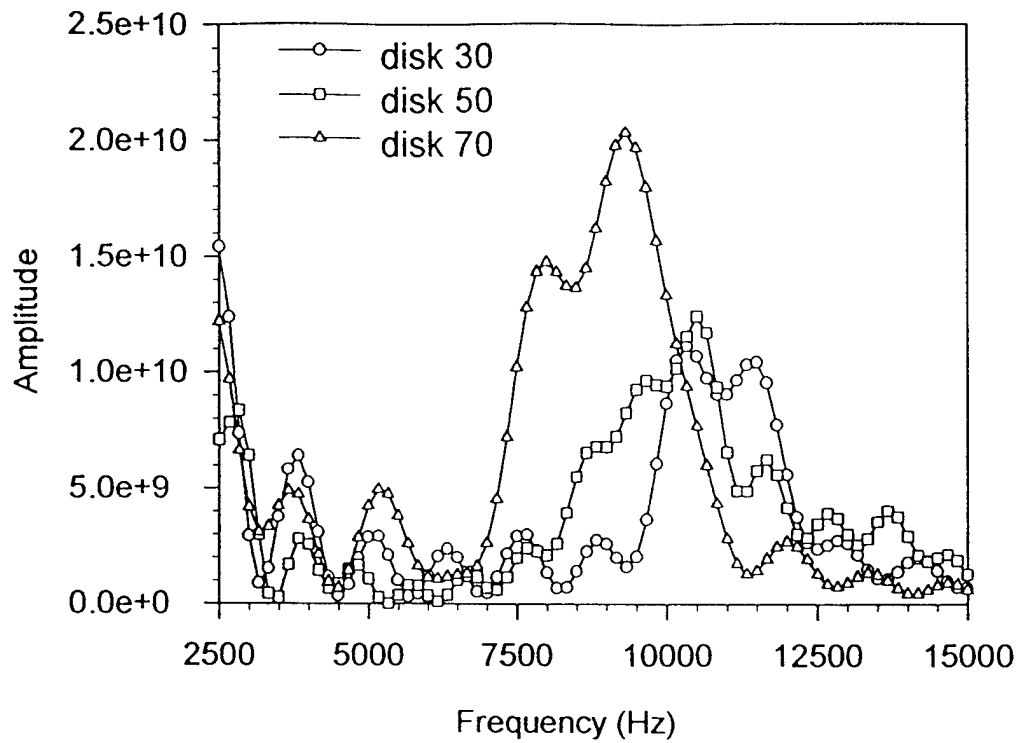
Figure 5.18. High frequency component in disk chain (input Pulse duration ΔT = 490 μs).
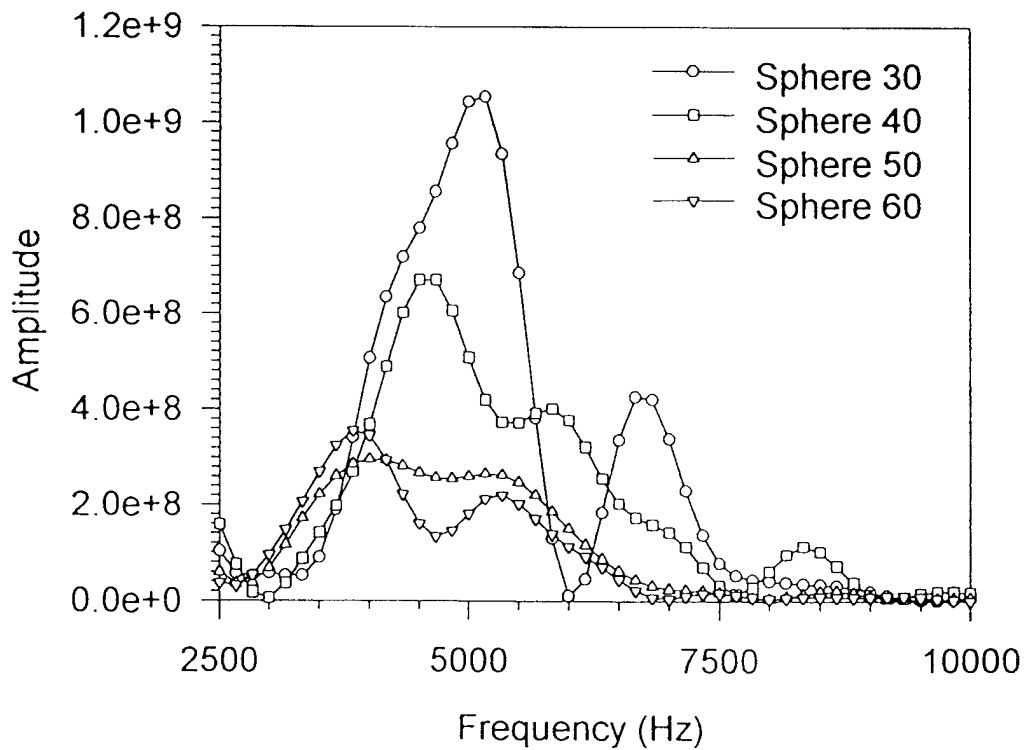
Figure 5.19. High frequency component in sphere chain (input Pulse duration ΔT = 480 μs).

135
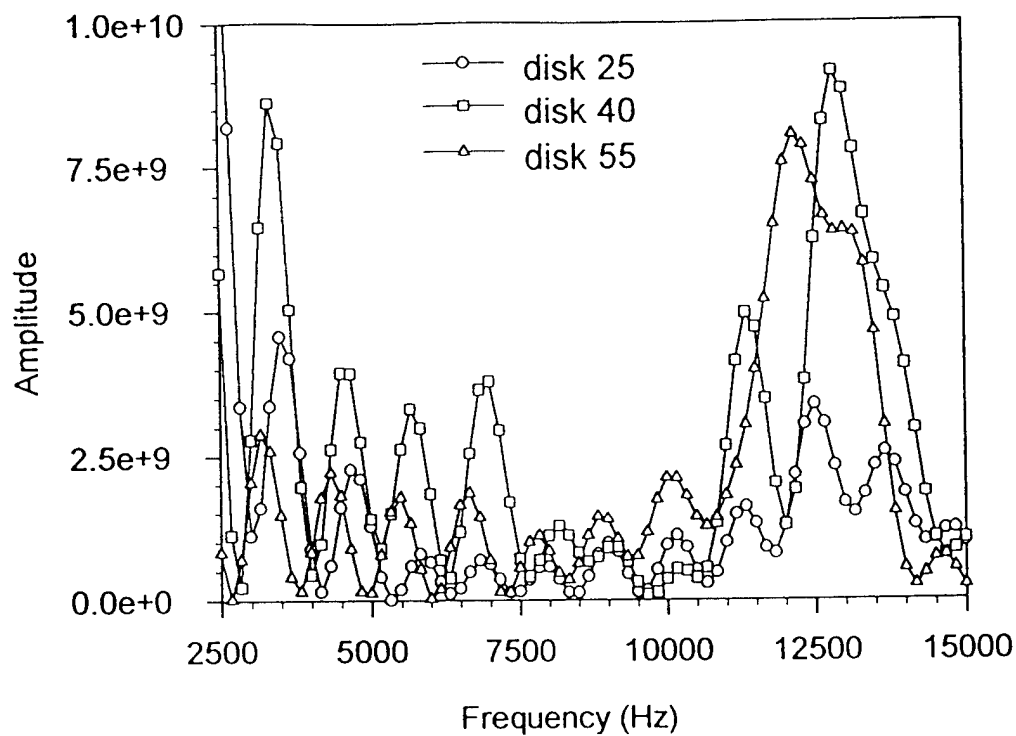
Figure 5.20. High frequency component in disk chain (input Pulse duration ΔT = 1330 μs).
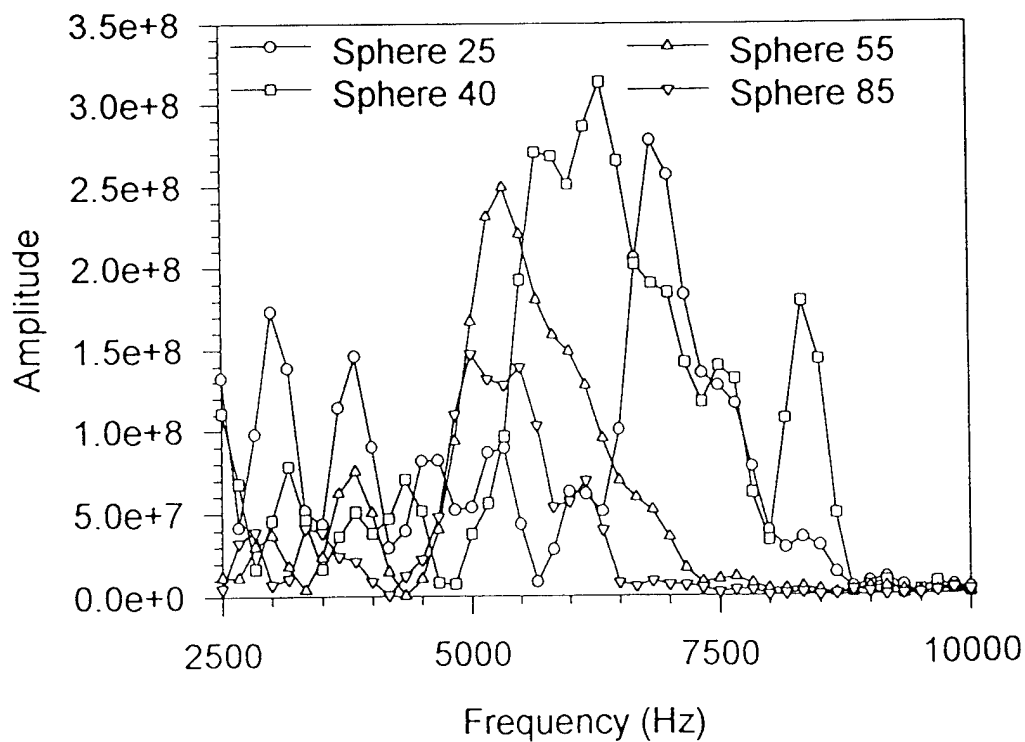
Figure 5.21. High frequency component in sphere chain (input Pulse duration ΔT = 1190 μs).

CHAPTER 6

PRELIMINARY STUDY OF THE EFFECT OF CEMENTATION ON THE DYNAMIC LOAD TRANSFER PHENOMENON

6.1 Summary

The effect of interparticle cementation on dynamic load transfer in granular materials was studied utilizing dynamic photoelasticity in conjunction with high speed photography. Granular assemblies were constructed with cements of various stiffness and circular disks of Homalite-100, a photoelastic polymer. The cementation was placed between individual particles with varying widths and thicknesses. The cemented assemblies were loaded dynamically by means of a small amount of explosive which produced a compressive stress wave. The wave propagated down the assembly and the load transfer as well as the stress field in the cemented particles was captured. Static results, which were confirmed in the dynamic regime as well, indicate that the cement produces different effects on the stress field in the particle depending on the relative stiffness of the cement when compared with that of the particle. Specifically, a stiff cement produces high stress around the edges of the cement region while soft cement produces the highest stresses at the center of the cement region. Additionally, for dynamic wave propagation, stiff cements result in higher average wave speeds while soft cements produce dramatically slower wave speeds. In both cases, stiff and soft cement, there was significant wave reflection at the interface between the cement and the particle primarily due to the acoustic impedance mismatch. Additional preliminary experimentation was conducted to investigate the load transfer behavior through angled cemented contacts. Specifically, load transfer through single chains of particles where each successive particle in the chain alternated between ±15° or ±40° from the vertical. An experiment was conducted where a chain of particles was cemented at 90° from the vertical to determine if, unlike uncemented chains, the stress wave would propagate across the perpendicular contact. The experiments showed that due to the cementation, the wave would propagate across the perpendicular contact. Initially, static experimentation was conducted to characterize the nature of the stress field and a combined experimental/numerical analysis scheme was developed. The scheme allows the extraction of contact load from photoelastic

images of the cemented disks.

6.2 Introduction

This chapter represents a preliminary attempt at studying the effect of cementation on the wave propagation phenomenon. Dynamic wave propagation has been studied in recent years for its importance in such diverse applications as dynamic compaction of powders, shock forming of modern composites, and in various shock absorbing and isolating applications. These studies have primarily looked at the particle to particle interaction of dry contacts. While this may apply to the fore-mentioned applications, the study of seismic phenomenon needs to account for other parameters. One of these parameters is cementation between particles.

In the past, researchers have studied many aspects of load transfer in granular materials (see, e.g., Proceedings of U.S.-Japan Seminar, 1988, Proceedings of IUTAM, 1982, Deformation and Failure of Granular Materials, 1982, and Micromechanics and Inhomogeneity, 1989). These studies have concentrated on the behavior of cohesionless particles with particular emphasis on macroscopic response. Few studies have been conducted to investigate the behavior of granular materials at particulate levels (see, e.g., Oda, et al., 1980, Shukla and Rossmanith, 1982, and Zhu, et al., 1991). When experimentally modeling granular media to study the contact mechanics at the particle level, it is common practice to model the particles as disks. Shukla and Nigam (1985) have shown that when analyzing assemblies of disks with dry contacts, the disk-to-disk contact stress distribution is quite similar to Hertzian theory and a least squares Newton-Raphson scheme can be used to extract the contact load from the photoelastic fringes. This type of assembly, however, does not always adequately describe that encountered in nature. Geological formations commonly contain some type of cementation between the particles that make up the aggregate. Thus if the study of the particle-to-particle interactions is to be applied to geological phenomena, attempts should be made to realistically simulate this media. For these reasons, the effects of cementation on the particle-to-particle interaction has been studied.

Trent (1989) and Trent and Margolin (1992) investigated, numerically, the behavior of cemented granular materials under both low-strain and high-strain loads and showed that the effective properties of the specimens were governed by the inter-granular bond properties

138

and distribution. Later work has shown that the stress distribution between cemented particles in contact does not resemble a Hertz stress distribution (Dvorkin, et al., 1991), as it would for particles without any cementation. The distribution is actually related to the ratio of the stiffness of the cement to the stiffness of the particle. Stiffer cements result in higher stresses at the edges of the cement region while softer cements have higher stresses at the center of the bonded region. Such changes in the stress field have been experimentally verified. Also, a numerical scheme has been developed which combines the theory and the experiments to compute the complete stress field around cemented contacts for normal loading.

6.3 Numerical Analysis

A combined experimental/numerical technique was developed to obtain the complete stress field distribution and the normal loads in cemented granular materials simulated by circular disks. The technique was motivated by the shapes of the stress profiles obtained by using a theoretical model (Dvorkin, et al., 1991). A brief description of this theoretical model and the development of the hybrid experimental/numerical scheme is given below.

For the plane case, the cement layer between two deformable disks is approximated by an elastic foundation, where the contact region has been assumed to be small compared to the disk so that the stress distribution in the disk is close to that of a half-plane.

Normal displacements of the disk surface, $v(x)$, are related to normal stress, $p(x)$, as (Johnson, 1985)

$$v(x) = \frac{1 - v}{\pi G} \int_{-a}^{a} p(s) \ln|x - s| \, ds + const ,$$ (6.1)

where v is the disk's Poisson's ratio, G is the shear modulus, and x is a coordinate along the contact interface.

The displacement of the center of the disk relative to the median plane of the cement layer, δ, can be related to the displacements of the surface of the cement layer, V, and of the surface of the disk, v, as

$$\delta = v(x) - V(x) .$$ (6.2)

It was shown in Dvorkin, et al. (1991) that a thin cement layer can be accurately approximated as an elastic foundation and therefore normal stresses, p, acting on the surface of the disk are related to the displacements of the surface of the cement, V, as

$$p(x) = -\frac{2\,G_c\left(1 - v_c\right)}{1 - 2\,v_c}\frac{V(x)}{h(x)} \; , \tag{6.3}$$

where G_c, v_c, and h are the shear modulus, Poisson's ratio, and half-thickness of the cement, respectively (Figure 6.1).

Assuming that shear stresses at the disk surface do not significantly influence its normal deformation (Johnson, 1985), equations (6.1)-(6.3) can be combined into an integral equation :

$$V(x) = \Gamma \int_{-a}^{a} \frac{V(s)}{h(s)}\ln|x - s|\, ds \; + \; const \; ,$$

$$\Gamma = \frac{2G_c}{\pi G}\frac{\left(1 - v\right)\left(1 - v_c\right)}{1 - 2v_c} \; . \tag{6.4}$$

The constant in the right hand side can be found using the condition of a given integral compressional force per unit length, F, of an elastic cylinder:

$$F = -\frac{2G_c\left(1 - v_C\right)}{\left(1 - 2v_c\right)}\int_{-a}^{a} \frac{V(s)}{h(s)}ds \; . \tag{6.5}$$

Equation (6.4) can be solved using the quadrature method.

Since the theoretical model requires the applied load to be known a priori, a method was sought which would extract the applied load from supplied experimental data. The combined experimental/numerical technique utilized the stress distribution profiles obtained using the theoretical method described above. It was assumed that stress distribution curves could be represented by a family of polynomials containing parameters that would provide the appropriate shape for given material parameters. Several distributions were used ranging from convex parabolic to concave parabolic. All these curves could be represented by the

140

polynomial

$$f(\phi) = F_c \left[1 + (m - 1) \left(\frac{\phi}{\alpha} \right)^n \right],$$

(6.6)

where F_c is the force per unit length at the center of the cement region, m is the ratio of the central force to the force at the edge of the cement region, ϕ is the angle which defines the position at which the stress is being applied, α is the angle which defines the edge of the cement region, and n is a fitting parameter.

The hybrid scheme utilizes the distributed loading, $f(\phi)$, given by equation (6.6) combined with the experimental technique of photoelasticity through the governing stress-optic law. The resulting equations are solved using the Newton-Raphson procedure coupled with the non-linear least squares technique (Shukla and Nigam, 1985).

Classic elasticity theory (Timoshenko and Goodier, 1970) gives the stress field for the plane problem of a disk loaded with a pair of equal and opposite edge forces, p, as depicted in Figure 6.2. The results are

$$\sigma_x = -\frac{2p}{\pi} \left[\frac{\sin^2(\theta_1)\cos(\theta_1)}{r_1} + \frac{\sin^2(\theta_2)\cos(\theta_2)}{r_2} \right] + \frac{p}{\pi R}\cos(\phi) \ ,$$

$$\sigma_y = -\frac{2p}{\pi} \left[\frac{\cos^3(\theta_1)}{r_1} + \frac{\cos^3(\theta_2)}{r_2} \right] + \frac{p}{\pi R}\cos(\phi) \ ,$$

(6.7)

$$\tau_{xy} = \left[\frac{\sin(\theta_1)\cos^2(\theta_1)}{r_1} - \frac{\sin(\theta_2)\cos^2(\theta_2)}{r_2} \right] .$$

where the equation parameters are also given in Figure 6.2.

Using superposition, the edge loading can be integrated to determine the interior stress for a distributed loading, $f(\phi)$. The results yield equation (6.8).

$$\sigma_x = \int\limits_{-\alpha}^{\alpha} \left\{ -\frac{2f(\phi)}{\pi}\left[\frac{\sin^2(\theta_1)\cos(\theta_1)}{r_1} + \frac{\sin^2(\theta_2)\cos(\theta_2)}{r_2}\right] + \frac{f(\phi)}{\pi R}\cos(\phi)\right\}Rd\phi \; ,$$

$$\sigma_y = \int\limits_{-\alpha}^{\alpha} \left\{ -\frac{2f(\phi)}{\pi}\left[\frac{\cos^3(\theta_1)}{r_1} + \frac{\cos^3(\theta_2)}{r_2}\right] + \frac{f(\phi)}{\pi R}\cos(\phi)\right\}Rd\phi \; ,$$

$$(6.8)$$

$$\tau_{xy} = \int\limits_{-\alpha}^{\alpha} \left\{ \frac{2f(\phi)}{\pi}\left[\frac{\sin(\theta_1)\cos^2(\theta_1)}{r_1} - \frac{\sin(\theta_2)\cos^2(\theta_2)}{r_2}\right]\right\}Rd\phi \; .$$

Coupling these equations to the experimental data was accomplished through the use of the governing stress-optic law. The resulting equation is (6.9), where f_σ is the material stress optic coefficient, N is the fringe order, and h is the material thickness. The maximum shear stress, τ_{max}, can be computed from the photoelastic data and what remains is to solve for the parameters that define the force distribution, $f(\phi)$.

$$\tau_{max} = \sqrt{\left(\frac{\sigma_x - \sigma_y}{2}\right)^2 + \tau_{xy}^2} = \frac{Nf_\sigma}{2h} \; . \qquad (6.9)$$

A number of data points obtained from the photographic images gave an over determined system of equations which were used to compute the appropriate values for F_c, m, and n. Here we used a set of correction factors for each of the parameters. The correction factors were used to improve the accuracy throughout the iterative process.

Equation (6.6) describes the force distribution at the face of the disk which was then integrated to find the total applied load:

$$P_r = 2\int_0^\alpha f(\phi)Rd\phi = 2F_c\alpha R\frac{m + n}{n + 1} \, . \qquad\qquad (6.10)$$

Lastly, we used either the set of stresses acting on the face of a disk or an expression for the stress distribution on the face to numerically generate the set of corresponding fringes. The disk was reduced to a grid of coordinate points and τ_{max} was computed for each point. Using equation (6.9) and the computed value of τ_{max}, all coordinate pairs that yielded an integer value of fringe order, N, were determined and plotted.

6.4 Experimental Procedures

The method of photoelasticity was used to obtain full field stress information in the particles. Specimens were loaded in static diametrical compression and photographs were taken of the resulting fringe patterns at various load levels. Disks were machined from PSM-1, a photoelastic material which becomes birefringent when stressed. To simulate stiff cements between the disks, aluminum and acrylic pieces were machined to match the disk radius. For a soft cement, urethane was cast between the disks. Disk diameters were machined to 76 mm to allow for clarity of the fringe patterns close to the contact region. Cement widths were 16mm for the urethane and 18.5 mm for the aluminum and the acrylic. Figure 6.3 shows the specimen geometry used. Initially these experiments were conducted using Homalite-100 disks with a diameter of 31.75 mm and a cyanoacrylate adhesive with a bond length of 3 mm. The high fringe density near the contact region facilitated the change to the larger diameter disks. However, the data from these early experiments has been included in the results. The Young's moduli and the Poisson's ratios for the disk material and the cements are listed in Table 6.1.

In the cases of the aluminum and the acrylic cements, the pieces were machined from stock material and then the machined pieces were bonded to the disks. The radius was carefully machined to match the disk radius and the bonding agent was Measurements Group's PMC-1 special purpose adhesive. The adhesive is formulated for bonding complex photoelastic models and has an elastic modulus almost identical to that of PSM-1 (2.9 GPa for the adhesive and 2.6 GPa for the model material).

In the early experiments, a drop of the cyanoacrylate based adhesive was placed

143

between the disks and allowed to cure overnight. The width of the cement was controlled by the size of the drop placed between the disks. The urethane cement was manufactured by Hexcel and was made by mixing a hardener and a resin. The disks were placed onto a plastic sheet and a mold cavity of the appropriate shape was formed between them. Liquid urethane was poured into the cavity and allowed to cure according to the manufacturer's instructions.

As mentioned, the specimens were loaded statically and photographs were taken at various load levels. The loading took place on an Instron loading machine and the specimens were photographed through a light field circular polariscope. A loading frame was used to prevent buckling of the assembly during the loading. Notice in the photographs to follow that there are no fringes originating from the boundaries that would signify that the specimens were experiencing edge loading due to the presence of the fixture.

Following the static experiments, dynamic experiments were begun where the cementation procedures followed those in the static case. The dynamic experiments were conducted for smaller particles and the cementation scaled accordingly. A single chain of 25 mm diameter cemented particles was placed in the optical bench of the camera and an explosive charge was detonated to initiate the stress wave. The resulting twenty photographs of the propagating wave were analyzed to obtain average group wave velocity and pulse length. Both of which can be directly measured from the photographs.

During the course of the experimentation, the cement stiffness was varied from very soft with respect to the disk material, to very stiff. Also, the width of the cement region was varied to a maximum of approximately one fourth the disk diameter. As with the static experiments, stiffness variations were accomplished by means of casting from a liquid resin, or machining from stock material and bonding.

6.5 Results and Discussion

6.5.1 Static Loading

The theoretical model (Dvorkin, et al., 1991) gives the normal stresses on the face of a disk which were used to generate fringe patterns in it. Figure 6.4 shows the theoretical fringe patterns compared to the actual experimental photograph. The theoretical fringe patterns correspond to stresses that are slightly smaller than those found experimentally (10% difference). By increasing the theoretical input load by 10% we obtained a close match

144

between the theory and the experiment. The theoretical model was able to reconstruct the stresses in the disk reasonably well, however, the technique requires prior knowledge of the applied load.

The combined experimental/numerical technique was used to compute the net contact load for a number of different types of cement. These loads are shown in Table 6.2 along with the experimental data. This table represents experiments covering a variety of cement/disk combinations with stiffness ratios ranging from 0.001 (urethane cement) to 20 (aluminum cement). Comparison with the measured values shows that in all cases the relative error was less than 10% . The computed value for the contact load was practically insensitive to the fitting parameter, n. The fitting parameter was actually more critical to the resulting fringe pattern produced. For this reason, n was fixed as an input value and the computer program found F_c and m. Once these parameters were determined, n was iterated from the fringe pattern produced by the computed data. It was found that a good starting point was n=4. After allowing the code to solve for F_c and m, the resulting fringe pattern was generated and compared to the experimental photograph and n was adjusted if necessary.

Figure 6.5 shows a plot of the normalized force along the cement/disk interface as predicted by the theoretical model, for the case shown in Figure 6.4, using the experimental load value and the approximation for the actual experimental load, and for one increased by 10%. The results from the combined experimental/numerical approximation are also shown (solid line). The figure shows good agreement for more than 60% of the contact region and although the plots deviate toward the outer edge of the cement region, integration of the curves reveals that the net loads predicted by both schemes differ by less than 5%.

The iteration scheme for determining the parameter n involved plotting the fringe pattern resulting from the computer generated solution using values of F_c, m and the input value of n. If the pattern did not match the experimental photograph, n was changed slightly and the fringes were generated again. This iterative scheme is nothing more than slightly modifying the computer simulated applied load. If F_c and m are held constant and n is changed in the fringe generation program, the result is that the area under the force distribution curve is changed. By increasing n, the net load is decreased, and by decreasing n, the net load is increased. Figure 6.6 shows this as a plot of normalized force distribution along the cement for various values of n. So, after looking at the first estimate of fringes, one can determine

whether the net load needs to be adjusted slightly upward or downward.

Figure 6.7 shows the case where the cement material was acrylic. The stiffness ratio (E_{cement}/E_{disk}) between the cement and the disk in this case is about 1.4. The figure shows the first iteration for n=3. One can easily see that the computer generated fringes represent a load that is slightly lower than the fringes in the experimental photograph represent. The parameters were used in equation (6.10) and the computed loads are also shown in the figure. The first iteration of load produced a value of 585 N which did not match the experimental photograph. The value of n was changed to 4 and the fringes were regenerated. This produced a net load of 513 N and the fringe pattern matched quite well. The next iteration shows the fringe pattern for n=4.5. This is clearly an underestimate of n because the τ_{max} fringes are not of high enough order when compared to the experiment.

Figure 6.8 shows the experimentally obtained photoelastic fringes for the case where aluminum was used as the cement material, along with the fringes obtained by utilizing the computer algorithm. The fringe patterns match reasonably well at n=4. In this case, the stiffness ratio between the cement and the disk material is approximately 25. Note that this is the same case as that shown in Figure 6.4 where the experimental photograph was compared to the results from the theoretical model.

6.5.2 Dynamic Loading

Figure 6.9 shows typical photographs of two different 25 mm diameter cemented disk chains as the dynamic wave propagates. The photographs show that there is a considerable amount of energy reflected at each of the contacts due to the acoustic impedance mismatch between the disk material and the cement material. Figure 6.9 a.) shows the case of an aluminum cement while 6.9 b.) represents the other extreme with a urethane cement. The group wave velocity was determined by measuring the position of the wave front at various times and plotting the distance propagated versus time. For the two cases shown in Figure 6.9, the velocities were found to be approximately 1600 and 300 m/s, respectively.

Figure 6.10 shows the plot for a number of nearly identical single chain experiments of cemented particles with a small amount of cyanoacrylate adhesive. The average velocity for these cases was determined to be 1240 m/s. This is higher than the reported velocity for a single chain of particles without cementation by approximately 20%. The velocity for

146

particles without cementation was found to be 1050 m/s.

The effect of cement width with respect to the particle diameter was investigated for two different cements and it was discovered that as the cement width increases, the group wave velocity also increases. Figure 6.11 shows a plot of normalized group wave velocity as a function of cement width. The plot shows that the velocity increase appears asymptotic to about 75 percent of the P-wave velocity in continuous Homalite-100. Cement width was varied from zero to approximately 0.35 times the disk diameter.

Experiments were also conducted with the particles staggered from the vertical, by some angle, α. Figure 6.12 shows the particle arrangement for the staggered configuration. To date, only two different angles, $\alpha = 15°$ and $\alpha = 40°$, have been used in the experiments. Figures 6.13 and 6.14 show the typical isochromatic fringes obtained using these particle arrangements. The cement used was a cyanoacrylate based adhesive with a fixed width of approximately 0.13 times the disk diameter.

The wave speeds have been determined and are shown in Figure 6.15. These velocity measurements represent the vertical velocity of the wave front as it propagates in the chain. Since the data only represents a few experiments, the reported velocities are still considered estimates. The trend however would lead one to believe that the greater the angle, the lower the wave velocity. It is difficult to discuss pulse length in terms of particle diameters but it is easy to see that the pulse is loading approximately 6 particles in Figure 6.13, the 15° angle case, and 5 particles in Figure 6.14, the 40° angle case.

Notice that there was energy still propagating in the particles (this is most noticeable for the 40° angle case) after the main pulse had passed. This energy is due to reflections taking place in the particles and presumably would lead to greater attenuation of the pulse. Evidence of this can be seen in Figure 6.14. The magnitude of the fringe orders seen in the photographs decreases dramatically as the loading pulse travels down the chain. As complete confidence in the current analysis technique for dynamic analysis has not yet been established, no load data will be presented at this time.

Another set of experiments, still in the preliminary stages, is the investigation of stress wave propagation at angles of 90° and greater from the incident wave direction. The particles in these experiments were cemented together. Figure 6.16 shows typical isochromatic fringes from such an experiment. Note that in previous work from this laboratory (Shukla et. al.,

1988) the wave would not propagate at angles of 90° or greater using uncemented particles.

Figure 6.16 shows that energy does indeed transfer to the particle chain that is at a right angle to the incident pulse. A careful look at these photographs reveals that damage growth has begun in the first disk in the right angle chain. The stress on the contact is almost entirely shear stress and the damage originates at the edge of the cementation zone. The origin of the damage coincides well with the numerical predictions made by Dvorkin (1991) with regard to the maximum stress location for a cemented contact.

Velocity measurements were also made for the pulse propagating in the near vertical straight chain and it was found that the ratio of cementation width to particle radius, w/r, also has an effect on the velocity of the pulse. The velocity was found to be higher in this straight chain (w/r = 0.12), approximately 1330 m/sec, than that of the previous straight chain (w/r = 0.10), 1240 m/sec. The difference between the two chains was that the ratio, w/r, was higher in the chain with the higher velocity. Further experimentation will be done to explore this phenomenon.

6.6 Conclusion

A hybrid experimental/numerical scheme has been developed to compute the complete stress field within cemented particles subject to normal loads. The method combines a theoretical solution of the problem with the experimental technique of photoelasticity. The resulting over-determined set of equations are solved using the Newton-Raphson method and non-linear least squares techniques. In the analysis, the stress distribution between the center and the edge of the cement bond is approximated with a power law equation. Excellent agreement, within 10%, between the experimental and computed contact loads has been shown. In addition to the contact load, the entire stress field in the particle can also be reproduced with reasonable accuracy.

The results of this investigation have shown that contact stresses and contact loads for a disk under diametric compression with cementation present at the contact can be determined from either an a priori knowledge of the net confining load or simply the photoelastic fringes. As yet this does not hold true for the dynamic regime. The nature of the stress field around the cement region qualitatively matches that seen in the static regime. However, the whole stress field in the particle is not so easily described and therefore, the

coupling of the photoelastic fringes to the stress field equations through the stress optic law is less than perfect. The combined experimental/numerical computer algorithm helps determine the net confining load for either the case where the cement was stiff compared to the disk material or where the cement was much softer than the disk material. The theoretical stress distribution reproduces the experimental fringe contours with high accuracy.

Cementation proved to have an impact on the nature of wave propagation phenomenon. The velocity of the group wave as compared to uncemented contacts increased by approximately 20%, for vertical chains of particles. The effect seen on the group wave velocity would seem to be consistent with the physical changes made to the medium. The cementation is bringing the particulate medium closer to a continuous medium and the wave velocity is increasing accordingly.

The change in the pulse length, when compared to uncemented particles, needs to be explored further. Long chain experiments with strain gages will be conducted to determine the entire effect.

The effect of contact angle, while not complete, would seem to indicate that the angle affects the velocity, the pulse length, and the load attenuation. One possible explanation for the changes to the velocity and attenuation is that the pulse undergoes more scattering and dispersion upon encountering particle boundaries.

Table 6.1. Material properties for the disk and the cements.

	PSM-1 (disk)	Aluminum	Acrylic	Urethane
Young's Modulus (GPa)	2.6	72.0	2.8	3.0
Poisson's Ratio	0.38	0.33	0.38	0.46

Table 6.2. Comparison of the experimental and numerical determinations of contact load.

| Experimental and Numerical Load Determination for Various Cement Types											
Urethane			Super Glue			Acrylic			Aluminum		
Exp (N)	Num (N)	Err (%)	Exp (N)	Num (N)	Err (%)	Exp (N)	Num (N)	Err (%)	Exp (N)	Num (N)	Err (%)
200	192	4.0	267	268	0.3	91	97	6.0	95	100	4.3
222	217	2.4	690	642	7.0	134	138	3.0	191	204	6.5
			1291	1293	0.2	181	191	5.1	270	293	8.5
			1389	1387	0.1	225	221	1.7	357	380	6.6
			1772	1811	2.2	270	280	3.6	447	481	7.5
			1905	1968	3.3	314	332	6.0	537	573	6.6
			2226	2367	6.3	359	378	5.3	629	646	2.8
						407	422	3.8	722	751	4.1
						448	453	1.2	812	855	5.4
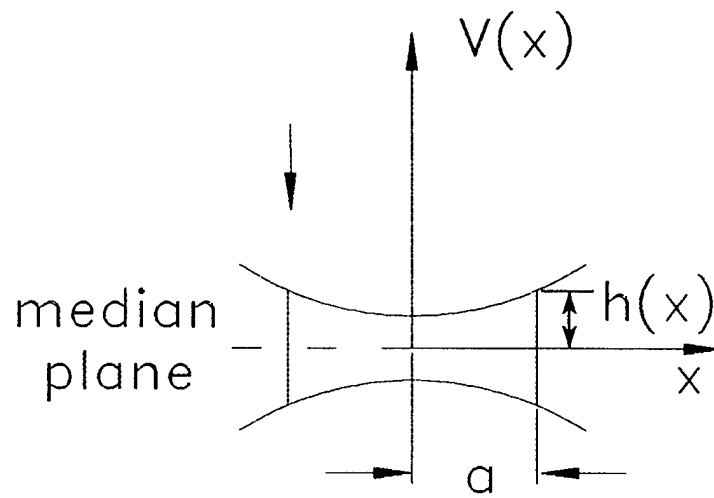
Figure 6.1. Geometry for theoretical analysis.
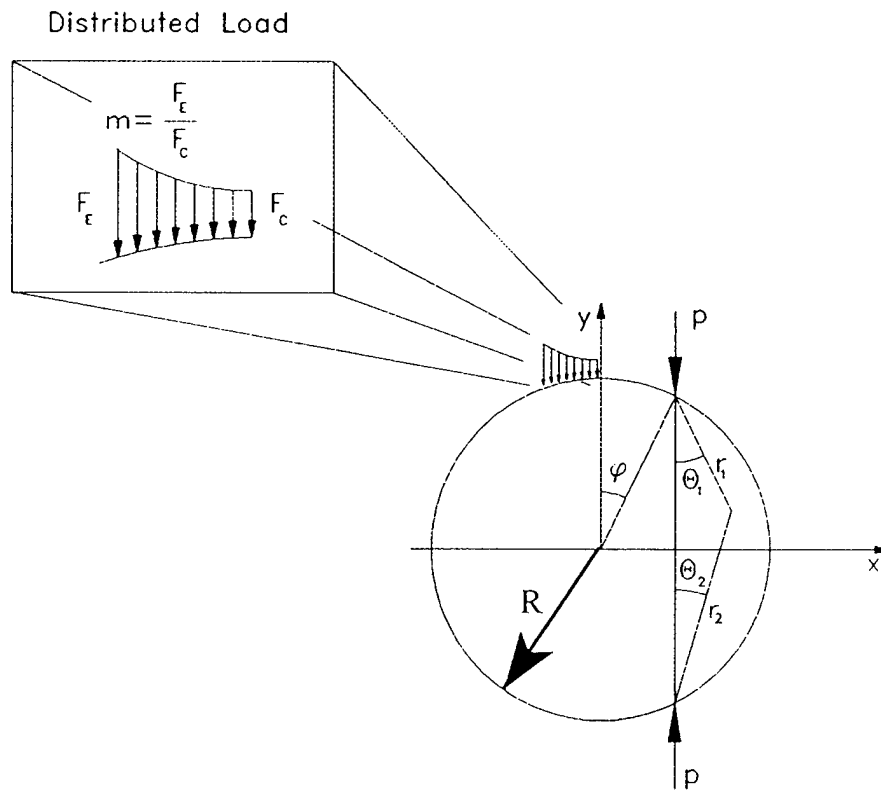
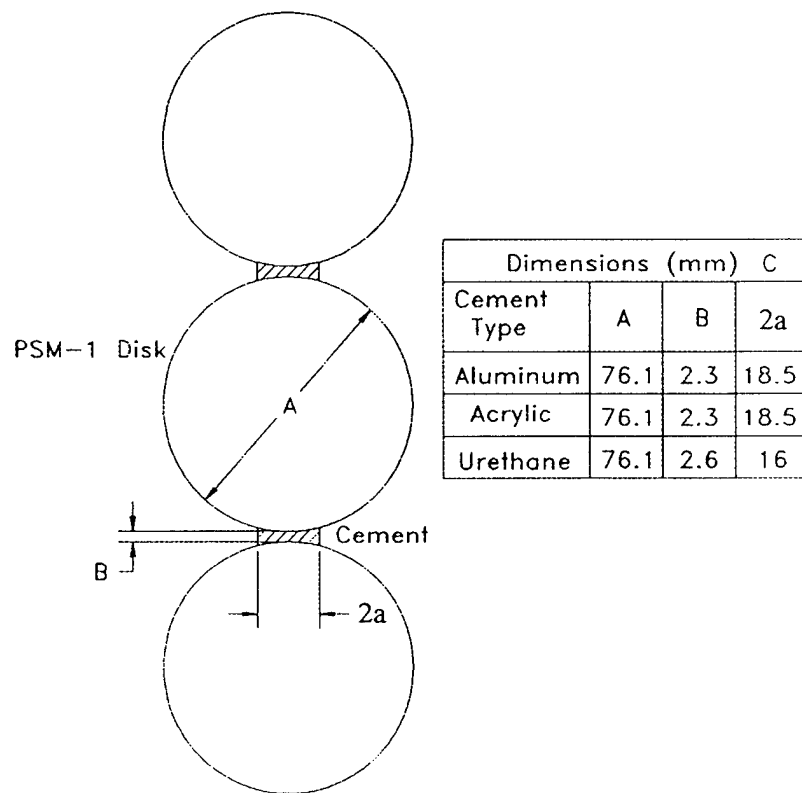Figure 6.2. Disk loaded with opposite edge forces showing variables used for analysis.

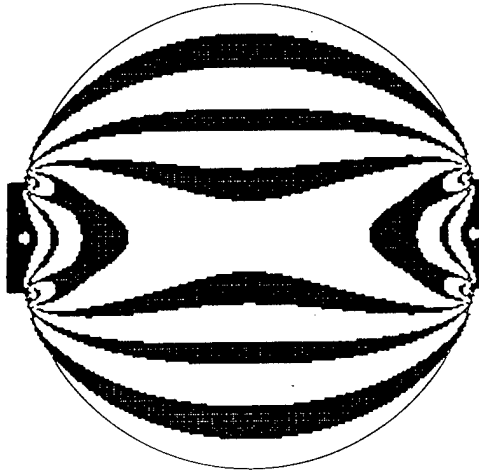| Dimensions (mm)			C
Cement Type	A	B	2a
Aluminum	76.1	2.3	18.5
Acrylic	76.1	2.3	18.5
Urethane	76.1	2.6	16

Figure 6.3. Specimen geometry for the static diametral compression of disks with cement at the contact.

Computer Generated

Experimental Photograph

Experimental Load

Experimental Load + 10%

Figure 6.4. Photograph of experimental fringe contours for the case with aluminum cement and the fringe contours produced by the theoretical model for both the experimental load and the experimental load plus 10%.
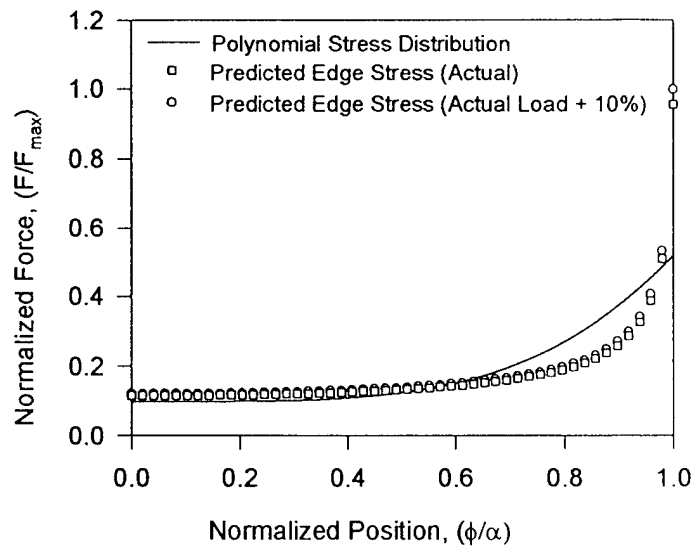
Figure 6.5. Edge predictions from the theoretical model and the combined experimental/numerical technique.
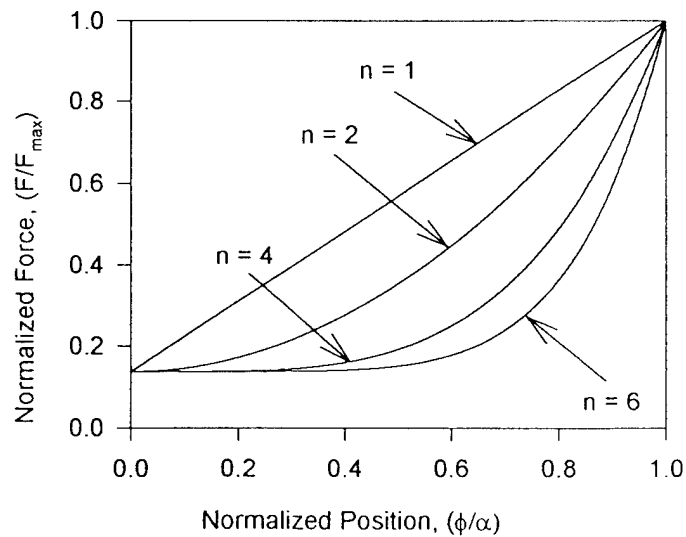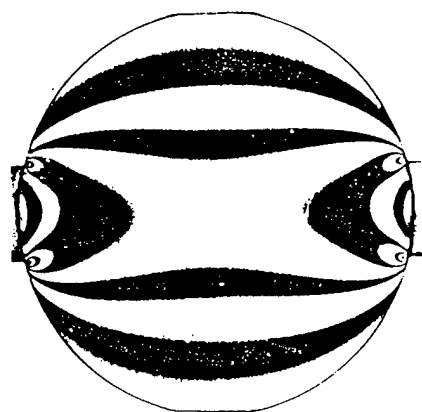

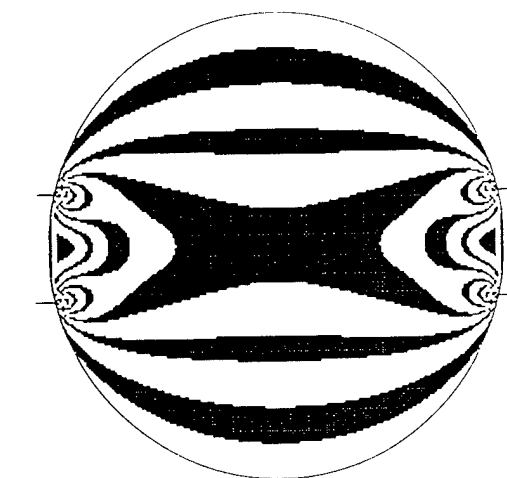Figure 6.6. Normalized force versus position for various values of the parameter n.

154

Experimental Photograph

Load=448 N

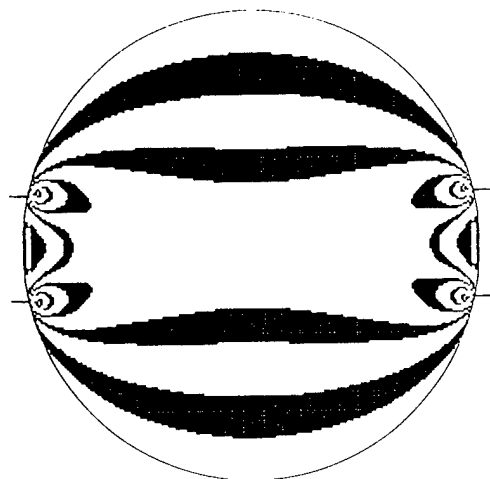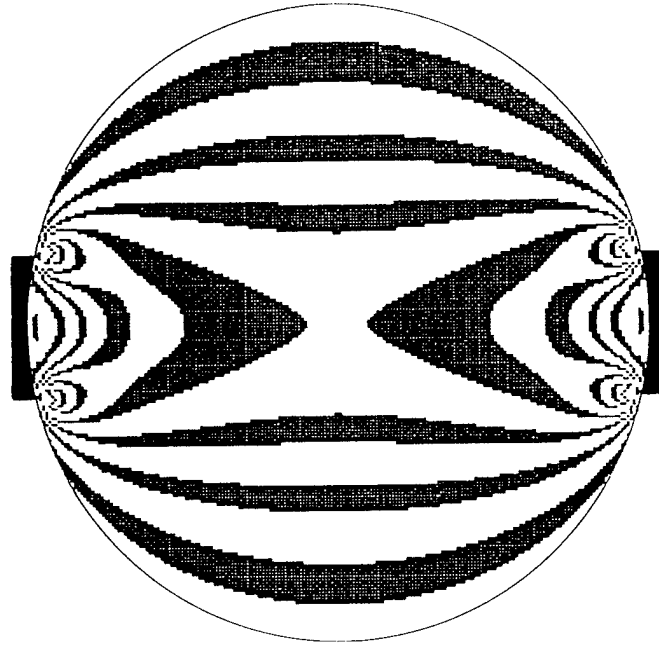**Computer Generated**

Load=487 N
n=4.5

Load=513 N
n=4

Load=585 N
n=3

Figure 6.7. Photograph of experimental fringe contours for the case with acrylic cement and the contours predicted by the combined experimental/numerical scheme illustrating the iteration of the parameter n.

Computer Generated

Load=780 N
n=4

Experimental Photograph

Load =722 N

Figure 6.8. Photograph of the experimental fringe contours for the case with the aluminum cement and the contours predicted using the combined experimental/numerical scheme where no iteration of n was required.

↓Explosive

| Frame 1 84 μsec | Frame 5 108 μsec | Frame 10 131.5 μsec | Frame 12 152 μsec | Frame 20 265 μsec |

b.)

↓Explosive

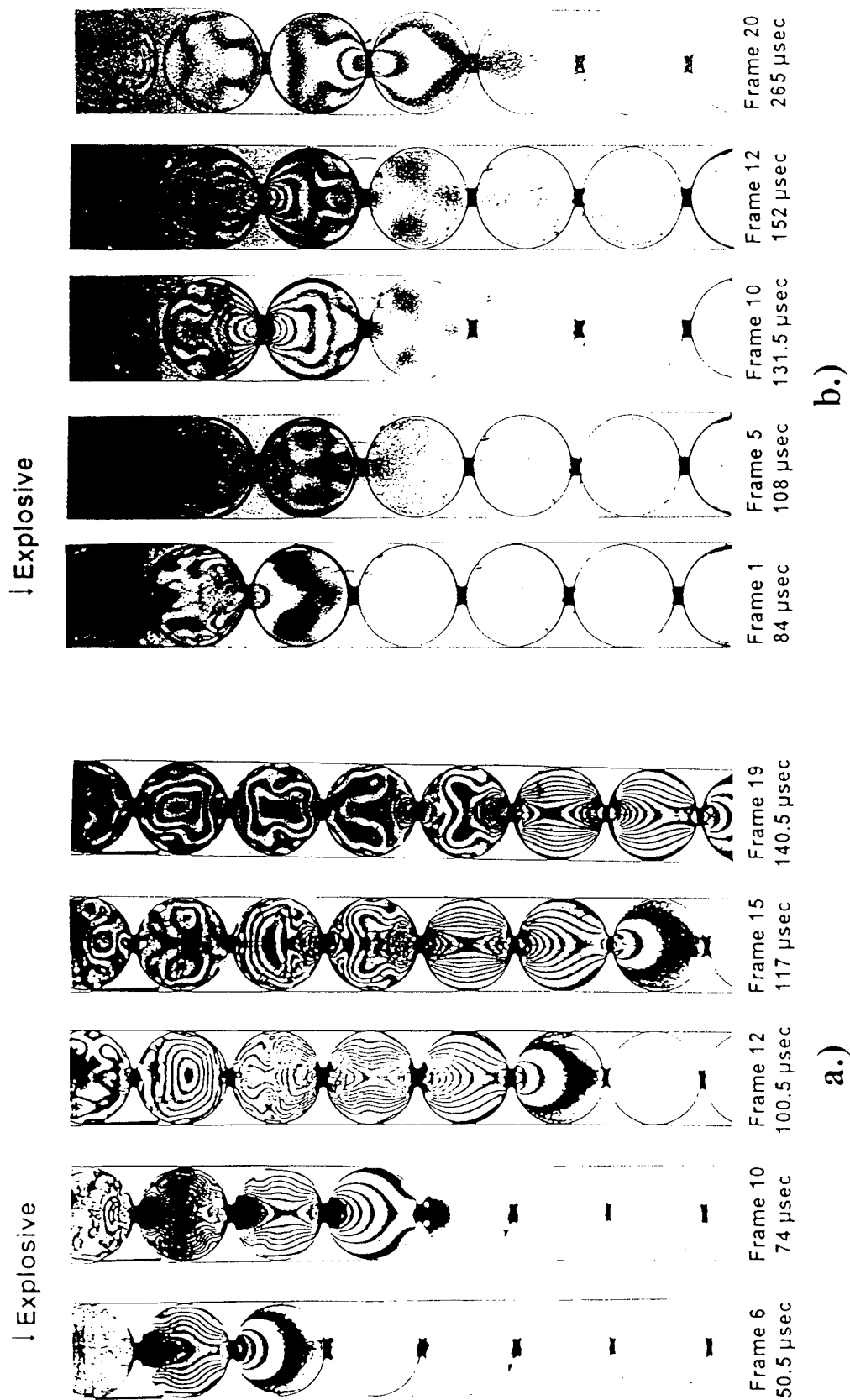| Frame 6 50.5 μsec | Frame 10 74 μsec | Frame 12 100.5 μsec | Frame 15 117 μsec | Frame 19 140.5 μsec |

a.)

Figure 6.9. Typical isochromatic fringe patterns obtained from dynamic experiments with H-100 particles and a.) an aluminum cement, b.) a urethane cement.
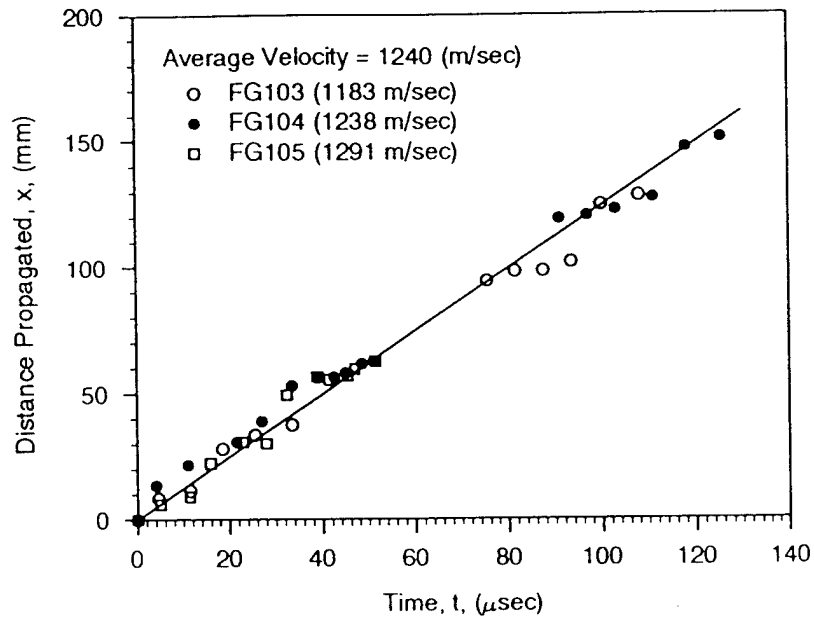
157

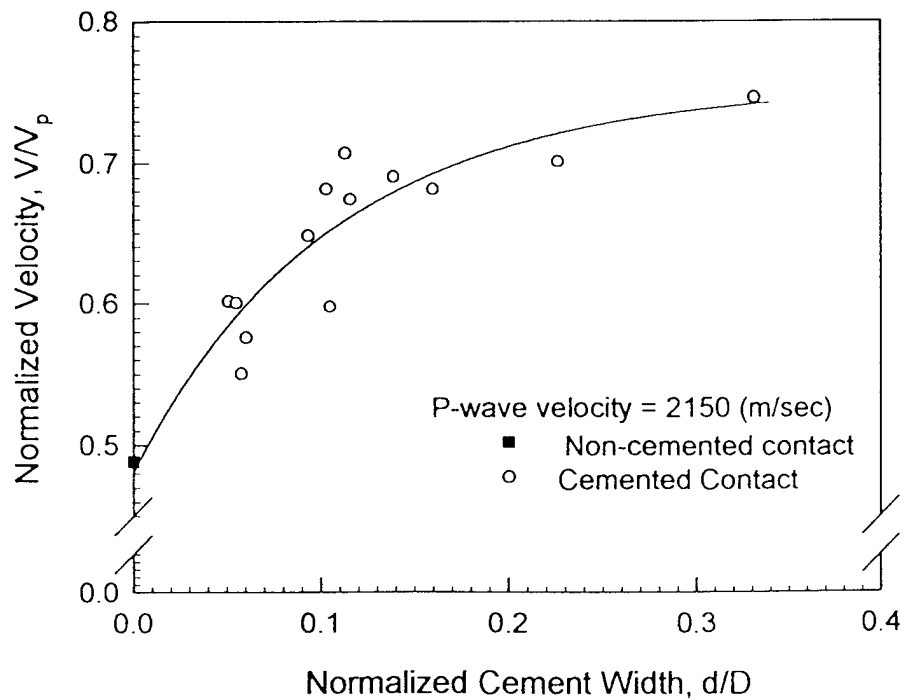Figure 6.10. Distance versus time plot for determination of group wave velocity.

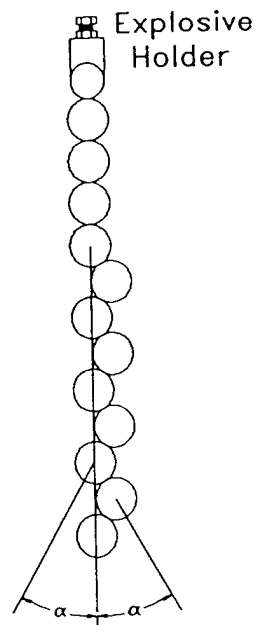Figure 6.11. Plot of normalized group wave velocity as a function of cement width.

Figure 6.12. Schematic of the disk chain used for the cemented, angled contact experiments.
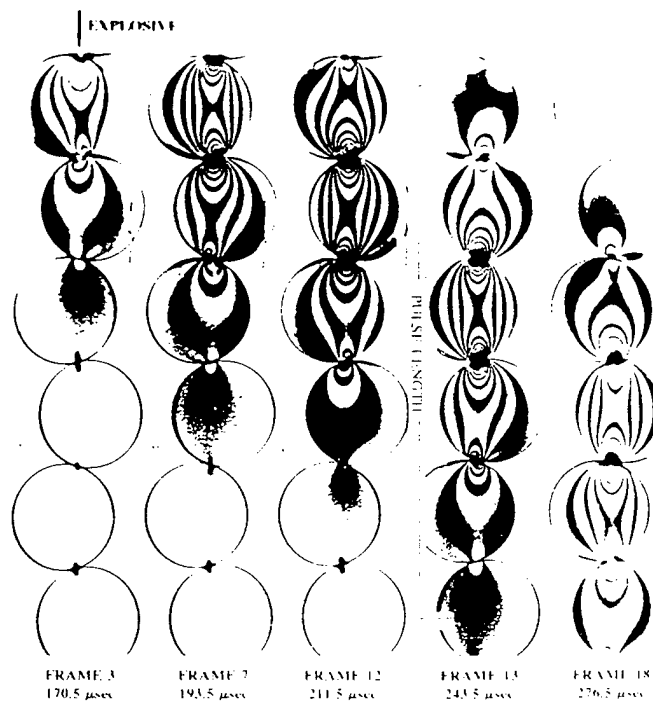

Figure 6.13. Typical isochromatic fringes obtained from a single, 15° angle chain of particles.
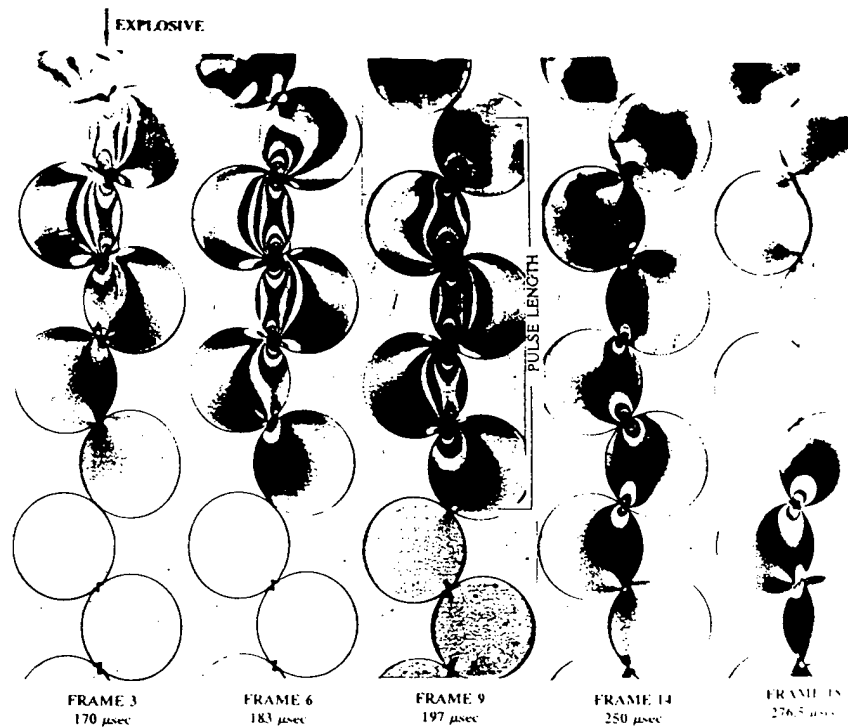
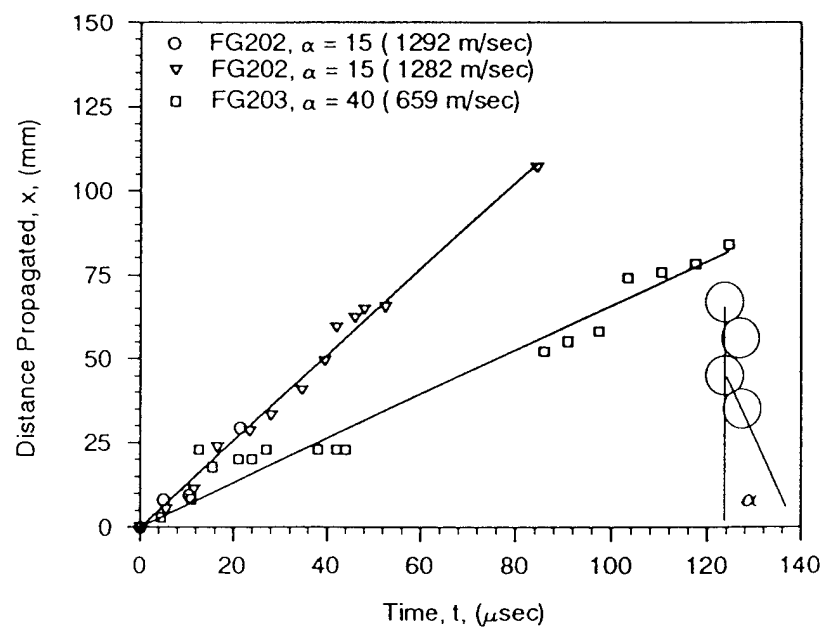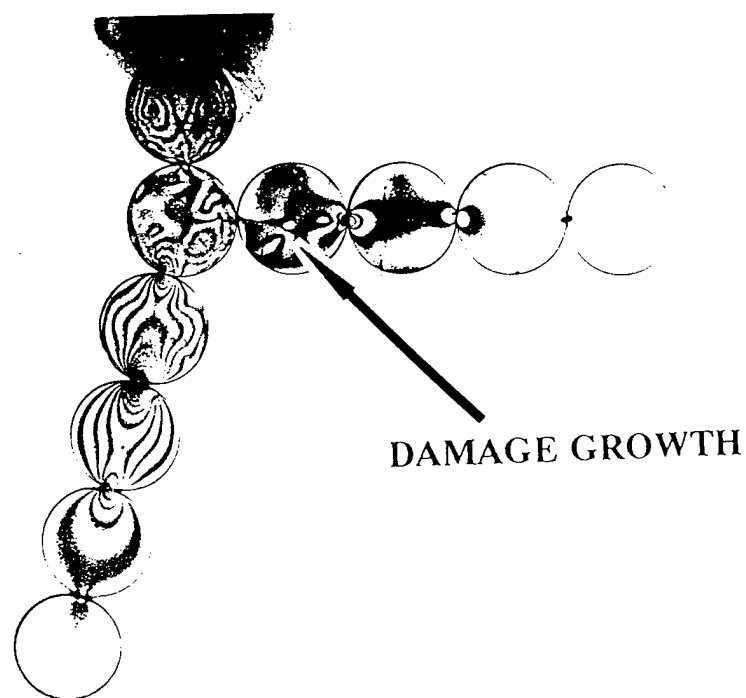Figure 6.14. Typical isochromatic fringes obtained from a single, 40° angle chain of particles.

Figure 6.15. Distance versus time plot for determination of group wave velocity for the angled particles chains.

160

DAMAGE GROWTH

FRAME 10
111.5 μsec

Figure 6.16. Typical isochromatic fringes obtained for two cemented disk chains showing energy transfer into the 90° chain.

CHAPTER 7

THE EFFECT OF SATURATION AND PORE FLUID ON DYNAMIC WAVE PROPAGATION

7.1 Summary

A computational modeling scheme has been developed to study wave propgation through granular materials saturated with pore fluid. The scheme incorporates an interparticle contact law developed from a simplified elastohydrodynamic solution for two disks interacting through a viscous fluid. Studies to date have shown good correlation with average branch vector fabric measures in that higher wave speeds and less attenuation were found for wave propagation in preferred directions of high branch vector distribution. The results are also consistent with the well-known inverse relationship between wave speed and porosity. An experimental study has also been undertaken in which the effect of pore fluid has been investigated in assemblies of circular disks. The fluid saturation level ranged from fully saturated assemblies to just a small amount of fluid placed between the circular disks. The experimental data indicates that load attenuation through the saturated assemblies is higher than that in dry assemblies. Additionally, for partially saturated assemblies, the transfer of energy from the propagating wave to kinetic energy of the pore fluid has been shown to be quite significant.

7.2.1 Introduction

Due to the microscopic heterogeneity, wave propagation in porous and granular geomaterials is governed by complex micro-processes which offer considerable challenges in developing predictive models. The term *microscopic* is used here to apply to behaviors occuring at the scale of the heterogeneity; e.g. length scales of pore or particle size. The presence of fluid occupying a portion of the pore space within the solid fraction requires a modeling strategy which incorporates the coupled mechanical response between the pore fluid and solid skeleton.

Classic continuum mechanics laws of elastodynmaics and their extensions including viscoelastic response have had limited success in predicting such wave propagation behavior.

162

One of the more successful continuum mechanics modeling schemes occured through the development of *poroelasticity theory* (see review by Detournay and Cheng, 1993). Based largely on the remarkable efforts of M.A. Biot (fundamental papers reprinted in Tolstoy, 1992), poroelasiticty theory is constructed on the concept of a coherent solid skeleton containing a fully connected, fluid filled pore space. Coupling between the fluid and solid phases is included, with the solid behavior governed by an elasticity theory and the fluid motion modeled through a diffusion (Darcy) equation. The definition of pore pressure places some restrictions on the time scale at which the coupled diffusion-deformation processes can be analyzed. This occurs because the pore pressure must be locally equilibrated between neighboring pores, and this length scale is linked to a time scale through the fluid diffusion behavior. Thus in principle, Biot theory is limited to quasi-static processes where the acceleration of the constituents is neglected. Bowen and Lockett, 1983 investigated this issue of neglecting the pore fluid inertia and found that for a specific problem under harmonically varying loading conditions, the solutions with and without inertia did not agree. In spite of this fact, Biot theory has been applied to dynamic problems involving wave propagation (Stoll, 1989) and predictions of the theory have been experimentally verified, e.g. Plona, 1980 and Ogushwitz, 1985. In a recent study, Gajo, 1995 investigated the role of viscous coupling between the solid and fluid phases of saturated porous media within the context of Biot theory for transient wave propagation. Hsieh and Yew, 1973 developed dynamic equations of fluid-saturated porous media by replacing the Biot mass-coupling theory with a constitutive assumption for the porosity change. Katsube, 1985 also re-investigated Biot theory in order to develop a clearer understanding of the pore-fluid mechanics. In related work viewing geomaterials as multiphase, Vardoulakis and Beskos, 1983 and Prevost, 1987 presented an approach to the dynamics of saturated porous and granular media using general *mixture theory*. It has been shown (Bowen, 1982) that under appropriate linearization conditions, mixture theory can be reduced to the poroelastic Biot model.

Another interesting approach to the dynamic micromechanical behavior of saturated porous media is the so-called *squirt-flow theory* where pore fluid is rapidly squeezed out of the media pores deformed by the passing stress wave. This mechanism was initially developed by examining fluid flow in an individual crack pore (Mavko and Nur, 1979) or at a grain contact

163

point (Palmer and Traviolia, 1980). Within this approach, attenuation and wave velocities were calculated by considering viscous energy losses or through a complex modulus. Mavko and Nur, 1979 have shown that the squirt-flow theory predicts much higher and more realistic attenuation values in partially saturated rocks than predictions from Biot theory. These initial studies treated the squirt-flow mechanism independent of Biot's theory; however, recently Dvorkin and Nur, 1993 have combined these two behaviors into a single unified model. Applications by Dvorkin, et al., 1994, have shown that the combined Biot/Squirt (BISQ) model can relate compressional wave speed and attenuation to the elastic properties of the drained skeleton, porosity, permeability, saturation, fluid viscosity and a parameter called the *squirt flow length*. It is assumed in the model that the squirt flow length is a fundamental rock property independent of frequency, fluid viscosity or compressibility. Results from the unified BISQ model indicate that the squirt-flow mechanisms dominate Biot mechanisms in predicting wave velocity dispersion and attenuation, and that BISQ predictions more accurately reflect observed dispersion and attenuation data.

Another large body of research exists dealing with micromechanical modeling of granular materials from the paticulate mechanics point of view. Many microstructural or fabric tensor theories have been proposed to model the static and dynamic behaviors of granular geomaterials; see for example Jenkins and Satake, 1983, Mehrabadi, 1992 and Voyiadjis, 1992. With regard to applications for wave propagation problems, Shukla, et al., 1988, 1993, and Sadd, et al. 1993 have investigated the dynamic response of unsaturated particulate materials. These studies have shown that from a micromechanical perspective, load is transferred in a dry granular medium primarily through contact mechanisms between neighboring particles. Furthermore, for the dynamic case it has been observed that the propagation of mechanical waves through such a medium occurs along complex networks of paths determined by the material's granular microstructure. Thus, local microstructure or fabric plays an important role in the transmission of mechanical loadings through such materials, and the wave speed and amplitude attenuation are related to material fabric.

The present work is concerned with the application of a numerical micro-mechanical modeling scheme to predict wave propagation in idealized granular materials saturated with pore fluid. The modeling uses the *discrete element method* to construct a numerical procedure to simulate dynamic load transfer associated with wave propagation processes.

This computational method was originally developed by Cundall, et.al. 1979, to model the response of discontinuous materials by studying the behavior of individual idealized particles in assembly systems. For applications to wave propagation, this scheme employs large assemblies of idealized particles to model the dynamic behavior of granular geomaterials. Numerous studies by Sadd, et.al. (1989, 1990 and 1993) have shown that such modeling techniques can simulate granular materials and predict results which compare with experimental data. The discrete element methodology commonly uses the simplfying assumption of Newtonian rigid-body dynamics to calculate the translational and rotational motion of each particle in model assemblies. Thus the dynamic response of the model system can be determined, and parameters such as wave speed and amplitude attenuation can be calculated for specific material models. Furthermore, these wave propagational characteristics can be related to the model material's *microstructure or fabric*.

Proper modeling of the contact forces between adjacent particles is essentail for the correct application of this numerical technique. This local contact behavior can be thought of as the microscopic constitutive law for the material. In order to apply our previous discrete element modeling schemes, a new contact law has been developed for particles interacting with each other through a fluid. The presence of pore fluid can have significant effects on the dynamic response of granular materials by adding viscous forces on particles and by changing the contact response between adjacent particles through *squeeze-film elastohydrodynamic action*.

Details of the development of the discrete element modeling scheme and elastohydrodynamic contact law will be presented. Model simulation results for one- and two-dimensional assemblies are given and compared with measured and expected behaviors. In order to help bridge the gap between our micromechanical modeling and macro observations, two-dimensional, *meso-domain* simulations are presented for assemblies with various fabric anisotropies. The term meso-domain is used here to indicate a model material composed of sufficiently large numbers of particles (micro-length scale units) such that average measures of fabric and mechanical behavior have reasonable meaning.

7.2.2 The Discrete Element Method

As mentioned, the discrete or distinct element method is a modeling strategy which

165

uses simplifying constitutive assumptions (commonly assuming Newtonian rigid-body mechanics) to model the translational and rotational motion of particles in model material assemblies (Figure 7.1). Contact laws between adjacent particles are constructed which serve to determine the contact force as a function of the relative displacement or relative velocity between the particles. Applying Newton's law to the i-th particle would yield

$$\sum_{j=1}^{n} F^{(ij)} + F^{(i)} = m_i \ddot{x}_i$$

$$\sum_{j=1}^{n} M^{(ij)} + M^{(i)} = I_i \ddot{\theta}_i$$

(7.1)

where $F^{(ij)}$ and $M^{(ij)}$ are the j-contact forces and moments on the I-th particle, $F^{(i)}$ and $M^{(i)}$ represent any resulting non-contact forces and moments, m_i and I_i are the particle mass and moment of inertia, and x_i and θ_i are the particle position and rotation. Equations (7.1) would then yield the particle linear and angular accelerations with given contact and non-contact forces. The technique establishes a discretized time stepping numerical routine, in which granule velocities and positions are obtained from numerical integration of the computed accelerations. New particle locations then establish new contact forces for the next time increment. It is assumed that during each time step, disturbances cannot propagate from any particle further than its immediate neighbors. Under these assumptions, the method becomes explicit, and therefore at any time increment the resultant forces (and thus the accelerations) on any particle are determined solely by its immediate neighbor interactions. In wave propagation applications, the movements of the individual particles are a result of the propagation through the medium of disturbances originating at particular input loading points. Consequently, wave speed and amplitude attenuation (intergranular contact force) will be functions of the physical properties of the discrete medium, i.e. the microstructure. In order to model actual geomaterials, the method is typically applied to granular systems containing large numbers of idealized particles (e.g. circular disks or spheres) in regular or random packing geometries. Such model materials can be computationally generated with varying degrees of microstructural fabric.

7.2.3 Fluid Contact Law

As mentioned, the presence of pore-fluid will create several new forces at the particulate level, and this requires the development of new contact laws governing particle interactions through a fluid. For fully saturated conditions, the capillary forces would vanish, whereas the viscous and squeeze-film contact lubrication actions would produce sizeable particulate forces. Viscous effects would be predominant for large particle spacings where neighboring interaction forces are vanishingly small. On the other hand, squeeze-film contact forces would be the most significant for dense packings of particulate systems, and this would seem to be the predominant case for most consolidated geomaterials.

The contact force for such a problem can be modeled using the theory of *elastohydrodynamics* (Cameron, 1967 and Gohar, 1988). Consider the case of two particles (approximated as two circular disks) embedded in a viscous fluid, and approaching each other with a relative normal velocity $V(t)$, see Figure 7.2. The fluid film in the contact zone will be squeezed, and a sizeable pressure is thus built up in this contact region. The fluid pressure distribution in the gap will exert a loading on each particle surface, and this loading is sufficient in certain cases to produce significant particle deformation. In this fashion, the micro-contact law governing particle interactions for saturated granular materials involves the complication of coupling both fluid and solid behavior, and this creates significant differences from behaviors found in the dry case. Past studies of this elastohydrodynamic problem have been carried out by Christensen, 1961, Kerrebrugh, 1970 and Lee and Cheng, 1973. These studies have developed very elaborate and complicated solutions methods to determine the fluid pressures and deformation profiles between converging circular cylinders or disks. Solutions were commonly formulated as integral equations, and numerical evaluations normally used some type of iteration strategy.

The problem geometry is shown in Figure 7.2 where the distance between particle surfaces is denoted by $h(x,t)$, a function of coordinate x and time t, and $\delta(x,t)$ is the particle deformation. Under certain assumptions the fluid pressure $p(x,t)$ can be related to $h(x,t)$ by the *Reynolds equation of lubrication theory*

$$\frac{\partial}{\partial x}(h^3 \frac{\partial p}{\partial x}) = 12\eta \frac{\partial h}{\partial t} \tag{7.2}$$

where η is the viscosity of the fluid.

Since $h(x,t)$ can include particle deformation $\delta(x,t)$ which is determined by elasticity theory, equation (7.2) is a *coupled relation*, and as mentioned typically an iterative numerical method would be required to solve this equation for the pressure distribution $p(x,t)$. Incorporating such a numerical scheme into the discrete element method would result in a very computationally intensive procedure, and would therefore result in unreasonable amounts of CPU time to run the simulations. Thus a simplified alternative procedure was developed in order to avoid the numerical complexities. This simplified approach first assumes that the particle is rigid, and this allows a closed-form solution for $p(x,t)$ from equation (7.2). Once this pressure distribution is found, the particle deformation may be calculated from simple Hertz contact stress theory, and this new particle shape may be then used to calculate a new pressure distribution. Thus initially let $w(x,t) = 0$, and the undeformed particle surface can be approximated by the relation

$$h(x,t) \approx h(0,t) + \frac{x^2}{2R} \tag{7.3}$$

where R is the particle radius. The solution to the Reynolds equation (7-2) for this case is found to be

$$p(x,t) = -6R\eta \frac{V(t)}{h^2(x,t)} \tag{7.4}$$

With the pressure distribution known, the total contact load between the particles is given by integrating the pressure, i.e. $F = H \int p \, dx$, where H is the disk thickness. Carrying out the integration over the disk surface yields

$$F(t) = 3\sqrt{2}\pi\eta H \left(\frac{R}{h(0,t)} \right)^{3/2} V(t) \tag{7.5}$$

In order to included the effects of particle deformation, a combined model with two, series-connected stiffness (spring) elements may be used. One spring element represents the fluid stiffness while the other element includes the solid (particle) stiffness resulting from the

elastic deformation within the particle. The pressure loading will produce deformations such that the distance between particle surfaces will change from h to $h(x,t) + \delta(x,t)$, where $\delta(x,t)$ is the contact deformation for the dry case. If the disk shape is assumed to be unchanged, then the new load $F(t)$ is still given by equation (7.5) using the modified value of $h(x,t)$, i.e.

$$F(t) = 3\sqrt{2}\pi\eta H \left(\frac{R}{h(0,t) + \delta} \right)^{3/2} V(t) \tag{7.6}$$

In dry granular materials, our previous research (Sadd, et.al., 1993) has indicated that the normal contact force F can be related to contact deformation by the relation $F = K\delta^{1.4}$, where K is a material constant. Obviously the forces in the fluid and solid springs should be equal, and this leads to the result

$$3\sqrt{2}\pi\eta H \left(\frac{R}{h(0,t) + \delta} \right)^{3/2} V(t) = K\delta^{1.5} \tag{7.7}$$

where on the right-hand side, the exponent on δ has been modified for convenience to the value of 1.5. Solving equation (7.7) for δ and substituting the result into equation (7.6) yields

$$F(t) = \frac{C_1 V(t)}{\left(0.5 \left(h(0,t) + \sqrt{h^2(0,t) + 4(\frac{C_1}{K})^{2/3}} \right) \right)^{3/2}} \tag{7.8}$$

where $C_1 = 3\sqrt{2}\eta\pi R^{3/2}H$. Equation (7.8) then gives the normal contact force when two disks approach to each other. For the case when the two particles move apart, contact law (7.8) is not suitable since a negative velocity V, may lead to a negative value within the square root. For this case the solid contact law will be used.

The above results address only the normal contact response between particles. For the tangential contact behavior, a simple modeling scheme (Adhakari, 1995) based upon the simple shearing of a Newtonian fluid within the small inter-particle gap. If the gap is small then the fluid motion may be approximated by a linearly varying distribution, and the resulting shear stress between a pair of particles will then be given by

$$\tau = \eta \frac{\partial U}{\partial z} \approx \eta \frac{\Delta U}{\Delta z} \approx \eta \frac{U_1 - U_2}{h} \qquad (7.9)$$

where U is the relative tangential velocity between particles, and U_1 and U_2 are the absolute tangential velocities of each particle. Thus the tangential force between any two generic particles can be estimated by the product of this shear stress times an effective area within the gap zone. However, as the particle spacing h, becomes very small (on the order of a micrometer), relation (7.9) breaks down and predicts unrealisticly high shear stresses. For this case it is well known that the *no-slip condition* of classical fluid mechanics should be modified to include a tangential slip velocity along neighboring particle surfaces. This will act to soften the unrealisticly high velocity gradient calculated in relation (7.9). It has been suggested that for very thin fluid gaps, the frictional characteristics of the lubricant are determined by the properties of the surface layers and the underlying solids. The viscosity of the lubricant has little effect, and thus a simple Coulomb frictional equation may be used with an appropriate value of the coefficient of dynamic sliding. Therefore when the spacing parameter h becomes less than or equal to a prescribed critical value h_{cr}, the tangential force is given by $F_t = \mu F_n$, where μ is determined by requiring F_t to be continuous at $h = h_{cr}$.

7.2.4 Results

In order to investigate the predictions of the proposed modeling scheme, several one- and two-dimensional material models were created, and the discrete element computer code was then applied to each of these models under specific dynamic loading conditions designed to simulate wave propagation.

7.2.4.1 One-Dimensional, Single Chain Simulations

In order to gain an understanding of basic model predictions, numerical experiments have been conducted on one-dimensional granular material simulated by a single straight chain of circular particles as shown in Figure 7.3. Considering the modeling of a coarse sand, the circular particles had a diameter of 2mm, thickness of 1mm, and were assumed to be of quartz with a density of 2650 kg/m³. The simulations incorporated different interparticle gap openings (of the order of one micrometer) between neighboring particles, and the model

170

system was assumed to be completely saturated with water of viscosity of 0.001 N-s/m^2. The input loading applied to one end of the particle chain was taken to be a triangular time dependent pulse of duration of 5 μs with a peak value of 2 N to simulate a wave front pressure of approximately 10^6 N/m^2.

Using these parameters, a computer simulation was conducted and wave speed and attenuation results are shown in Figures 7.4, 7.5 and 7.6. The effects of the gap distance and pore fluid viscosity on the wave speed are shown in Figure 7.4. As expected, the wave speed decreases with the gap distance, and when the gap is small, these effects are rather pronounced. An increase of fluid viscosity leads to a slight increase of the wave speed, although these effects are small for the physical parameters in the chosen model. As pointed out by Dvorkin, 1994, increases in the compressional wave speed with increasing pore fluid viscosity have been observed, and unfortunately Biot theory predicts the opposite trend. Figures 7.5 and 7.6 illustrate amplitude behavior where amplitude is measured by the interparticle contact force normalized by the input value. It was found that the attenuation is quite large during the passage through the first several particles, but then the attenuation rate rapidly decreases with the propagational distance. Figure 7.5 showns the effect of the interparticle gap spacing on the attenuation , and it is seen that larger gap spacings produce higher attenuation. The effect of pore fluid viscosity on attenuation behavior is illustrated in Figure 7.6 for a fixed interparticle spacing of 0.1 μm. Higher viscosities result in slightly higher attenuation rates.

7.2.4.2 Two-Dimensional Simulations

In order to investigate the use of the compuatational scheme for multi-dimensional simulation, several two-dimensional granular assembly models were generated. These assemblies were created using three different *random media generators* which have been previously developed by Tai, 1993. These generating codes can create large random particulate assemblies with varying degrees of microstructural fabric such as porosity, coordination number (average number of contacts per particle), particle contact normal and branch vector distributions, void characteristics, etc. Figure 7.7 illustrates some of these fabric variables for a general granular medium. The branch vector, defined as the vector drawn between adjacent particle mass centers, is a commonly used microstructural fabric

measure that relates the relative positions between particles. Previous studies have shown that load transfer in particulate media can be correlated with the spatial distribuiton of branch vectors. Based on this concept, our three media generating schemes have been designed to construct model granular materials with *highly, moderately* and *weakly anisotropic* distributions of branch vectors.Results of a set of DEM simulations are summarized in Table 7.1.

Figure 7.8 shows one example assembly model that is referred to as a *highly anisotropic* medium. The model contains 378 particles which have been randomly arranged while being subject to generation preferences allowing particular fabric anisotropies. In order to quantify and correlate such fabric or material microstructure to wave propagational behaviors, the distribution of branch vector orientations of the assembly was computed, and a polar diagram plot of this distribution is shown in Figure 7.8. It can be observed from the distribution plot that this model material system shows preferred directions (anisotropy) with more branch vectors distributed in the vertical direction than in the horizontal. Thus we would expect wave transmission to be correlated with this anisotropic fabric.

Dynamic input for wave propagation was created through simultaneous loading of particles along left and bottom edges of the assembly as shown. Input loadings were applied with identical magnitude and time history as used in the one-dimensional simulations. The transmitted wave output (measured by the inter-particle contact forces) was collected among the particles along the right and top sides of the assembly, and thus this technique can provide comparisons of horizontal and vertical wave propagational behaviors.

Discrete element simulation results of the wave propagation through this assembly are shown in Figure 7.9. Normalized average wave transmission through the assembly for the horizontal and vertical loading cases are illustrated. The vertical scale represents the average of all interparticle load transfers at the output side of the assembly normalized with respect to the input. These results indicate that the wave transmission is clearly related to the anisotropic fabric of the model particulate material in that less wave attenuation occurs for the vertical propagation case. Figure 7.10 shows vertical propagation results of the same model material for the case with different inter-particle gap spacing. It can be observed that with an increase of gap spacing, average attenuation will increase as will the arrival time of the signal, thus implying a reduction in the wave speed. These results are consistent with our

172

one-dimensional simulations. For the case of vertical propagation, an average wave speed of 1100 m/s was found for the gap spacing of 0.1 μm, while for the 0.2 μm spacing case, the wave speed was found to be 540 m/s. In order to investigate the effect of particle size on the wave propagational characteristics, an indentical assembly as shown in Figure 7.8 was constructed which had the same branch vector distribution but with particles of 1 mm diameter. Comparison of the simulation results of vertical wave propagation for the two assemblies with constant input stress loading is shown in Figure 7.11. These results indicate that the smaller particles had an average wave speed of approximately 950 m/s, which is smaller than that found in the 2 mm particle case. This trend is consistent with our previous studies on unsaturated granular material.

A second material model was generated using a *moderately anisotropic* granular media generator. The material assembly contains 441 particles and is shown in Figure 7.12 along with the branch vector distribution. It can be observed from the branch vector diagram that this assembly has a slight preference for wave transmission in the horizontal direction. Discrete element simulations of wave propagation in the horizontal and vertical directions are shown in Figures 7.13 and 7.14. Computational model parameters used in this case are identical to those of the previous example. The results shown in Figure 7.13 indicate that, as expected, the wave attenution is less in the horizontal direction, thus correlating with branch vector fabric. Figure 7.14 compares the horizontal wave transmission for two different particle gap spacings, and again it is observed that both attenuation and wave speed are sensitive to particle spacing.

Using yet another generating scheme, a third material model was constucted which could be referred to as *weakly anisotropic*. The assembly model and its branch vector distribution are shown in Figure 7.15. This model contains 179 particles and its branch vector fabric indicates a slight preference in the vertical direction. Computer simulations of wave propagation in the vertical and horizontal directions are shown in Figures 7.16 and 7.17. It is again observed that wave propagational behaviors correlate to some extent with the branch fabric distribution.

7.2.5 Conclusions and Discussion

A computational modeling scheme has been developed to study wave propagation

through granular materials saturated with pore fluid. The primary focus of the study has been to investigate microstructural or fabric effects and to relate such features with wave propagational behaviors. The modeling procedure uses an interparticle contact law developed from a simplified elastohydrodynamic solution for two circular disks interacting through a viscous fluid. This fluid contact law has been incorporated in a discrete element computer code to analyze the dynamic response of model particulate materials.

The presence of pore fluid effects the manner in which dynamic loadings are transmitted through particulate materials and these have been related to the fluid viscosity and interparticle liquid gap spacing. Results from this study indicate that very little viscosity effects were found on wave attenuation, while a small increase in transmitted wave velocity was observed with increasing pore fluid viscosity. It has been pointed out by Bourbie, et.al., 1987 that trapped or bound pore-fluid may behave as having a higher apparent viscosity than free fluid. The dimension of the fluid gap between particles had more sizeable effects on wave propagation. Wave speed was found to be inversely related to the gap size, and attenuation increased with particle spacing dimension.

Several two-dimensional, meso-domain studies were conducted in which material models were simulated by large numbers of particles randomly arranged so as to create an average anisotropy within the entire mass. This method was used to provide a bridge between the micromechanical modeling and observable data on macroscale material. Wave propagation simulations generally correlated with average branch vector fabric in that higher wave speeds and less attenuation were found for wave propagation in preferred directions of high branch vector distribution. The results are also consistent with the well-known inverse relationship between wave speed and porosity.

Presently our discrete element model includes the effect of pore fluid only through interparticle lubrication theory. It has been our belief and that of others that pore fluid inertia should also be accounted for at the micromechanical level. A plausible method to do this would be to incorporate a squirt flow theory as suggested by Dvorkin and Nur, 1993 into our discrete element computer model. This would allow this modeling technique to simulate the two most important microstructural mechanisms of saturated granular sediments; i.e. viscous and intertial pore fluid behaviors. Arguments have been made that incorporation of squirt flow mechanisms will provide better simulation results and can more easily be extended to

materials with variable saturation. Additional work also needs to be done to provide a micromechanical description and connection with several Biot parameters including: *apparent* or *added mass, tortuousity, pore size parameter, frame modulus, etc.* The specific parameters related to the overall mobility of the pore fluid and its interaction with the skeletal frame would be of prime interest.

7.3.1 Pore Fluid Behaviors: Experimental

Wave propagation in a discontinuous media is of great interest to the soil and rock mechanics community. The propagation of elastic waves in the earth's crust is most intimately related to the properties of the sand, soil, and rocks which make up the various layers. These properties are greatly affected by the amount of fluid contained in the layer, porosity, particle size , and any binding material which may be present.

Current interest in geomechanics is focused on transient phenomena occurring in earthquakes, wave loading, and consolidation. For all of these, the coupling between the deformation of the 'solid skeleton' of the soil or rock and the motion of the pore fluid is of primary importance. Researchers have looked at the effects of particle size, moisture content, and peak load magnitude on the transmissibility of pressure waves in a granular or soil medium. However, little attention has been paid to the effect of viscosity of the fluid which saturates the granular media. As an example, the soil or rock could be saturated with pure water or crude oil, whose viscosities are quite different. The viscosity is believed to affect the shear force transfer between particles. This study deals primarily with loadings which have small shear components compared to the magnitude of the normal component. A complete understanding of the normal component in wave propagation must be ahcieved before the work will then focus on the shear transfer.

An experimental investigation is under way using dynamic photoelasticity and high speed photography to study stress wave propagation and dynamic load transfer in fluid-saturated granular media. An explosive charge is used to create a compressive stress wave which propagates in model granular assemblies. The granular media is simulated by circular disks fabricated from Homalite-100, a clear plastic, arranged in a specific orientation. Various fluids including water, glycerin, and two Dow Corning 200 fluids are being used in the study. Fully saturated assemblies are being studied as well as partially saturated

assemblies. The data presented represents work that is currently under way in the laboratory.

7.3.2 Experimental Procedure

Experimental models for one and two dimensional arrangements are shown in Figure 7.18. Two basic geometries are being investigated, namely single chain and hexagonal close-packed assemblies. A water tight container is constructed from acrylic sheets to which the circular disks and fluid are added. The fluids being used in this investigation include water, two Dow Corning 200 fluids with viscosities 10 times and 100 times the viscosity of water, respectively, and also glycerin, with a viscosity 1000 times that of water. Experiments have been conducted with fully saturated assemblies and partially saturated assemblies. At this point in the investigation, the partially saturated work only includes single chain assemblies.

Fully saturated assemblies are completely filled with fluid after the disks are arranged into the desired geometry. Partially saturated assemblies only have fluid at the contact region. For the partially saturated experiments, approximately 0.01 cc of fluid was added to the contact region as the disks were placed into the single chain assembly.

The wave propagation phenomena due to explosive loading was studied using the technique of dynamic photoelasticity in conjunction with high speed photography. This technique has been discussed in great detail in other publications (see Shukla and Nigam, 1985) so only a brief explanation will be given here. Photoelasticity is an experimental technique whereby full field stress information is obtained for a specimen under load. Photographs are taken of the resulting fringe pattern at various times during the loading event. The fringe patterns are lines of constant maximum shear stress in the specimen and appear as light and dark bands in the specimen. An appropriate set of stress field equations allows one to solve for things such as contact load, half contact width, etc.

Dynamic photoelasticity implies high speed events and therefore a high speed camera is needed to record the resulting fringe patterns. The high speed photographic system in use operates as a series of high intensity, extremely short duration (about 500 ns) pulses of light which provide photoelastic images at discrete times during the dynamic event. Typically the total duration of the experiment is about 200-300 μs. These photographs of the wave propagation process at different stages of development provides the necessary data to obtain the velocity and attenuation of the peak contact load of the stress wave.

176

The wave velocity is obtained by plotting the instantaneous position of the wave front with respect to time. The slope of this line yields the average wave velocity. The contact load between disk pairs is obtained by analyzing the fringe patterns around the contact using the Hertz stress field equations which were generalized for plane stress by Smith and Liu (1953).

7.3.3 Results and Discussion

The first series of experiments were conducted with a one dimensional disk assembly. Figures 7.19, 7.20, and 7.21 show typical isochromatic fringes obtained from single chain arrangements saturated with water, 10 cs fluid, and 100 cs fluid, respectively. These photographs show little qualitative difference with respect to the propagating wave. Also, the nature of the stress field in the disks appears unaffected by the fluid when compared to a dry assembly. Therefore, unlike a cemented contact, Hertz theory and the analysis techniques utilized for a dry contact (Shukla and Nigam, 1985) will yield accurate contact loads.

A typical plot of contact load as a function of time for a water saturated single chain assembly is shown in Figure 7.22. The plot shows that the nature of the wave propagating through the assembly is similar to that seen in assemblies without fluid saturation. There is no significant dispersion (which would appear as a spreading of the pulse) or dramatic changes in the load profile shapes. From plots like these, the peak contact load is extracted for each disk-to-disk contact point and is used to determine the attenuation characteristics for various assemblies. Figure 7.23 shows the attenuation data for dry, water saturation, 10 cs fluid saturation, and 100 cs fluid saturation. The amplitude attenuation for four disk lengths (102 mm) is about 20% for the case with water and only varies by about 4% for the different fluids. Comparing this to the dry case, where the attenuation has been shown to be only around 14%, there is approximately a 10% increase in attenuation across four disk lengths.

Figures 7.24 and 7.25 show typical isochromatic fringes obtained from experiments with partially saturated contacts where the fluids are water and glycerin, respectively. The two figures show generally the same wave propagation phenomena. Using load versus time plots similar to that shown earlier, attenuation data was obtained for the case partially saturated with water and is shown in Figure 7.26. One can see that the attenuation across four disks for this case is approximately 35%. Compared to both the dry case and the fully saturated cases, this is quite dramatic. More energy is being lost in the partially saturated media than in the

177

fully saturated media.

A possible explanation for the increased energy loss is the movement of the pore fluid from between the particles. In Figure 7.24, the fluid can be seen to be ejected from between the first few disks in the last three frames of the figure. Figure 7.27 shows a plot of the half-width of this fluid as a function of time. The plot represents the horizontal component of the velocity of the fluid as it is ejected from the contact area. Fluid velocity ranges from a high of about 60 m/s for the first wet contact down to 15-20 m/s for the later contacts. Although the net mass of the moving fluid is not known, the kinetic energy of the ejected fluid is primarily dependant on the square of the velocity which appears significant in this case. In the fully saturated cases, the fluid at the contact is constrained by the surrounding fluid in the assembly, which prevents the large amount of energy transfer in the form of kinetic energy.

The wave front position as a function of time was plotted for each assembly and Table 7.2 shows the resulting average wave front velocities for the various cases tested as well as that for air. The case with air as the saturating fluid is included for the sake of comparison. This table also includes velocity values for the two dimensional assemblies. For these cases the velocity reported is the average wave front velocity for the wave traveling in the main chain (defined in Figure 7.18 b.)).

The maximum percent difference between the velocity for air saturation and the 100 cs fluid, for either the one or two dimensional assemblies, is about 12%. Between the two different Dow Corning fluids the difference is negligible. These results differ from that reported earlier in this chapter with regard to what is predicted by the Biot / squirt flow model and what has been observed in the field. As these are only preliminary results, further study is required to confirm the observations. So, while the results show a small drop in average velocity, no significant conclusions can be drawn based on the viscosity change.

However, average wave velocities for the two partially saturated cases are quite different. The assembly partially saturated with water produced an average wave velocity of approximately 1100 m/s while the glycerin case produced approximately 1250 m/s. The results might imply that for the partially saturated assembly, the increase in wave velocity corresponds to the increase in fluid viscosity but at this time there is an insufficient amount of data to conclusively state this.

Future work will include a more thorough investigation of fluid viscosity effects,

including maintaining nearly constant fluid density while varying viscosity, and maintaining nearly constant fluid viscosity while varying density. Density plays an important role in determining the acoustic impedance mismatch between the disk material and the fluid while viscosity plays a role in fluid motion. If two materials have highly mismatched acoustic impedance, the wave will not propagate easily from the low acoustic impedance material to the high acoustic impedance material. Generally, the denser the material, the lower the acoustic impedance. In the case of glycerin placed between Homalite disks, the densities are nearly the same (1260 kg/m^3 for glycerin and 1230 kg/m^3 for Homalite). The result is excellent wave propagation characteristics through the glycerin.

Figures 7.28, 7.29, and 7.30 show wave propagation in a hexagonal close-packed granular media saturated with water, the 10 cs fluid, and the 100 cs fluid, respectively. Recall that the wave velocities listed in Table 7.2 for the two dimensional assemblies are almost the same as those from single chain experiments. However, unlike the single chain experimental results, the contact load attenuation in the main chain for saturated granular media is less than that for unsaturated media. The attenuation data is shown in Table 7.3.

It can be seen from the photographs in the fore-mentioned figures that most energy transfer occurred in the two main chains. This is based on the higher order fringes that occur at the contacts in the main chains when compared to contacts in other locations. However, for unsaturated HCP models, as shown in Figure 7.31, the energy transfer not only occurred in the main chains, but also in the disks adjacent to the main chain. The lesser attenuation rate reflects the observed energy transfer phenomenon.

However, questions arise for these assemblies because the fringe patterns are not symmetric about a vertical line passing through the point at which the input loading occurred. Regardless of the fluid saturating the assembly, the symmetry of the assembly geometry should result in a symmetric spreading wave. At this point, several possible causes are being considered, including the following; 1.) the contacts were not all uniformly wetted, and 2.) a buoyancy force which would depend on the density of the saturation fluid. The first concern can be easily verified by wetting each contact as the assembly is being constructed so that when it is filled with fluid, the contacts have been pre-wetted and there is little chance of some remaining dry. The second concern is currently under consideration. If a small variation in buoyancy force were present, the fluid film between particles could be affected. The film

179

thickness would be dependant on the weight of the disks above the contact in question which changes with saturation fluid density. Computer simulations have shown that the fluid film thickness between the disks does play a dominant role in the resulting wave speed.

Model Type	No. of Particles	Gap Space (μm)	Porosity %	Propagation Direction	Wave Velocity (m/s)	Attenuation Transmission Ratio (%/m)
Hly Anisotropic	378	0.1	32	Horizontal	1020	0.048
Hly Anisotropic	378	0.1	32	Vertical	1100	1.19
Hly Anisotropic	378 (D=1mm)	0.1	32	Vertical	950	5.14
Hly Anisotropic	378	0.2	32	Vertical	540	0.61
Mod Anisotropic	441	0.1	21	Horizontal	1170	0.45
Mod Anisotropic	441	0.1	21	Vertical	1200	0.065
Mod Anisotropic	441	0.2	21	Horizontal	530	0.19
Wkly Anisotropic	179	0.1	22	Horizontal	1220	0.38
Wkly Anisotropic	179	0.1	22	Vertical	1010	2.46
Wkly Anisotropic	179	0.2	22	Vertical	520	1.08

Table 7.1. Summary of Discrete Element Simulations.

Stress Wave Velocity (m/s)						
Assembly Type	Fully Saturated				Partially Saturated	
	Air (1/55 cs)	Water (1 cs)	10 cs Fluid	100 cs Fluid	Water (1 cs)	Glycerin (10^3 cs)
1-D	1050	965	950	940	1100	1250
2-D	1010	960	950	900	-	-

Table 7.2. Wave velocities for fully saturated and partially saturated assemblies.

Contact Load Attenuation Across 4 Disks (102 mm)				
Assembly Type	Fully Saturated			
	Air (1/55 cs)	Water (1 cs)	10 cs Fluid	100 cs Fluid
1-D	18%	24%	25%	23%
2-D	70%	62%	52%	53%

Table 7.3. Load attenuation data for fully saturated assemblies.
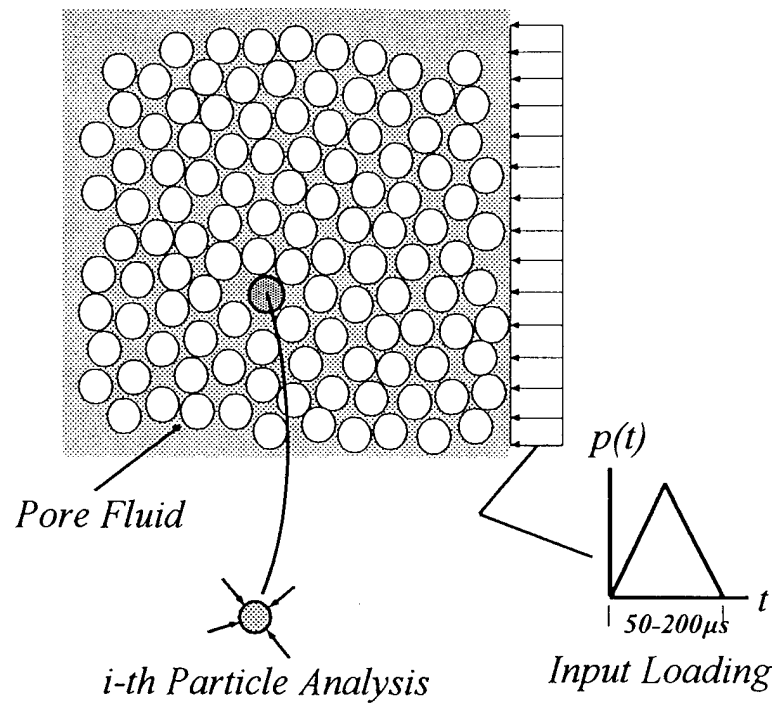
Figure 7.1. Discrete Element Modeling Procedure
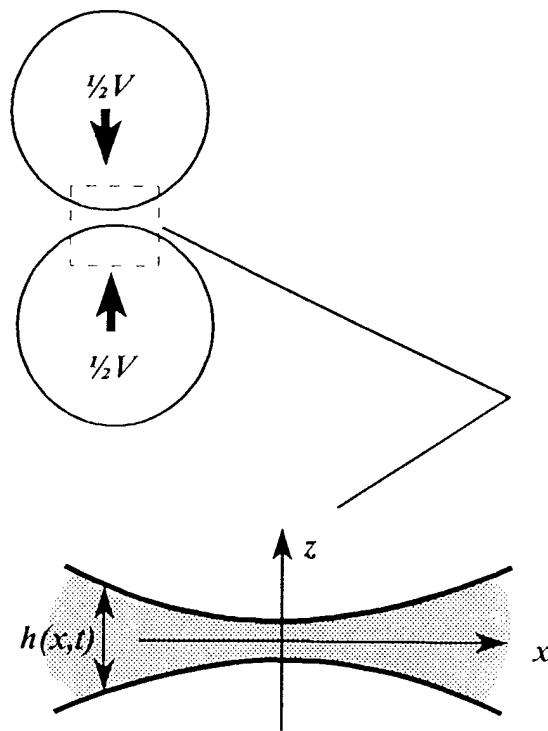
Figure 7.2. Particle Interaction Through a Viscous Fluid

Input

Fluid Filled Gaps
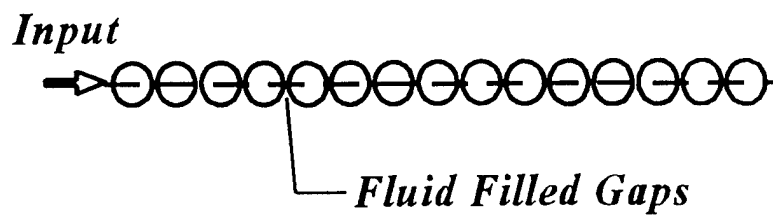
Figure 7.3. One Dimensional Example
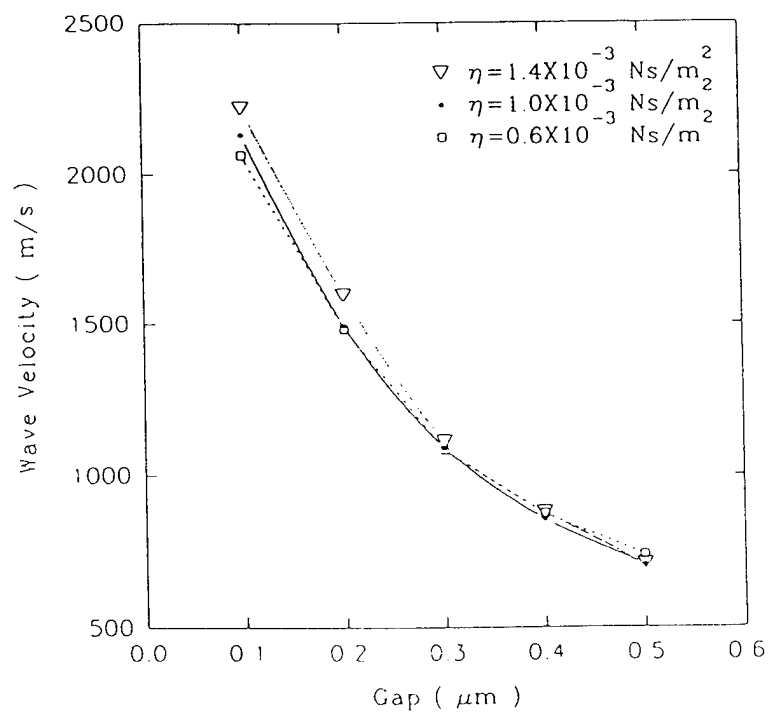
Figure 7.4. Wave Velocity Behavior vs. Particle Spacing

184
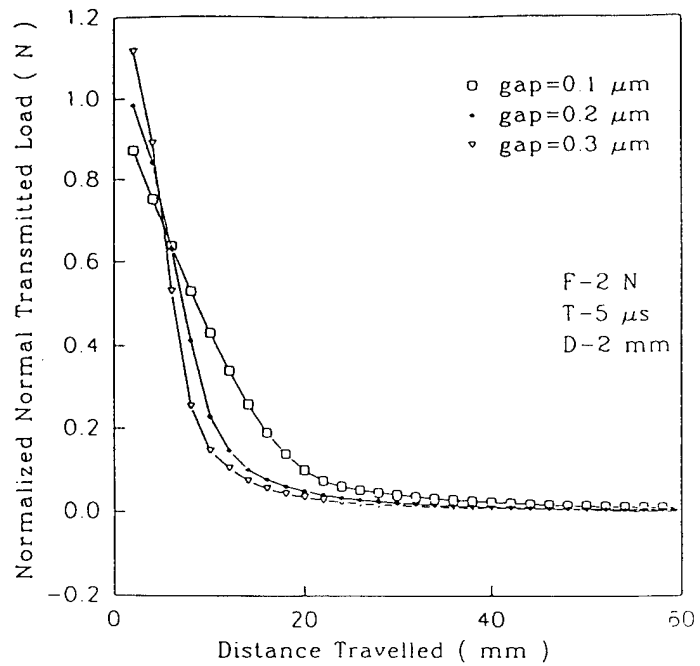
Figure 7.5. One Dimensional Attenuation Behavior for Different Particle Spacings
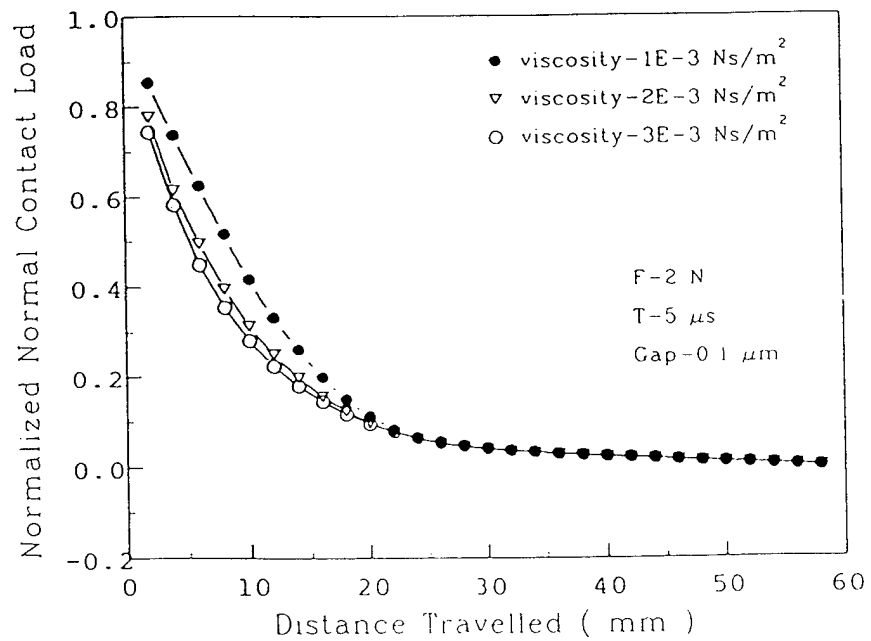
Figure 7.6. One Dimensional Attenuation Behavior for Different Viscosities

185
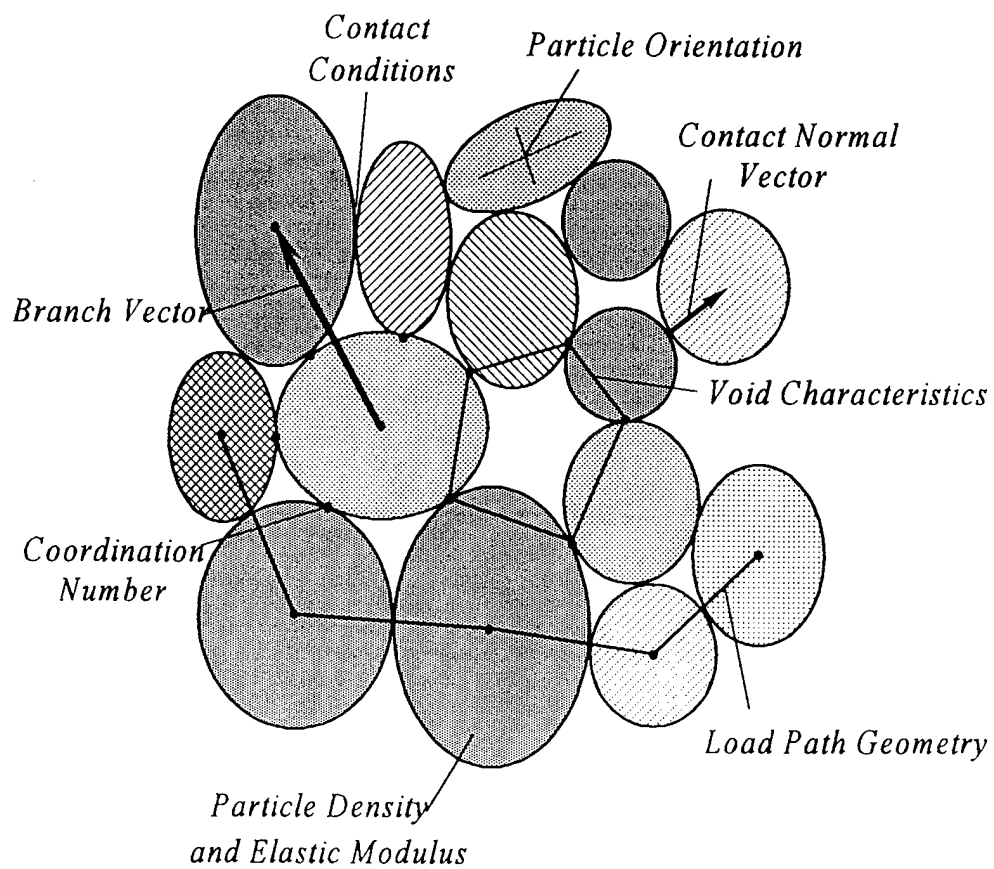
Figure 7.7. Various Fabric Measure Used for Particulate Materials
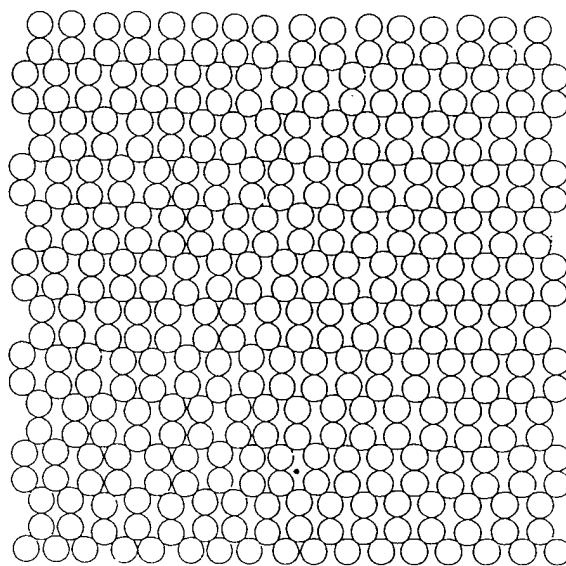
(Assembly)
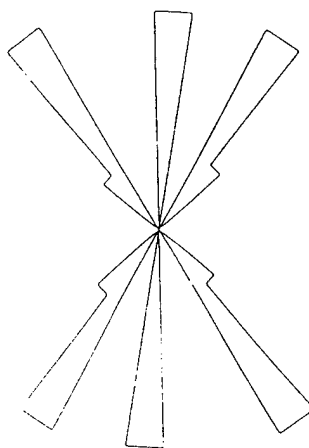
(Branch Vector Distribution)

Figure 7.8. Highly Anisotropic Material Model

187
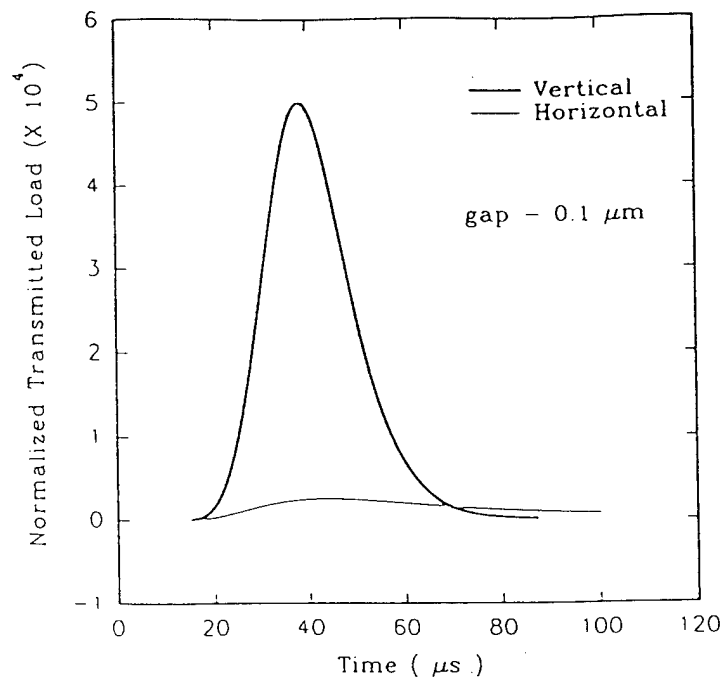
Figure 7.9. Average Transmitted Wave Amplitude

For Highly Anisotropic Assembly.
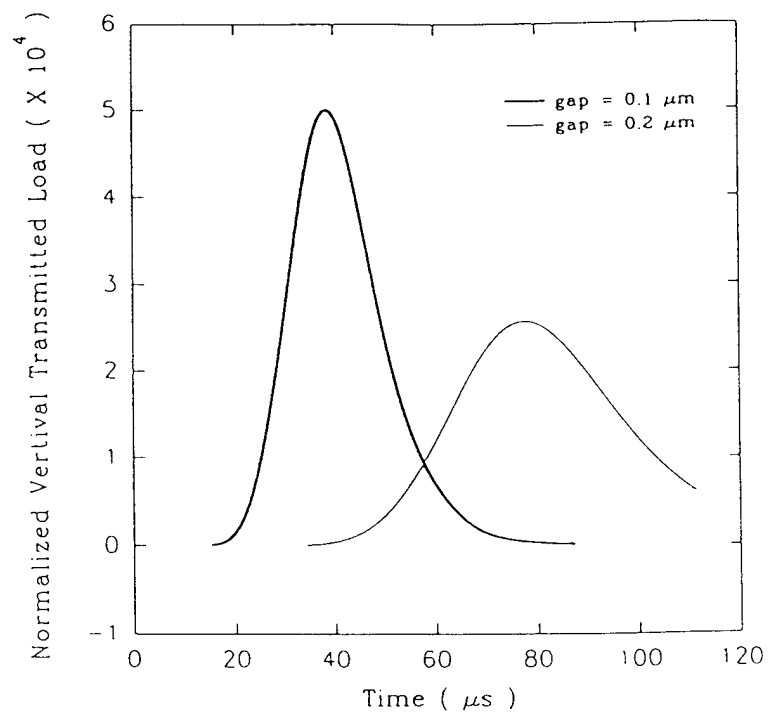
Figure 7.10. Vertical Transmission for Highly Anisotropic Model
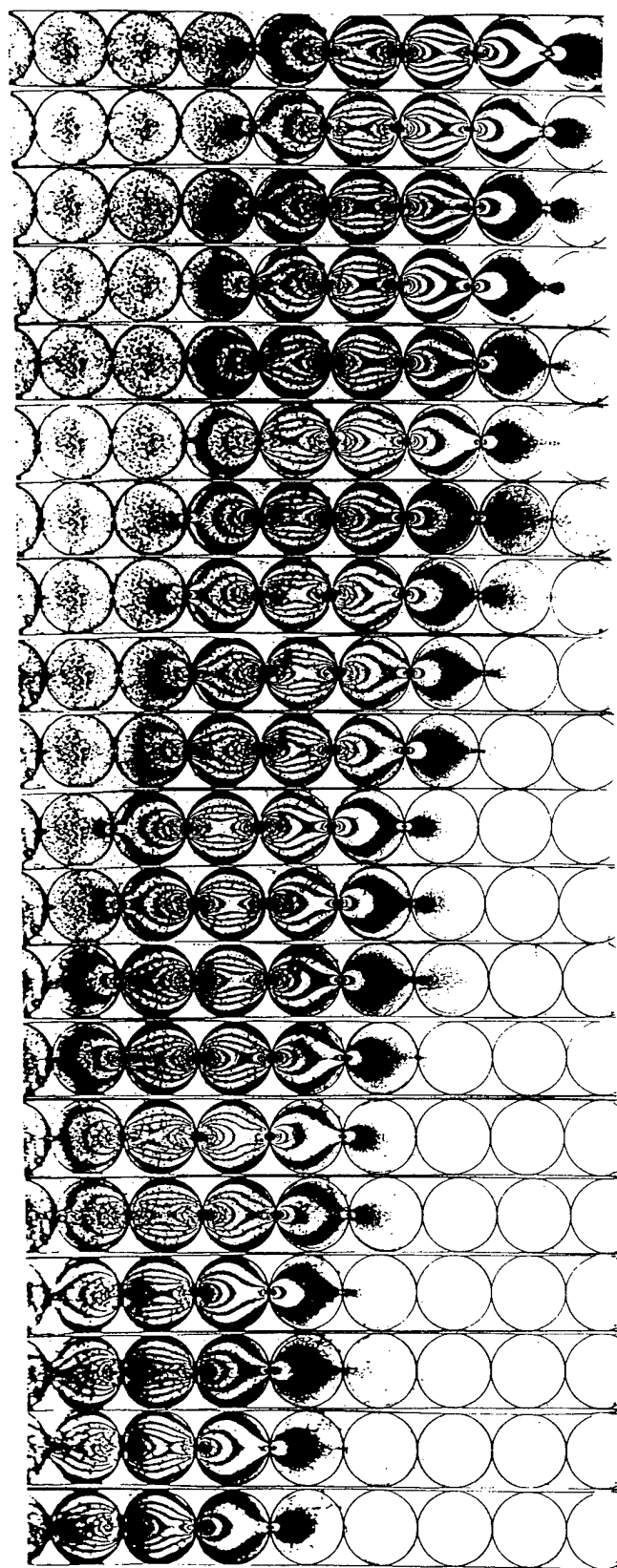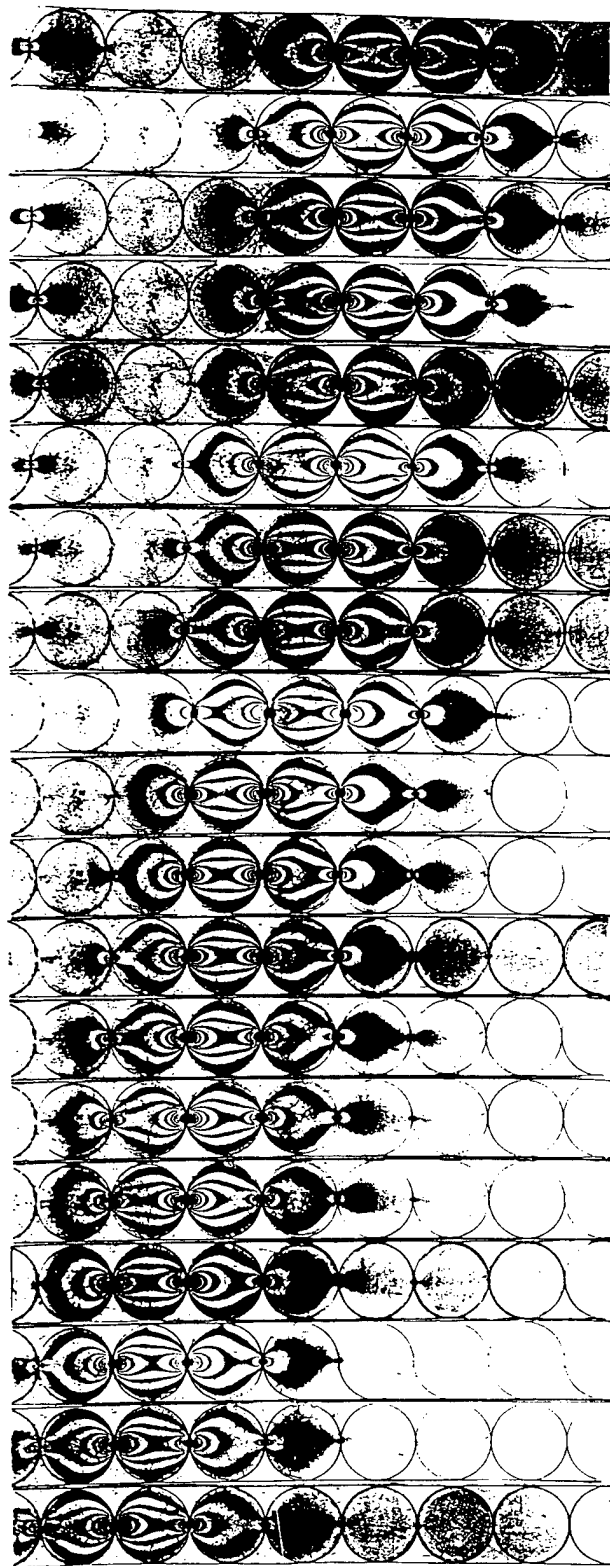
with Different Initial Particle Gap Spacings

188
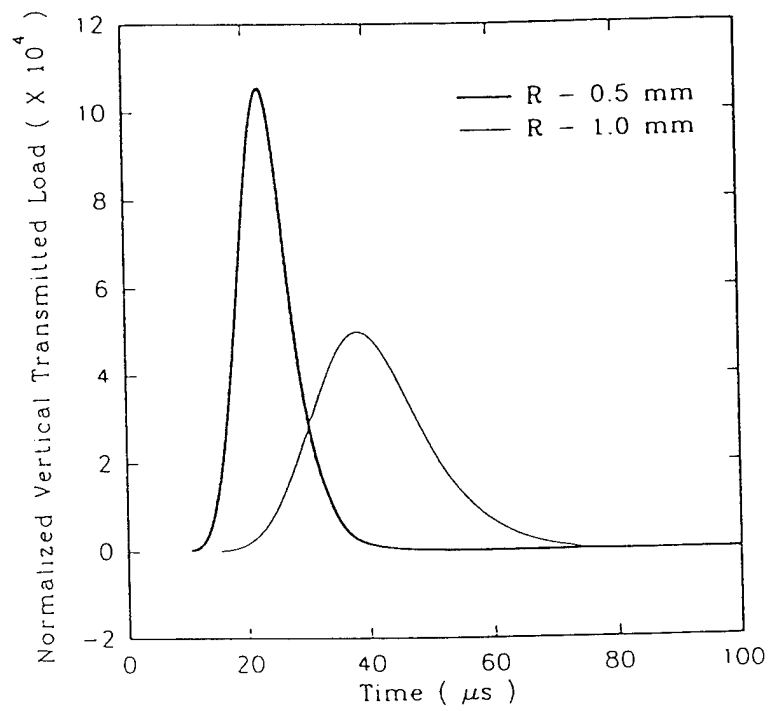
Figure 7.11. Vertical Wave Transmissions for Highly Anisotropic
Model with Different Sized Particles
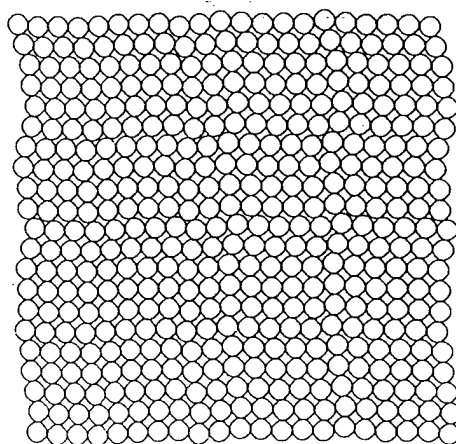
(Assembly)
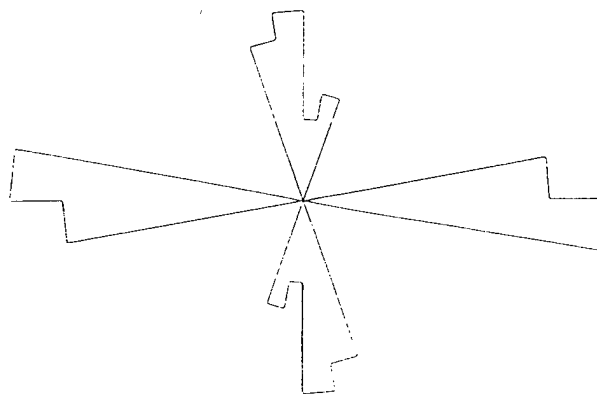
(Branch Vector Distribution)

Figure 7.12. Moderately Anisotropic Material Model
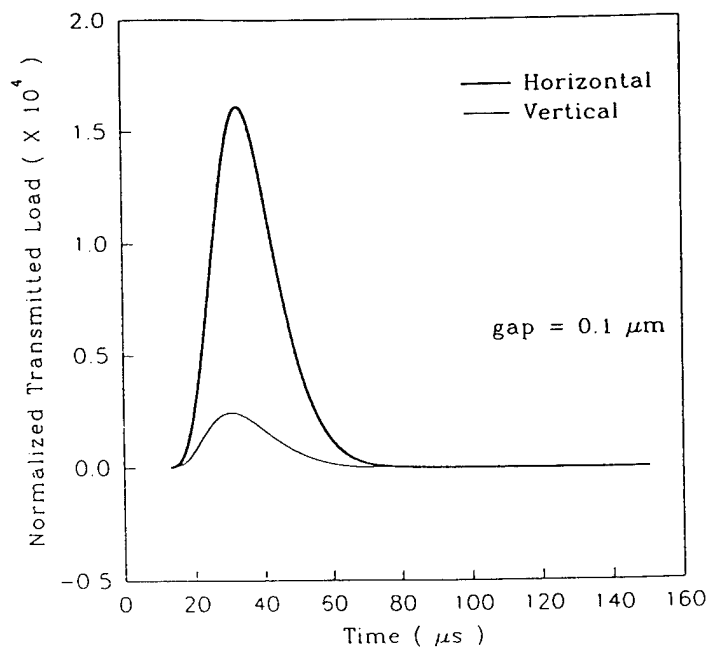
Figure 7.13. Average Transmitted Wave Amplitude
For Moderately Anisotropic Assembly
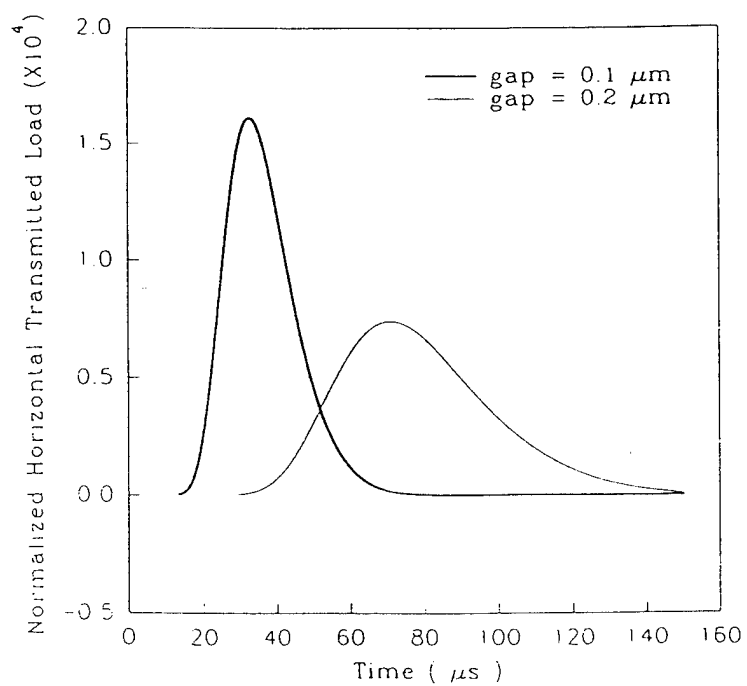
Figure 7.14. Horizontal Transmission for Moderately Anisotropic Model
with Different Initial Particle Gap Spacings

191
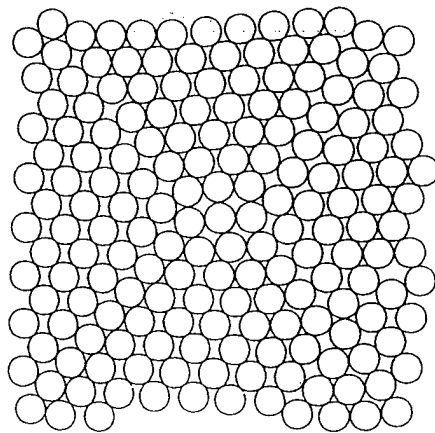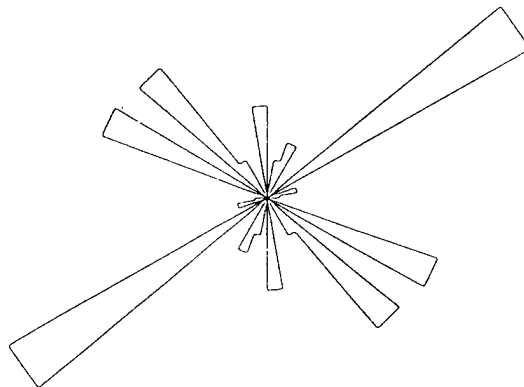
(Assembly)

(Branch Vector Distribution)

Figure 7.15. Weakly Anisotropic Material Model
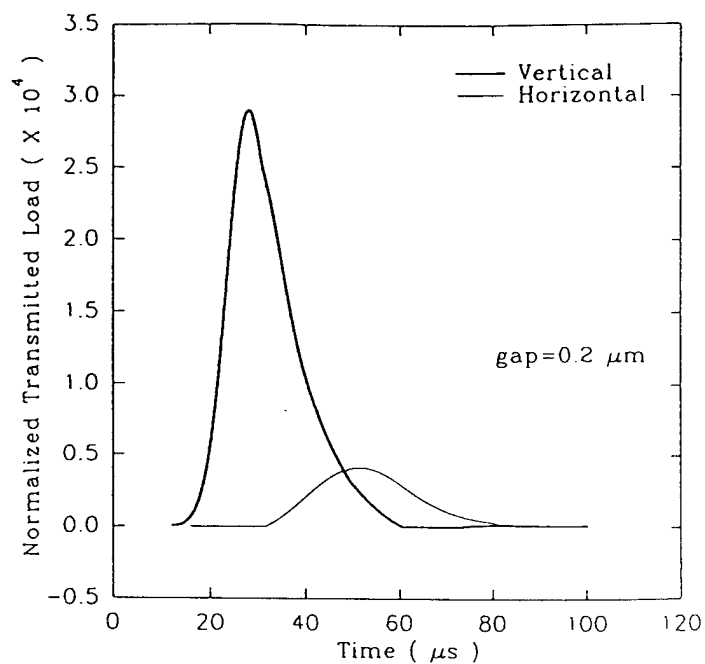
Figure 7.16. Average Transmitted Wave Amplitude

For Weakly Anisotropic Assembly
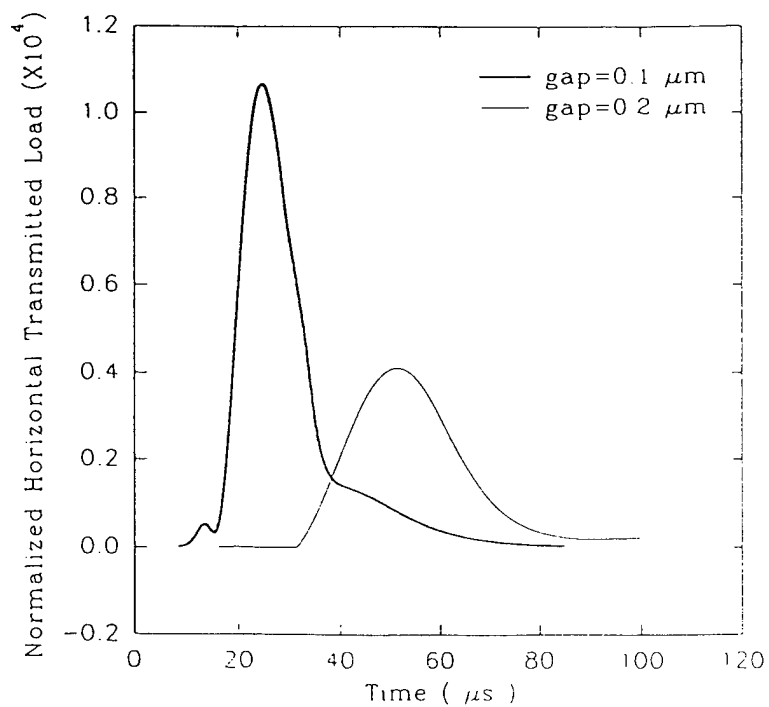
Figure 7.17. Horizontal Transmission for Weakly Anisotropic Model

with Different Initial Particle Gap Spacings

193

Detonator Cable

Explosive

Fluid Saturation

Main Chains

a.) Single Chain

b.) Hexagonal Close Packed (HCP)
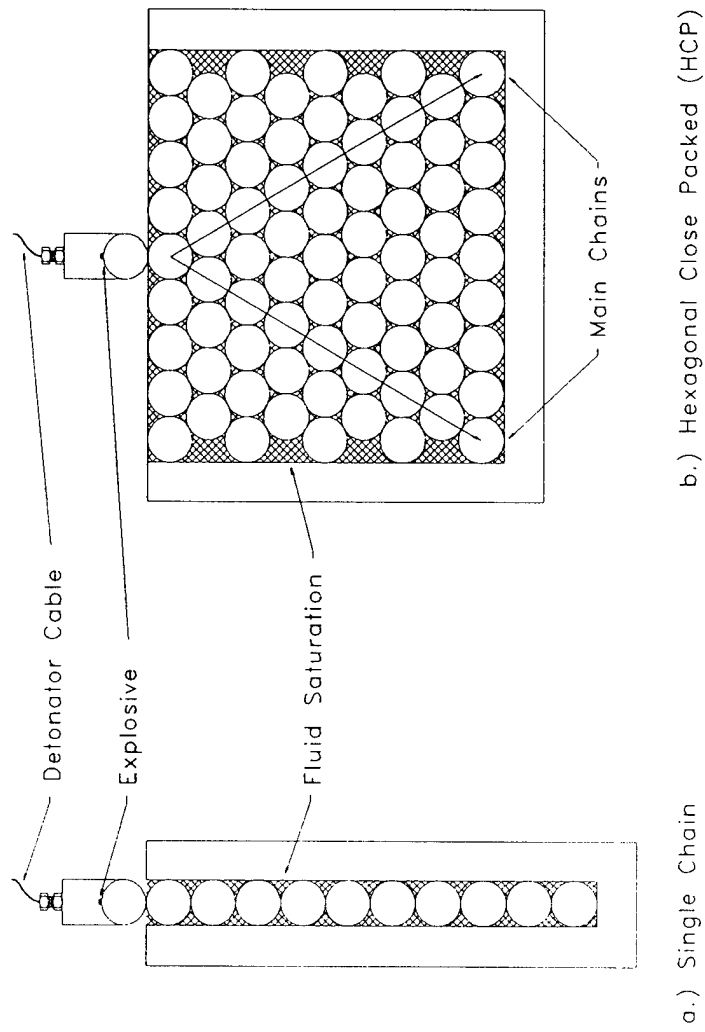
Figure 7.18. Experimental arrangement for 1-D and 2-D saturated assembly experiments.

Frame 1 Frame 2 Frame 3 Frame 4 Frame 5 Frame 6 Frame 7 Frame 8 Frame 9 Frame 10 Frame 11 Frame 12 Frame 13 Frame 14 Frame 15 Frame 16 Frame 17 Frame 18 Frame 19 Frame 20
t=138 μs t=142 μs t=146 μs t=152 μs t=157 μs t=163 μs t=168 μs t=174 μs t=179 μs t=185 μs t=197 μs t=203 μs t=208 μs t=213 μs t=219 μs t=225 μs t=231 μs t=236 μs t=243 μs t=249 μs

Figure 7.19. Photoelastic fringe patterns of a single chain model saturated with water.

Frame 1 Frame 2 Frame 3 Frame 4 Frame 5 Frame 6 Frame 7 Frame 8 Frame 9 Frame 10 Frame 11 Frame 12 Frame 13 Frame 14 Frame 15 Frame 16 Frame 17 Frame 18 Frame 19 Frame 20
t=164 μs t=169 μs t=175 μs t=181 μs t=183 μs t=194 μs t=200 μs t=205 μs t=211 μs t=217 μs t=233 μs t=238 μs t=242 μs t=249 μs t=253 μs t=258 μs t=264 μs t=270 μs t=276 μs

Figure 7.20. Photoelastic fringe patterns of a single chain model saturated with Dow Corning 200 fluid (10 cs).
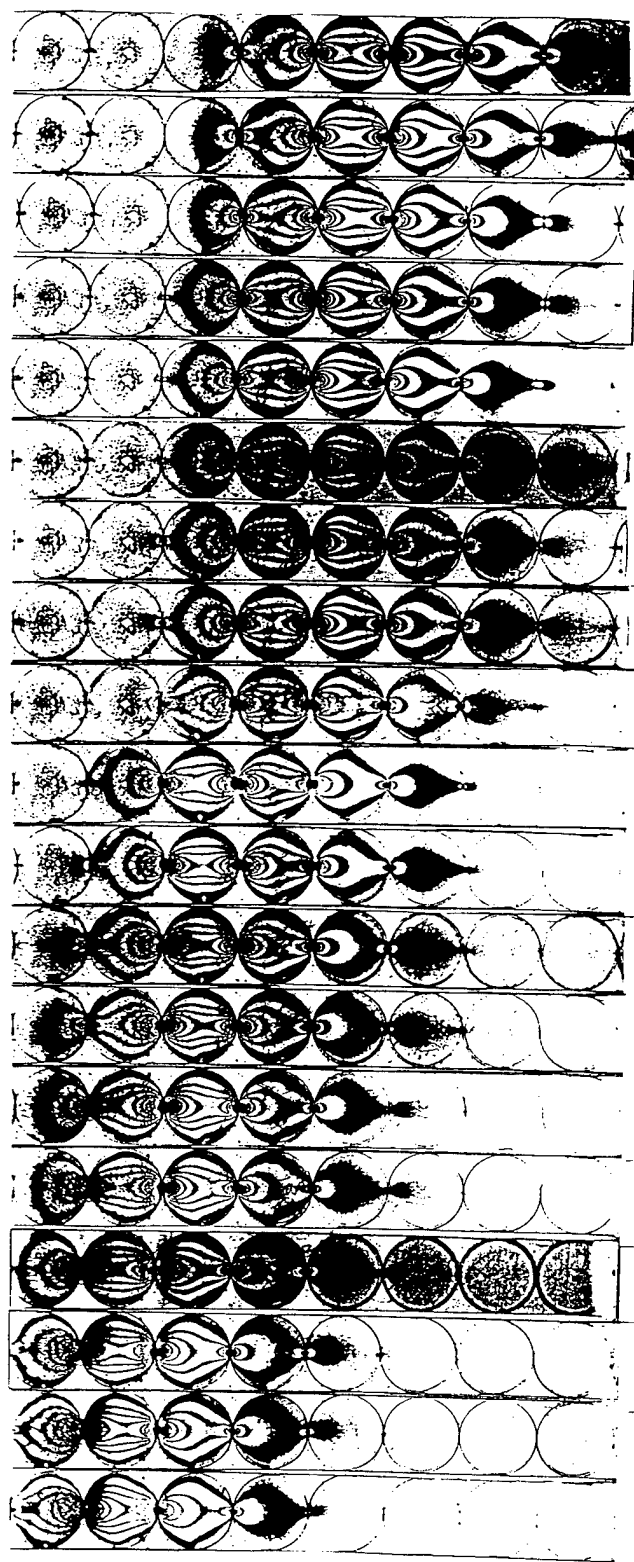
196

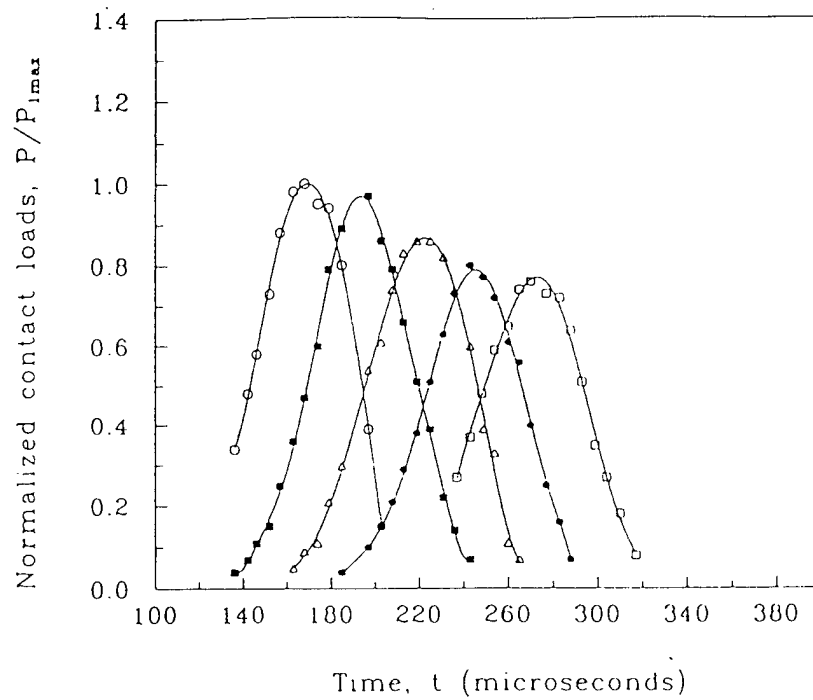Figure 7.21. Photoelastic fringe patterns of a single chain model saturated with Dow Corning 200 fluid (100 cs).

Frame 1 Frame 2 Frame 3 Frame 4 Frame 5 Frame 6 Frame 7 Frame 8 Frame 9 Frame 10 Frame 11 Frame 12 Frame 13 Frame 14 Frame 15 Frame 16 Frame 17 Frame 18 Frame 19 Frame 20
t=215 μs t=221 μs t=226 μs t=232 μs t=238 μs t=244 μs t=249 μs t=255 μs t=261 μs t=267 μs t=280 μs t=291 μs t=297 μs t=302 μs t=307 μs t=312 μs t=318 μs t=324 μs t=330 μs

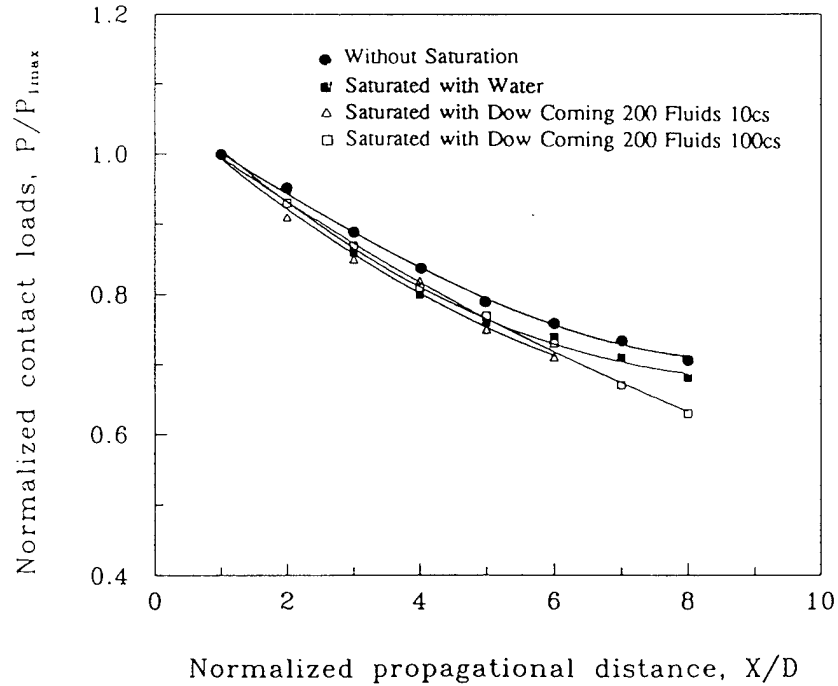Figure 7.22. Contact load as a function of time for 1-D disk chain saturated with water.

Figure 7.23. Comparison of wave amplitude attenuation in 1-D disk chain saturated with different fluids.
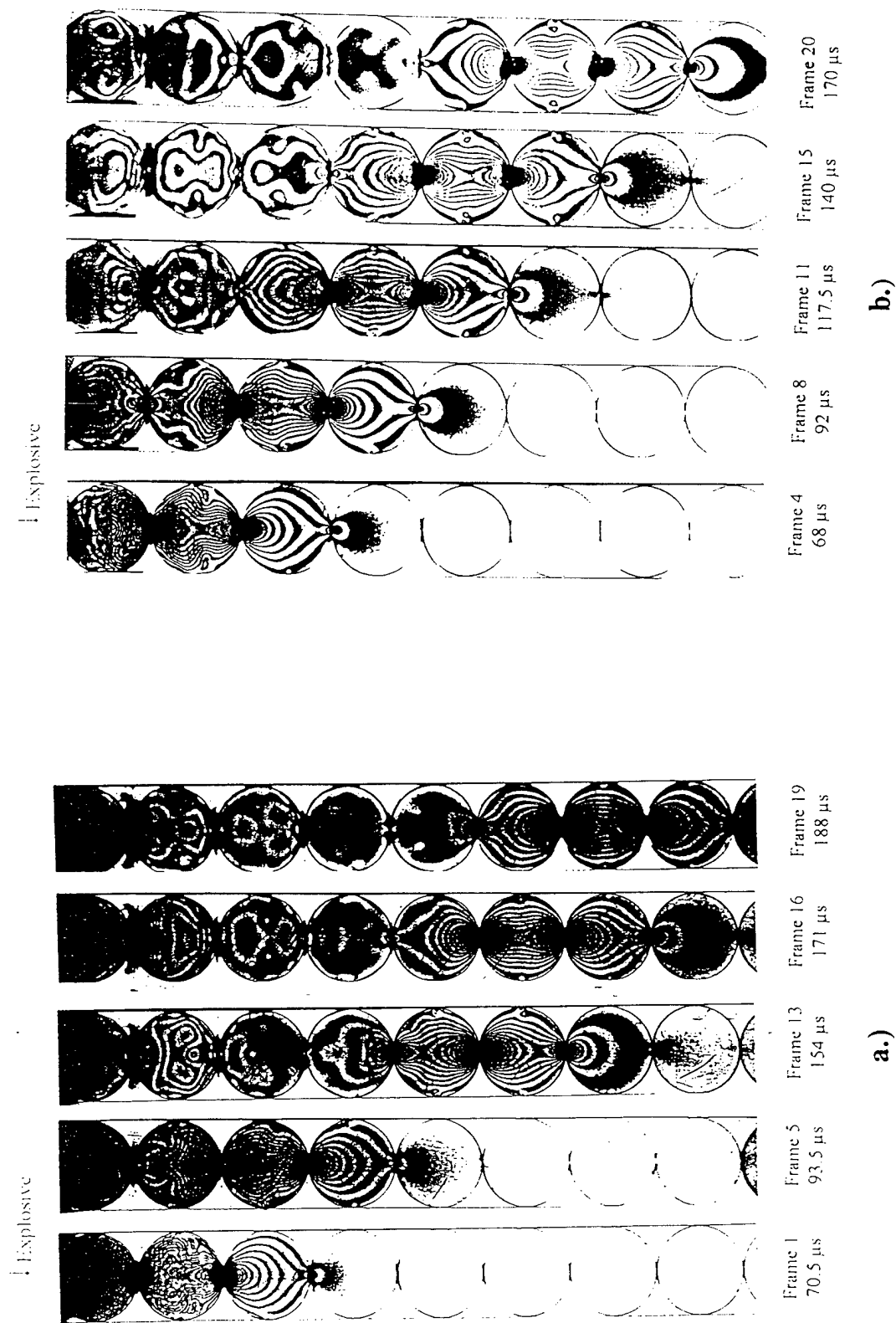
Figure 7.24. Typical isochromatic fringe patterns from dynamic experiments with H-100 particles and a.) partial water saturation and b.) partial glycerin saturation.
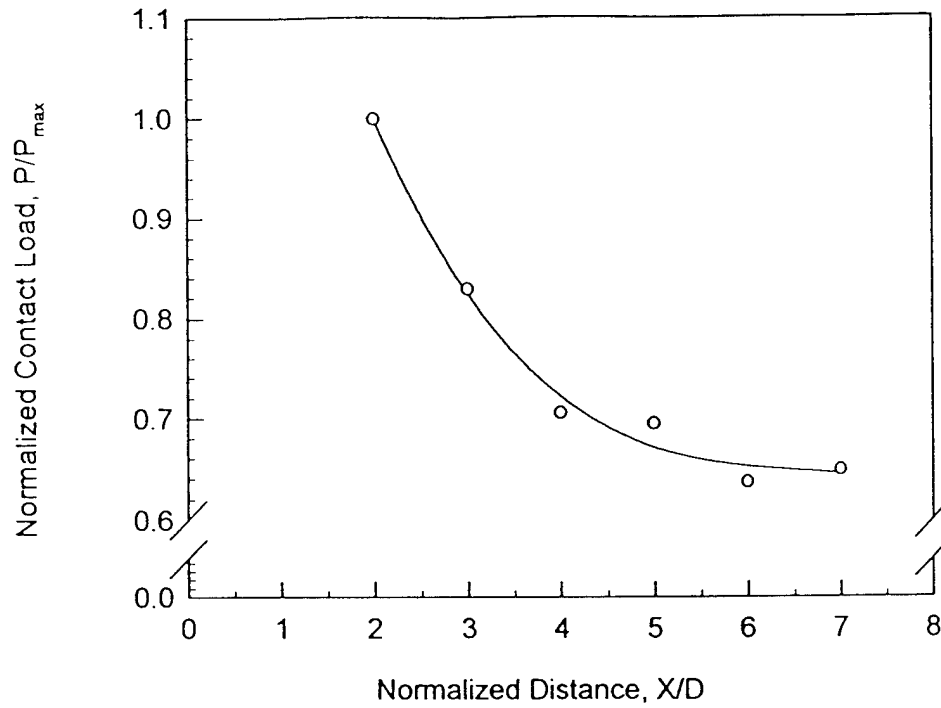
Figure 7.25. Plot of peak contact load as a function of distance propagated for a single chain of disks partially saturated with water.
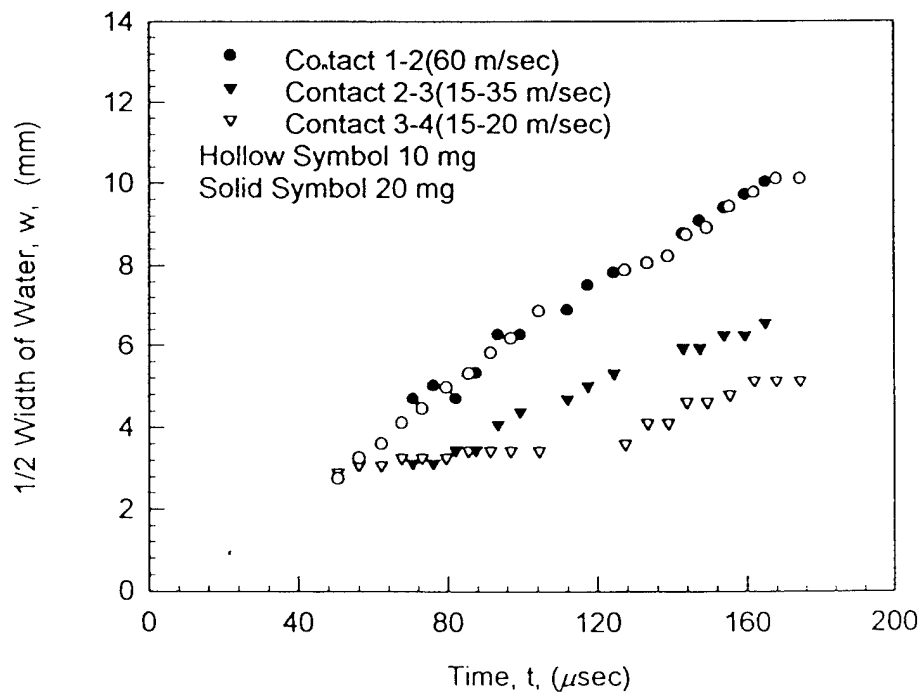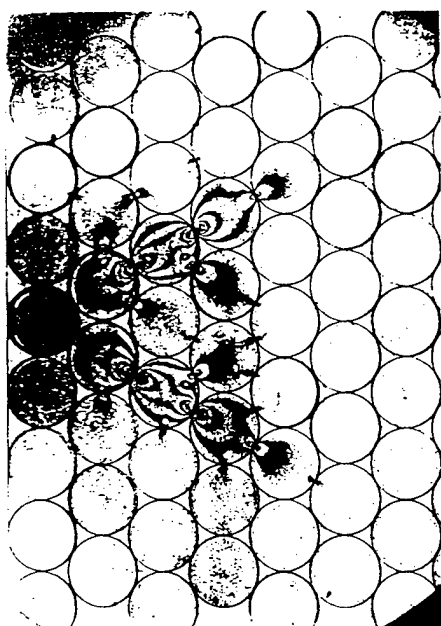

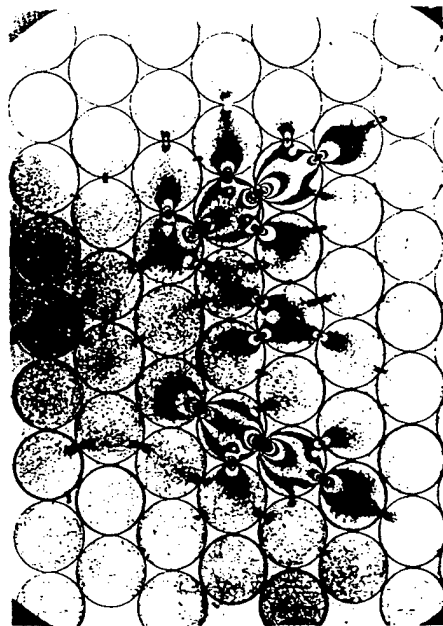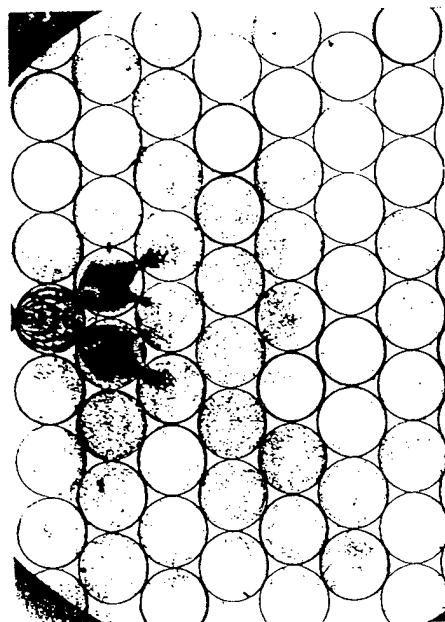Figure 7.26. Plot of half width of water versus time to determine water velocity.

Frame 5, t = 113 μs

Frame 12, t = 150 μs

Frame 1, t = 64 μs
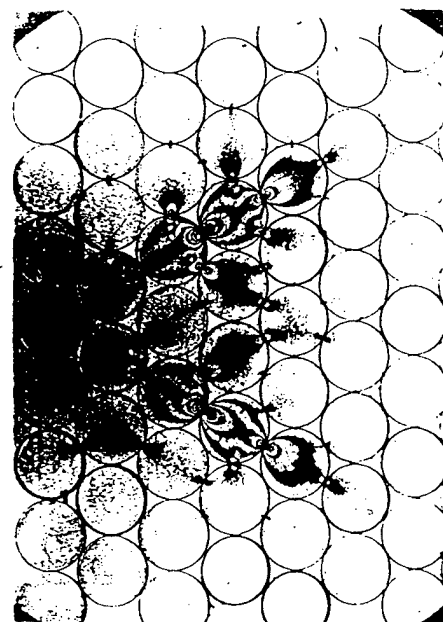
Frame 7, t = 129 μs

Figure 7.27. Photoelastic fringe patterns of HCP model saturated with water.

Frame 6, t = 84 μs

Frame 14, t = 136 μs

Frame 2, t = 63 μs
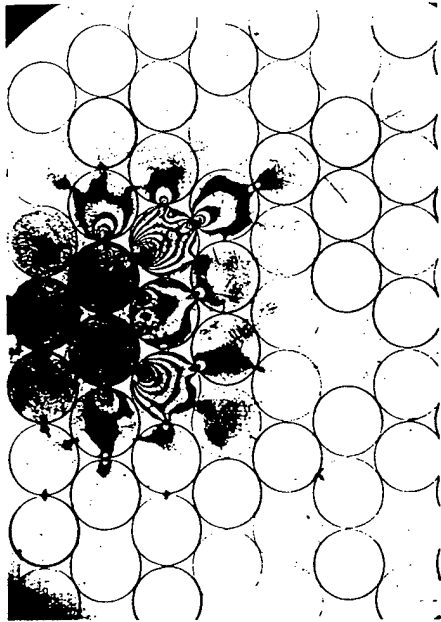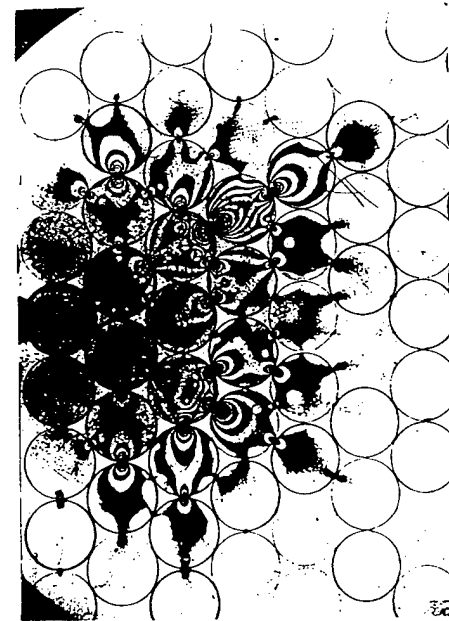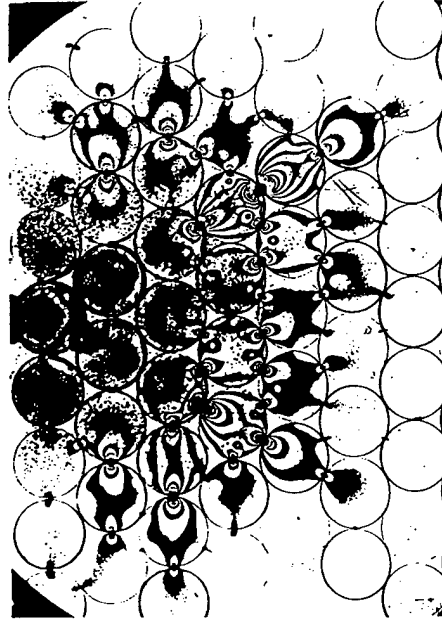
Frame 10, t = 117 μs

Figure 7.28. Photoelastic fringe patterns of HCP model saturated with 10 cs fluid.
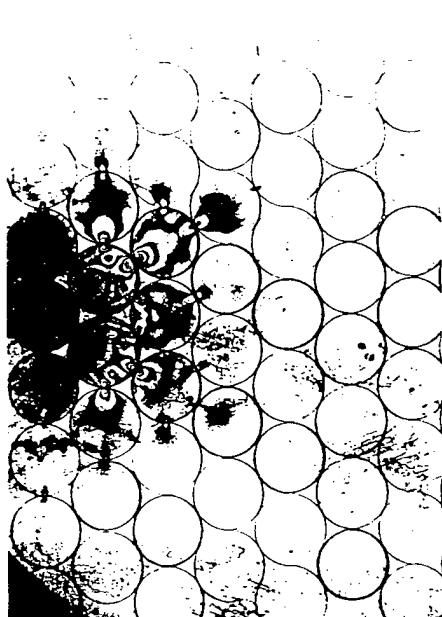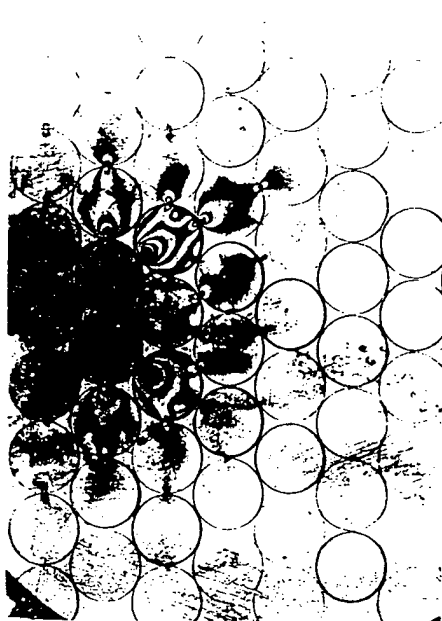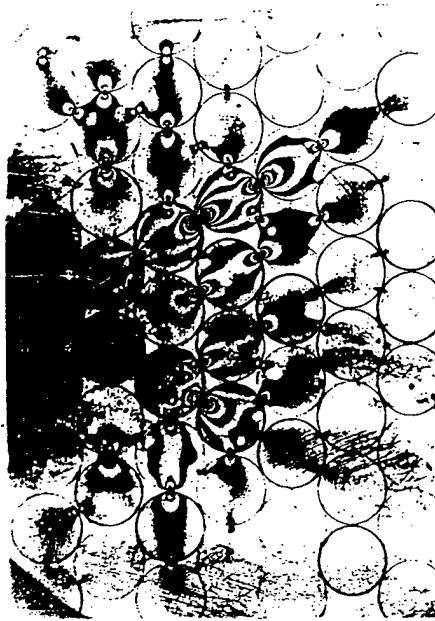
Figure 7.29. Photoelastic fringe patterns of HCP model saturated with 100 cs fluid.

Frame 6, t = 85 μs

Frame 14, t = 135 μs

Frame 3, t = 68 μs

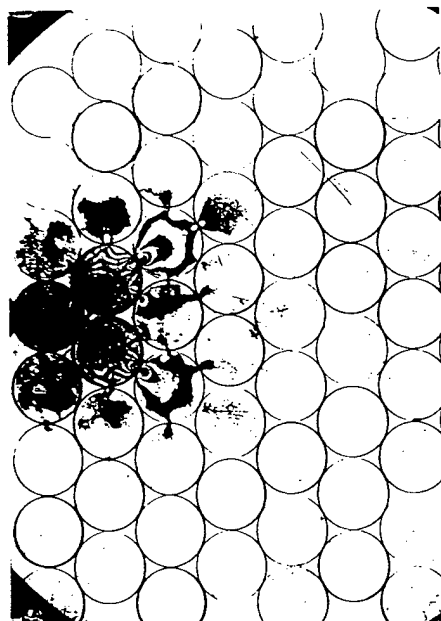Frame 10, t = 118 μs

FRAME 5, t = 72 μs

FRAME 16, t = 148.5 μs

FRAME 3, t = 60.5 μs
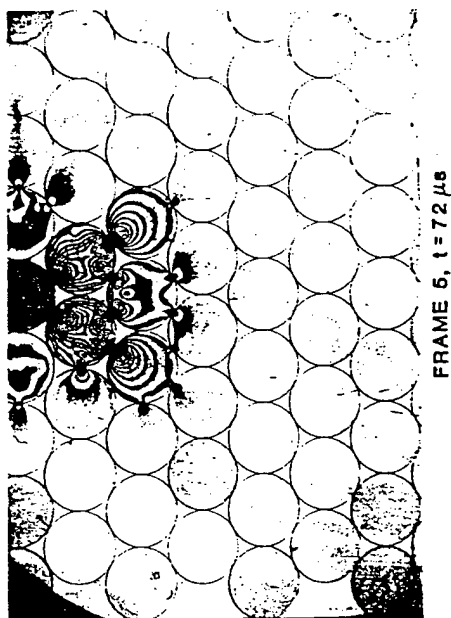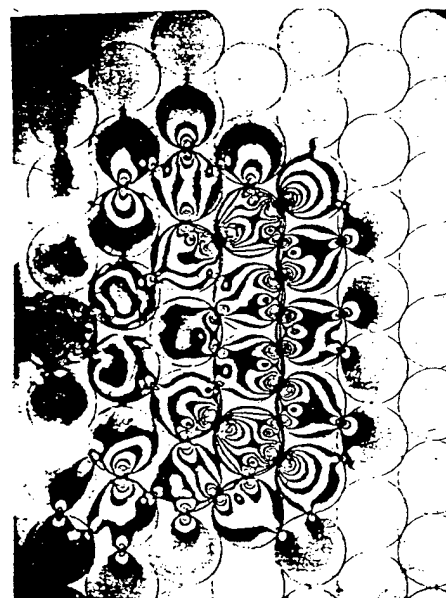
FRAME 12, t = 125 μs

Figure 7.30. Photoelastic fringe patterns of HCP model saturated with air.

CHAPTER 8

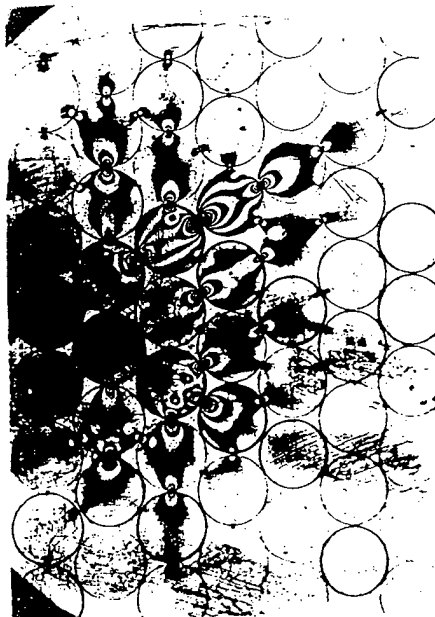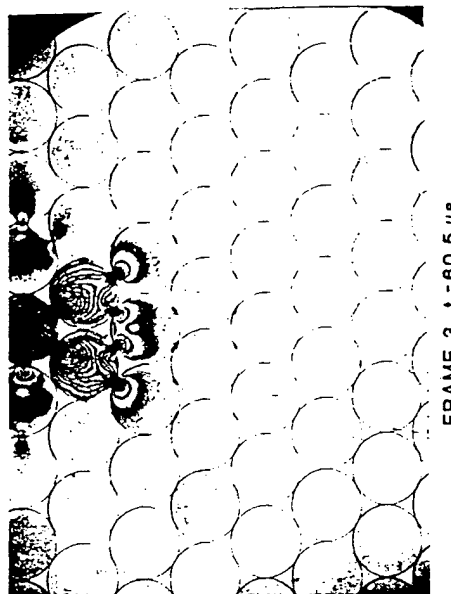# EVALUATION OF FIBER OPTIC SENSORS FOR STRAIN MEASUREMENTAND PRELIMINARY APPLICATIONS TO CONTACT MECHANICS

8.1 Summary

Three different fiber optic sensors have been evaluated for their potential application to contact mechanics problems. The sensors included the Mach-Zehnder and Fabry Perot interferometers and the figure of eight intensity based sensor. In general, the sensors all responded to the strains or displacements which resulted from static diametral compression of disks and or spheres. The individual sensors each had their intrinsic positive features as well as drawbacks.

The Mach-Zehnder interferometer shows promise for laboratory based research where the local environment can be more closely controlled. Interferometric sensors typically provide much finer resolution and as such must be more closely controlled. The sensor suffers from lead in and lead out sensitivity which would be more difficult to control outsitde of the lab. In contrast, the Fabry-Perot interferometer suffers none of the lead sensitivity problems of the Mach-Zehnder due to its unique design. Additionally, interferometric sensors require a monochromatic, coherent light source which is typically a laser or laser diode.

The intensity based sensors typically are fed with a light emmitting diode (LED) as monochromatic, coherent light is not needed. The mechanism by which the light is affected and the resolution capabilities of the detection equipment result in a sensor which does not have the absolute sensitivity of interferometric sensors, however, the sensor tends to be more robust and less susceptibel to environmental effects. With this in mind, an intensity based sensor was developed and subsequently evaluated.

The sensor incorporates an extremely simple design, light source, and detector. Testing was done using quasi-static extension, a simple oscillating cantilever beam, and a small shaker capable of frequencies up to 10 kHz. The sensor shows response over a wide range of 410 mm. The response has two distinct linear regions with a central non linear region. For small displacements, the sensor shows excellent frequency response up to 10 kHz.

At this stage, no attempt has been made to theoretically predict the light loss behavior associated with this macrobend sensor(Marcuse, 1976, Lagakos, et.al., 1987), but rather to simply demonstrate the basic function of the novel geometry of the sensing element and determine the applicability to contact mechanics.

8.2 Introduction

In this chapter, an attempt has been made to study the applicability of both attached and embedded fiber optic sensors to measure in plane and out of plane strain due to contact loadings, as well as displacements due to the same. Both two and three dimensional experiments have been conducted. Prior to applying fiber optic sensors to contact mechanics problems, they were evaluated to determine the maximum strains that could be measured reliably. In the past, resistive foil strain gages have been used successfully to evaluate contacts in both static and dynamic problems (Xu and Shukla, 1993). However, strain gages are limited in their use to surface strain measurements. Also, they cannot be easily bonded to certain kinds of materials like rock and concrete. Fiber optic sensors on the other hand can be used for both surface (Sirkis and Taylor, 1988) and interior strain measurements (Murphy *et. al.*, 1989). Fiber optic sensors have also been shown to be applicable for use in electrically noisy environments (Griffiths, 1991), and in high temperature areas (Wang, 1992). The ultimate aim of the study is to accurately predict local strains at any point in a three dimensional body for both static and dynamic loading.

Fiber optic sensors have long been touted for their potential application to 'smart structures' applications. With the development of smart materials several off shoot technologies have also evolved. In particular, the use of optical fibers as sensors for the measurement of mechanical quantities has seen considerable growth. Most of these sensors are still intricate in their construction and require elaborate electronics. This paper presents a rather simple design for an intensity based displacement transducer with a large operating range.

A sampling of the benefits of fiber optic sensors over their conventional counterparts include their resistance to electromagnetic interference, resistance to hostile environments, light weight and small size. Also, an extensive array of ancillary components and systems have been developed by the communications industry and are available at relatively low cost. These

206

many benefits are being exploited more and more for modern sensor design. Several studies using fiber optics for sensor design have appeared in recent years. A complete review of all of these is beyond the scope of this document but the following will serve to demonstrate the depth of the field of fiber optics as sensing elements.

One of the first demonstrations of the potential for optical fibers to be used as sensors was published in 1978 (Butter and Hocker, 1978). Butter and Hocker (1978) showed that optical fibers could be configured as a Mach-Zehnder interferometer and strain applied to one arm of the arrangement would result in a spatial shift of the interference pattern. This shift of the interference fringes was directly related to the applied strain. After this demonstration, many different groups and laboratories have accelerated the progress (e.g., Sirkis and Taylor, 1988, Lee, et. al., 1989, and Narendran, et. al., 1991, 1992 and 1993).

Applications of fiber optic sensors cover many diverse fields and needs. In recent years fiber optic sensors have gained considerable interest from the engineering community with the greatest interest lying in the development of 'smart materials' (Claus, 1990, and Measures, 1992). Their inherent geometry also makes them ideal for embedding in modern composite structures and applications exist for non destructive testing (DePaula, et. al., 1982, and Narendran, et. al., 1995).

Fiber optic sensors have also found many applications in structural civil engineering problems (Ansari, 1993). One area of testing and experimentation that has not yet been fully explored with regard to fiber optic sensors is soil mechanics. As an example, strain measurements during axial or triaxial testing of soils and granular substances is mostly restricted to measuring the platen or end plate displacements. This method produces average strains over the entire specimen but is not adequate for measuring local deformations. An alternative is to place instrumentation directly on the specimen membrane. One of the disadvantages of this technique is that the sensing mechanism may either reenforce the local region or the weight of the sensor may produce adverse effects on the measurement. The problems of reenforcement and sensor weight can be eliminated with the use of fiber optic sensors. Fibers are extremely small and light in weight, and combined with proper sensor configuration, the reenforcing effects can be virtually eliminated.

8.3 Sensor Construction

8.3.1 Mach-Zehnder Interferometer

Construction of a Mach-Zehnder sensor is quite simple, and a schematic of the setup is shown in Figure 8.1. A laser beam is split with a beam splitter and the two resulting beams are then coupled into two separate single mode optical fibers. One of the fibers is chosen as the reference path and the other fiber becomes the sensing arm. The two separate beams are then recombined and the resulting interference pattern is projected onto a photodiode. The interference fringes produced can be related to the axial strain seen by the sensor.

In operation, the fringe pattern remains stationary when the sensor undergoes no strain and the output from the photodiode is constant. When the sensor experiences axial strain, the fringe pattern shifts across the face of the photodiode resulting in a sinusoidal type output. It is this sinusoidal output that can be related to the applied strain.

Care must be taken with the Mach-Zehnder interferometer because all of the fiber in the setup has the potential to affect the light propagating through it. In other words, the entire length of fiber, in either arm, can be the sensing element. Care must be taken to ensure that only the desired measurand is affecting the output signal. This is one of the drawbacks to the sensor and therefore, it is not easily applicable to field applications.

8.3.2 Fabry-Perot Interferometer

Figure 8.2 shows a schematic of an extrinsic Fabry-Perot sensor. The experimental setup is almost the same as that for the Mach-Zehnder and is shown in Figure 8.3. The schematic of the actual sensor, Figure 8.2, shows two pieces of optical fiber that are bonded into a glass tube. The fiber ends are partially mirrored to provide the necessary reflections for a low finesse Fabry-Perot cavity. Fiber diameter that is used in the laboratory is 125 microns due to the availability of the appropriate couplers and equipment for this size fiber. Purchasing ready made sensors is quite expensive and since the sensors may become damaged during experiments, a simple method to manufacture them was needed.

Since this sensor is an interferometric sensor, a single mode fiber rated to carry the particular input wavelength is used. A helium-neon laser is used in the laboratory so the single mode fiber is purchased to support the 633 nm wavelength. Approximately 0.5 m of single mode fiber is cleaved for the sensor. The completed sensor is later coupled   to the

experimental setup using Norland Lab Splices. The fiber that provides the opposite mirrored surface is a multimode fiber because of its lower cost. This fiber only needs to be long enough to insert into the glass tube but is generally cut to approximately 50 mm for ease of handling.

The mirroring is done with sputtering equipment and aluminum is used to create the mirrors. The fibers are first carefully cleaved and cleaned to provide a flat surface upon which to sputter the aluminum. Sputtering times may vary with equipment so a glass slide is first placed in the sputterer to determine an appropriate time. Reflectivity should be approximately 25% on the single mode fiber and from 25% to 100% on the multimode fiber.

After the fibers were coated, the glass tube was prepared. A short length of glass tubing, approximately 25 mm, was cut and one end cleaved flat. The tubing measured 135 microns on the inside diameter and 190 microns on the outside diameter. Both the prepared tubing and one of the coated fibers were placed into a jig that was developed to allow alignment of the fiber and the tube under an optical microscope. The jig is shown in Figure 8.4 and consists of an X-Y positioner with Z translation and a mirror holder/positioner that is used to allow the fiber and the tube axes to be made parallel. This jig was angled, with respect to the horizontal, to allow viewing of the tube end while the fiber was being positioned for insertion. This open tube end always faces up and is located over the small white reflective surface to provide back-lighting.

The first fiber was inserted into the prepared end of the tube and bonded using a five minute epoxy. The fiber was inserted so as to achieve the desired gage length and to allow approximately 10-40 microns between coated fiber ends when the sensor was completed. After the epoxy was cured, the tube was cleaved again to the desired gage length, the second fiber was inserted and positioned for the correct gap, and the epoxy was applied to the second fiber. Once the epoxy has cured, an accurate measurement of the finished gage length is made under the microscope, and the sensor is ready for use.

8.3.3 Figure of Eight Microbend Sensor

The figure eight sensor utilizes a continuous piece of multimode optical fiber (Corning 62.5/125 μm LNF™, NA=0.275) 'tied' into the shape of a figure of eight. A sketch of the sensor is shown in Figure 8.5, where the dimension z will hereto be referred to as sensor size. The geometry allows the natural stiffness of the fiber to act as a restoring force which holds

the shape of the sensor during extension and compression. Put simply, the fiber will attempt to 'unwrap' itself and return to a straight line were it not for the constraint imposed by the knot geometry. Some improvements over previously reported bend loss type sensors are that the sensor requires no external mechanism to cause the bends and unlike sensors incorporating pre-molded sinusoidal deformations (Weiss, 1989) or etching (Vaziri and Chen, 1992), this sensor responds equally as well in tension and compression.

This sensor functions as an intensity based optical fiber strain or displacement transducer when the fiber is bonded to a body at two points, one on each side of the loops. Note that the loops remain free to move and it is the fiber on each side of the loops that is to be bonded. The initial distance between the bond points will determine the initial gage length, while the dimension z determines the sensitivity. As the sensor is extended, the distance between bond points will change, and will be referred to as x. Since multimode fiber is used in the construction, a simple LED/PIN diode can be used for the light source and detector. Figure 8.6 shows a schematic of the setup for the sensor with the associated electronics for light source and detection.

As the two fixed points are displaced with respect to each other, the radii of curvature of the sensor loops changes. A tensile strain (extension) would result in a shrinking of the sensor loops and drop in light intensity measured at the detector. Conversely, a compressive strain would result in an expansion of the loops and an intensity increase at the detector.

The light source was a Motorola MFOE1200 diode coupled to a driving circuit utilizing a 10V DC supply. The detector was a Motorola MFOD1100 (matching component for the diode) with an 18V DC bias, which was coupled to a twenty times amplifier with a variable DC offset. The amplifier was powered with ±12V DC supply.

8.4 Calibration

The principle of operation of a Mach-Zehnder interferometric fiber optic sensor was mentioned above. The axial strain, ϵ_x, is directly proportional to the number of fringes, N, moving past a fixed point and can be given as (Butter and Hocker, 1978)

$$\epsilon_x = DN \tag{8.1}$$

where D is the proportionality constant and can be written as

$$D = \left(\frac{\lambda}{nl} \right) \left[\frac{1}{1-c} \right] \qquad (8.2)$$

where λ is the vacuum wavelength of the optical beam, l is the gage length of the sensor, n is the refractive index of the fiber, and c is a constant which depends on strain optic coefficients, the refractive index, and Poisson's ratio of the fiber. It is possible to calculate D for pure silica, however, dopants are used to alter the refractive index of the core of the fiber to keep the light propagating in the fiber. Hence, the fiber has to be calibrated to determine the constant D.

The Mach-Zehnder sensor was calibrated using a cantilever beam setup as shown in Figure 8.7. The fiber sensor was mounted to a cantilever beam, opposite a conventional strain gage. The beam was displaced and a plot of the axial strain recorded from the strain gage vs. the fringes was made for a particular gage length of the fiber. A straight line was fit through the data points. The slope of this straight line was the constant D as shown in Figure 8.8. The strain required to cause one fringe to move across a fixed point is inversely proportional to the gage length of the sensor. In other words, equation (8.1) can be written as shown in equation (8.3) where A is the fringe strain sensitivity constant for the sensor. The fringe strain sensitivity can be defined as the strain required to cause one fringe to move across a given

$$\epsilon_x = \left(\frac{A}{l} \right) N \qquad (8.3)$$

point for a unit gage length of the sensor. The experimentally obtained value for A was found to be 625 μmm/mm fringe^{-1} mm.

Strain is obtained from the Fabry-Perot sensor in much the same way as the Mach-Zehnder sensor. However, the relationship between the number of fringes passing and the strain is only dependant on the wavelength of the light propagating and the gage length of the sensor. Calibration of the sensor is not necessary. The relationship between the fringe shift and the axial strain is explicitly given by equation (8.4). Again, N is the number of fringes, λ is the wavelength of light, and L is the measured gage length of the sensor.

$$\epsilon_x = \frac{\lambda N}{2l} \qquad\qquad (8.4)$$

The figure eight sensor must be calibrated much the same as the Mach-Zehnder sensor. The output intensity and strain gage data was measured and cross plotted. Figure 8.9 shows the resulting calibration plot whose slope was found to be 36 μm/mV.

8.5 Evaluation of the Fiber Optic Sensor

8.5.1 Tension Testing/ Extension

The Mach-Zehnder sensor was used for the initial evaluation of the fiber optic sensor. A single mode fiber with an outer diameter of 80 microns was stripped of its plastic jacket in the region that was to be bonded to the specimen. The plastic jacket must be stripped to ensure proper strain transfer between the specimen and the optical fiber. Also, the surface of the specimen must be treated in accordance with conventional strain gage techniques prior to attachment. Two pieces of tape were placed on the specimen leaving the desired gage length exposed between the tape pieces. These tape pieces serve as masks so that only the desired length of fiber will be bonded. The tape mask was then sliced along the direction that the fiber will run. This was done to allow the tape to be removed after the fiber is bonded. Figure 8.10 shows the specimen with the tape mask in place. The fiber was then laid into the slice and bonded. After the adhesive cures, the tape is removed.

A simple tension test was used to characterize the fiber sensor under axial loading conditions. A schematic of the setup for the Mach-Zehnder interferometer was shown in Figure 8.1. The specimen was a dog bone specimen with a resistance type strain gage bonded to one side of the specimen and the fiber-optic sensor bonded to the other side, directly opposite the strain gage. The experiments were designed for axial strain measurements only. To standardize the bonding procedure, both sensors were bonded with M-Bond 200, a cyanoacrylate based adhesive, using the technique described in Measurements Group Bulletin 309A. Ambient conditions in the laboratory are maintained at 21°C, ± 3, and 65% relative humidity, ± 5.

The specimens were then loaded at a constant strain rate and the strain gage signal was recorded, along with the light intensity signal from the photodiode, with a Lecroy data

212

acquisition system. In each experiment, loading was continued until failure of either the strain gage or the fiber-optic sensor.

Another series of experiments was conducted in which the specimen was loaded in incremental values from an unloaded condition to a failure condition. The specimen was unloaded and removed from the fixture at 500 microstrain increments and taken to an optical microscope for inspection. The specimen was examined and photographs were taken of any significant changes in the adhesive bond. After reconnecting the two sensors to the data acquisition equipment, the specimen was strained to the next incremental value and the procedure was repeated.

Figure 8.11 shows typical output from the strain gage and the Mach-Zehnder sensor for the axial loading experiments. The strain data from both the strain gage and the fiber sensor is shown in Figure 8.12.

It can be seen that the Mach-Zehnder sensor was linear and the sensor can be used for strain measurements. However, the fiber-optic sensor was found to fail at strain levels far below the levels at which conventional strain gages fail. Failure modes could be characterized in two ways:

- the fiber fractures and the sensing signal is lost.
- the fiber delaminates with matrix cracking, resulting in a change in effective sensor gage length.

Note that the delamination and matrix failure is related to the bonding of the fiber and does not represent a shortcoming of the glue. A separate experiment was conducted with only a thin layer of glue and the glue did not show cracking or failure during the experiment. The maximum value reached during this experiment was 2 percent strain.

The data presented in Figure 8.12 shows failure by fracture of the fiber which resulted in loss of the sensing signal and therefore, loss of the interference fringes. Both modes of failure produced unusable data at values between 1.2-1.8 percent strain. Photographs taken during the incremental loading are shown in Figure 8.13. Figure 8.13(a) shows the fiber in an unstrained state and as it appears up until failure. The bright line running down the center of the fiber is the contact between the fiber and the specimen. Note that the glue does not cover the entire fiber but rather forms a bed under the fiber.

In Figure 8.13(b), the delaminated region shows up as a wide, bright band. This is

213

caused by the defracting of the microscope light from the air gap that opened up between the fiber and the specimen. Under actual observation the band appears as colored fringes. Note also that the glue matrix shows cracking. These cracks will always curve toward the portion of the fiber that is unattached and unstrained, and therefore show that delamination has occurred from left to right in the photograph. The right side of the photograph shows the portion of fiber that has not yet delaminated.

Figure 8.13(c) represents an experiment in which the fiber fractured. There is a central crack in the matrix that is aligned with the fracture in the fiber. All other cracks curve toward the fracture area. This matrix cracking shows that subsequent delamination of the fiber occurred after the fracture and ran outward from the fiber fracture in both directions.

Figure 8.14 shows strain data obtained from the incremented experiment. The strain gage data was plotted using a linear regression curve fit. The data shows that the specimen remained linearly elastic throughout the experiment. The first run, represented by the circles, and the second run, represented by the inverted triangles, was made up to 1 and 1.5 percent strain, respectively. Following the second run, observation of the fiber sensor showed delamination, see Fig. 8.13.

Analysis of the raw data showed the effect of the delamination on the fiber sensor output. Figure 8.15 shows an anomaly that occurred at approximately 13,200 microstrain, during the 2nd run. The fringes from the 1st run, where no anomaly was seen, and those that precede and follow the anomaly in the 2nd run, are regular and do not appear distorted.

Since the strain calculation, given in equation (8.1), is based on the gage length, the observed strain will be affected if a change in gage length is not accounted for. This affect can be seen in Figure 8.15, runs 3 and 4. Runs 3 and 4 were made up to 1.6 and 1.7 percent strain, respectively. Fringes from both of these runs showed numerous anomalies.

From these observations, it is believed that the initial delamination occurred at the end of the second run and the damage grew during the 3rd and 4th runs. This damage growth is illustrated by the difference in strain observed in those runs.

From the initial failure experiments, it was determined that the fiber sensor typically failed at strains around 1.5%. The first strain level at which to stop was set at 1% strain, or 10,000 microstrain. In all experiments, the sensor showed no significant changes before reaching this strain level. The 500 microstrain increment was then followed until failure.

From these characterization experiments it was determined that fiber optic sensors which were bonded along their entire length could be confidently used up to a strain level of 1.5 percent. With the figure eight sensor only two points are bonded and the glass fiber does not see the high strains that the specimen does. The sensor geometry is such that the sensor is capable of responding over a larger displacement range.

To investigate the range of the figure eight sensor an experiment was performed on an Instron testing machine using a sensor with an initial dimension of $z=150$ mm (see Figure 8.5) measured from one end of the loops to the other. Outside of the loop region, the fiber was attached to the fixed head and the movable crosshead of the testing machine ($x_{initial}=200$ mm). The crosshead on the testing machine was then extended at a slow speed (12.7 mm/min) while the sensor output was captured on a Nicolet digital storage oscilloscope. The complete plot of sensor output versus extension, x-$x_{initial}$, is shown in Figure 8.16 with the experimental points shown as symbols. Due to the large number of data points, only every 50th data point has been shown. The figure shows three distinct regions; a linear region with shallow negative slope, a nonlinear region, and a second linear region with a large negative slope. Each of these regions have been curve fit with equations. It should be noted that the plot is actually a composite of two separate runs. During the experiment the signal change exceeded the capabilities of the amplifier circuit so the test was stopped and the DC offset was utilized to shift the output level. The amount of the shift was then accounted for when compiling the data into the plot shown.

In the first linear region (0-200 mm crosshead extension from initial), a least squares, first order curve fit was applied. A multiple correlation coefficient squared value, $R^2 = 0.957$, was obtained. Similar treatment was given to the third region (380-410 mm crosshead extension from initial) with an $R^2 = 0.996$. The mean deviation from linearity in these regions was found to be 1.2 and 0.02 percent for the first and second regions, respectively. The maximum deviations from linearity were found to be 7.1 percent for the former and 8.4 percent for the latter region.

The central nonlinear region was fit with a hyperbolic expression of the form given in equation (8.5)

$$y = \frac{ax}{b + x} \ . \tag{8.5}$$

Equation (8.5) represents a rectangular hyperbola where the curve rises asymptotically from 0 to a. The constant b represents the value of x at which the function y has reached 0.5a. Comparing this description of the behavior of the curve described by equation (8.5) to the graph shown in Figure 8.16, it should be obvious that some manipulation of the expression is required before it can be utilized to fit the experimental data.

The first step is to solve equation (8.5) for x in order that the curve may be mirrored about the y axis by multiplying the resultant expression by negative one. Additionally, the curve must be shifted by some constant values in both the x and y directions (constants c and d, respectively, below). The new expression for x is given as

$$x = - \frac{(y + d)b}{a - (y + d)} + c \ . \tag{8.6}$$

Lastly, solving equation (8.6) for y and combining constants yields

$$y = \frac{e + fx}{g - x} \ , \tag{8.7}$$

where linear combinations of a, b, c, and d have been incorporated into the new constants e, f, and g for brevity.

A Marquardt-Levenberg algorithm was used to determine the parameters which minimize the least squares of the sum of differences between the dependant variables and the observed values. The result for the three curve fitting operations is a set of three functions which depend upon the extension from the original sensor size of z=150 mm

$$f(x) = \begin{cases} y = m_1 x + b_1 & 0 \le x \le 200 \\ y = \dfrac{e x + f}{g - x} & 200 < x \le 380 \\ y = m_2 x + b_2 & 380 < x < 410 \end{cases}, \tag{8.8}$$

216

corresponding to the three regions described earlier. An important note is that Figure 8.16 represents a complete calibration plot for the sensor. However, as the extension from the original size is a somewhat impractical reference, a relationship between sensor size, z, and crosshead extension, x was sought.

Another experiment was conducted in which the sensor was extended over approximately 375 mm. The initial sensor size was set to z=150 mm and extension was begun. Sensor dimension was measured at discrete points during the extension and the resulting plot is shown in Figure 8.17. The figure shows a linear relationship between sensor size, z, and extension, x, which allows a direct transformation between the two through another first order least squares curve fit.

The data of Figure 8.16 was used to evaluate the sensitivity of the sensor. Figure 8.18 shows the sensitivity, defined as the change in output per unit input, as a function of sensor dimension. The linear relationship derived from figure 4 transforms sensor extension to sensor size. The sensitivity is defined as the derivative of the output with respect to the input which in this case is done for the three separate functions of equation (8.9). Figure 8.18 better illustrates the various sensitivity regions and the fact that the sensitivity is directly related to the size of the sensor. As the sensor size decreases, the loop radii also decreases causing more light to be lost for a given input and thus increasing sensitivity.

Using the parameters obtained from the curve fitting of Figure 8.16 and the derivatives of the functions defined in equation (8.9), the sensitivities were determined for the three regions. As stated, the smaller the sensor dimension, the higher the sensitivity. In its most sensitive configuration, (z=8-12 mm loop-to-loop dimension) the calibration constant was found to be approximately 475 mV/mm. Referring back to Figure 8.16, the linear range at the highest sensitivity corresponds to the region of maximum extension (380-410 mm). So according to the data presented, the sensor has a sensitivity of 475 mV/mm over a range of approximately 30 mm at the highest sensitivity level. The second linear region shows a lower sensitivity but has a broader range. Namely, the sensitivity is approximately 8 mV/mm over a range of 200 mm. The nonlinear region represents a continuously changing sensitivity over approximately 160 mm.

As the figure eight sensor was developed in our laboratory, significantly more characterization was required in order to obtain a degree of confidence in the sensors

behavior. Further experimentation was required to explore such things as repeatability and frequency response.

The plot of Figure 8.19 shows the results of an experiment to assess the repeatability of sensor construction and performance with minimum effort expended in sensor construction and bonding. For this or any other experiment, there were no special fixtures or jigs used. Four sensors were bonded on one end to a fixed point and the other end to a micometer driven translation stage. The sensors were individually connected to the light source and detector and displaced approximately 3 mm while the output was recorded. The plot demonstrates good repeatability in sensor performance without sophisticated sensor construction fixtures or bonding procedures.

The sensor was then bonded to a cantilever beam opposite an electrical resistance strain gage as shown in Figure 8.20. The beam was displaced and allowed to vibrate freely while both the strain gage output and the optical fiber sensor output were captured on an oscilloscope. The fiber sensor output was zero shifted and linearly scaled to fit the strain gage data with the result being shown in Figure 8.21. The figure shows that the fiber optic sensor matched the electrical resistance strain gage quite well and showed no hysterisis. The match is so good that the two signals are virtually indistinguishable from each other and, consequently, only every 10th data point is plotted for the fiber sensor. The reader should not be mislead into thinking that the peak values from the fiber sensor do not correspond to those of the strain gage as this is only an artifact of the plotting scheme. In fact, the mean of the error between the strain gage signal and the fiber optic sensor was found to be less than 1 percent. This experiment also served as a low frequency response test (25 Hz) for the sensor.

Lastly, one side of the sensor was bonded to a fixed surface and the other end was attached to a Wilcoxon Research F4/F7 electromagnetic/piezoelectric shaker system. The system was driven by a Hewlett-Packard spectrum analyzer which was also used to collect data from both a built in accelerometer and the fiber optic sensor. The shaker was driven with a sinusoidal signal at 1,3,5,7 and 10 kHz. Figure 8.22 shows a portion of the time series for both the fiber optic sensor and the accelerometer subject to a frequency of 3 kHz. Fast Fourier transforms (FFT's produced automatically by the analyzer) for the 3 kHz run are shown in Figure 8.23.The frequency plots show that the fiber optic sensor is in excellent agreement with the accelerometer with a much sharper peak in the fiber optic sensor data. It

should also be noted that this data is for a single run with no averaging which would tend to smooth the baseline noise in the data. All other tests produced similar results and the frequency plot for an oscillatory frequency of 10 kHz is shown in Figure 8.24 for further comparison.

These frequency plots show excellent modal response from the sensor. However, the fiber optic sensor seems to suffer from a phase problem between 5-7 kHz. In this region the fiber optic sensor output shifts 180° in phase with respect to the accelerometer. Then at 10 kHz the fiber optic sensor flips 180° again. This phase shift shows no effect on the frequency resolution capabilities but it should be acknowledged that the time domain data would not be in agreement. So, while the sensor works quite well for frequency resolution, the data can not yet be reliably transformed into absolute displacements at higher frequencies.

8.6 Experimental Procedures for Contact Strain or Displacement Measurements

The first set of experiments was aimed at applying fiber optic sensors to measure strains due to a static load. Disks 32 mm in diameter were machined from 6 mm thick plexiglass sheets. A fiber-optic Fabry-Perot strain sensor was bonded to the surface of the disk, close to the point of the applied load. The disk was then loaded in compression and data was collected from a PCB load cell and a photodiode using a Lecroy data acquisition system. The disk was loaded to approximately 1000 N.

The second set of experiments were designed to measure out of plane strains in a disk using the same loading configuration as that used with the Fabry-Perot, however, a Mach-Zehnder sensor was used. A 2 mm hole was drilled through the thickness of the disk. The jacket on the fiber was removed and the fiber was embedded through the thickness using a chemical called Envirotex, whose mechanical properties are very similar to those of plexiglass.

Again, a piezoelectric load cell placed directly below the disk was used to acquire the loading data. From theory, strains can be calculated at any point on the disk if the load is known. As mentioned, the fiber was embedded on the loading axis and close to the contact point so that Hertz equations could be utilized for the analysis. A Lecroy data acquisition system was used to record both the fiber optic and load cell signals.

For the figure eight sensor, the experiment again invloved circular disks but two disks were used and the sensor was bonded from the center of one disk to the center of the second.

In short, the relative displacement between centers due to an applied load was measured. The disks were loaded at 0.01 inch per minute and the output light intensity was recorded during the loading.

For the three dimensional experiments, 25.4 mm plexiglass spheres were embedded with a fiber, utilizing the Mach-Zehnder sensor, through a 2 mm hole. The experimental procedure was the same as that for the disks with the embedded fiber.

8.7 Theory

8.7.1 Two dimensional strains

The stress field equations for a disk are given in (8.5), (8.6), and (8.7) (Smith and Liu, 1953).

$$\sigma_{zz} = -\frac{b}{\pi\Delta}\left[z(b\phi_1 - x\phi_2) + \beta z^2\phi_2\right] \tag{8.5}$$

$$\sigma_{xx} = -\frac{b}{\pi\Delta}\left[z\left(\frac{b^2 + 2z^2 + 2x^2}{b}\phi_1 - \frac{2\pi}{b} - 3x\phi_2\right)\right.$$
$$+ \beta\left((2x^2 - 2b^2 - 3z^2)\phi_2 + \frac{2\pi x}{b}\right.$$
$$\left.\left. + 2(b^2 - x^2 - z^2)\frac{x}{b}\phi_2\right)\right] \tag{8.6}$$

$$\sigma_{zx} = -\frac{b}{\pi\Delta}\left[z^2\phi_2 + \beta\left((b^2 + 2x^2 + 2z^2)\frac{z}{b}\phi_1\right.\right.$$
$$\left.\left. - 2\pi\frac{z}{b} - 3xz\phi_2\right)\right] \tag{8.7}$$

The terms ϕ_1 and ϕ_2 are given by the following

$$\phi_1 = \frac{\pi(M + N)}{MN\sqrt{2MN + 2x^2 + 2z^2 - 2b^2}} \qquad \phi_2 = \frac{\pi(M - N)}{MN\sqrt{2MN + 2x^2 + 2z^2 - 2b^2}}$$

$$M = \sqrt{(b + x)^2 + z^2} \qquad N = \sqrt{(b - x)^2 + z^2}$$

220

The term Δ is a parameter that is dependant on the material elastic properties, E and ν, and the radii of curvature of the two objects in contact, and is given in equation (8.8).

$$\Delta = \frac{1}{\left(\dfrac{1}{2R_1}\right) + \left(\dfrac{1}{2R_2}\right)}\left(\frac{1-\nu_1^2}{E_1} + \frac{1-\nu_1^2}{E_2}\right) \tag{8.8}$$

The friction factor, β, is taken to be zero because there is no tangential load and the half contact width, b, is found using the load data and given by equation (8.9).

$$b = \sqrt{\frac{2P\Delta}{\pi h}} \tag{8.9}$$

The strain along the loading axis, ϵ_{zz}, is given by equation (8.10). The assumption of plane stress conditions, $\sigma_{yy}=0$, has been made due to the geometry of the disks and equation (8.10) reduces to equation (8.11).

$$\epsilon_{zz} = \frac{1}{E}\left(\sigma_{zz} - \nu(\sigma_{xx} + \sigma_{yy})\right) \tag{8.10}$$

$$\epsilon_{zz} = \frac{1}{E}\left(\sigma_{zz} - \nu(\sigma_{xx})\right) \tag{8.11}$$

Equation (8.11) is the theoretical strain on the surface of the disk given the geometrical conditions and the load.

From theory, the transverse strain, ϵ_{yy}, is given by equation (8.12).

$$\epsilon_{yy} = \frac{1}{E}\left(\sigma_{yy} - \nu(\sigma_{xx} + \sigma_{zz})\right) \tag{8.12}$$

Again, a plane stress assumption is made given the disk geometry and (8.12) is reduced to (8.13).

$$\epsilon_{yy} = -\frac{\nu}{E}\left(\sigma_{xx} + \sigma_{zz}\right) \qquad (8.13)$$

To summarize, if the load is known and the geometry of the two bodies in contact is given, the surface strain, equation (8.11), and the transverse strain, equation (8.13), can be calculated.

If the fiber is far away from the diametrically opposite side, the effect of the load from the opposite side is relatively small and this has been shown in Figure 8.19. This plot shows the percent error in the calculation of transverse strain, ϵ_{yy}, as a function of the normalized position of the sensor.

8.7.2 Stress in a sphere

Johnson (1985) presents equations for the stresses along the z-axis in a sphere. These equations are

$$\sigma_r = \sigma_\theta = p_0\left(-(1+\nu)\left(1 -\frac{z}{a}\tan^{-1}\frac{a}{z}\right) +\frac{1}{2}\left(1+\frac{z^2}{a^2}\right)^{-1}\right) \qquad (8.14)$$

$$\sigma_z = -p_0\left(1+\frac{z^2}{a^2}\right)^{-1} \qquad (8.15)$$

The terms in these expressions are given in the following equations.

$$a=\left(\frac{3PR}{4E^{\,*}}\right)^{1/3} \qquad (8.16)$$

$$\frac{1}{R}=\frac{1}{R_1}+\frac{1}{R_2} \qquad (8.17)$$

$$\frac{1}{E^*} = \frac{1-v_1^{\,2}}{E_1} + \frac{1-v_2^{\,2}}{E_2} \tag{8.18}$$

$$p_o = \frac{3P}{2\pi a^2} \tag{8.19}$$

$$\epsilon_x = \frac{1}{E}\left(\sigma_x - v(\sigma_y + \sigma_z)\right) \tag{8.20}$$

The effect of superposition from the diametrically opposite load was neglected for the reasons stated above in the theoretical derivation for a disk under diametral compression.

8.8 Results and Discussion

From the results, it is seen that the Mach-Zehnder fiber optic sensor can be embedded in bodies and used to record strains. Fig. 8.25 and 8.26 are theoretical plots of expected strain values and expected number of fringes for varying loads and varying the position of the embedded sensor on the z-axis. Figure 8.27 and 8.28 show a comparison of the experimental and theoretically obtained strain values for the disk experiments. Figure 8.29 shows the typical outputs of the fiber optic sensor and the piezoelectric load cell. Figure 8.30 is a plot of the experimental and theoretical half contact width vs. the contact load. A consistent deviation in the slope of the theoretical and experimental plot was observed in all the experiments using the Mach-Zehnder embedded in disks. A number of reasons for these errors were explored and are listed below:

- improper measurement of the gage length of the fiber. Due to the nature of embedding, the measured value of embedded length of fiber, or in other words the gage length, might not be accurate because the effective load carrying length of the fiber is dependent upon the embedding technique.

- the equations used to compute the strain were based on infinite elastic half spaces with a Hertz contact area. An attempt to include the effect of the force being applied at the diametrically opposite side was made based on the work

223

in Johnson (1985). A concentrated force was assumed for the opposite side and the superposition principle was applied. The theoretical plot of the expected error is shown in Figure 8.26. The superposition of the opposite force did not contribute significantly to the strain computations.

- the Mach-Zehnder sensor yields an average value of the strain over the embedded length but the theoretical equations are valid for a point on the body. The development of an integral expression for strain along the embedded length might produce more accurate results. Another alternative would be to use a "point" sensor, such as a Fabry-Perot sensor, because of its ability to measure strain within a small gage length.

- the presence of air bubbles in the filling compound might have altered the effective gage length.

Figure 8.31 shows the data obtained from the Fabry-Perot sensor attached to a disk under diametral compression. Again, the theoretical line was obtained using load data from the load cell and applying Hertz contact theory to calculate the strain at the sensor location. The plot shows agreement with the theoretical prediction within 14%.

The figure eight sensor was used to measure the relative displacement between disk centers when the disks were subject to loading. Figure 8.32 shows the resulting plot of load versus displacement. The center to center displacement was chosen because of its value to numerical codes such as the Discrete Element Method. These codes make use of rigid bodies and Newtonian mechanics to predict particle overlap. This overlap is then used to develop contact force through particular stiffness and / or damping characteristics. Typically the center to center displacement is what is tracked throughout the numerical simulation. Additionally, the load / displacement behavior is often modeled as a power law relationship which is verified in Figure 8.32 by the figure eight sensor.

Predicting stress and strain profiles in three dimensional bodies is an order of magnitude more complicated. For the three dimensional experiments, a sphere, which is the most simple representation of a 3d body, was used as the specimen and a fiber was embedded using the same process as for the disks. To avoid numerical procedures, strains were computed for a point along the z-axis.

As was the case in disks, a very significant deviation in slope was observed between

the theoretical and experimental values of strain. Once again, the experimentally obtained value of strain is the average value of strain along the embedded length where as the theoretically obtained values are for a point on the z-axis. In a sphere, the strain increases in magnitude from the free surface to a interior point on the z-axis (Johnson, 1985). Perhaps an arithmetic mean of the theoretical strain would afford better comparison with the experimentally obtained value of average strain along the embedded length.

Figure 8.33 shows the characteristic fiber optic and load cell output for a sphere under compression. The theoretical equations are non linear and a slight amount of non linearity was observed in the strain vs. load plots as seen in Figure 8.34.

8.9 Conclusion

The Mach-Zehnder fiber-optic sensor measured axial strains with acceptable accuracy and these strain measurements have been shown to be linear up until the failure point of the sensor. This failure point, using the technique described in this paper, has been shown to be much lower, typically 1.2-1.8 percent strain, than that taken to be accepted maximums for attached resistance type strain gages, 3-6 percent strain. Failure has been shown to be either due to fiber fracture or delamination and glue failure. For applications in our laboratory, this upper limit of measurement is above the strains encountered. Experiments were also conducted in which the entire fiber was covered with glue. Covering the fiber entirely with glue produced fiber fracture only. The glue showed cracking at the fiber fracture point and the failure strains were comparable with the values presented in this paper.

The Mach-Zehnder sensor can be embedded through bodies to measure strains. The strains predicted by the sensor are an average over the gage length and can only approximate the actual strain value at a unique point. The technique used to embed the fibers is critical for accurate prediction of strain values. The experiments using the 32 mm diameter disks proved that transverse strains due to Poisson's ratio effect can be approximately predicted by these sensors. Sub surface strains in spherical bodies under diametral compression can also be predicted by Mach-Zehnder fiber optic sensors. However, the value of the strain predicted is an average strain over the embedded length of the sensor. This strain prediction is very large when compared to the theoretical strain at a point inside of the sphere. For comparison to the theory, a more suitable sensor would be the Fabry-Perot interferometric sensor.

225

Fabry-Perot sensors have been shown to be applicable for determining contact parameters. The sensor was within 14 percent agreement with the theoretical values.

The mechanisms of failure described for the Mach-Zehnder sensor are speculated to be indicative of those for the Fabry-Perot sensor. However, preliminary work has shown that there is a dependance of the failure strain on both the diameter and the material properties of the glass tube used in constructing the Fabry-Perot.

In the case of the figure of eight sensor, the sensor shows two distinctly linear regions with mean deviations from linearity of 1.2 and 0.02 percent. The maximum deviations from linearity in these regions was found to be 7.1 and 8.4 percent. One of the linear regions shows a sensitivity of 475 mV/mm over a 30 mm extension. The second region yields a broader range of 200 mm but a lower sensitivity, 8 mV/mm. When applied to the contact problem, the sensor verified the power law behavior assumption between load and displacement.
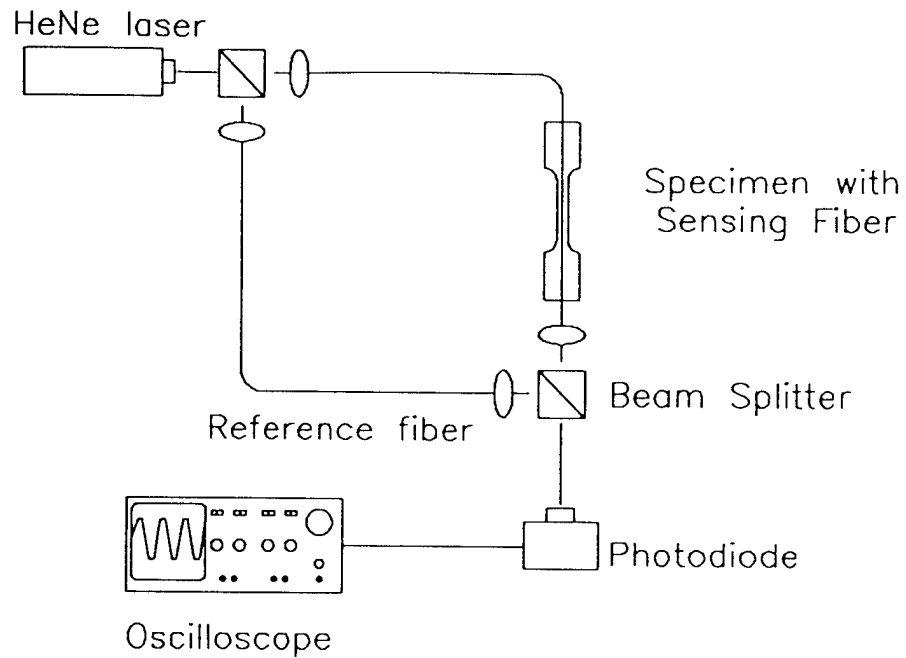
Figure 8.1. Schematic of the experimental setup for the Mach-Zehnder sensor.
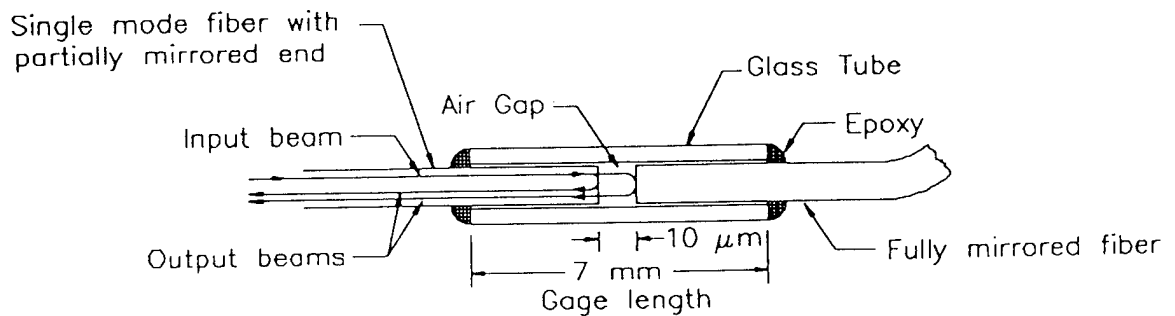
Figure 8.2. Schematic of the Fabry-Perot sensor.
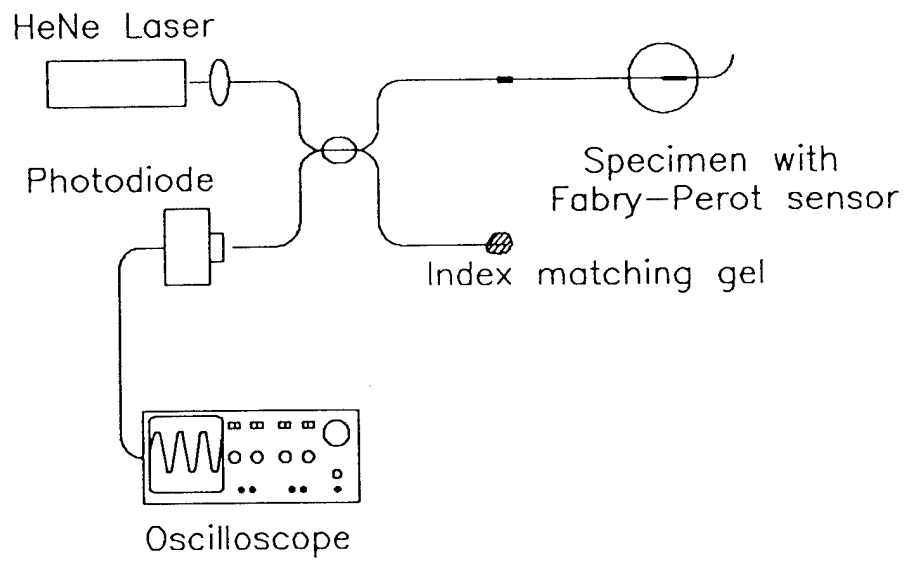
Figure 8.3. Schematic of the experimental setup for the Fabry-Perot sensor.
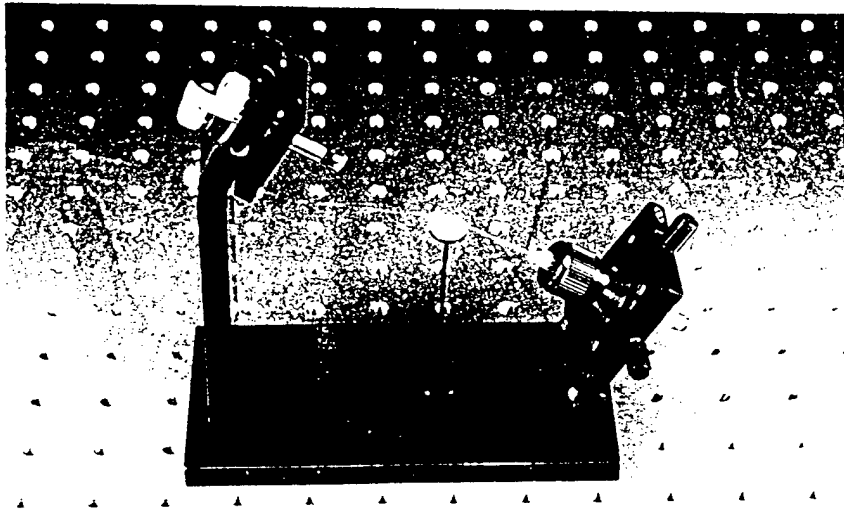
Figure 8.4. Jig for construction of Fabry-Perot sensor.
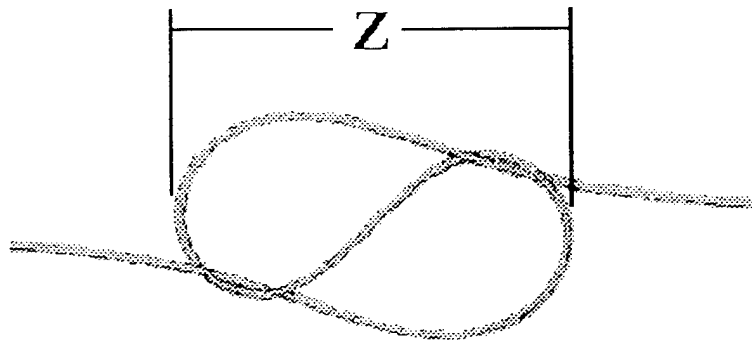
Figure 8.5. Sketch of the fiber sensor configuration.
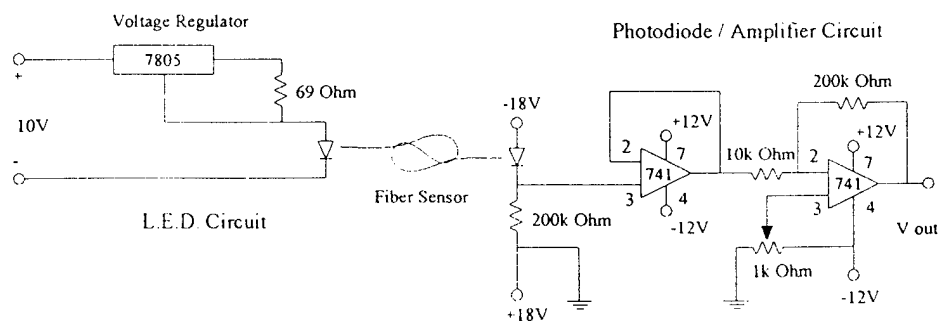
Figure 8.6. Schematic of the circuit set up for the fiber sensor.
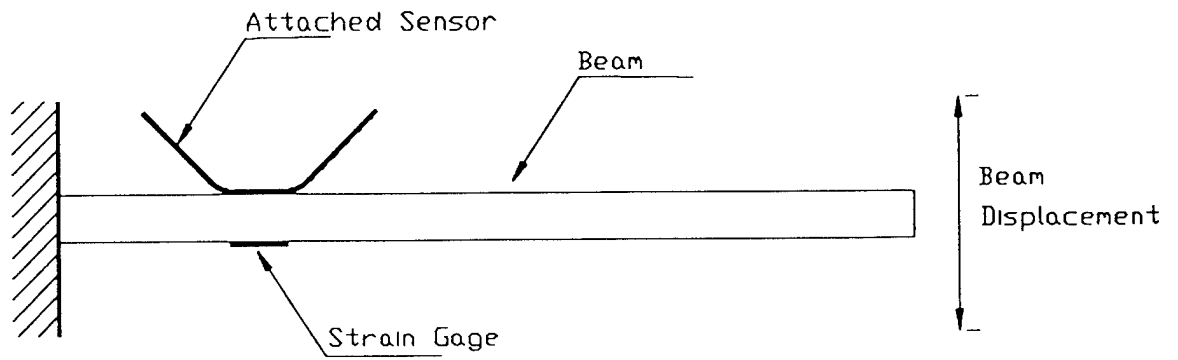
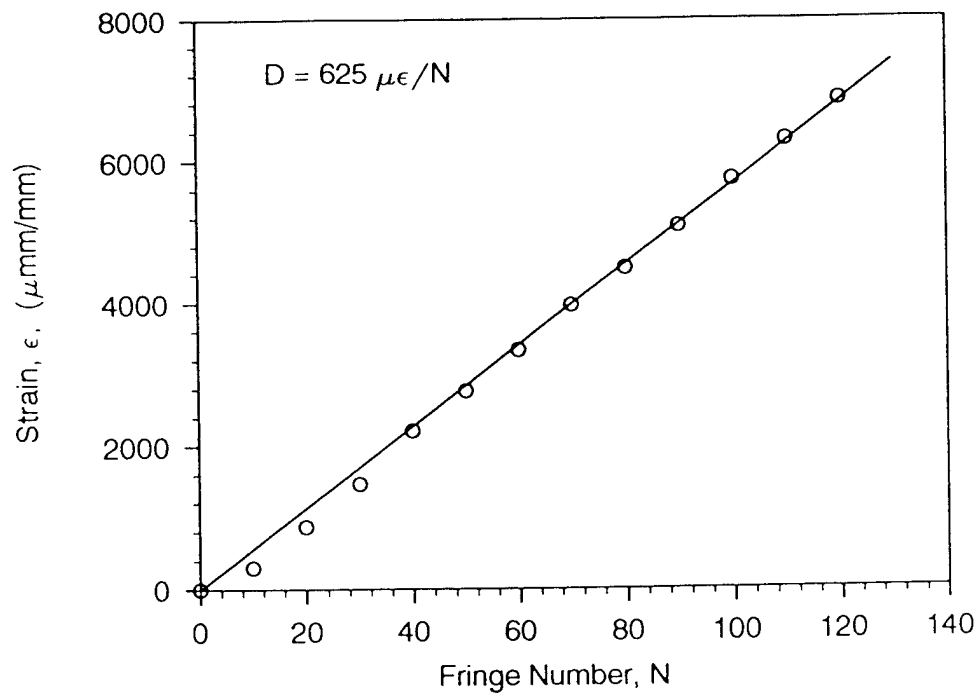Figure 8.7. Schematic of cantilever beam for calibration of the Mach-Zehnder sensor.

Figure 8.8. Calibration plot for the Mach-Zehnder sensor.
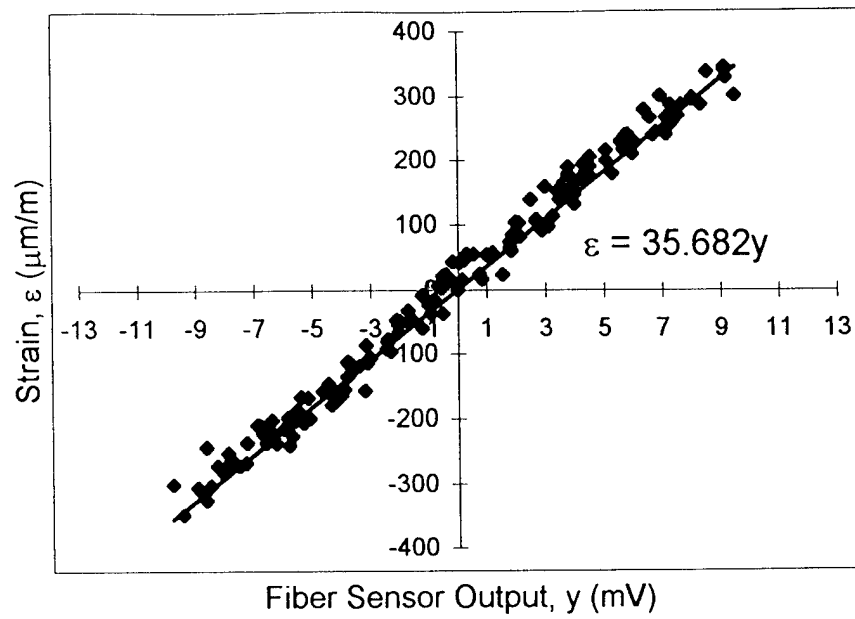
Figure 8.9. Calibration of figure 8 sensor.
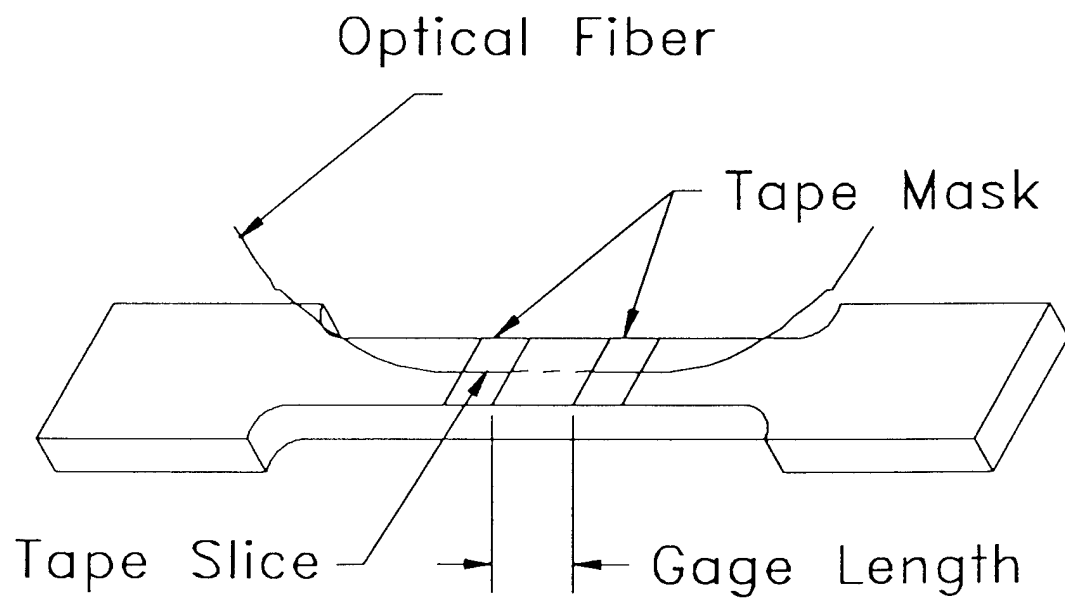
Figure 8.10. Typical specimen for tension testing showing masked are and exposed gage length.

231
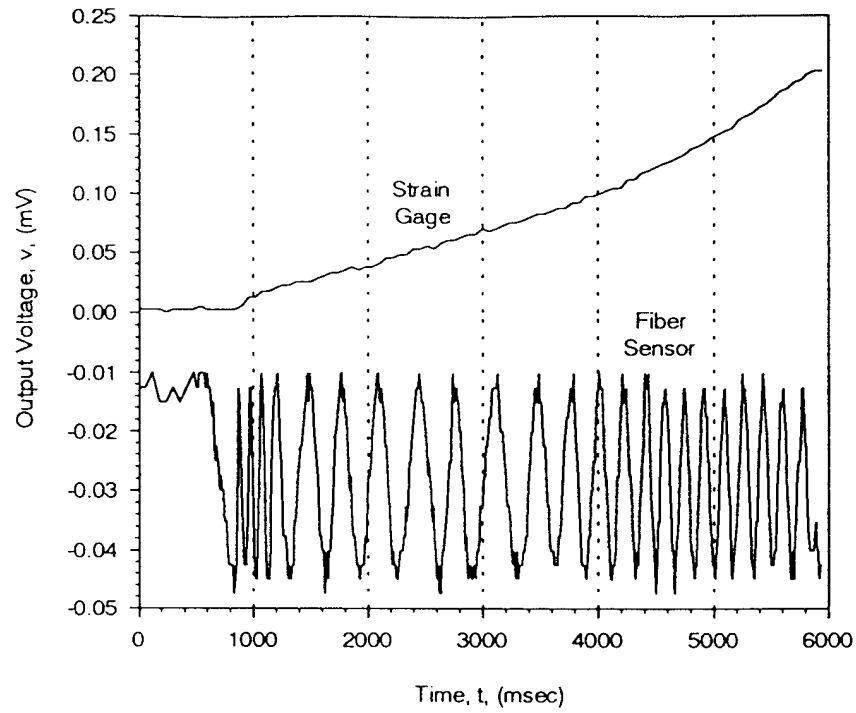
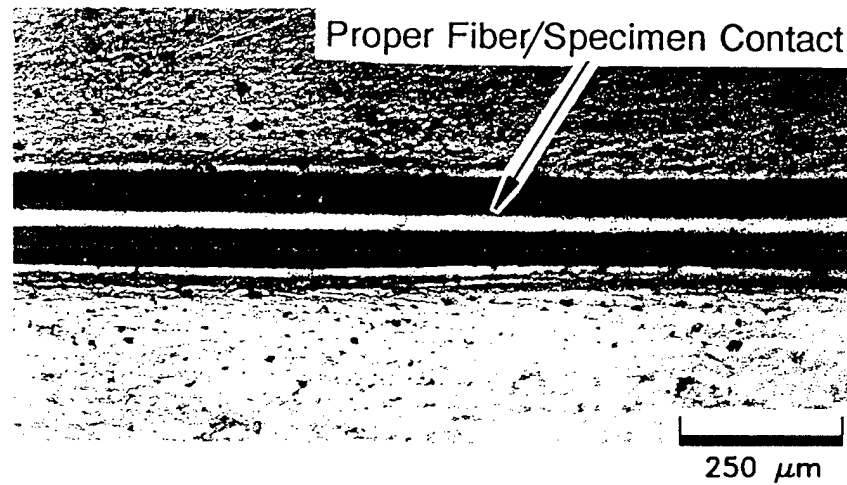Figure 8.11. Typical output from the strain gage and the fiber optic sensor during tension testing.
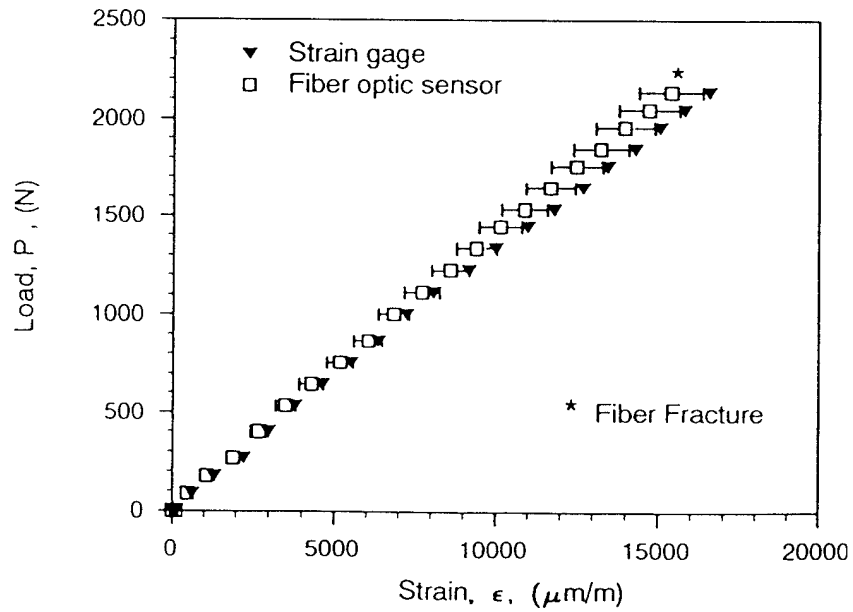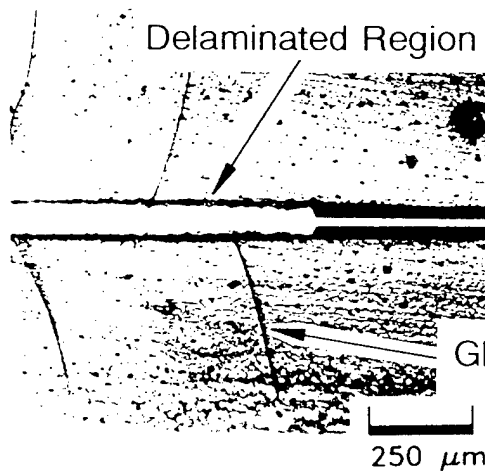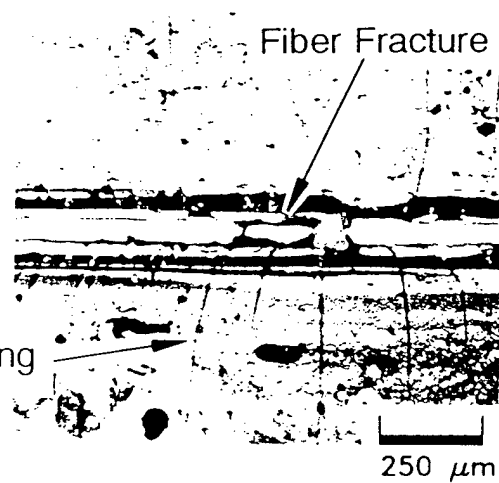

Figure 8.12. Typical strain data obtained from the strain gage and the fiber optic sensor.

232

a). fiber section as it appears unstrained, and up until failure.

b). delamination of fiber
(13,200 μ strain).

c). fiber fracture
(15,000 μ strain).

Figure 8.13. Photographs of the fiber sensor, taken at different strain levels, illustrating undamaged state and failure mechanisms.

233
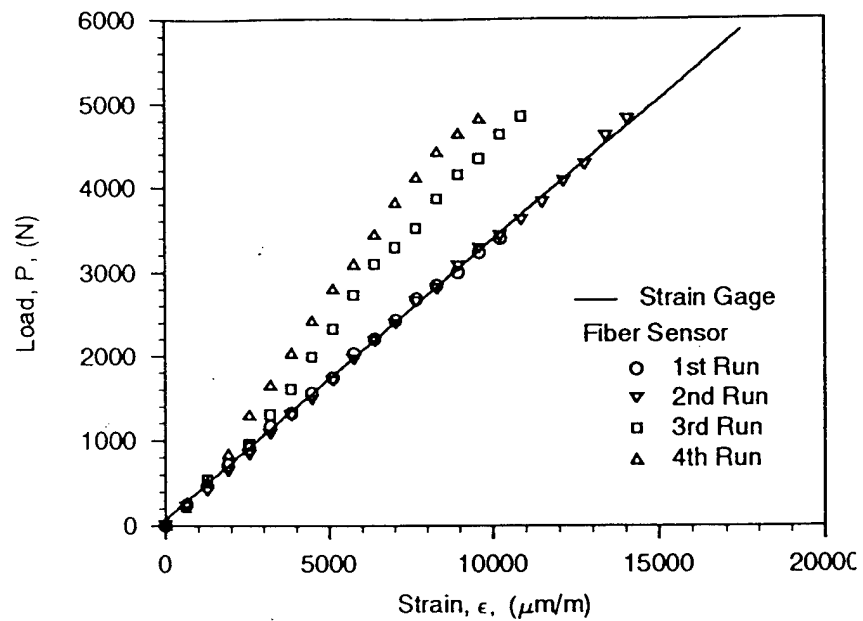
Figure 8.14. Strain gage and fiber sensor data from an incremented experiment showing the effect of fiber declamination.
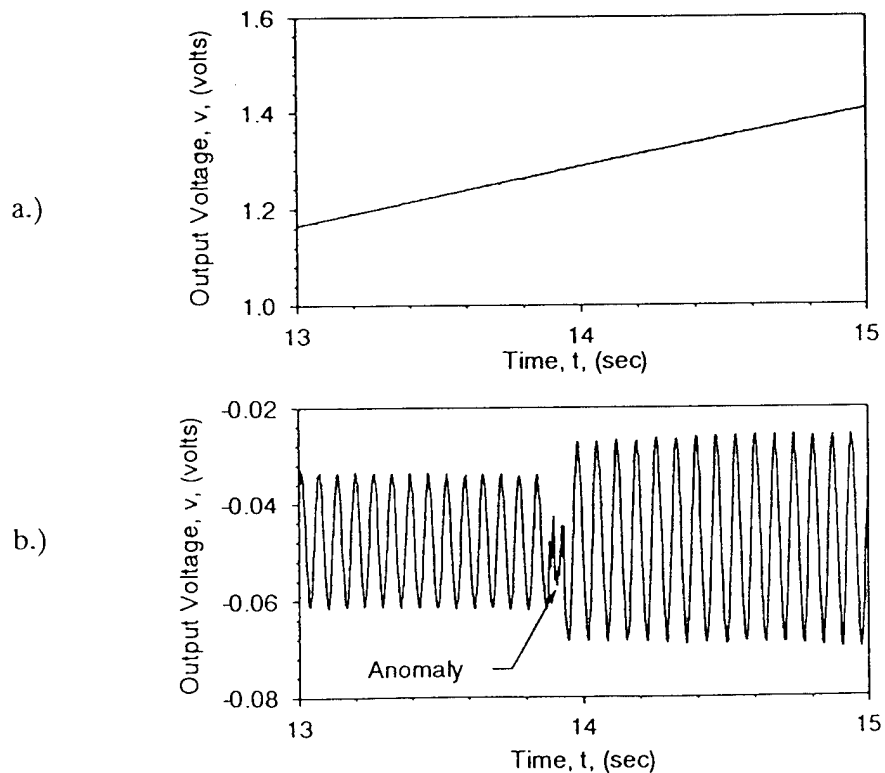
a.)

b.)

Figure 8.15. Output from both the a.) Strain gage, and b.) The fiber sensor which has begun to delaminate (taken from 2nd run).
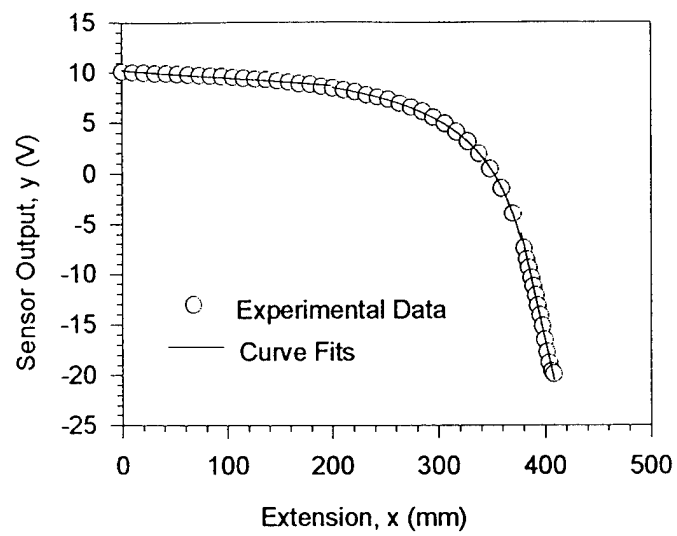
234

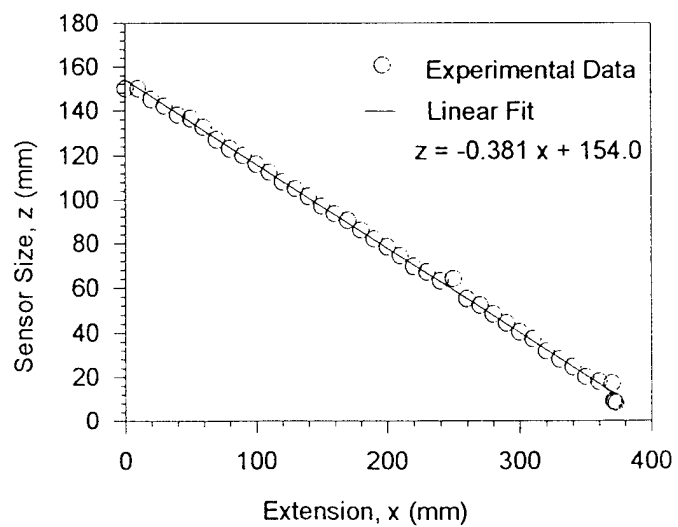Figure 8.16. Entire plot of sensor output for a total extension of 410 mm.

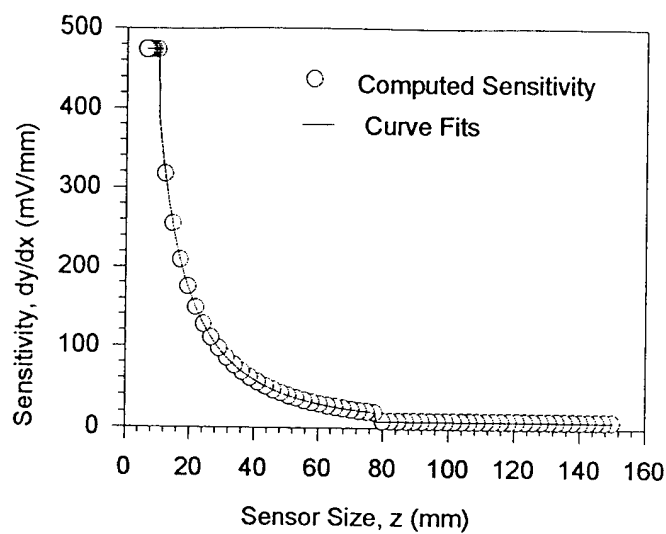Figure 8.17. Linear relationship between sensor size and sensor extension.

Figure 8.18. Plot of sensitivity (calibration factor) versus sensor size for the fiber sensor.
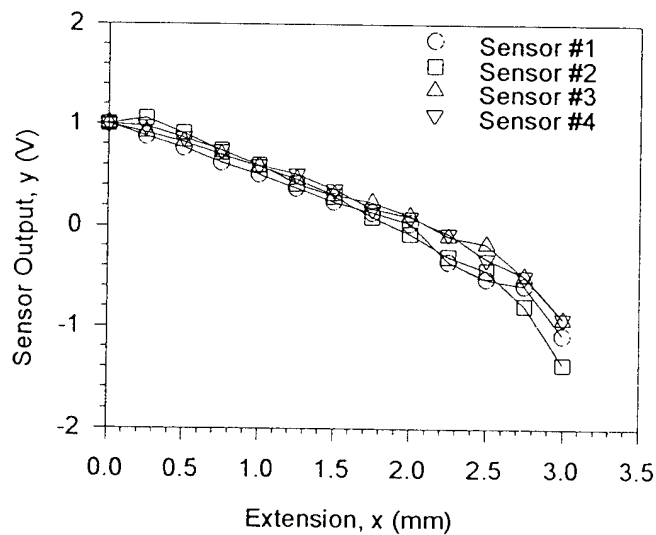

Figure 8.19. Plot of sensor output versus extension for four different sensors to determine the repeatability of construction.

236
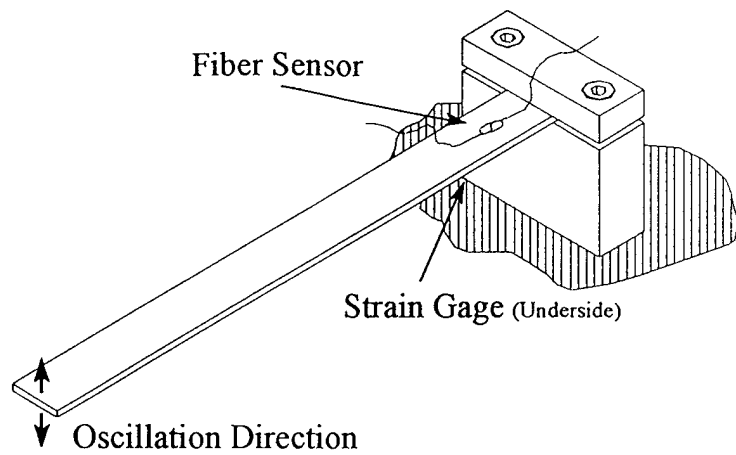
Figure 8.20. Illustration of a cantilever beam with fiber sensor and strain gage mounted to opposite sides.
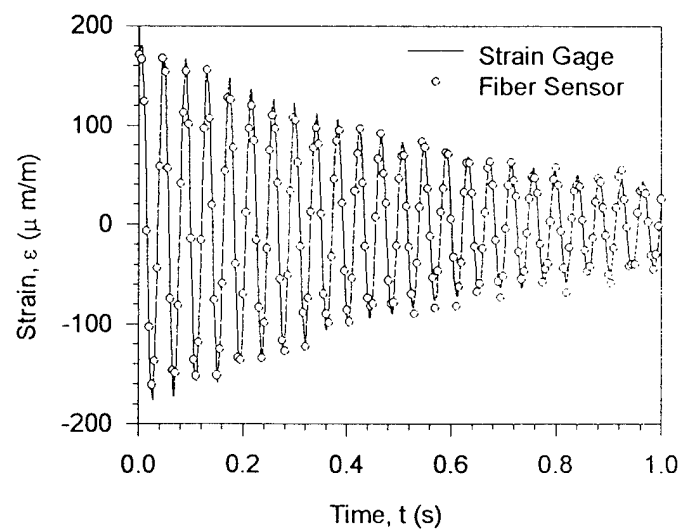
Figure 8.21. Plot of fiber sensor output and strain gage output for a vibrating cantilever beam (25 Hz).

237
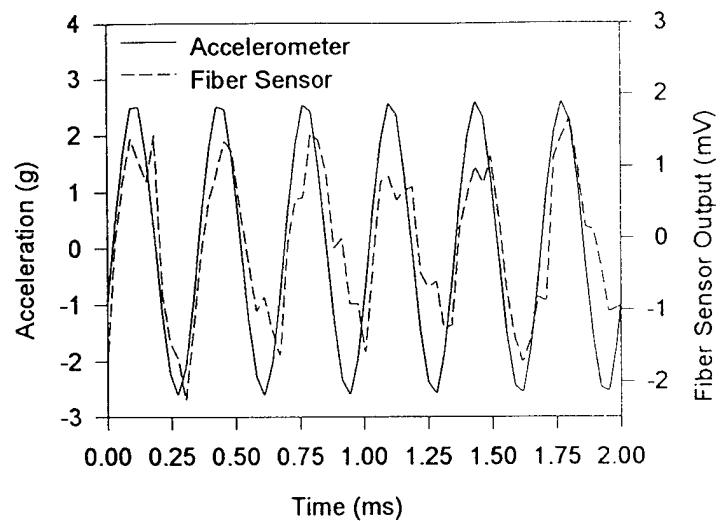
Figure 8.22. Simple time series comparing the accelerometer output in g's and fiber sensor output in volts.
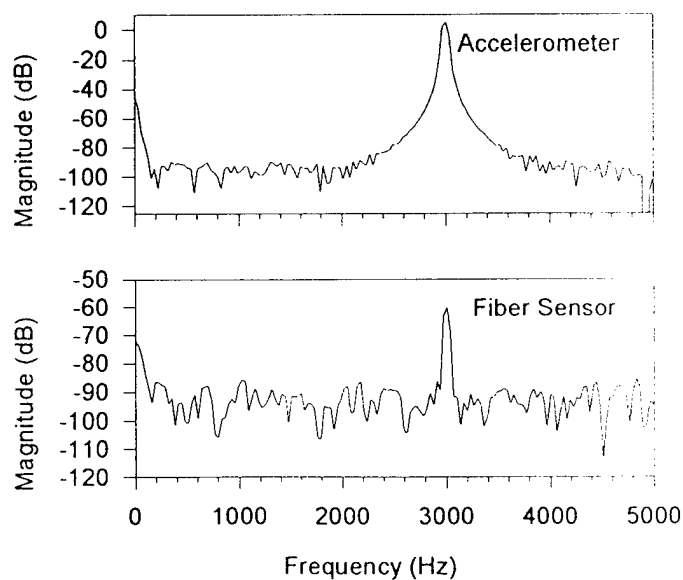
Figure 8.23. Fast Fourier transform of the data from the 3 kHz experiment showing the good correspondence between the accelerometer and the fiber sensor.

238
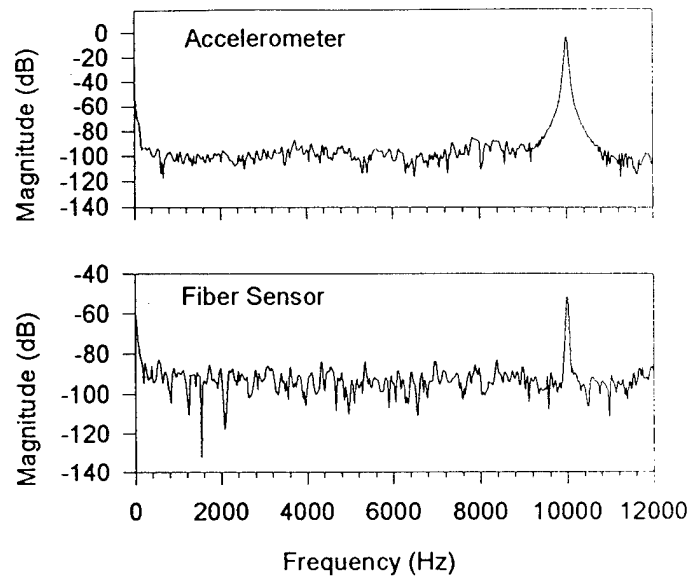
Figure 8.24. Fast Fourier transform of the 10 kHz data showing that the fiber sensor is still in excellent agreement with the accellerometer.
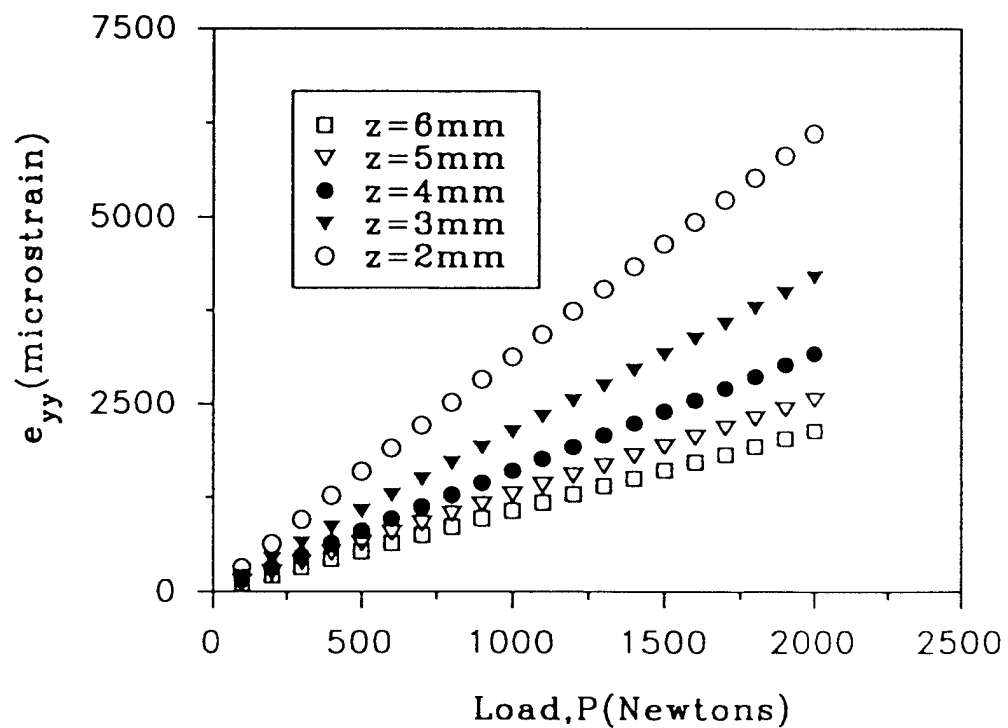
Figure 8.25. Plot of theoretical transverse strain vs. Contact load for two 25.4 mm diameter Homalite 100 disks in contact.
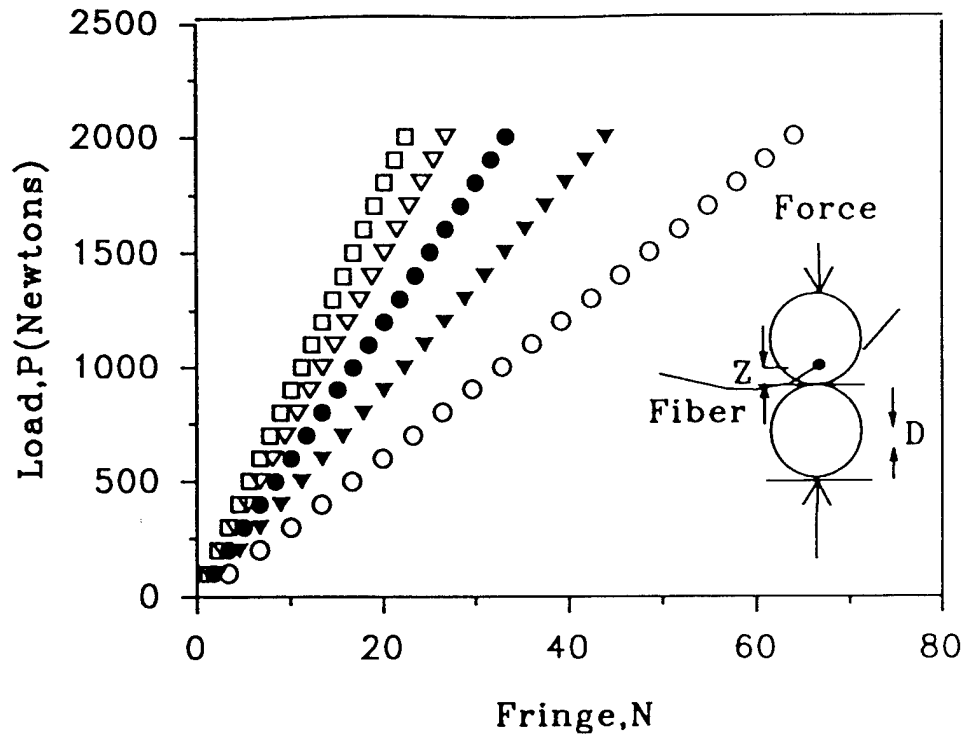
Figure 8.26. Plot of theoretical contact load vs. Fiber optic sensor fringe number for two 25.4 mm diameter Homalite 100 disks in contact.
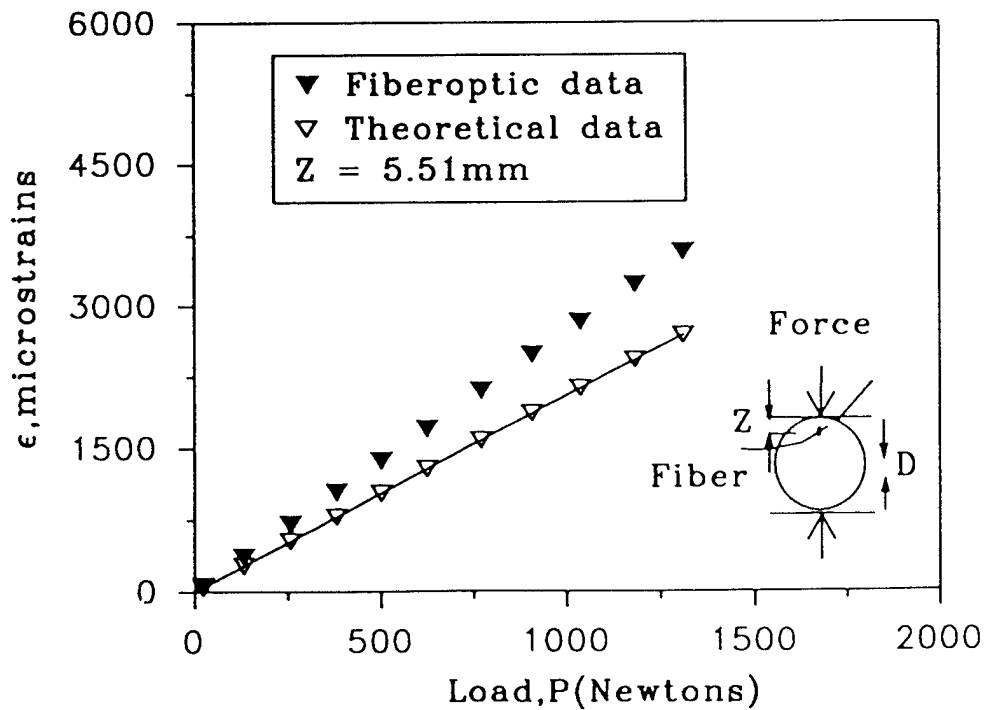
Figure 8.27. Plot of theoretical strain and strain from an embedded sensor vs. Load for the disk under diametral compression.
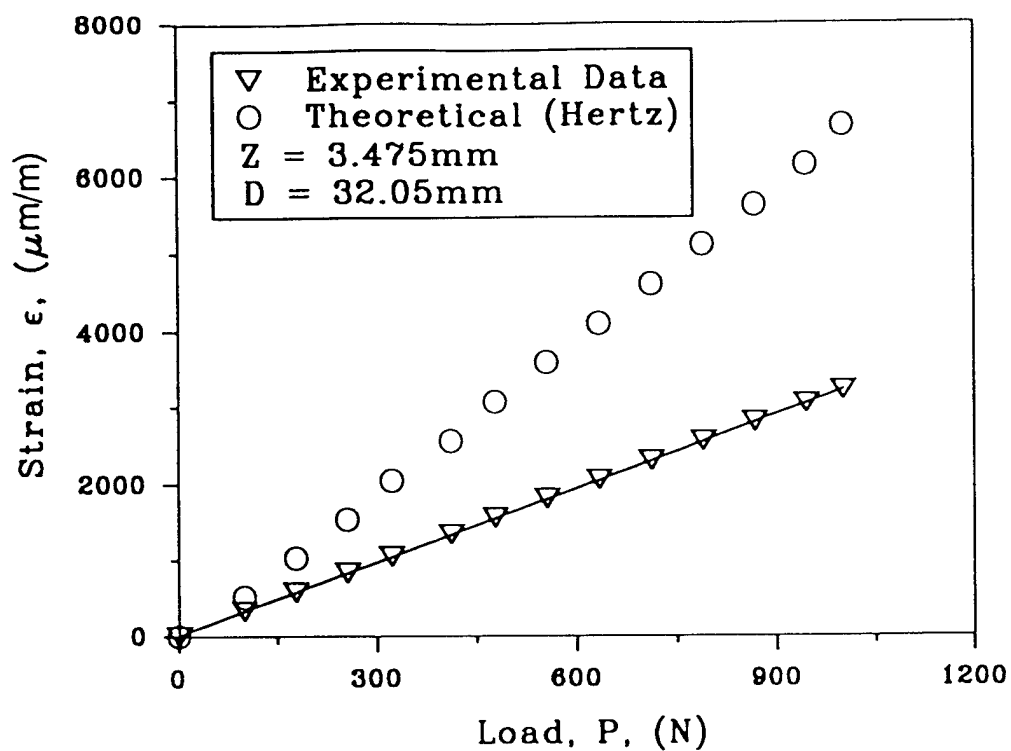
Figure 8.28. Plot of theoretical strain and experimental strain from a fiber optic sensor for a disk under diametral compression.
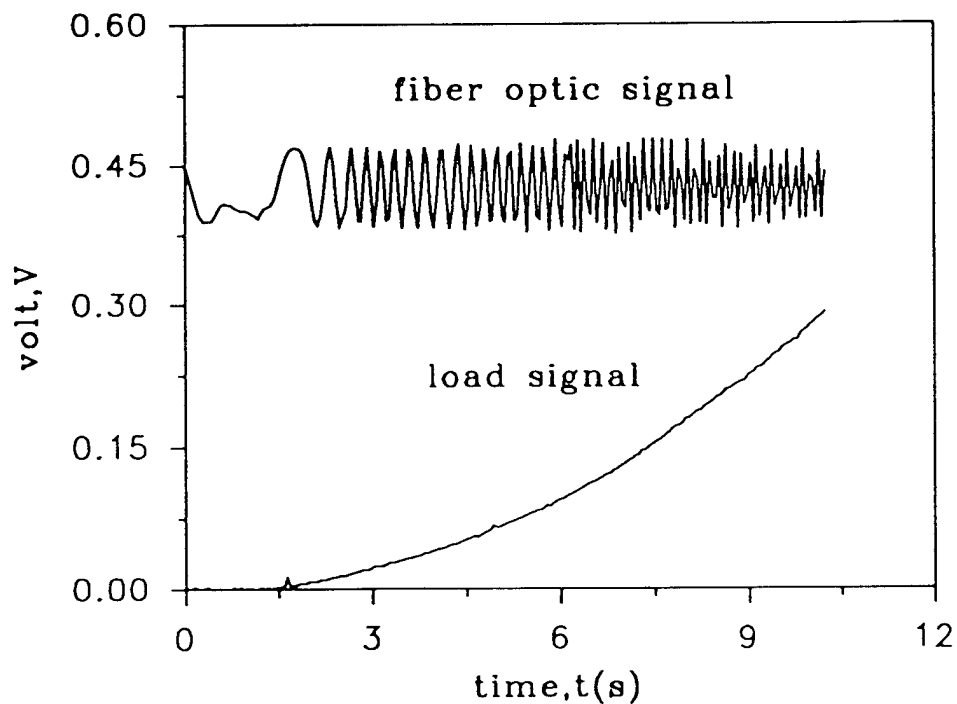
Figure 8.29. Typical output from the load cell and the fiber optic sensor for the disk under diametral compression.
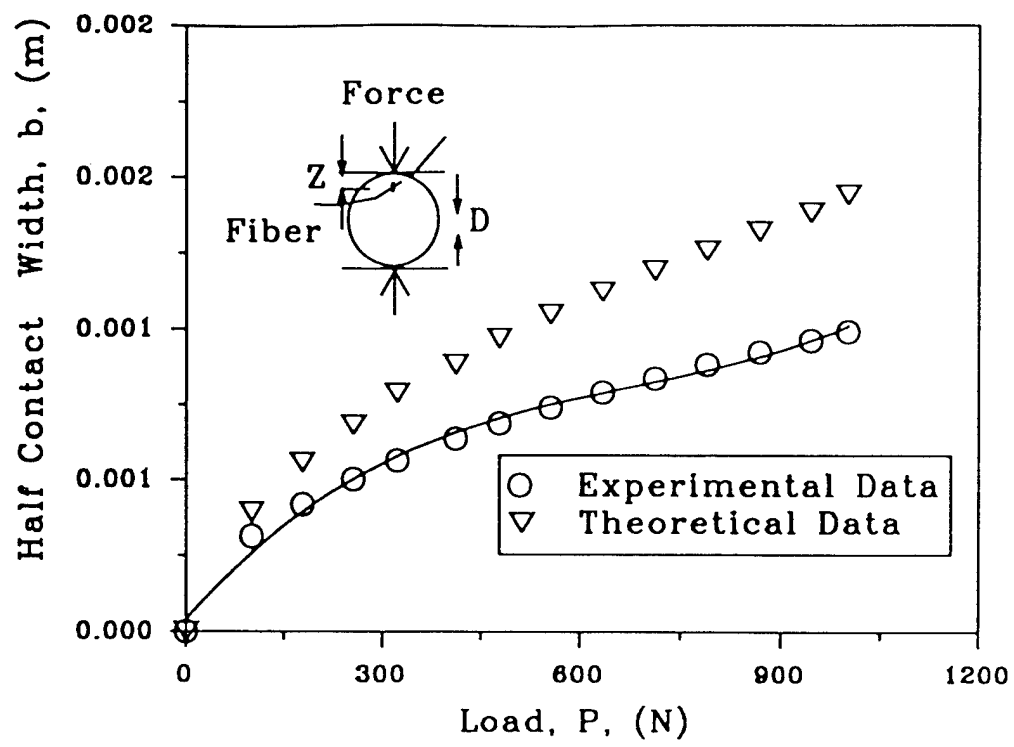
Figure 8.30. Plot of half contact width, b, vs. Load for a plexiglass® disk under diametral compression.
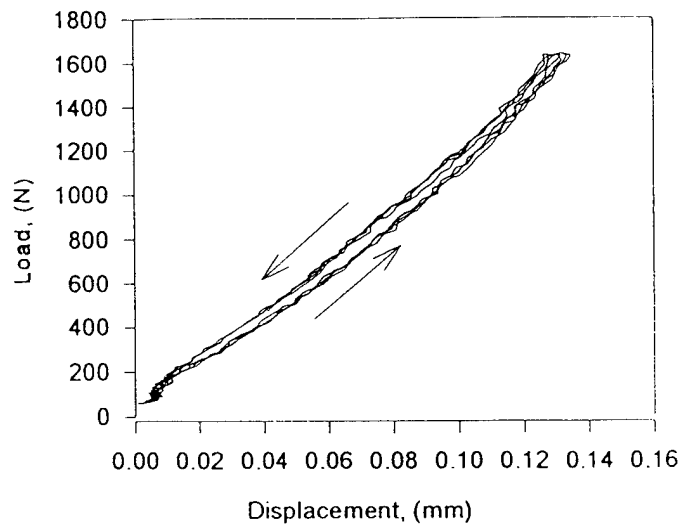
Figure 8.32. Plot of load versus displacement for the figure eight sensor bonded to two disks under diametral compression.
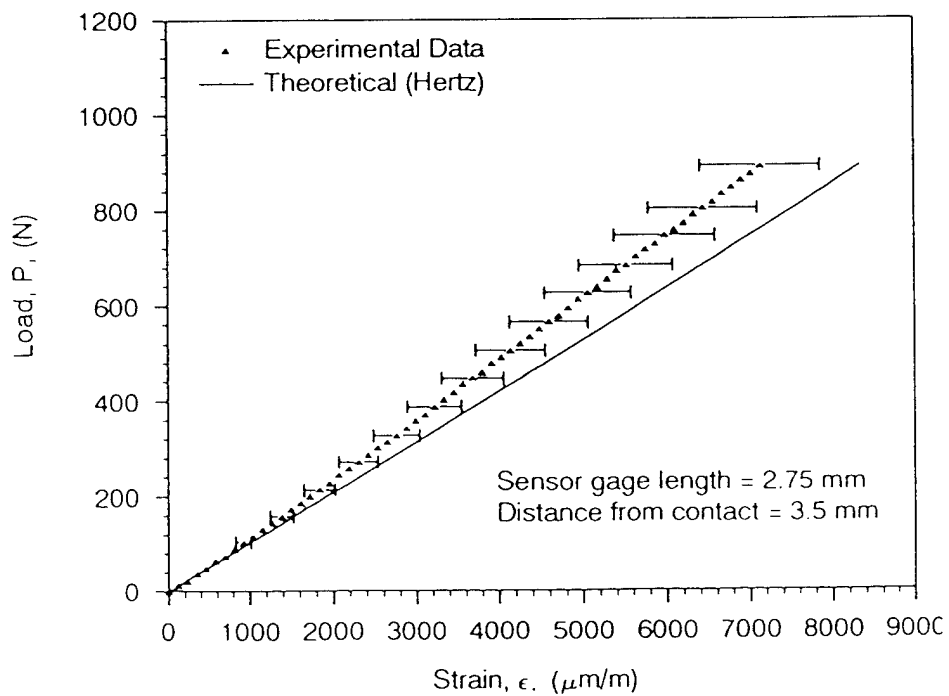
Figure 8.31. Typical data from the surface attached Fabry-Perot sensor as compared to theoretical values.

243
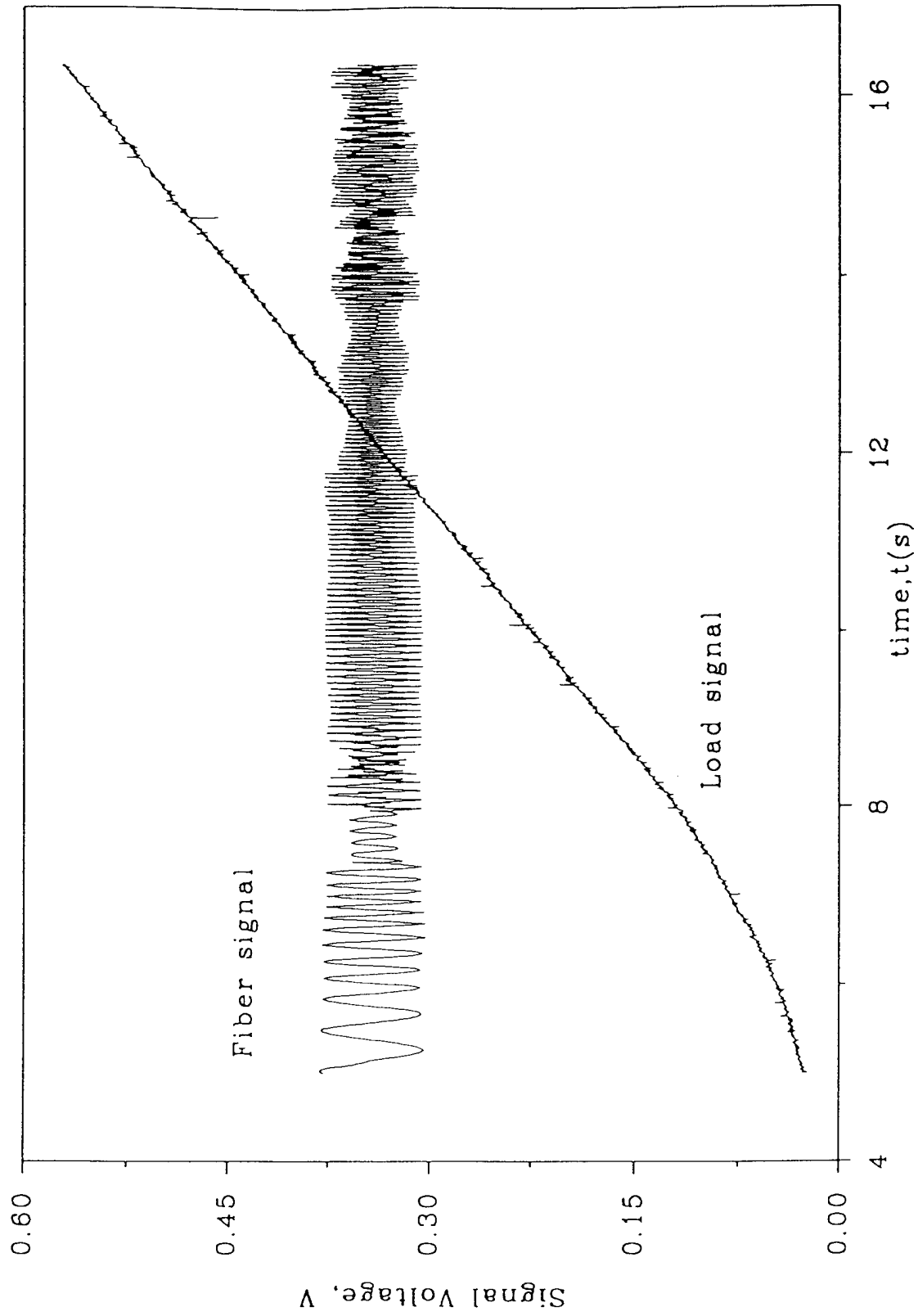
Figure 8.33. Typical output from the load cell and the fiber optic sensor for the sphere under diametral compression.
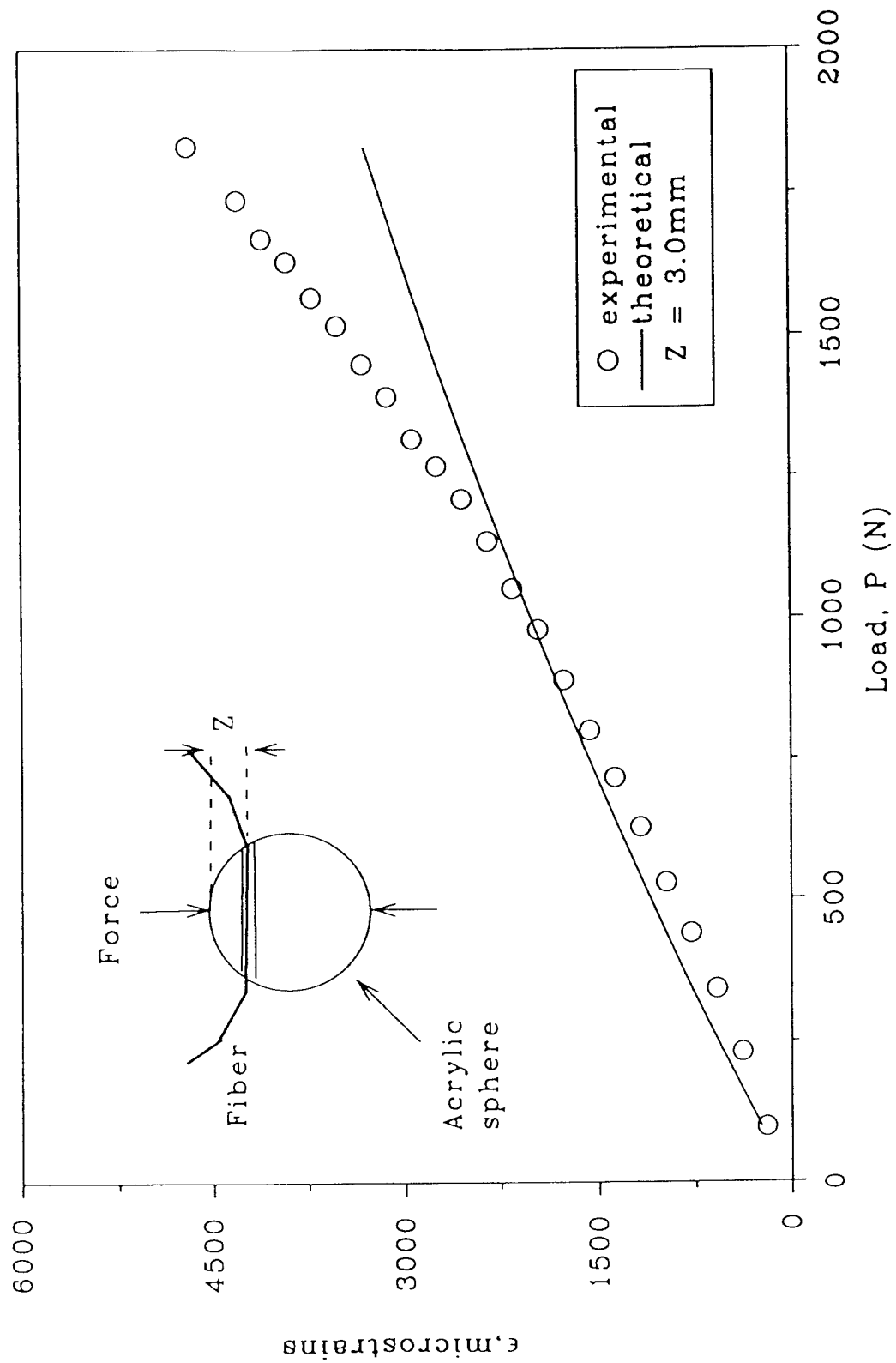
Figure 8.34. Plot of radial strain *vs.* Compressive load for a 25.4 mm Plexiglass® sphere under diametral compression.

Bibliography

Ansari, F., ed., <u>Applications of fiber optic sensors in engineering mechanics: a collection of state-of-the-art papers in the application of fiber optic technologies to civil structures</u>, American Society of Civil Engineers, New York, 1993.

Bathurst, R.J. and Rothenburg, L., Micromechanical aspects of isotropic granular assemblies with linear contact interactions, *J. Appl. Mech.* **55**, pp. 17-23, 1988.

Bourbié, T., Coussy, O., and Zinszner, B., *Acoustics of Porous Media*, Gulf Publishing Co., Houston, 1987.

Bowen, R.M., "Compressible Porous Media by Use of the Theory of Mixtures", *Int. Jour. Engng. Sci.*, **20**, pp. 679-735, 1982.

Bowen, R.M. and Lockett, R.R., "Inertial Effects in Poroelasticity", *Jour. of Appl. Mech.*, **50**, pp. 334-342, 1983.

Butter, C.D. and Hocker, G.B., "Fiber optics strain gauge", *Appl. Opt.*, **17**, pp. 2867-2869, 1978.

Cameron, A., <u>The Principles of Lubrication</u>, 1967.

Chang, C.S. and Ma, L., Modeling of discrete granulates as micropolar continua, *J. of Engineering Mechanics*, **116**, pp. 2703-2721, 1990.

Christensen, H., Ehd "Theory of Spherical Bodies in Normal Approach", *Jour. Lubrication Tech.*, **92**, pp. 145-154, 1961.

Claus, R., "Virginia Tech. Smart Structures Research Overview", *OE/Fibers '90*, San Jose, California, USA, 1990.

Cundall, P.A., "Formulation of a three-dimensional distinct element model - part I: a scheme to detect and represent contacts in a system composed of many polyhedral blocks," *International Journal of Rock Mechanics Mining Sciences and Geomechanics Abstract*, 25(3), pp. 107-116, 1988.

Cundall, P.A. and Strack, O.D.L., A discrete numerical model for granular assemblies, *Geotechnique.* **29**, pp. 47-65, 1979.

<u>Deformation and Failure of Granular Materials</u>, ed., Vermeer, P.A. and Luger, H.J., A.A. Balkema, 1982.

DePaula, R., Flax, L., Cole, J., and Bucaro, J., "Single-Mode Fiber Ultrasonic Sensor", *IEEE*

J. Quant. Elect., **QE-18**, pp 680-683, 1982.

Deresiewicz H., "Stress-strain relations for a simple model of a granular medium," *J. of App. Mech.*, **25**, pp. 402-406, 1958.

Detournay, E. and Cheng, A., "Fundamentals of Poroelasticity", Chaper 5, in Comprehensive Rock Engineering: Principles, Practice & Projects, Volume II, Analysis and Design Method, Pergamnon Press, 1993.

Digby, P. J., "The effective elastic moduli of porous granular rocks," *J. of App. Mech.*, **48**, pp. 803- 808, 1981.

Duffy, J., "A differential stress-strain relation for the hexagonal close-packed array of elastic spheres," *J. of App. Mech.*, **26**, pp. 88-94, 1959.

Duffy, J. and Mindlin, R. D., "Stress-Strain Relations and Vibrations of a Granular Medium," *J. Appl. Mech. 24*, pp. 585-593, 1957.

Dvorkin, J., Mavko, G., and Nur, A., "The effect of cementation on the elastic properties of granular material," *Mechanics of Materials*, **12**, pp. 207-217, 1991.

Dvorkin, J., Nolen-Hoeksema, R. and Nur, A., "The Squirt-Flow Mechanism: Macroscopic Description", *Geophysics*, **59**, pp. 428-438, 1994.

Dvorkin, J. and Nur, A., "Dynamic Poroelasticity: A Unified Model With the Squirt and the Biot Mechanisms", *Geophysics*, **58**, pp. 524-533, 1993.

Gajo, A., "Influence of Viscous Coupling in Propagation of Elastic Waves in Saturated Soil", *Jour. Geotechnical Eng.*, **121**, pp. 636-644, 1995.

Ghaboussi, J. and Barbosa, R., "Three-dimensional discrete element method for granular materials," *Int. J. Numerical and Analytical Methods in Geomechanics*, **14**, pp. 451-472, 1990.

Gill, J.J., The microstructural response of granular soil under uniaxial strain, Report No. PL-TR-92-1064, Phillips Laboratory, Kirtland AFB, New Mexico, 1993.

Gohar, R., Elastohydrodynamics, Ellis Horwood Limited, 1988.

Goodman, M.A. and Cowin, S.C., "A continuum theory for granular materials," *Archive of Rational Mechanics and Analysis*, **44**, 1972.

Hardin, B.O. and Blandford, G.E., "Elasticity of particulate materials," *J. of Geotech. Eng.*, **115**, 788-805, 1989.

Herrebrugh, K., "Elastodynamic Squeeze Films Between Two Cylinders in Normal

Approach", *Jour. Lubrication Tech.*, **92**, pp. 292-302, 1970.

Hryciw, R.D. and Raschke, S.C., "Soil characterization and experimental micromechanics through computer vision and digital image processing," AFOSR Particulate Mechanics Contractor's Meeting, Tyndall AFB, FL, September 1995.

Hsieh, L. and Yew, C.H., "Wave Motions in Fluid-Saturated Porus Medium", *Jour. App. Mech.*, **40**, pp. 873-878, 1973.

Ida, K., "The Velocity of Elastic Waves in Sand," *Bulletin Earthquake Research Institute, Japan*, **17**, 1939.

Jenkins, J.T. and Satake, M., *Mechanics of Granular Materials - New Models and Constitutive Relations*, Proc. U.S./Japan Seminar, Elsevier, 1983.

Johnson, K.L., Contact Mechanics, Cambridge University Press, Cambridge, U K, 1985.

Katsube, N., "The Constitutive Theory for Fluid-Filled Porous Materials", *Jour. App. Mech.*, **52**, pp. 185-189, 1985.

Kishino, Y., "Disc model analysis of granular media," *Micromechanics of Granular Materials*, Ed. by M. Satake and J.T. Jenkins, Elsevier Science Publishers, Netherlands, 1988.

Konishi, Y., "Microscopic Model Studies on the Mechanical Behavior of Granular Materials," *Proc. U.S.-Japan Seminar on Continuum-Mechanical and Statistical Approaches in the Mechanics of Granular Materials*, ed., Cowin, S.C. and Satake, M., Gakujutsu Bunken Fukyukai, Tokyo, Japan, pp. 114-122, 1978.

Konshi, J. and Naruse, F., "A Note on Fabric in Terms of Voids," *Micromechanics of Granular Materials*, Ed. M. Satake and J.T. Jenkins, Elsevier Science Pub., Netherlands, 1988.

Konishi, J., Oda, M., and Nemat-Nasser, S., "Inherent Anisotropy and Shear Strength of Assembly of Oval Cross-Sectional Rods," *IUTAM Conf. On Deformation and Failure of Granular Materials.* Delft, A.A. Balkema, Rotterdam, pp. 403-412, 1982.

Lee, K.M. and Cheng, H., "The Pressure and Deformation Profiles Between Two Normally Approaching Lubricated Cylinders," *Jour. Lubrication Tech.*, **95**, pp. 308-320, 1973.

Lee, C., Taylor, H., Markus, A., and Udd, E., "Optical-fiber Fabry-Perot embedded sensor", *Opt. Lett.*, **14**, pp. 1225-1227, Nov., 1989.

Lin, X. and Ng, T.T., "Numerical Modeling of Granular Soil Using Randon Arrays of Three-

Dimensional Elastic Ellipsoids," *Computer Methods and Advances in Geomechanics*, Balkema, Rotterdam, 1994.

Mavko, G.M. and Nur, A., "Wave Attenuation in Partially Saturated Rocks," *Geophysics*, **44**, pp. 161-178, 1979.

Measures, R., "Advances Toward Fiber Optic Based Smart Structures," *Optical Engineering*, **31**(1), pp. 34-47, 1992.

Mehrabadi, M.M., Ed., Mechanics of Granular Materials and Powder Systems, A.S.M.E. Materials Division, **AMD-Vol. 37**, 1992.

Micromechanics and Inhomogeneity-The Toshio Mura Anniversary Volume, ed., Weng, G.L., Taya, M., and Abe, H., Springer-Verlag, New York, 1989.

Narendran, N., Letcher, S., and Shukla, A., "Optical-Fiber Strain Sensor Using Combined Interference and Polarization Technique," *Optics and Lasers in Engineering*, **18**, pp. 121-133, 1993.

Narendran, N., Shukla, A., and Letcher, S.,"Determination of Fracture Parameters Using Embedded Fiber-optic Sensors," *Experimental Mechanics*, **4**, pp. 360-366, 1991.

Narendran, N., Shukla, A., and Letcher, S., "Optical-Fiber Interferometric Strain Sensor Using a Single Fiber," *Experimental Techniques*, **16**(6), pp. 33-36, 1992.

Narendran, N., Zhou, C., Letcher, S., and Shukla, A.,"Fiber-optic Acoustic Sensor for Nondestructive Evaluation," *J. of Optics and Lasers in Engineering*, **22**(2), pp. 137-148, 1995.

Nemat-Nasser, S., "Fabric and its influence on mechanical behavior of granular materials," *IUTAM Conference on Deformation and Failure of Granular Materials*, pp. 37-42, 1982.

Nemat-Nasser, S. and Mehrabadi, M.M., "Stress and fabric in granular masses," *Mechanics of Granular Materials: New Models and Constitutive Relations*, Ed. J.T. Jenkins and M. Satake, Elsevier Science Pub., Netherlands, 1983.

Nesterenko, V.F., "Propagation of Nonlinear Compression Pulse in Granular Media," *Journal of Applied Technical Physics*, **5**, pp. 733-743, 1983.

Ng, T.T. and Dobry, R., "A non-linear numerical model for soil mechanics," *Int J. Nonlinear Mech.*, **16**, pp. 247-263, 1992.

Oda, M., "Significance of Fabric in Granular Mechanics," *Proc. U.S.-Japan Seminar on*

Continuum-Mechanical and Statistical Approaches in the Mechanics of Granular Materials, ed., Cowin, S.C. and Satake, M.,Gakujutsu Bunken Fukyukai, Tokyo, Japan. 7-26, 1978.

Oda, M., Konishi, J., and Nemat-Nasser, S. , "Some experimentally based fundamental results on the mechanical behavior of granular materials," *Geotechnique*, **30**, pp. 479-495, 1980.

Oda, M., Konishi, J., and Nemat-Nasser, S., "Experimental Micromechanical Evaluation of Strength of Granular Materials: Effects of Particle Rolling," *Mech. Mater.*, **1**, pp. 269-283, 1982.

Oda, M., Nemat-Nasser, S., and Mehrabadi, M.M., "A statistical study of fabric in a random assembly of spherical granules," *Int. J. Num. Anal. Geomech.* **6**, pp. 77-94, 1982.

Ogushwitz, P.R., "Applicability of the Biot Theory, I. Low-Porosity Materials; II. Suspensions; III. Wave Speeds Versus Depth in Marine Sediments," *Jour. Acous. Soc. Amer.*, **77**, pp. 429-464, 1985.

Palmer, I.D. and Traviolia, M.L., "Attenuation by Squirt Flow in Undersaturated Gas Sands," *Geophysics*, **45**, pp. 1780-1792, 1981.

Pande, G.N., "Influence of Grain Shape and Size on the Behavior of Granular Materials," *Proc. International Conf. on Numerical Methods in Engineering: Theory and Applications*, Swansea, 1987.

Petrakis, E. and Dobry, R., "A two-dimensional numerical micromechanical model for a granular cohesionless materials at small strains," *Proc. Amer.Phys. Soc*, New Orleans, LA, 1988.

Petrakis, E., Dobry, R., and Ng, T., "Small strain response of random arrays of elastic spheres using a nonlinear distinct element procedure," Report CE-88-02, Resselaer Polytechnic Institute, Troy, NY., 1988.

Plona, T.J., "Observations of a Second Bulk Compressional Wave in a Porous Medium at Ultrasonic Frequencies," *Appl. Phys. Letters*, **36**, pp. 259-261, 1980.

Prevost, J.H., "Dynamics of Porous Media," Chapter 3, <u>Geotechnical Modeling and Applications</u>, S.M. Sayed, Ed., Gulf Publishing, 1987.

Proceedings of IUTAM Conference on Deformation and Failures of Granular Materials, 1982.

Proceedings of U.S.-Japan Seminar on Continuum Mechanical and Statistical Approaches in Mechanics of Granular Materials, 1988.

Rossmanith, H.P., Wien, and Shukla, A., "Photoelastic Investigation of Dynamic Load Transfer in Granular Media," *Acta Mech*, **42**, pp. 211-225 1982.

Rothenburg, L. and Bathurst, R.J., "Micromechanical Features of Granular Assemblies with Planar Elliptical Particles," *Geotechnique*. **42**, pp. 79-95, 1992.

Rothenburg, L. and Bathurst, R.J., "Influence of Particle Eccentricity on Micromechanical Behavior of Granular Materials," *Mechanics of Materials*. **16**, pp. 141-152, 1993.

Sadd, M.H., Shukla, A., and Mei, H., "Computational and Experimental Modeling of Wave Propagation in Granular Materials," Proc. 4th Intl. Conf. Computational Methods and Experimental Measurements, Capri, Itlay, pp. 325-334, 1989.

Sadd, M.H., Shukla, A., Mei, H. and Zhu, C.Y., "The Effect of Voids and Inclusions on Wave Propagation in Granular Materials", Micromechanics and Inhomogeneity-The Toshio Mura Anniversary Volume, Ed. G.J. Weng, M. Taya and H. Abe, Springer-Verlag, pp. 367-383, 1990.

Sadd, M.H., Shukla, A, Tai, Q.M, and Xu,Y, "Micromechanical Constitutive Behavior of Granular Media Under Dynamic Loading Conditions," *Proc. Third Intnl. Conf. Constitutive Laws For Engineering Materials*, Univ. of Arizona, Tucson, AZ, 1991.

Sadd, M.H., Tai, Q.M, and Shukla, A., "Contact law effects on wave propagation in particulate materials using distinct element modeling," *Int. J. Nonlinear Mech.*, **28**, pp. 251-265, 1993.

Satake, M., "A discrete-mechanical approach to granular materials," *Int. J. Engng. Sci.*, **30**, pp. 1525-1533, 1992.

Sawada, S. and Pradham, T.B.S., "Analysis of Anisotropy and Particle Shape by Distinct Element Method," *Computer Methods and Advances in Geomechanics*, Balkema, Rotterdam, 1994.

Shukla, A. and Damania, C., "Experimental investigation of wave velocity and dynamic contact stresses in an assembly of disks," *Experimental Mech.*, **27**, pp. 268-281, 1987.

Shukla, A. and Nigam, H., "A Numerical-Experimental Analysis of the Contact Stress Problem," *J. of Strain Analysis*, **20**(4), pp. 241-245, 1985.

Shukla, A. and Rossmanith, H.P., "Photoelastic investigation of dynamic load transfer in granular media," *Acta Mech.*, **42**, pp. 211-225, 1982.

Shukla, A., Sadd, M.H., Singh, R., and Tai, Q.M., and Vishwanthan, S., "Role of Particle Shape and Contact Profile on the Dynamic Response of Particulate Materials," *Optics and Lasers in Engineering*, **19**, pp. 99-119, 1993.

Shukla, A., Sadd, M.H., Xu, Y., and Tai, Q.M., "Influence of loading pulse duration on dynamic load transfer in a simulated granular medium," *J. Mech. Phys Solids*, **41**, pp. 1795-1808, 1993.

Shukla, A., Zhu, C. Y., and Sadd, M. H., "Angular dependence of dynamic load due to explosive loading in two dimensional granular aggregate," *J. of Strain Analysis.* **23**, pp. 121-127, 1988.

Shukla, A., Zhu, C.Y., and Sadd, M., "Angular Dependence of Dynamic Load Transfer Due To Explosive Loading in Granular Aggregate Chains," *J. Strain Analysis*, **33**, pp. 121-127, 1988.

Shukla, A.,Zhu, C.Y., and Xu, Y., "Dynamic Stresses in Granular Assemblies with Microstructural Defects," *Journal of Engineering Mechanics*, **118**(1), pp.190-201, 1992.

Sirkis, J., and Taylor C.,"Interferometric-fiber-optic strain sensor", *Expt. Mech.*, **28**, pp. 170-176, 1988.

Smith, J.O. and Liu, C.K., "Stresses due to Tangential and Normal Loads on an Elastic Solid with Applications to Some Contact Problems," *J. Appld. Mech.*, **20**, pp. 157-166, 1953.

Sternberg, E. and Rosenthal, F., (1952) "The Elastic Sphere Under Concentrated Loads," *Journal of Applied Mechanics*, **12**, pp. 413-421.

Stoll, R.D., <u>Sediment Acoustics</u>, Vol 26, Lecture Notes in Earth Sciences, Springer-Verlag, 1989.

Subhash,G., Nemat-Nasser, S., Mehrabadi, M.M., and Shodja, H.M., "Experimental Investigation of Fabric-Stress Relations in Granular Materials," *Mech. Mater.*, **11**, pp. 87-106 ,1991.

Tai, Q.M, Ph.D. Thesis, University of Rhode Island, 1993.

Takahashi, T. and Sato,Y., "On the Theory of Elastic Waves in Granular Substance,"

Bull. Earthquake Res. Inst.,Japan, **27**, pp. 11-16, 1949.

Thornton, C. and Barnes, D. J., "Computer simulated deformation of compact granular assemblies," *Acta Mechanica.* **64** () 45-61, 1986.

Thorton, C., and Randall, C.W., "Applications of theoretical contact mechanics to solid particle system simulation," *Micromechanics of Granular Media*, Ed. M. Satake and J.T. Jenkins, Elsevier Science Pub., Netherlands, 1988.

Timoshenko, S.P. and Goodier, J.N. (1970), Theory of Elasticity, McGraw-Hill, New York.

Ting, J.M., "An Ellipse-based Micromechanical Model for Angular Granular Materials," ASCE Eighth Eng. Mech. Conf., Columbus, Ohio, May, 1991.

Ting, J.M., "A Robust Algorithm for Ellipse-based Discrete Element Modeling of Granular Materials," *Computer and Geotechnics,* **13**, pp. 175-186, 1992.

Ting, J., Corkum, B.T., Kauffman, C., and Greco, C., "Discrete numerical model for soil mechanics," *J. Geotech. Eng.,* **115**, pp. 379-398, 1989.

Ting, J.M., Khwaja, M., Meachum, L.R., and Rowell, J.D., "An Ellipse-Based Discrete Element Model for Granular Materials," *International Journal for Numerical and Analytical Methods in Geomechanics.* **17**, pp. 603-623 1993.

Ting, J.M. and Meachum, L.R., "Effect of Bedding Plane Orientation on the Behavior of Granular Systems," *Mechanics of Materials With Discontinuities and Heterogeneities, ASME,* **AMD-Vol 201**, pp. 43-57, 1995.

Tolsoty, I., "Acoustics, Elasticity, and Thermodynamics of Porous Media: Twenty-One Papers by M.A. Biot," *Acousitc Society of America,* 1992.

Trent, B.C., "Numerical Simulation of Wave Propagation Through Cemented Granular Materials," *Wave Propagation in Granular Media, Proc. Winter Annual Meeting of ASME*, pp. 9-15, 1989.

Trent, B.C. and Margolin, L.G. (1992), "A numerical laboratory for granular solids, *Eng. Comp.,* **9**, pp. 191-197.

Vardoulakis, I.G. and Beskos, D.E., "One the Dynamic Behavior of Nearly Saturated Granular Media", A.S.M.E. Applied Mechanics Division, **AMD-Vol.** 57, pp. 56-73, 1983.

Vaziri, M. and Chen, C., "Etched Fibers as Strain Gauges," *J. Lightwave Tech.,* **10**(6), pp.836-841, 1992.

Voyiadjis, G.Z., Ed., "Microstructural Characterization in Constitutive Modeling of Metals and Granular Media," A.S.M.E. Materials Division, **AMD-Vol 32**, 1992.

Walton, K., "The Oblique Compression of Two Elastic Spheres," *J. Mech. Phys. Solids,* **26**, pp. 139-150, 1978.

Walton, O., "The effective elastic moduli of a random packing of spheres, *J. Mech. Physics Solids.* **35**, pp.213-226, 1987.

Walton, O.R., Maddix, D.M., Butkovich, T.R., and Heuze, F.E., "Redirection of dynamic compressive waves in materials with nearly orthogonal and random joint sets," *Proc. ASME Appl. Mech. Conf. on Recent Adv. in Mech. of Structured Continua,* Columbus, Ohio, 1991.

Williams, J.R., "Contact analysis of large numbers of interacting bodies using modal methods for microscopic failure analysis," *Int. J. Comp. Aided Methods in Eng. - Eng. Comp.,* **5**, 1988.

Williams, J.R. and Pentland, A., "Superquadrics and Modal Dynamics for Discrete Elements in Interactive Design," *Engineering Computations,* **9**, pp. 115-127, 1992.

Xu, Y., and Shukla, A., "Evaluation of Static and Dynamic Contact Stresses in Simulated Granular Particles Using Strain Gages," *ASTM Journal of Testing and Evaluation,* **21**(3), pp. 178-187, 1993.

Zhu, C.Y., Shukla, A., and Sadd, M.H., "Prediction of dynamic contact loads in granular assemblies," *J. of App. Mech.,* **58**, pp. 341-346, 1991.

Zhu, Y., Shukla, A., and Sadd, M.H., "The effect of microstructural fabric on dynamic load transfer in two dimensional assemblies of elliptical particles," to appear in *Journal Mechanics & Physics of Solids,* 1996.

Summary of Publications and Theses/Dissertations

All of this previous work has resulted in several journal publications, conference presentations and thesis and dissertations as listed below.

Publications

1. "Role of Particle Shape and Contact Profile on the Dynamic Response of Particulate Materials," *Optics and Lasers in Engineering*, 19, 1993, pp. 99-119.

2. "Dynamic Response of Damaged Particulate Media," *Proceedings of the 1993 SEM "50th Anniversary" Spring Conference on Experimental Mechanics*, June 1993, pp. 1119-1128.

3. "On the Role of Pore Fluid and Interparticle Cementation on Wave Propagation in Granular Materials," Wave Propagation and Emerging Technologies, AMD- 188, eds. V.K. Kinra, R.J. Clifton and G.C. Johnson, 1994, pp. 11-28.

4. "A Photoelastic Investigation of Stress Wave Propagation in Cemented Granular Media," *Proceedings of the 1995 SEM Spring Conference and Exhibit*, June 1995, pp. 299-305.

5. "Effect of Flaws on the Stress Wave Propagation in Particulate Aggregates: Near and Far Field Observations," *International Journal of Solids and Structures*, 32(17/18), 1995, pp. 2523-2546.

6. "A Combined Experimental and Numerical Scheme for the Determination of Contact Loads Between Cemented Particles," Mechanics of Materials, 22, 1996, pp. 43-50.

7. "Displacement Measurements Over a Wide Range Utilizing a Simple Intensity Based Fiber Optic Sensor," to appear in *Proceedings of SPIE's 1996 Symposium on Smart Structures and Materials, Bridges, Structures, and Highways*, San Diego, Feb. 26-29, 1996.

8. "Wave Propagational Behaviors Through Assemblies of Elliptical Particles," presented at ASME - Particulate Mechanics Symposium, 1996, and to appear in *Computers and Geotechniques*.

9. "The Effect of Microstructural Fabric on Dynamic Load Transfer in Two Dimensional Assemblies of Elliptical Particles," *Journal of Mechanics and Physics of Solids*, 44(8), pp. 1283-1303, 1996.

10. "A Comparison of Explosively Generated Pulse Propagation in Assemblies of Disks

255

and Spheres," submitted to the *Journal of Engineering Mechanics.*

11. "A Discrete Element Study of the Relationship of Fabric to Wave Propagational Behaviors in Granular Materials," to appear in *International Journal for Numerical and Analytical Methods in Geomechanics.*

12. "Explosively Generated Pulse Propagation Through Particles Containing Natural Cracks," to appear in Mechanics of Materials.

Theses and Dissertations

1. Mr. S. Vishwanathan, Title of Thesis: "Study of Various Experimental Techniques and Their Application to Static and Dynamic Fields in Granular Media," M.S., 1994.

2. Mr. Gautam Adhikari, Title of Thesis: "Computer Simulation of Wave Propagation and Dynamic Load Transfer through Saturated Particulate Media," M.S., 1995.

3. Mr. Qiming Tai, Title of Dissertation: "Computational Studies of Wave Propagation in Granular Media," Ph.D., 1995.

4. Dr. Harry Zervas, Title of Dissertation: "Study of Stress Wave Propagation in Damaged Particulate Media," Ph.D., 1995.

5. Mr. Yan Zhu, Title of Dissertation: "Particle Shape Effects on Dynamic Load Transfer in Granular Media," Ph.D. in progress.

6. Mr. JiYong Gao, Title of Dissertation: "Numerical Studies of Dynamic Load Transfer in Granular Materials," Ph.D. in progress.

7. Mr. Frank Sienkiewicz, Title of Dissertation: "Influence of Cementation and Moisture on Load Transfer in Particulate Materials," Ph.D. in progress.

8. Mr. Victor Evora, Title of Thesis: "Development of a Dynamic Compression Loading Apparatus and Its Application to Particulate Composite," M.S., 1996.

Other Graduate Participants

Dr. Raman Singh, Z. Zhang, and S. Venkatram.

Interactions/Transitions

During the past year we have had several interactions with other civilian and DOD laboratories. In addition, several presentations of our work have been made at national

meetings.

- We presented an overview of our research at the *Workshop on Mechanics and Statistical Physics of Particulate Materials* hosted by the *Institute for Mechanics and Materials* at the University of California - San Diego, June, 1994.

- We have interacted with the **Naval Undersea Warfare Center** at Newport, RI. *Mr. Harry Zervas*, a senior engineer at NUWC, worked on his doctorate on this project. He is a co-author on our papers on damaged particles.

- Our work has been presented at the Spring Conference of the Society of Experimental Mechanics at Baltimore, MD, 1995. Two papers dealing with cementation effects and fiber-optic sensors were presented.

- Interaction with *Dr. Jack Dvorkin* of **Stanford University's Department of Geophysics**, Stanford, California, has continued this year. Use of his cemented particulate model has been done, and a joint paper has been developed and published.

- Some results of our studies dealing with wave propagation in saturated granular media have been presented at the *128th Annual Meeting of the Acoustic Society of American* in Austin, Texas, November, 1994.

- September, 1995, we presented an overview of our research work on wave propagation in granular materials to a NRL workshop on *Shock Wave Propagation Prediction* organized by Mark Emery at NRL, Washington, DC.

- Interactions have taken place with Mike Richardson of NRL at the Stennis Space Center in Mississippi, related to the NRL *Coastal Benthic Boundary Layer Program*. URI hosted a Wave Propagation Workshop in November, 1995, related to marine sediment behavior.

- Results of our work on cementation and pore fluid effects on wave propagation were presented at the ASME Winter Annual Meeting in Chicago, Illinois on November 1994. The paper was part of a symposium on *Wave Propagation and Emerging Technologies.*

- Results of our work on particle shape effects were presented at the ASME *Particlulate Mechanics Symposium*, June, 1996, at John's Hopkins University and

257

will appear in *Computers and Geotechniques.*

- Our research dealing with wave propagation in saturated granular and particulate systems has been of interest to a geomechanics research team at URI. This multi-disciplinary research group includes faculty from departments of civil, ocean and mechanical engineering. *Dr. Armand Silva* is head of the *Marine Geomechanics Laboratory*, and is the current leader of the *Geomechanics Research Group*. Current interaction activities include joint seminars and graduate student thesis committee work.

- Results of our work were presented at Texas A&M University Department of Mechanical Engineering in a seminar given by A. Shukla, April, 1995.

- Results of our work were presented at California Institute of Technology Department of Aeronautics and Mechanics, May, 1995.

Honors/Awards

- Professor Arun Shukla was elected *Fellow* of the *Society of Experimental Mechanics,* 1994.

- Mr. Raman Singh was awarded a *Doctoral Fellowship* from the *University of Rhode Island,* 1994, 1995.

- Professor A. Shukla was elected Fellow of the American Society of Mechanical Engineers.

- Mr. Yan Zhu received the Outstanding Paper Award at the Mechanics Conference held at Worcester Polytechnic Institute, 1996.